Advancements in structural and functional imaging using Fourier domain optical coherence tomography

by

Cerine Lal

Supervisors: Prof. Martin J. Leahy

Dr Sergey Alexandrov

A thesis submitted in partial fulfillment of the requirements for the degree of Doctor of Philosophy,

Tissue Optics and Microcirculation Imaging,

School of Physics, College of Science,

National University of Ireland, Galway

September 9, 2019

CONTENTS

Abstract

Optical Coherence Tomography (OCT) is a non-invasive optical imaging modality based on low coherence interferometry that enables high resolution, cross sectional imaging in biological tissues and materials. One major advantage of OCT is that it can be used to obtain both structural and functional information from the same data set. OCT has established itself as a clinically approved imaging technique in applications ranging from excised tissue imaging to high speed ocular imaging and intra coronary imaging. Research is still underway to enable faster volumetric data acquisition, to increase the axial and spatial resolution of imaging and to develop new processing techniques to enhance structural and functional imaging. Conventional structural OCT imaging is based on contrast from spatial variations in tissue scattering that exploit the changes in refractive index within the imaged sample. However, while taking the inverse Fourier transform of the interference signal to reconstruct the OCT structural image, the spatial frequency information which corresponds to small, submicron structure, is lost. This reduces the sensitivity of conventional OCT signal processing to detect submicron changes in the scattering structures.

Studying nanoscale structural and dynamic changes *in vivo* is fundamental to understanding changes occurring at cellular level before the changes manifest at the tissue level. Detecting these submicron structural changes could help scientists and clinicians to diagnose the onset of a disease, its progression and in determining treatment effectiveness of drugs. Along with structural imaging, functional imaging capability has been explored in the recent past especially for high resolution microvascular blood flow imaging. Functional extensions of OCT utilize the endogenous contrast mechanisms within the biological sample or the use of exogenous contrast agents. Functional OCT offers great potential in oncological applications, with emphasis on tumour vasculature, angiogenic processes, photodynamic therapy, targeted drug delivery and monitoring treatment efficacy. The motivation for this thesis is to explore the enhancement of structural and functional imaging capability using OCT based on endogenous and exogenous contrast mechanisms.

This thesis guides the reader towards the subject of OCT covering the fundamentals of Fourier domain OCT and the various functional extensions that have been developed over the years. Further, the thesis explores the optimization of correlation mapping OCT angiography using a high speed swept source OCT system for *in vivo* imaging applications in particular for ocular imaging. Moving on, the thesis describes ocular imaging of a pre-clinical rat burn model using a 200 kHz swept source OCT system. In order to assess the impact of the ocular burn and to monitor the wound healing process *in vivo*, graph based segmentation technique is developed to extract the central corneal thickness. The estimated central corneal thickness is then used to study the impact of stem cell based treatment for the wound healing process. Further, to map the corneal thickness over a 3D volume, a distance regularized level set based segmentation approach is implemented to generate pachymetry maps and used to assess the impact of corneal injury and the wound healing process.

Next, the thesis discusses the application of nano-sensitive OCT to detect the spatial and temporal structural changes within the cornea. The ability of nano-sensitive OCT to map structural changes within the cornea during the injury and subsequent wound healing process using just a single B-frame was confirmed. The study revealed that nano-sensitive OCT was able to detect structural changes with nano scale sensitivity between healthy cornea, injured cornea and also during the reparative phase of the injury at all depths within the cornea with high statistical significance. Further, a novel approach based on time-frequency decomposition of nano-sensitive OCT images is introduced which revealed corneal dynamics which otherwise have not been observed by conventional OCT processing techniques. Analysis of time varying spatial period signals within the cornea revealed five frequency bands corresponding to endothelial (0.-2 – 0.085 Hz), neurogenic (0.085 – 0.25 Hz), myogenic (0.25 -0.5 Hz), respiratory (0.5 – 1.5 Hz) and cardiac band (1.5 -5 Hz). Also, changes in energy content within the endothelial and neurogenic bands were observed between the healthy cornea and injured cornea that demonstrates the potential of the described technique for functional assessment. Analysis of these dynamic changes within the cornea can be used as a tool to study the effects of noxious stimuli on the corneal surface and its effects on the physiological signalling within the organism.

Further, the thesis discusses the design and development of a photothermal OCT system to detect the enhanced imaging depth capability of gold nanostars having a plasmon resonance at 1064 nm. Though many studies have reported the use of gold nanorods, nanoshells, nanospheres, nanorose and single walled carbon nanotubes as contrast agents for photothermal

OCT imaging, these studies used laser excitation wavelengths of 800 nm or below. Gold nanoparticles that has a localised surface plasmon resonance (LSPR) in the NIR region of the electromagnetic spectrum where both the absorption and scattering would be at their minimum can facilitate deeper imaging and provide better scattering contrast for biological tissue imaging. The characterization and optimization of the developed OCT system for photothermal imaging applications is discussed. Further, the photothermal signal enhancement by silica coating of the gold nanostars is explored. The experimental results demonstrated that silica coated gold nanostars of the same optical density can produce about two-fold higher photothermal signals compared to uncoated nanostars. Also, to investigate the deeper imaging capability of silica coated GNS within a scattering medium, photothermal studies were carried out on capillary phantoms having an inner diameter of 4 mm which demonstrated the enhanced imaging depth beyond 2 mm.

In summary, this thesis illustrates the methods in which a high speed optical coherence tomography can be employed as a tool for structural and functional imaging based on endogenous and exogenous contrast mechanisms.

Declaration

The work in this thesis is based on the research carried out at the Tissue Optics and Microcirculation laboratory (TOMI), School of Physics, National University of Ireland Galway. I, Cerine Lal , hereby certify that this thesis has been written by me, that it is the record of work carried out by me and that it has not been submitted in any previous application for a degree or qualification.

Where work of other people has been consulted, quoted, or made use of in any other way, it has been fully acknowledged and referenced accordingly.

Cerine Lal

15th September 2019

Acknowledgements

I would like to express my gratitude to all the people who have contributed to this thesis. First and foremost, the person to whom I am so ever grateful is my advisor Prof. Martin Leahy for giving me an opportunity to pursue PhD and for the guidance he has provided to me over the last number of years. I feel very fortunate for having Martin as my teacher and PhD mentor. It's been a long road and I appreciate all the advice, encouragement, concern and support he has given me along the way. Sincere thanks to Martin for being extremely patient during the initial years of my PhD. I would also like to thank my co-supervisor Dr Sergey Alexandrov for all his guidance, helpful discussions and advice. This thesis would not have been possible if not for you both. I am immensely indebted to you both for the time and resources you have invested in me. Sincerely, thank you.

I would like to especially thank Dr Hrebesh Subhash for all his encouragement and assistance during my early training and which continues onto this day. I thank for his time and patience in teaching me the details of OCT, which has provided the ground work for this thesis. A great amount of work described in this thesis came about as a result of collaborative work with Prof. Thomas Ritter and Dr Sweta Mehta. I owe special thanks to them. If not for their collaboration, this thesis may not have been possible.

To all the past members of TOMI group – Dr Paul, Dr Roshan, Dr Vijay, James, Sean, Aedan, Gillian and Dr Kai – thank you! Coming to the lab and working would not have been fun and exciting if not for you guys. Words cannot express how grateful I am to all of you for accommodating me into the TOMI group and for helping me settle into a new life in Galway city and making Galway my second home over the past many years. Also, thank you so much for motivating me, guiding me and being there for me when I felt lost. The time I spent with you all have been personally and professionally rewarding. I would also like to thank all the present members of the TOMI group - Anand, Ryan, Soorya, Rajib, Aron, Dr Andrew, Dr Yi and Dr Nandan. Thank you for your friendship and all the help that you guys have provided me over the past one year. My heartfelt gratitude to all the colleagues, technical staff and my graduate committee members for your support, encouragement and motivation during my time at School of Physics, NUIG.

To two special friends – Fernando and Salvo for your friendship. You guys have been amazing friends and great people to work with. Thank you for motivating and encouraging me to work with your work ethic and passion for science. To Ray and Tara, for welcoming me to 11 Sylvan Avenue and making it my home for the past four years – thank you so much! I also thank all the present and past housemates for your love, warmth, support, and for all the shared moments together. Thank you Damien, Thu, Alex, John, Laura, Sukanya and Nitin. I would also like to thank the Malayalee community in Galway for their love, warmth and support they have given me over the past number of years especially to Sunny uncle, Rajani chechi and their kids. Also, my heart felt gratitude to Sudip and Sayani, for all the love, support, fun, food and for being there for me through my personal and professional struggles. Galway would not have been the same for me if not for you all and this thesis may never have been brought to completion.

I would like to express my sincere gratitude to the priests and staffs of Galway cathedral. Thank you for your concern, love and quiet encouragement that I received over the past years and for helping me grow spiritually.

Finally, I would like to thank my friends back in India and around the world for their unwavering support and inspiration. Thank you all for keeping in touch and spending time and energy for making sure that I was doing well. Special thanks to Michael, Vaishak, Manish, Anu and Anand. I will be forever thankful to you all for your continuous and persistent efforts and for your infectious enthusiasm for research that you have shown to support me. I would not have persevered to finish my PhD if not for you all.

I am deeply grateful to my parents and my brother for their constant support, love and encouragement all through the years. Thank you so much for being supportive and letting me pursue my dreams despite social and personal pressures. Thank you for everything!

As in every other endeavour of my life, I thank Almighty God, for giving me the opportunity, abilities and circumstances to complete my PhD and I hope I have done justice to it, as far as I was able to. The years I spent in Ireland have taught me humility, kindness and patience and most importantly to be grateful for the people I have met in life. Having You beside me gives me the courage and strength to set out on uncertain paths without hesitation.

"In His time, He makes all things beautiful".

List of Publications

Refereed journal articles:

1. Lal Cerine, Molly Subhash *et al.* "Feasibility of correlation mapping optical coherence tomography angiographic technique using a 200 kHz vertical-cavity surface-emitting laser source for in vivo microcirculation imaging applications." *Applied Optics* 57.22 (2018): E224-E231.

2. Lal Cerine, and Martin J. Leahy. "An updated review of methods and advancements in microvascular blood flow imaging." *Microcirculation* 23.5 (2016): 345-363.

3. Lal Cerine, Sergey Alexandrov, Sweta Rani, Yi Zhou, Thomas Ritter, and Martin Leahy, "Nanosensitive optical coherence tomography to assess wound healing within the cornea," *Biomed. Opt. Express* 11, 3407-3422 (2020)

4. Martin Leahy, Pejuin Gong, **Cerine Lal**, Paul McNamara, David Sampson, 'Angiography and lymphangiography with optical coherence tomography', *(to be submitted to Journal of Biomedical Optics)*

Conference presentations:

1. Lal C., Alexandrov, S., Rani, S., Ritter, T., & Leahy, M. (2020, March). Probing temporal structural changes within cornea using 200 kHz swept source nano sensitive optical coherence tomography (nsOCT). In *Dynamics and Fluctuations in Biomedical Photonics XVII* (Vol. 11239, p. 1123909). International Society for Optics and Photonics.

2. Lal, **C**., Alexandrov S, Rani, S., Ritter, T., & Leahy, M,. "Nanosensitive optical coherence tomography to probe structural changes within the cornea". SPIE Photonics West, 2018.

3. Lal, **C**., Raghavan V, Subhash, H., & Leahy, M.,"Comparison of Si - coated and uncoated gold nanostars for photothermal OCT applications", Photonics Ireland (2017).

4. Lal, **C**., McGrath, J., Subhash, H., & Leahy, M. (2016, March). Optimization of modified scanning protocol based correlation mapping optical coherence tomography at 200 kHz VCSEL source for in vivo microcirculation imaging applications. In *Optical Coherence Tomography and Coherence Domain Optical Methods in Biomedicine XX* (Vol. 9697, p. 96973C). International Society for Optics and Photonics.

5. Lal, **C**., McGrath, J., Subhash, H., Rani, S., Ritter, T., & Leahy, M. (2016, March). Quantitative assessment of rat corneal thickness and morphology during stem cell therapy by high-speed optical coherence tomography. In *Ophthalmic Technologies XXVI* (Vol. 9693, p. 96931U). International Society for Optics and Photonics.

6. Ritter, T., **Lal**, **C**., Treacy, O., O'Malley, G. A., Naicker, S., Elbadawy, H., ... & Rani, S. (2016). Extracellular vesicles derived from human mesenchymal stem cells promote corneal wound repair by increasing epithelial cell proliferation and reducing neovascularisation in a rat corneal alkali burn model. *Investigative Ophthalmology & Visual Science*, *57*(12), (Conference Abstract).

7. Ritter, T., **Lal, C**., Treacy, O., O'Malley, G., Naughton, M., Naicker, S., ... & Leahy, M. (2016). Extracellular vesicles derived from Mesenchymal Stem Cells for treatment of Ocular Surface Injuries. *The FASEB Journal*, *30*(1_supplement), 373-1.

Manuscripts in preparation:

1. Lal Cerine, Alexandrov Sergey *et al*. "Probing time varying structural changes within cornea using optical coherence tomography". *(Manuscript in preparation).*

2. Lal Cerine, Raghavan V *et al*. "Plasmonic Gold Nanostars as a contrast agent for Near Infrared Photothermal Optical Coherence Tomography". *(Manuscript in preparation).*

3. Lal Cerine, Hrebesh Subhash *et al*. "Quantitative assessment of rat corneal thickness and morphology during stem cell therapy by high-speed optical coherence tomography". *(Manuscript in preparation).*

4. Sweta Rani, **Cerine Lal** *et al*. "Topically administered human mesenchymal stem cell-derived extracellular vesicles accelerate healing of acute corneal injury". *(Manuscript in preparation).*

Acronyms and Abbreviations

2-D	Two-dimensional
3-D	Three-dimensional
ARPAM	Acoustic resolution PAM
CAM	Chorioallantoic membrane
CCD	Charge-coupled device
CCT	Central corneal thickness
CDV	Complex differential variance
cmOCT	Correlation mapping OCT
CMOS	Complementary metal-oxide-semiconductor
CNR	Contrast to noise ratio
CNT	Carbon nanotube
CNV	Choroidal neovascularization
CSNR	Correlation signal to noise ratio
CT	Computerized tomography
CWS	Continuous wave spectroscopy
CWT	Continuous wavelet transform
DC	Direct current
DCM	Dichroic mirror
DCS	Diffuse correlation spectroscopy
DRLS	Distance regularized level set
DWP-OCT	Dual-wavelength photothermal OCT
ECG	Electrocardiogram
EEG	Electroencephalogram
EGFR	Epidermal growth factor receptors
ED	Eigen decomposition
EM	Electromagnetic
EMG	Electromyogram

EV	Extracellular vesicles
FDA	Food and drug administration
FD-OCT	Fourier domain OCT
FDML	Fourier domain mode locked Laser
fNIRS	Functional near infrared spectroscopy
FT	Fourier transform
FWHM	Full-width half maximum
GAG	Glycosaminoglycan
GI	Gastro intestinal
GNP	Gold nanoparticle
GNR	Gold nanorod
GNS	Gold nanostars
hMSC	Human mesenchymal stem cells
hMSC – EV	Human mesenchymal stem cells derived EV
HSI	Hyperspectral imaging
IDFI	Incident dark field imaging
IR	Infrared
LCI	Low coherence interferometry
LED	Light emitting diode
LDF	Laser Doppler flowmetry
LDPI	Laser Doppler perfusion imaging
LIC	Lesser iris circle
LSCI	Laser speckle contrast imaging
LSPR	Localised surface plasmon resonance
MEMS-VCSEL	Microelectromechanical systems based vertical cavity surface emitting Laser
MIC	Major iris circle
MIP	Maximum intensity projection
MSF	Mean spatial frequency
MSC	Mesenchymal stem cells
MSC-EV	MSC-derived extracellular vesicles

MRI	Magnetic resonance imaging
NA	Numerical aperture
NIR	Near infra-red
nsOCT	Nano-sensitive OCT
OCE	Optical coherence elastography
OCT	Optical coherence tomography
OCTA	Optical coherence tomography angiography
OD	Optical density
OMAG	Optical microangiography
OPD	Optical path displacement
OPL	Optical path length
ORPAM	Optical resolution PAM
PAI	Photoacoustic imaging
PAM	Photoacoustic microscopy
PAT	Photoacoustic tomography
PBS	Phosphate buffered saline
PET	Positron emission tomography
PSF	Point spread function
PS-OCT	Polarisation sensitive OCT
PT-OCT	Photothermal OCT
RIA	Radial iris arteries
RBC	Red blood cells
SaO2	Blood oxygenation
SDF	Side stream dark field imaging
SD-OCT	Spectral domain OCT
SLD	Super luminescent diode
SNR	Signal to noise ratio
SPIO	Supra magnetic iron oxide
SSADA	Split-spectrum amplitude-decorrelation angiography
SS-OCT	Swept source OCT
STED	Stimulated emission depletion tomography
STFT	Short-time Fourier transform

SV	Speckle variance
TD-OCT	Time domain OCT
TEM	Transmission electron microscope
UV	Ultraviolet

List of Figures

List of Tables

Chapter 1

BIOPHOTONICS AND OPTICAL IMAGING

1.1 Introduction

Biophotonics is a rapidly emerging field that utilizes photons to image, detect or manipulate biological materials [1]. The term 'optical imaging' refers to the use of electromagnetic radiation around the wavelength range of visible light to investigate and image structures of size ranging from molecular to macroscopic. The ability of light to observe and manipulate objects on a scale from several nanometers to centimeters with high precision and sensitivity without damaging them makes it an ideal technology for medical imaging and diagnostic applications. Beginning with the invention of microscopy, a multitude of increasingly sophisticated imaging methods that use the electromagnetic spectrum from UV to deep IR have been added and found widespread applications in material science, biology, and most importantly in medical imaging among others. Over the last 50 years, advances in the field of biophotonics have resulted in new high-resolution non-contact optical imaging techniques that have the potential to replace or complement existing ionizing /magnetic imaging modalities.

Medical optical imaging involves the use of visible or near infra-red (NIR) light to investigate the biological tissue. Medical optical techniques can be broadly divided into following categories based on the target features being probed or imaged [1]. They are:

a) Techniques based on the detection of morphological features either by measuring reflection, transmission/absorption or scattering within the tissue.
b) Techniques based on the detection of chemical signatures and their changes over time. E.g.: Raman and fluorescence imaging.
c) Techniques that detect movement within the tissue probed based on Doppler imaging or dynamic light scattering techniques.

Though optical imaging modalities offer great potential in clinical diagnostics and imaging for early detection of diseases, monitoring disease progression and treatment efficacy, they are limited in terms of their penetration depth in tissue, typically to a few millimetres. This limited penetration of light arises from the absorption and scattering of light by the chromophores and cellular structures within the biological tissue. However, the key advantage of optical imaging technique over other non-invasive, non-ionizing imaging techniques is its unprecedented spatial and temporal resolution. Also, optical imaging techniques can be employed using instrumentation that is compact, portable and economic compared to that of magnetic resonance imaging (MRI), computerised tomography (CT) or ultrasound based methods. The inherently strong spatio-temporal resolution of optical detectors is also an important asset in trying to observe time-varying physiological processes. Figure 1.1 illustrates the resolution vs. depth plot for the different medical imaging techniques that exist today. From figure 1.1, it can be observed that optical imaging techniques provide high axial resolution when compared to other commonly used diagnostic imaging modalities such as positron emission tomography, X-ray, computed tomography, magnetic resonance imaging or ultrasound imaging techniques.

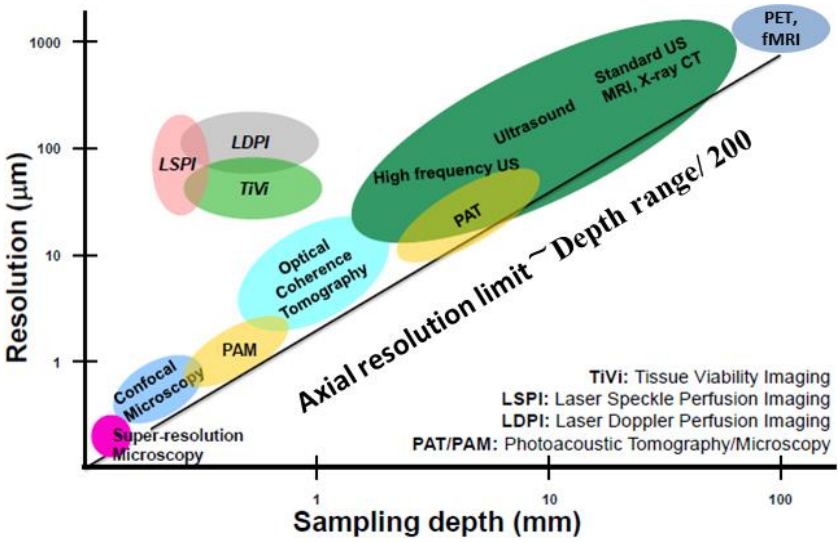

Fig. 1.1 Typical resolutions and penetration depths of selected label-free imaging techniques.

Also, figure 1.1 indicates that, for all imaging modalities, the depth of penetration within the tissue is inversely proportional to the voxel size in a 3D volume. This is due to the attenuation of light/sound waves coming back from deeper regions within the sample, thereby increasing the voxel size required to collect sufficient detectable signals from deeper regions. The likely cause of this is the fact that, the signal to noise ratios (SNR) are intrinsically proportional to the voxel volume or cube of spatial resolution (assuming its isotropic). This has been well established in fields such as X-ray, CT and ultrasound [2,3]. In a noise-limited scenario, the

PSF which is described as the response of an imaging system to a point source input is dependent on its SNR. The measured PSF is related to the standard deviation (uncertainty) of n measurements and this is proportional to $\sqrt{n}$ and hence local fluence (F) DV, where DV is the resolved volume [4]. Also, from figure 1.1, one can observe that, even wildly different imaging modalities, based on optics, ultrasound, magnetic resonance and X ray are limited to the same maximum depth-resolution quotient (200). Hence, we generally only have 200 useful pixels in depth when imaging scattering tissues; i.e. axial resolution for imaging in scattering tissues is generally limited to a maximum of (imaging depth)/200. Though several optical super-resolution and nanoscale detection techniques have been proposed recently, it remains a challenge to image structures that have large variations in size ($>10^4$) such as cells and whole organ using the same imaging technique [5].

There are many factors to be considered when designing an optical imaging system. An optical imaging system generates an image based on some interaction between light and tissue. Depending on the nature of the sample to be imaged, and the type of information sought (i.e. functional or structural), this interaction may be an absorption interaction (e.g. by haemoglobin or melanin), or a scattering mechanism (e.g. at boundaries, where the refractive index changes). The absorbing and scattering properties of tissue affect the penetration depth of light into the tissue. These properties are typically wavelength-dependent; thus, the choice of light source is of paramount importance.

In the next sections, an overview of different medical optical detection techniques that are used for structural and functional imaging are discussed. The optical imaging/detection modalities for clinical diagnostics can be broadly divided into superficial imaging techniques, subsurface imaging techniques, and deep tissue imaging techniques. The superficial imaging techniques include capillaroscopy, confocal microscopy, two-photon imaging, Raman imaging/spectroscopy and stimulated emission depletion tomography (STED). Subsurface imaging techniques consist of optical coherence tomography (OCT), hyperspectral imaging, sidestream dark field imaging (SDF), and incident dark field imaging (IDFI). The deep tissue imaging techniques described include diffuse correlation spectroscopy (DCS), functional near infra-red spectroscopy (fNIRS), and photoacoustic tomography (PAT).

1.2 Superficial Imaging Techniques

1.2.1 Video capillaroscopy

Video capillaroscopy is a simple and inexpensive imaging technique mainly used to study the morphology of superficial capillary structures within the first few micrometers from the skin surface. This technique uses white/green light source to illuminate the tissue of interest through a high-numerical aperture objective lens. Light backscattered from the tissue is collected by the objective lens and an image is formed on a CCD camera. Illuminating the tissue with green light, which is the isosbestic point of the absorption spectra of deoxy- and oxyhemoglobin instead of conventional white light, results in images with better sensitivity [6]. Video capillaroscopy has been used to study microangiopathologies occurring in the nail fold in many diseases such as Raynaud's phenomenon, systemic sclerosis, scleroderma, and connective tissue diseases [7,8]. Figure 1.2(a) shows the schematic of the setup and typical image obtained from the instrument.

1.2.2 Confocal microscopy and two-photon imaging

Confocal microscopy is a high-resolution, high-contrast 3D imaging technique that can image up to a depth of 200 µm *in vivo* mainly from the epidermis and superficial layer of dermis. The principle of confocal imaging was developed Marvin Minsky in 1955 [9]. In this technique, a small spot within the tissue is illuminated by a highly focused excitation beam. However, unlike conventional microscopy, the reflected light from the focal spot within the tissue is projected through a pinhole aperture onto a light detector. The use of a pinhole aperture allows only the focused light from the spot to pass through and completely eliminates the scattered light. Confocal microscopy uses reflected light or fluorescent light from the tissue for imaging. In order to create a 2D image, the focal spot is scanned across the surface of the sample [9]. Fluorescence confocal microscopy uses fluorescent dyes of fluorophores within the sample that fluoresce when stimulated by the excitation light. Fluorescence confocal microscopy has better sensitivity and specificity compared to reflection confocal microscopy. Figure 1.2(b) shows the schematic of a confocal microscope. Confocal microscopy has been used to study the principles of vessel regression [10], erythrocyte properties [11] and in detecting skin lesions in oncology [12].

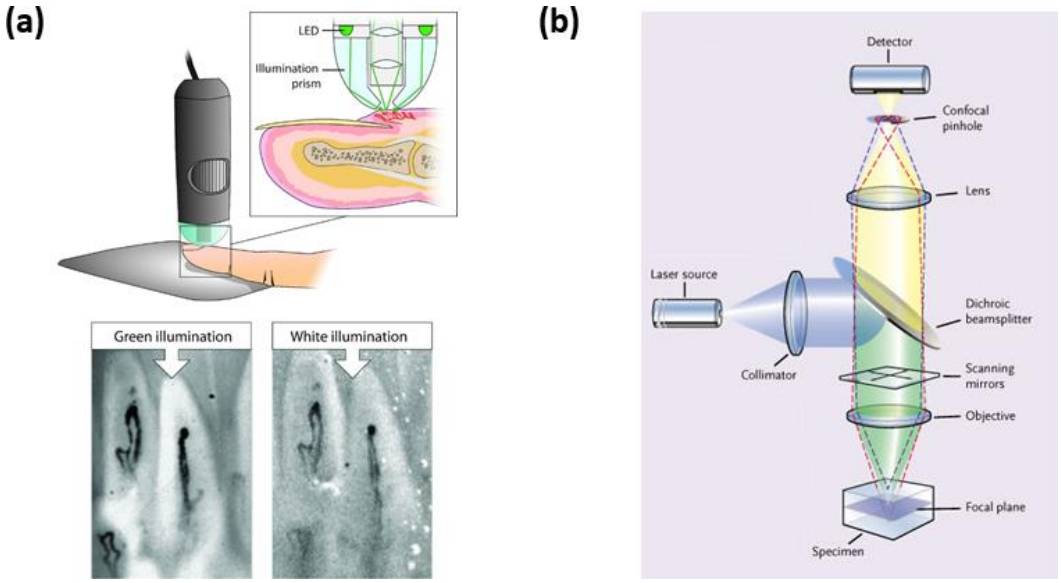

Fig. 1.2 (a) Illustration of the capillaroscope and its position on the nailfold (top). Bottom: two cropped abnormal capillaroscopic images of the same capillaries, magnification 200. Left acquired with green illumination. Right acquired with white illumination [7]. (b) Schematic of confocal microscopy imaging [10].

1.2.3 Two photon microscopy

Two-photon microscopy invented by Denk and co-workers provides an imaging depth of 1 mm in vivo in tissues. It is based on the simultaneous absorption of two infrared photons by a fluorophore causing it to fluoresce. Tight focusing brought about by near-simultaneous absorption of photons causes the out-of-focus fluorescent light to be eliminated without the use of a pin hole (as used in confocal microscopy). As the probability of near-simultaneous absorption is low, this technique requires the use of femtosecond lasers with short-pulse duration for excitation [13]. Since it uses NIR light, it has much deeper penetration within the tissue compared to confocal microscopy. A schematic of two photon microscopy is shown in Figure 1.3. Two-photon microscopy is used in rodent cerebrovascular analysis and neurocoupling studies [14,15], cancer research [16], microvasculature [17,18], and drug delivery [19].

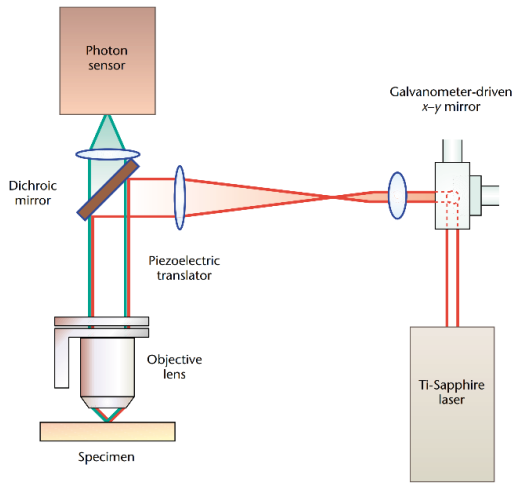

Fig. 1.3 Schematic of two-photon microscopy [14]

1.2.4 Stimulated emission depletion microscopy

STED introduced by Stefan W. Hell and Jan Wichmann in 1994 is one of the several super resolution microscopy imaging techniques that overcomes the diffraction limits of microscopy enabling high spatial resolution of 20 nm and axial resolution of 50 nm [20]. STED is based on the principles of fluorescence microscopy, however achieves super resolution imaging by selective deactivation of the excited fluorescent molecules by a second laser (doughnut shaped), thus only enabling the localised fluorescent emission to be detected and producing high resolution imaging. It has been used to image live brain slices [21], mitochondrial and live cell studies [22]. Aside from STED, various other super resolution microscopy imaging techniques have been developed and used for cellular imaging studies [23].

1.2.5 Raman imaging

Raman imaging is based on mapping the chemical constituents within a sample based on the acquired Raman spectra. It is based on the principle of inelastic scattering of light within a sample when excited with photons of appropriate energy [24]. To generate an image, Raman spectra are acquired at each sampling point of the target, and spectral signatures corresponding to the chemical constituents are mapped using false colour coding approach [25]. Raman imaging can produce images with a spatial resolution of 250-300 nm depending on the laser wavelength and the objective used. Though Raman spectroscopy has high sensitivity to molecular structure, when applied to biological tissue imaging, it is able to only detect the biomolecules present within the sample such as lipids, nucleic acids and proteins and hence

lacks specificity [26,27]. Raman imaging has been combined with autofluorescence imaging to delineate cancerous cells within a tissue [28].

1.3 Sub surface imaging techniques

1.3.1 Hyperspectral imaging

HSI or imaging spectroscopy originally introduced in remote sensing has become an emerging medical imaging technology over the past years [29,30]. HSI is a hybrid imaging modality that combines spatial information together with spectroscopic measurements with NIR light. HSI technique consists of light source (visible, near-infrared, or mid-infrared sources), dispersion elements (such as prism, grating), and spatial detectors (hyperspectral camera). The working principle of HSI is shown in figure 1.4. Light from the light source is used to illuminate the sample. The diffused reflected light from the sample, is then passed through a collimator, and after being diffracted by a grating element, is focused onto a spatial detector. Thus, at each spatial location, the camera registers the spectral signature. Two dimensional HSI imaging has been performed either by spatial scanning or by the spectral scanning approach. In the spatial scanning approach, 2D images are created by scanning the sample and creating a hypercube with two spatial dimensions and one spectral dimension [29,30]. In the spectral approach, the whole sample is captured using 2D detectors at each wavelength to form a hypercube. Hypercube data over a large number of wavelengths (10–100) having spectral resolution of 2 nm can be obtained using HSI. HSI has been used in clinical applications for microcirculation assessment and in detecting the tissue metabolic environment in tumor cells [31,32].

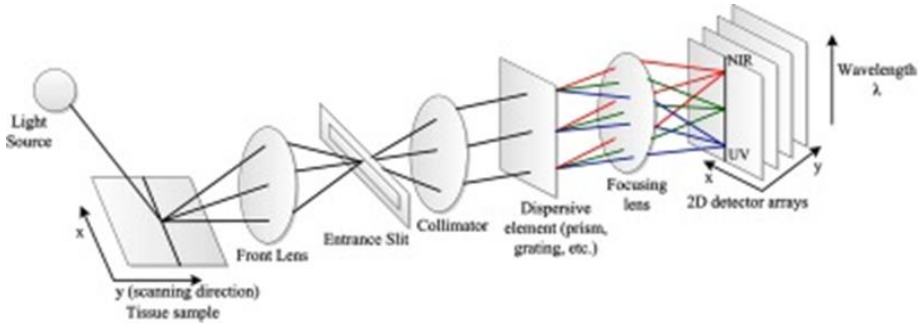

Fig.1.4 Working principle of hyperspectral imaging [31].

1.3.2 Laser doppler flowmetry and laser speckle contrast imaging

Laser Doppler Flowmetry (LDF) is a non-invasive real time measurement method to estimate the blood perfusion in the microcirculation. The method was first introduced over 45 years ago and has undergone a continuous development since [33,34]. It is based on the principle of Doppler shift in frequency of light backscattered by the moving red blood cells (RBC's) in the

microvascular bed of the tissue. Based on the detected Doppler shift in the backscattered light, mean blood flow over the target area can be measured. In order to enable spatial measurements, the laser Doppler perfusion imaging (LDPI) technique was developed. In this technique, the surface of the tissue is scanned by a freely impinging laser beam, thus generating an image of the spatial variability of blood perfusion [35]. Also, whole field LDPI was developed that utilizes CMOS sensors having high frame rates (1000 fps) that produces high speed imaging of the microvasculature.

Laser speckle contrast imaging (LSCI) first introduced in 1980's is a non-invasive, non-contact and whole field technique for blood flow measurement [36] based on speckle imaging. Laser speckle is a random interference effect that gives rise to a grainy appearance to objects illuminated by laser light. Photons interacting with moving scatterers such as RBC's undergo a Doppler shift that results in change of phase of the backscattered light thereby producing random intensity fluctuations within the speckle pattern. These temporal fluctuations of the speckle pattern can be captured by a CCD camera, and depending on the degree of movement within the imaged area, the level of blurring of the speckle image varies. In LSCI, this blurring of speckle patterns is used to map the underlying microvasculature. LSCI and LDPI have been used for retinal imaging [37], to evaluate microcirculation in the lower extremities of ulcer patients and in psoriatic plaques before and after treatment [38].

1.3.3 Sidestream dark field (SDF) and incident dark field imaging (IDF)

SDF and IDFI techniques are mainly used to assess microvasculature. SDF techniques consist of an illumination unit used to illuminating the tissue at 530 nm, a central light guide unit with lens system, and an imaging module with a CCD camera [39]. The illumination unit consists of concentrically placed LED surrounding the central light guide unit. SDF provides visualization of microcirculation at the cellular level; however, the maximum measurable flow velocities are limited by the frame rate of the camera (e.g., ~1 mm/sec at 30 frames per second). It has been used to image nail fold capillaries, to study buccal and cutaneous microcirculation [40]. IDF which is the successor of SDF uses incident dark field illumination [41]. IDFI is shown to better quantify (by 30%) micro vessels compared to SDF [42]. Also, IDF images have better image contrast and sharpness compared to SDF images. Schematic of SDFI and IDFI is shown in figure 1.5.

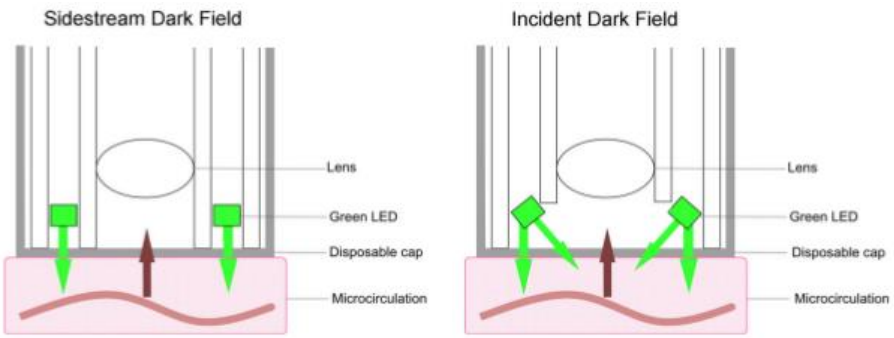

Fig.1.5 Schematic of SDFI and IDFI [42]

1.3.4 Optical coherence tomography (OCT)

OCT is a 3D tomographic imaging technique that provides high spatial and axial resolution over a depth of few millimetres (1–3 mm) for in vivo imaging [43]. OCT detects ballistic photons that are backscattered from various depths within the sample by utilizing coherence gating. Since its introduction in 1990's, it has been used for structural and functional imaging in a diverse set of medical and surgical applications, including ophthalmology, gastroenterology, dermatology, cardiology, and oncology, among others. The image penetration depth of OCT is determined by the optical scattering and is up to 2–3 mm in tissue. Although this depth is shallow compared with other clinical imaging techniques, the image resolution of OCT is 10–100 times finer than conventional ultrasound imaging, magnetic resonance imaging or computed tomography which makes OCT a promising technique for clinical diagnostics and imaging [44]. One of the major advantages of OCT is that it provides both morphological and functional information (angiography) from the same data set.

More details on the theory and applications of OCT are described in chapter 2.

1.4 Deep Tissue Imaging Techniques

1.4.1 Diffuse correlation spectroscopy

DCS is a dynamic scattering method based on the temporal variations in multiple scattered NIR light and has been used to study microvascular perfusion [45]. When light undergoes multiple scattering in a thick medium, at each scattering event, its phase is changed. Detection of these multiple scattered light fields creates a speckle pattern that varies over time. The penetration depth of NIR light in DCS experiments depend on the source to detector separation on the tissue surface. DCS has been able to measure changes in perfusion deep down to 3 cm on an

adult human head. DCS has been used to study changes in cerebral blood flow haemodynamics following ischemic stroke [46], brain injury and for neurovascular coupling studies [47] within the brain.

1.4.2 Functional near-infrared spectroscopy (fNIRS)

The application of NIRS in biological tissue was first demonstrated by Jobsis in 1977 [48]. The basic principle of fNIRS is that the differences in the absorption spectra of oxy-Hb and deoxy-Hb at two or more wavelengths within the spectral window can be used to measure the relative changes in oxy-Hb concentration. In fNIRS, the intensity changes of the backscattered light from the sample are quantified to detect the chromophore concentrations using the modified Beer–Lambert law [49]. Currently, there are three different variants of NIRS, namely continuous wave spectroscopy (CWS), time-of-flight spectroscopy, and frequency domain spectroscopy [50]. CWS is preferred over frequency domain and time-of-flight spectroscopy as these techniques are much more sophisticated and expensive. CWS uses an NIR light source to illuminate the sample and the changes in intensities of the diffusely reflected light collected from the sample is analysed to map the level of oxygenation within the probed tissue. Since its introduction, CWS has been used to study cerebral hemodynamics due to neurovascular coupling. Together with functional MRI, fNIRS has been used to study cerebral blood oxygenation changes during stimulation of the human brain [51,52].

1.4.3 Photoacoustic tomography (PAT) and microscopy (PAM)

In Photoacoustic Imaging (PAI), light pulses within the NIR region are used to generate ultrasound waves within the tissue produced by the optical absorption of chromophores [53,54]. Nanosecond pulses are delivered onto the tissue of interest, wherein it is locally absorbed by the tissue chromophores and is converted to heat. This generated heat causes the generation of pressure waves by thermoelastic expansion and the pressure waves propagate as ultrasound/photoacoustic waves, which can be detected by an ultrasound transducer. PAI is able to generate high contrast vascular maps based on the haemoglobin oxygen saturation in the blood. PAI is mainly of two types: PAT and PAM [54]. PAT uses low frequency ultrasound probes as transducers to detect the acoustic waves and hence can image up to a depth of 5 cm within a biological tissue. PAT provides spatial resolution of 0.1–1 mm and an axial resolution of 1 mm depending on the bandwidth of the ultrasound detector used and the light pulse duration, respectively. PAT is shown to be capable of imaging up to 5 mm

in biological tissue [55]. PAT generally uses low frequency ultrasound transducers <10 MHz to image depths greater than 1 cm.

Compared to PAT, PAM is able to achieve superior spatial resolution of 0.2–60 µm and imaging depth of several millimetres [56]. PAM is further divided into optical resolution PAM (ORPAM) and acoustic resolution (AR-PAM) based on tight optical focusing and acoustic focusing, respectively. OR-PAM provides high spatial resolution of 1–2 µm but has limited imaging depth of ~1 mm in muscle and ~0.6 mm in tissue due to the optical scattering in turbid media [54], whereas ARPAM has an imaging depth of several millimetres, but has spatial resolution of 50–60 µm. PAT and PAM have been used to image tumor microenvironment [57], tissue microvasculature and to quantify blood flow [58].

In conclusion the discussion above attests that optical imaging achieves high contrast and high resolution compared to non-optical methods such as MRI, CT, PET and ultrasound. However, these optical techniques have limited penetration depth within biological tissue. Most of the optical imaging techniques that perform the 3D volumetric structural imaging of tissues, are limited to a depth of imaging of 200 µm except OCT and PAT. However, as PAT is based on the absorption of light pulses by the chromophores within the probed volume, it mainly provides underlying functional information and not the 3D volumetric structural information within the probed volume.

Among the optical imaging techniques, OCT can provide both structural and functional information within a 3D volume, with high spatial and axial resolution. Although OCT has established itself as a clinically approved imaging technique in various applications ranging from excised tissue imaging to high speed ocular imaging and intravascular coronary imaging, research is still underway to enable faster volumetric data acquisition, to increase the axial and spatial resolution of imaging and to develop new processing techniques to enhance the sensitivity to structural and functional imaging. The motivation for this thesis is to explore the enhancement of structural and functional imaging capability using OCT based on endogenous and exogenous contrast mechanisms.

1.5 Structure of the thesis

A summary of the chapters of this thesis is as follows:

Chapter 1 introduces the area of biophotonics and existing medical optical imaging modalities together with their applications, penetration depths and resolution are discussed. The chapter

also provides the motivation and significance of this work including the key scientific contributions and a list of academic achievements generated from this thesis.

Chapter 2 describes the basic theory of OCT and fundamental system metrics are explained. A brief account of the various OCT modalities - time domain and Fourier domain are explained providing information on the basic theory, considerations, existing implementations of the technology and recent important developments in the field. The chapter also provides details on the existing structural and functioning imaging techniques using OCT and thus gives the technical background for the subsequent chapters discussed in this thesis.

Chapter 3 presents the feasibility study of correlation mapping (cmOCT) based OCT angiography technique using high speed (200 kHz) scanning system for *in vivo* imaging applications. The chapter begins with the introduction to OCT angiography, and provides an overview of existing angiographic techniques. Further, the chapter describes the optimization of an amplitude based cmOCT angiographic technique for a 200 kHz swept source OCT system. cmOCT angiography is compared with the widely used speckle variance (SV) angiographic technique based on phantom and *in vivo* imaging studies and cmOCT is shown to provide better image contrast metrics compared to SV angiography. This chapter also demonstrates the suitability of cmOCT angiography for ocular imaging.

Chapter 4 describes the ocular imaging of a pre-clinical rat burn model using 200 kHz OCT system. Details of the imaging protocol and pre-clinical burn model is presented. In order to assess the impact of the ocular burn and to monitor the wound healing process *in vivo*, graph based segmentation technique is used to extract the central corneal thickness. Further, the estimated central corneal thickness is used to study the impact of stem cell based treatment for the wound healing process following alkali injury. Due to the limitations of the graph based segmentation technique to map the corneal thickness over a 3D volume, a distance regularized level set based segmentation approach is used to segment the 3D volumetric corneal data and the developed technique is used to generate pachymetry maps. The generated pachymetry maps are used to assess the impact of corneal injury and the wound healing process.

Chapter 5 discusses the use of nano-sensitive OCT (nsOCT) to detect the spatial and temporal structural changes within a sample. The chapter begins with an account of the principles underlying the theory of nsOCT, moving on to describe the processing steps involved in

reconstructing a nsOCT image. Further, the applicability of nsOCT to probe the structural changes within the cornea following superficial alkali burn is presented. Also, this chapter describes novel wavelet based nsOCT approach to study corneal dynamics before and after the alkali injury.

Chapter 6 presents the development of a photothermal OCT system to detect the enhanced imaging depth capability of optical contrast agent - gold nanostars having plasmon resonance at 1064 nm. The characterization and optimization of the developed OCT system for photothermal imaging applications is discussed. Further, the photothermal signal enhancement by silica coating of the gold nanostars is described.

Chapter 7 provides a summary of the major results presented in this thesis and recommended future directions for this project.

1.6 Contributions of the thesis

The contributions of this thesis fall under two categories - technical novelties and pre-clinical applications. Key contributions are summarised as follows:

1. Optimization of cmOCT angiographic technique on a very high speed OCT system and the first reported demonstration of suitability of cmOCT angiography for wide field ocular imaging.
2. Corneal image segmentation and generation of corneal pachymetry maps demonstrating its suitability to monitor corneal wound healing process.
3. Demonstration of sub-micron sensitivity of nsOCT approach for *in-vivo* corneal imaging applications. The first description of time frequency decomposition of nsOCT signals to study corneal dynamics in healthy and burn injury pre-clinical corneal model.
4. Design and development of a photothermal OCT system for imaging gold nanostars having plasmon resonance peak at 1064 nm and demonstrating the enhanced depth of imaging in scattering phantoms. The first description of enhancement in imaging contrast by Si-coating of nanoparticle for photothermal OCT imaging applications.

REFERENCES

1. "Introduction to Biophotonics - Jürgens - 2012 - Major Reference Works - Wiley Online Library," https://onlinelibrary.wiley.com/doi/full/10.1002/9783527643981.bphot001.
2. R. S. Balaban and V. A. Hampshire, "Challenges in Small Animal Noninvasive Imaging," ILAR J. **42**, 248–262 (2001).
3. N. L. Ford, M. M. Thornton, and D. W. Holdsworth, "Fundamental image quality limits for microcomputed tomography in small animals," Med. Phys. **30**, 2869–2877 (2003).
4. H. H. Barrett and W. Swindell, *Radiological Imaging: The Theory of Image Formation, Detection, and Processing* (Elsevier Inc., 2012).
5. P. C. Montgomery and A. Leong-Hoi, "Emerging optical nanoscopy techniques," Nanotechnol. Sci. Appl. **8**, 31–44 (2015).
6. A. K. Murray, K. Feng, T. L. Moore, P. D. Allen, C. J. Taylor, and A. L. Herrick, "Preliminary clinical evaluation of semi-automated nailfold capillaroscopy in the assessment of patients with Raynaud's phenomenon.," Microcirc. N. Y. N 1994 **18**, 440–447 (2011).
7. M. Etehad Tavakol, A. Fatemi, A. Karbalaie, Z. Emrani, and B.-E. Erlandsson, "Nailfold Capillaroscopy in Rheumatic Diseases: Which Parameters Should Be Evaluated?," BioMed Res. Int. **2015**, (2015).
8. W. Grassi and R. De Angelis, "Capillaroscopy: questions and answers," Clin. Rheumatol. **26**, 2009 (2007).
9. A. Nwaneshiudu, C. Kuschal, F. H. Sakamoto, R. Rox Anderson, K. Schwarzenberger, and R. C. Young, "Introduction to Confocal Microscopy," J. Invest. Dermatol. **132**, 1–5 (n.d.).
10. C. A. Franco, M. L. Jones, M. O. Bernabeu, I. Geudens, T. Mathivet, A. Rosa, F. M. Lopes, A. P. Lima, A. Ragab, R. T. Collins, L.-K. Phng, P. V. Coveney, and H. Gerhardt, "Dynamic Endothelial Cell Rearrangements Drive Developmental Vessel Regression," PLoS Biol. **13**, (2015).
11. C. Saldanha, "Instrumental analysis applied to erythrocyte properties," J. Cell. Biotechnol. **1**, 81–93 (2015).
12. G. Pellacani, P. Pepe, A. Casari, and C. Longo, "Reflectance confocal microscopy as a second-level examination in skin oncology improves diagnostic accuracy and saves unnecessary excisions: a longitudinal prospective study," Br. J. Dermatol. **171**, 1044–1051 (2014).

13. P. T. So, "Two-photon Fluorescence Light Microscopy," in *eLS* (American Cancer Society, 2001).
14. T. Dalkara and L. Alarcon-Martinez, "Cerebral microvascular pericytes and neurogliovascular signaling in health and disease," Brain Res. **1623**, 3–17 (2015).
15. C. N. Hall, C. Reynell, B. Gesslein, N. B. Hamilton, A. Mishra, B. A. Sutherland, F. M. O'Farrell, A. M. Buchan, M. Lauritzen, and D. Attwell, "Capillary pericytes regulate cerebral blood flow in health and disease," Nature **508**, 55–60 (2014).
16. J. Liu and J. Liu, "Two-photon microscopy in pre-clinical and clinical cancer research," Front. Optoelectron. **8**, 141–151 (2015).
17. F. Ihler, M. Bertlich, B. Weiss, S. Dietzel, and M. Canis, "Two-Photon Microscopy Allows Imaging and Characterization of Cochlear Microvasculature In Vivo," https://www.hindawi.com/journals/bmri/2015/154272/.
18. H. Wang, U. Baran, Y. Li, W. Qin, W. Wang, H. Zeng, and R. K. Wang, "Does optical microangiography provide accurate imaging of capillary vessels?: validation using multiphoton microscopy," J. Biomed. Opt. **19**, (2014).
19. R. Khandelia, S. Bhandari, U. N. Pan, S. S. Ghosh, and A. Chattopadhyay, "Gold Nanocluster Embedded Albumin Nanoparticles for Two-Photon Imaging of Cancer Cells Accompanying Drug Delivery.," Small Weinh. Bergstr. Ger. **11**, 4075–4081 (2015).
20. G. Vicidomini, P. Bianchini, and A. Diaspro, "STED super-resolved microscopy," Nat. Methods **15**, 173–182 (2018).
21. R. Chéreau, J. Tønnesen, and U. V. Nägerl, "STED microscopy for nanoscale imaging in living brain slices," Methods **88**, 57–66 (2015).
22. T. Müller, C. Schumann, and A. Kraegeloh, "STED Microscopy and its Applications: New Insights into Cellular Processes on the Nanoscale," ChemPhysChem **13**, 1986–2000 (2012).
23. S. Cox, "Super-resolution imaging in live cells," Dev. Biol. **401**, 175–181 (2015).
24. Y. Zhang, H. Hong, and W. Cai, "Imaging with Raman Spectroscopy," Curr. Pharm. Biotechnol. **11**, 654–661 (2010).
25. L. Opilik, T. Schmid, and R. Zenobi, "Modern Raman Imaging: Vibrational Spectroscopy on the Micrometer and Nanometer Scales," Annu. Rev. Anal. Chem. **6**, 379–398 (2013).
26. N. K. Das, Y. Dai, P. Liu, C. Hu, L. Tong, X. Chen, and Z. J. Smith, "Raman Plus X: Biomedical Applications of Multimodal Raman Spectroscopy," Sensors **17**, (2017).

27. C. W. Freudiger, W. Min, B. G. Saar, S. Lu, G. R. Holtom, C. He, J. C. Tsai, J. X. Kang, and X. S. Xie, "Label-Free Biomedical Imaging with High Sensitivity by Stimulated Raman Scattering Microscopy," Science **322**, 1857–1861 (2008).
28. S. Cui, S. Zhang, and S. Yue, "Raman Spectroscopy and Imaging for Cancer Diagnosis," J. Healthc. Eng. **2018**, (2018).
29. M. A. Calin, S. V. Parasca, D. Savastru, and D. Manea, "Hyperspectral Imaging in the Medical Field: Present and Future," Appl. Spectrosc. Rev. **49**, 435–447 (2014).
30. G. Lu and B. Fei, "Medical hyperspectral imaging: a review," J. Biomed. Opt. **19**, 10901 (2014).
31. G. Lu, L. Halig, D. Wang, X. Qin, Z. G. Chen, and B. Fei, "Spectral-spatial classification for noninvasive cancer detection using hyperspectral imaging," J. Biomed. Opt. **19**, 106004 (2014).
32. J. Yoon, J. Joseph, D. J. Waterhouse, A. S. Luthman, G. S. D. Gordon, M. di Pietro, W. Januszewicz, R. C. Fitzgerald, and S. E. Bohndiek, "A clinically translatable hyperspectral endoscopy (HySE) system for imaging the gastrointestinal tract," Nat. Commun. **10**, 1902 (2019).
33. M. D. Stern, "In vivo evaluation of microcirculation by coherent light scattering," Nature **254**, 56 (1975).
34. J. D. Briers, "Laser Doppler, speckle and related techniques for blood perfusion mapping and imaging," Physiol. Meas. **22**, R35–R66 (2001).
35. T. J. H. Essex and P. O. Byrne, "A laser Doppler scanner for imaging blood flow in skin," J. Biomed. Eng. **13**, 189–194 (1991).
36. A. F. Fercher and J. D. Briers, "Flow Visualization by Means of Single-Exposure Speckle Photography," Opt. Commun. **37**, 326–330 (1981).
37. A. Rege, S. I. Cunningham, Y. Liu, K. Raje, S. Kalarn, M. J. Brooke, L. Schocket, S. Scott, A. Shafi, L. Toledo, and O. J. Saeedi, "Noninvasive Assessment of Retinal Blood Flow Using a Novel Handheld Laser Speckle Contrast Imager," Transl. Vis. Sci. Technol. **7**, (2018).
38. A. K. Murray, A. L. Herrick, T. L. Moore, T. A. King, and C. E. M. Griffiths, "Dual wavelength (532 and 633 nm) laser Doppler imaging of plaque psoriasis," Br. J. Dermatol. **152**, 1182–1186 (2005).
39. P. T. Goedhart, M. Khalilzada, R. Bezemer, J. Merza, and C. Ince, "Sidestream Dark Field (SDF) imaging: a novel stroboscopic LED ring-based imaging modality for clinical assessment of the microcirculation.," Opt. Express **15**, 15101–15114 (2007).

40. V. J. van den Berg, H. A. van Elteren, E. A. B. Buijs, C. Ince, D. Tibboel, I. K. M. Reiss, and R. C. J. de Jonge, "Reproducibility of Microvascular Vessel Density Analysis in Sidestream Dark-Field-Derived Images of Healthy Term Newborns," Microcirculation **22**, 37–43 (2015).
41. G. Aykut, G. Veenstra, C. Scorcella, C. Ince, and C. Boerma, "Cytocam-IDF (incident dark field illumination) imaging for bedside monitoring of the microcirculation," Intensive Care Med. Exp. **3**, (2015).
42. H. A. van Elteren, C. Ince, D. Tibboel, I. K. M. Reiss, and R. C. J. de Jonge, "Cutaneous microcirculation in preterm neonates: comparison between sidestream dark field (SDF) and incident dark field (IDF) imaging," J. Clin. Monit. Comput. **29**, 543–548 (2015).
43. D. Huang, E. A. Swanson, C. P. Lin, J. S. Schuman, W. G. Stinson, W. Chang, M. R. Hee, T. Flotte, K. Gregory, C. A. Puliafito, and J. G. Fujimoto, "Optical Coherence Tomography," Science **254**, 1178–1181 (1991).
44. J. G. Fujimoto, C. Pitris, S. A. Boppart, and M. E. Brezinski, "Optical Coherence Tomography: An Emerging Technology for Biomedical Imaging and Optical Biopsy," Neoplasia N. Y. N **2**, 9–25 (2000).
45. T. Durduran and A. G. Yodh, "Diffuse correlation spectroscopy for non-invasive, micro-vascular cerebral blood flow measurement," NeuroImage **85**, 51–63 (2014).
46. J. P. Culver, T. Durduran, D. Furuya, C. Cheung, J. H. Greenberg, and A. G. Yodh, "Diffuse optical tomography of cerebral blood flow, oxygenation, and metabolism in rat during focal ischemia," J. Cereb. Blood Flow Metab. Off. J. Int. Soc. Cereb. Blood Flow Metab. **23**, 911–924 (2003).
47. T. Durduran, G. Yu, M. G. Burnett, J. A. Detre, J. H. Greenberg, J. Wang, C. Zhou, and A. G. Yodh, "Diffuse optical measurement of blood flow, blood oxygenation, and metabolism in a human brain during sensorimotor cortex activation," Opt. Lett. **29**, 1766–1768 (2004).
48. F. F. Jobsis, "Noninvasive, infrared monitoring of cerebral and myocardial oxygen sufficiency and circulatory parameters," Science **198**, 1264–1267 (1977).
49. U. Dirnagl, K. M. Einhäupl, and A. Villringer, eds., *Optical Imaging of Brain Function and Metabolism*, Advances in Experimental Medicine and Biology (Springer US, 1993).
50. J. A. Wahr, K. K. Tremper, S. Samra, and D. T. Delpy, "Near-Infrared spectroscopy: Theory and applications," J. Cardiothorac. Vasc. Anesth. **10**, 406–418 (1996).
51. M. Strait and M. Scheutz, "What we can and cannot (yet) do with functional near infrared spectroscopy," Front. Neurosci. **8**, (2014).

52. M. A. Yücel, C. M. Aasted, M. P. Petkov, D. Borsook, D. A. Boas, and L. Becerra, "Specificity of Hemodynamic Brain Responses to Painful Stimuli: A functional near-infrared spectroscopy study," Sci. Rep. **5**, (2015).
53. L. V. Wang and J. Yao, "A practical guide to photoacoustic tomography in the life sciences," Nat. Methods **13**, 627–638 (2016).
54. J. Xia, J. Yao, and L. V. Wang, "Photoacoustic tomography: principles and advances," Electromagn. Waves Camb. Mass **147**, 1–22 (2014).
55. P. J. van den Berg, K. Daoudi, and W. Steenbergen, "Review of photoacoustic flow imaging: its current state and its promises," Photoacoustics **3**, 89–99 (2015).
56. J. Yao and L. V. Wang, "Photoacoustic microscopy," Laser Photonics Rev. **7**, 758–778 (2013).
57. M. Mehrmohammadi, S. J. Yoon, D. Yeager, and S. Y. Emelianov, "Photoacoustic Imaging for Cancer Detection and Staging," Curr. Mol. Imaging **2**, 89–105 (2013).
58. S. Hu and L. V. Wang, "Photoacoustic imaging and characterization of the microvasculature," J. Biomed. Opt. **15**, (2010).

Chapter 2

FUNDAMENTAL PRICIPLES OF OPTICAL COHERENCE TOMOGRAPHY

2.1 Optical Coherence Tomography

2.1.1 Basic theory

Optical Coherence Tomography (OCT) is an imaging technique based on low coherence (or broadband) interferometry (LCI) [1]. OCT relies on measuring the backscattered light to construct high resolution images of the internal structures of biological tissues with high axial and lateral resolution [2]. OCT is based on the principles of partial coherence interferometry, the widely used configuration being that of a Michaelson's interferometer. This consists of a light source, a beam splitter, a reference arm, a sample arm and a detector as shown in figure 2.1. The light from the source passes through beam splitter, that splits one portion of the incoming beam to a reference arm and other portion to a sample arm. At the detector, the two beams interfere if they have travelled the same optical pathlength in both the arms, and hence only the light backscattered from a selected depth within the sample is detected. The detector then passes the signal to a processor which processes the signal and forms the image. Scanning the light beam laterally across a sample gives a series of A-scans at different locations, can be used to form a 2D image known as a B-scan, or a B-frame. M-mode imaging is also commonly used, whereby repeated A-scans at the same location are performed over time (M-B mode) or where repeated B frames of the same location are acquired over time (B-M mode).

One of the advantages of OCT is that the axial resolution of the imaging system is decoupled from the lateral resolution [3]. The axial (depth) resolution of an OCT system is determined by the inverse of the bandwidth of the light source used, which in turn is related to the width of the coherence gate. At the detector, interference pattern is formed when the backscattered light within the sample has travelled approximately the same optical pathlength to that of the reference beam, with an error within the coherence length of the light source. The shorter the coherence length of the light source, the shorter the distance over which interference can occur.

Thus, the coherence length sets the limit to axial resolution of the system and it is for this reason that low coherence light is used in OCT. Hence, in order to resolve two neighbouring features depth-wise, they must be separated by a distance greater than the width of the coherence gate [4].

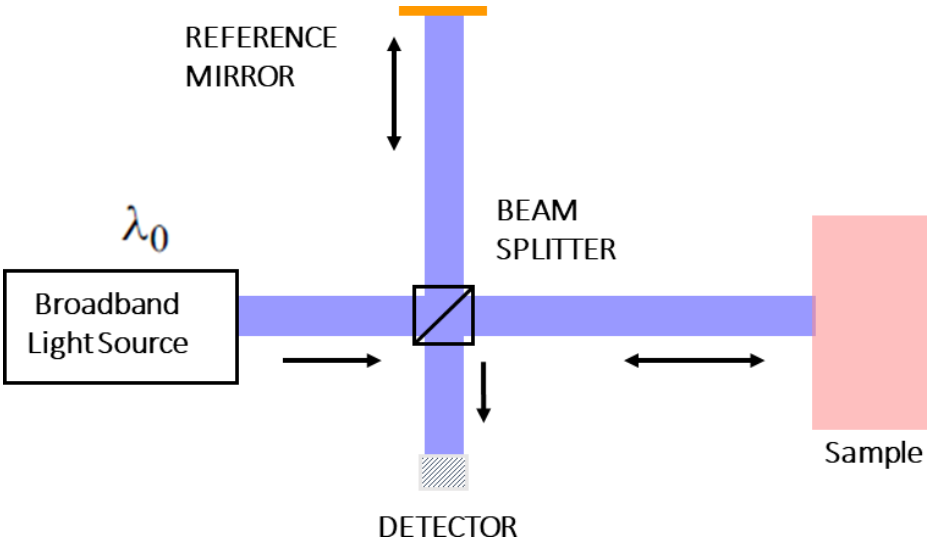

Fig.2.1 Schematic of a time domain OCT system

In most real-world applications, the sample to be imaged could be any random object such as a biological tissue. In the Michaelson interferometric set up shown in figure 2.1, the electric field incident on the beam splitter (50:50) after returning from the sample arm can be written as,

$$E_S = \frac{E_i}{\sqrt{2}} \sum_{n=1}^{N} r_{sn} e^{-i2kz_n} \qquad (2.1)$$

where E_i is the incident field and E_s is the scattered field, r_{sn} is the reflectivity of a scattering centre n at distance z_n within the sample and k is the wave number.

The electric fields at the beam splitter (50:50) after returning from the reference arm can be written as :

$$E_R = \frac{E_i}{\sqrt{2}} r_R e^{-i2kz_R} \qquad (2.2)$$

where E_R is the back reflected field from the reference mirror, r_R is the reflectivity of the reference mirror and z_R is the optical path length to the reference mirror measured from the beam splitter. The recombined optical signal from the reference arm and the sample arm at the photodetector can be written as :

$$I(k,w) = \frac{\rho}{2} < |E_S + E_R|^2 > \qquad (2.3)$$

where ρ is the responsivity of the detector (units Amperes/Watt) and the angular brackets denote integration over the response time of the photodetector [4]. Expanding equation (4) gives,

$$I(k) = \frac{\rho}{4}[S(k)(\, r_{s1} + \, r_{s2} + r_{s3} + \cdots)] \quad \text{'DC terms'}$$

$$+\frac{\rho}{2}[\, S(k) \sum_{n=1}^{N} \sqrt{r_R r_{sn}}\, (\, cos(2k(z_R - z_{sn}))\,)\,] \quad \text{'Cross correlation terms'}$$

$$+\frac{\rho}{4}[\, S(k) \sum_{n\neq m=1}^{N} \sqrt{r_{sm} r_{sn}}\, (\, cos(2k(z_{sm} - z_{sn}))\,)\,] \quad \text{'Auto correlation terms'} \qquad (2.4)$$

where $S(k) = < |s(k,w)|^2 >$ is the power spectral dependence of the light source, r_{sm} and r_{sn} are sample reflectivities at layer *m* and *n* respectively, z_{sm} and z_{sn} are the pathlengths to the layers *m* and *n* within the sample measured from the beam splitter. Equation 2.4 shows that the resulting interference signal is composed of a pathlength independent constant term with amplitude proportional to the power reflectivity of the reference mirror plus the sum of the sample reflectivities, 'cross-correlation' components for each sample reflector, which depend upon the pathlength difference between the reference arm and sample reflectors (desired OCT signal) and 'autocorrelation' terms representing interference between the different sample reflectors appear as artefacts in typical OCT system designs [4]. Thus, the detected interferogram $I(k)$ is the summation of the multiple sinusoids (from reflectors at different depths), shaped by the source spectrum $S(k)$.

In other words, TD-OCT measures the time delay of reflected light to retrieve depth information about the sample by scanning the reference arm mirror, and so the measured intensity is a function of time. Coherence gating, in which beams from the reference and sample arms will only interfere when their optical path length difference Δz is within the coherence length of the light source Δk, is used to differentiate backscattered light from different depths. As the reference arm mirror moves specific distances within the coherence length of the source, a single measurement is performed at each position of the mirror, thereby each one forming a point on an A-line. The reflections from the sample at different depths are measured as variations in the interference signal (intensity at the detector) at different times. By scanning separately in the axial and lateral directions, three-dimensional volume scans can be obtained. The major limiting factor of TD-OCT systems is the slow image acquisition rates which depend on how fast the reference mirror can move [7].

In OCT, the axial resolution of the system, Δz, is defined by the source coherence length (l_c) i.e. $\Delta z = l_c/2$. For a source with a Gaussian spectral distribution, the coherence length can be defined by the full-width at half maximum (FWHM) of the coherence function. This gives the axial resolution [4] as:

$$\Delta z = \frac{2\ln 2\,\lambda_o^2}{\pi\Delta\lambda} \approx \frac{0.44\lambda_o^2}{\Delta\lambda} \approx \frac{\lambda_o^2}{2\Delta\lambda} \quad (2.5)$$

where λ_o is the central wavelength of the source and $\Delta\lambda$ is the bandwidth.

The lateral (transverse) resolution, Δx, of an OCT system is independent of the axial resolution and is determined by the spot size of the focused light beam [3,4,6]. Thus, the choice of numerical aperture (NA) for the objective lens decides the lateral resolution of the system. Assuming a Gaussian source, the lateral resolution of OCT is given by equations (2.6) or (2.7) [4]:

$$\Delta x = \frac{4\lambda_o f}{\pi d} \quad (2.6)$$

where d denotes the diameter of the beam entering an objective lens of focal length, f. Lateral resolution is dependent of the numerical aperture of the objective lens used and is given by equation 2.7.

$$\Delta x = 0.37\,\frac{\lambda_o}{NA} \quad (2.7)$$

Numerical aperture, $NA = n\sin(\alpha)$, where α is half the angle optical aperture subtended by the objective and n is the refractive index. For high lateral resolution, a large NA is required to focus the beam to a small spot size. However, the lateral resolution is also tied to the depth of focus of the imaging system.

The depth of focus, or confocal parameter, b, is given as twice the Rayleigh range, z_R.

$$b = 2z_R = \frac{\pi\Delta x^2}{2\lambda_o} \quad (2.8)$$

From equation 2.8, it can be observed that, a high lateral resolution comes at the expense of depth of focus. While a low NA objective would limit the lateral resolution but provide a long depth of focus. This trade-off between the lateral resolution and the depth of focus is an important factor to consider in the design of any OCT system.

2.1.2 Time-domain and frequency-domain OCT

Since the introduction of OCT's, there has been numerous approaches to develop OCT systems based on the principles of low coherence interferometry. Currently, all commercial and research OCT systems belongs to either time - domain (TD-OCT) or Fourier - domain OCT (FD-OCT) systems. The first generation of OCT systems were based on TD-OCT [3,6]. In OCT, the intensity signal measured at the detector is that of an interference pattern, resulting from the superposition of the electric fields from the sample arm, E_S, and the reference arm, E_R given by equation 2.4. Since the introduction of OCT's, there have been three main approaches

to develop OCT systems based on the principles of low coherence interferometry. Currently, all commercial and research OCT systems belong to either time-domain (TD-OCT), Fourier-domain/Spectral-domain OCT (FD/SD-OCT), or Swept-Source OCT (SS-OCT) systems.

Unlike TD-OCT, FD-OCT measures the intensity of the interferogram as a function of wavelength rather than time. It then relates this frequency spectrum to the sample's depth profile through an inverse Fourier transform. FD-OCT is based on the Fourier relation between the scattering potential and the scattering amplitude [5,8]. The spectral interferogram i.e. the backscattered field amplitude, and the sample's depth profile i.e. its scattering potential, are a Fourier pair. The theory is explained in detail in chapter 5. The beam returning from the sample is made up of multiple partial waves from many backscatterers located at various depths. Thus, the spectrum at the detector is the sum of all the interference fringes generated by the interference of light reflected from various depths in the sample and the light reflected from the reference arm. In this way, FD-OCT acquires all points on an A-line at the same time. FD-OCT can be realized in two different ways; either by using a using a spectrometer as the detector [3,6,7] called the spectral domain OCT (SD-OCT) or by a wavelength tuning technique (swept-source OCT, SS-OCT) which sweeps the wavelength of the light source and utilises a photodiode as the detector as illustrated in figures 2.2(a) and 2.2(b) respectively.
The schematic of SD-OCT is shown in figure 2.2(a) and is based on the principles of spectral interferometry. It uses a broadband light source, such as a super luminescent diode, and a spectrometer, so that the different frequencies in the signal can be separated into different spatial locations and observed at the same time. Many publications have demonstrated that by using detectors with large number of pixels, SD-OCT can provide superior signal quality in regards of sensitivity and achieves scan speeds for video rate imaging tasks. The detector response can be depicted as [9].

$$q_{fdoct}(k) \sim \sqrt{r_R r_S} \int_0^{\frac{1}{f_{ascan}}} \int_k^{k+\delta k} S(k) cos\,(2kx) dk dt \qquad (2.9)$$

where $q_{fdoct}(k)$ is the quantity of photoelectrons collected over the duration of an A scan ($\frac{1}{f_{ascan}}$) in a charge-coupled device. The recorded frequency spectrum is then converted to sample depth profile by an inverse Fourier transform. The mathematical description of the detected sample depth profile (A-line) is given by equation 2.10.

$I(z) = \frac{\rho}{8}[\gamma(z)(\, r_{s1} + \, r_{s2} + r_{s3} + \cdots)]$ 'DC terms'

$+\frac{\rho}{4}[\,\gamma(z)\sum_{n=1}^{N}\sqrt{r_R r_{sn}}\,(\,\gamma[2(z_R - z_{sn})] + \gamma[-2(z_R - z_{sn})]\,]$ 'Cross correlation terms'

$+\frac{\rho}{8}[\,\gamma(z)\sum_{n\neq m=1}^{N}\sqrt{r_{sm} r_{sn}}\,(\,\gamma[2(z_{sm} - z_{sn})] + \gamma[-2(z_{sm} - z_{sn})]\,]$ 'Auto correlation terms'

(2.10)

where $\gamma(z)$ denotes the inverse Fourier transform of the source spectrum $S(k)$, r_{sm} and r_{sn} are sample reflectivities at layer *m* and *n* respectively, z_{sm} and z_{sn} are the pathlengths to the layers *m* and *n* within the sample measured from the beam splitter. From equation 2.9, it can be observed that each reflector within the sample is broadened by a width of about the coherence length of the source. For a Gaussian shaped spectrum, the normalized Gaussian function *S*(*k*) and its inverse Fourier transform $\gamma(z)$ are given by

$$\gamma(z) = exp\,[-z^2 \Delta k] \quad \overset{F}{\leftrightarrow} \quad S(k) = \frac{1}{\Delta k\sqrt{\pi}}\, exp\,[-\{(k - k_0)/\Delta k\}^2] \qquad (2.11)$$

Here, k_0 represents the central wavenumber of the light source spectrum and Δk represents its spectral bandwidth, corresponding to the half-width of the spectrum at 1/e of its maximum.

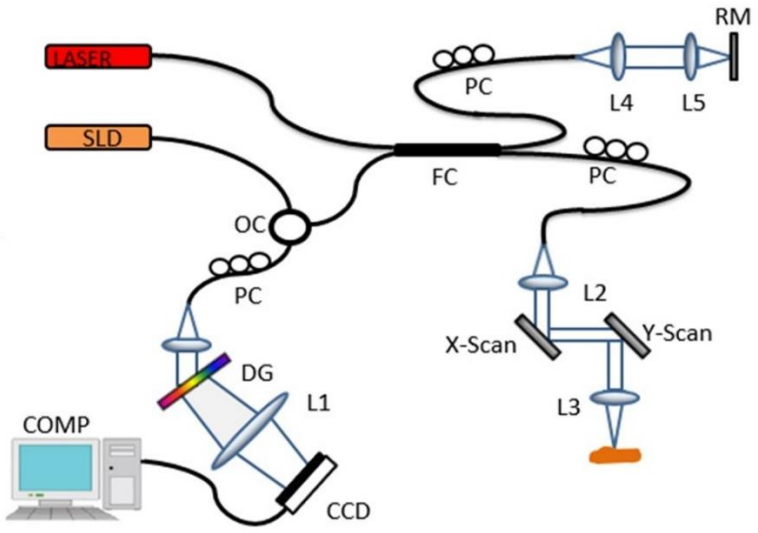

Fig. 2.2 (a) Schematic of SD-OCT system

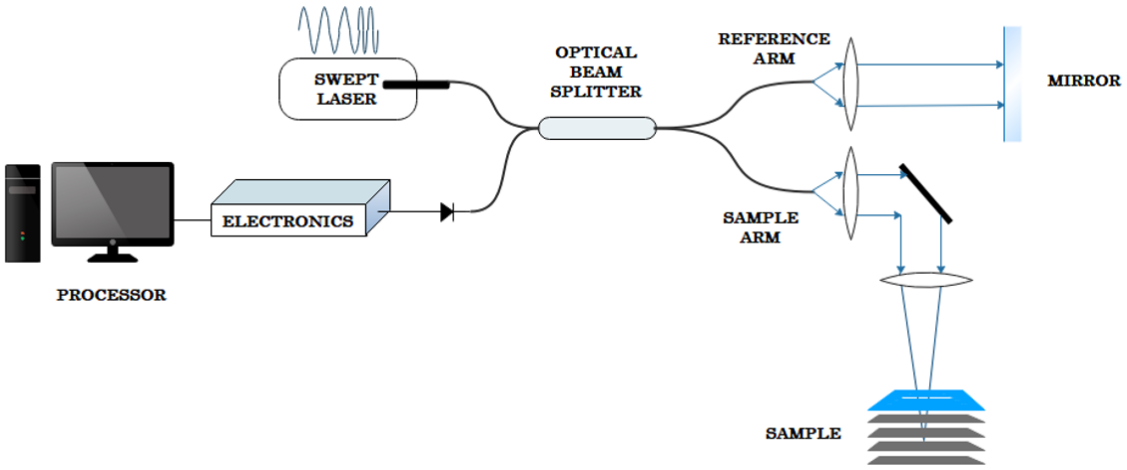

Fig. 2.2 (b) Schematic of SS-OCT system

Fourier domain OCT can be also implemented by adopting a wavelength-swept light source, known as swept-source (SS-OCT) as shown in figure 2.2(b). SS-OCT implementation is also known as optical frequency domain imaging. In swept source implementation, a narrowband swept-laser source is swept across the wavelength range, and a photodetector is used to record the spectral components *I(k)* during each sweep. The main difference between SD-OCT and SS-OCT is in the recording of the interferogram.

Assuming a simplified model where all swept frequency powers are constant over the whole sweep bandwidth, equation 2.11 can be modified by introducing a time dependent frequency change and a bandwidth δk_{SS} describing the line-width of the laser emission.

$$S(k(t)) = \frac{1}{\Delta k\sqrt{\pi}}\, exp\,[-\{(k - k_0(t))/\delta k_{SS}\}^2 \qquad (2.12)$$

In SS-OCT, the spectral components of $I_D(k)$ are captured sequentially by recording the signal in a single photodetector while synchronously sweeping the wavenumber of a narrowband swept-laser source. The wavenumber-dependent detector current $I_D(k)$ is given by [10]

$$I_D(k) \sim \sqrt{r_R r_S}\int_k^{k+\delta k_{SS}} S(k) cos\,(2kx) dk \qquad (2.13)$$

The sample reflectivity profile $r_S(z_S)$ is estimated from the inverse Fourier transform of $I_D(k)$. Making use of the Fourier transform pair,

$$\frac{1}{2}\{\delta(z(t) + z_0) + \delta(z(t) - z_0)\} \;\leftrightarrow\; cos\; k(t) z_0, \qquad (2.14)$$

the depth dependent output of the photodetector is given by

$$i_D(z(t)) = \frac{\rho}{8}\gamma(z(t))[r_R + r_{S_1} + r_{S_2} + \ldots] + \frac{\rho}{4}\sum_{n=1}^{N}\sqrt{r_R r_{S_n}}\{\gamma(2[z(t) - z_{S_n}]) + \gamma(-2[z(t) - z_{S_n}])\} + \frac{\rho}{8}\sum_{n\neq m=1}^{N}\sqrt{r_{S_n} r_{S_m}}\{\gamma(2[z_{S_n} - z_{S_m}]) + \gamma(-2[z_{S_n} - z_{S_m}])\} \qquad (2.15)$$

The frequency *f* detected by the photodetector depends also on the sweep time *T* which is for modern swept-sources in excess of 1 MHz [11,12]. The dependence of the interference frequency on the scanning time is similar to TD-OCT and can be calculated for SS-OCT by using the sweep bandwidth $\Delta\lambda$ and a center wavelength λ_c[13]

$$f_i = \frac{2\Delta\lambda}{T{\lambda_c}^2} z_i \tag{2.16}$$

Consequently, the acquisition of the time dependent photocurrent $i_D(z(t))$corresponds to the sequential recording of the sum of the sample reflection frequencies (spectrum) which can be performed with a single photodetector and a suitable digitizer. In other words, at each time *t*, a specific spectral channel is probed relating to a single depth scan. Although the time-dependent scanning has some notion of TD-OCT, the required Fourier transformation for SS-OCT indicates the difference of the signal properties between the two systems. The generation of rapidly swept frequencies was achieved in early systems by using rapid mechanical scanning of dispersed light on a grating with a polygon scanned filter. More modern swept sources use highly miniature MEMS based methods such as the vertical-cavity surface-emitting lasers (VCSELs)[14]. Other methods include fiber lasers and latest developments use akinetic swept sources [15- 17].

Axial imaging depth defines the axial range which is covered in an A- line. It is defined by the maximum fringe frequency that can be detected, because maximum frequency of the interference spectrum decodes the maximum depth. Therefore, the imaging depth z_{max} is defined by the number sample points *N* on the full recorded spectral width $\Delta\lambda$:

$$z_{max} = \frac{1}{4}\left(\frac{\lambda_o^2}{\Delta\lambda} N\right) \tag{2.17}$$

In SD-OCT systems, *N* is given by the number of pixels of the line detector. For SS-OCT systems, it is given by the number of readouts of the photo diode during one sweep of the light source. The maximum imaging range divided by 0.5 *N* gives the axial sampling of the B-Scan. This number characterizes how many micrometer per pixels are imaged and provide the axial scaling of the scan.

Another aspect regarding FD-OCT systems is the characteristic decrease in sensitivity with imaging depth, called sensitivity roll-off. It arises from the finite spectral resolution of the system component providing spectral separation. The backscattered signal from deeper layers are encoded in higher frequency fringes and therefore require higher spectral resolution to resolve them. However, in SD-OCT systems, the pixel size of the line detector is fixed, which

contributes to the sensitivity roll – off along with the finite spot size created by the spectrometer optics. For SS-OCT, since the spectral interferogram is sampled sequentially, and the spectral resolution is determined by the instantaneous line width of the swept laser source, sensitivity roll off depends on both the instantaneous laser line width and the bandwidth of the analog-to-digital convertor.

Another key aspect regarding OCT is the noise performance. One of the most important characteristic that facilitated the development of OCT as an established medical imaging is the sensitivity advantage of FD-OCT over the early TD-OCT systems [3,7,9]. The Fourier domain approach to OCT imaging has enabled high speed acquisitions by several orders of magnitude as compared to time domain OCT without compromising image quality. Mitsui [10] has compared a TD-low coherence interferometer setup with SD-OCT version. This has shown that the dynamic range of the SD-OCT was larger than that of TD-OCT version by a factor given by the number of spectral windows used in the spectrometer.

In OCT, the detected interference signal is measured via optical intensity. Under the limit of shot noise, though the noise in FD-OCT detection stays the same as that of the TD-OCT, due to parallelization in detection process in FD-OCT systems, the signal acquired during single A-scan is increased by a factor of *N*, where *N* corresponds to the total number of pixels on the spectrometer in SD-OCT systems or the number of wavelengths over the sweeping span in SS-OCT systems.

The SNR of an OCT system is defined as the quotient of the average squared signal divided by the noise variance [6, 7], i.e.

$$SNR = \frac{<I_{OCT}^2>}{\sigma_n^2} \tag{2.18}$$

where I_{OCT} is the optical intensity and σ^2 is the photoelectron noise contribution to each pixel along depth.

In a typical SD-OCT system, the light source used has an approximate Gaussian envelope centred at ν_o with a FWHM of $\Delta\nu$; the spectrometer has *N* pixels with an efficiency of η (including the quantum efficiency and spectrometer efficiency), with a set integration time τ; and a beam splitter for the interference set up. The SD-OCT signal obtained in the spatial domain (after applying discrete inverse Fourier transform) can be written in terms of the interferogram detected as given by equation 2.19,

$$S_{SDOCT} = \frac{\eta P_o \tau}{h\nu_o N}\sqrt{R_R R_S} \tag{2.19}$$

where P_o is the average optical power entering the interferometer, h is the Plank's constant and R_R and R_S are the intensity reflectivity of reference and sample arms respectively [3,6].

The detected signal at the spectrometer consists of three types of noise; namely shot noise, excess noise of the source and receiver noise. Shot noise is equal to mean number of photoelectrons (n_e) collected at the detector within the integration time and is given by equation 2.20,

$$\sigma^2_{sh\_SDOCT} = < n_e > = \frac{\eta P_o \tau}{h\nu_o N}(R_R + R_S) \tag{2.20}$$

The excess noise is often assumed to be dominated by relative intensity noise (RIN) and calculated by equation 2.21,

$$\sigma^2_{ex\_SDOCT} = \frac{(\Pi^2+1)}{2}\frac{\tau_{coh}}{\tau}\left(\frac{\eta P_o \tau}{h\nu_o N}(R_R + R_S)\right)^2 \tag{2.21}$$

where τ_{coh} is the coherence time of the source and where Π is the degree of polarization that values between 0 and 1 (0 for unpolarized light and 1 for linearly polarized light) [6].

The receiver noise (σ^2_{rec}) at the detector is the sum of dark noise of the detector and the read-out noise of the circuit. Since in a spectral domain OCT, the discrete Fourier transform is used to reconstruct the axial reflectance profile, there is an additional normalization factor of 1/N, hence the total noise, σ^2_n can be written as,

$$\sigma^2_n = \frac{\sigma^2_{sh} + \sigma^2_{ex} + \sigma^2_{rec}}{N} \tag{2.22}$$

It is desirable to operate SD-OCT as close as possible to the shot noise limit to achieve reasonable signal to noise ratio for biological imaging. Within the shot noise limit ($\sigma^2_n \approx \sigma^2_{sh}$) for biological imaging (where $R_R \gg R_S$), the SNR of the system can be written as,

$$SNR_{SDOCT} = \frac{<S^2_{OCT}>}{\sigma^2_n} = \frac{\eta P_o \tau R_S}{h\nu_o} \tag{2.23}$$

In case of SS-OCT systems, the integration time, τ is replaced by Δt, the single photodetector sampling time, where during time interval Δt, the detector detects an optical signal of bandwidth δk. Also, for photocurrent detectors used in SS-OCT systems, the receiver noise is replaced by thermal noise and is described per unit bandwidth using noise equivalent current [6,7].

$$S_{SSOCT} = \frac{\eta P_o \Delta t}{h\nu_o}\sqrt{R_R R_S} \tag{2.24}$$

$$\sigma^2_{sh\_SSOCT} = < n_e > = \frac{\eta P_o \Delta t}{h\nu_o}(R_R + R_S) \tag{2.25}$$

$$\sigma^2_{ex\_SSOCT} = \frac{(\Pi^2+1)}{2}\frac{\tau_{coh}}{\Delta t}\left(\frac{\eta P_o \Delta t}{h\nu_o}(R_R + R_S)\right)^2 \tag{2.26}$$

The total noise in SS-OCT can be written as,

$$\sigma_n^2 = \sigma_{sh}^2 + \sigma_{ex}^2 + \sigma_{thermal}^2 \quad (2.27)$$

Within the shot noise limit, the SNR of SS-OCT can be written as,

$$SNR_{SSOCT} = \frac{<S_{OCT}^2>}{\sigma_n^2} = \frac{\eta P_o R_S \Delta t\, N}{h\nu_o} \quad (2.28)$$

where the integration time of the detector in SD-OCT system is related to the photodetector sampling time Δt, by the relation $\tau = \Delta t\, N$.

As can be seen from equations 2.21 and 2.26, the SNR for Fourier domain OCT system is independent of source bandwidth unlike TD-OCT systems. Also comparing equations 2.23 and 2.28, one can observe that the ratio of $\frac{\sigma_{ex\_SSOCT}^2}{\sigma_{ex\_SDOCT}^2}$ = N.

2.2. Structural and functional imaging using OCT

Clinical applications of OCT were first reported in 1991 by Fujimoto [1], and since then OCT has been clinically demonstrated in a diverse set of medical and surgical applications, including gastroenterology, dermatology, cardiology, and oncology, among others. Conventional OCT imaging is based on contrast from spatial variations in tissue scattering that exploits the changes in refractive index within the imaged sample. Apart from obtaining structural information within the specimen, functional extensions of OCT have also been developed. These functional OCT's are based either on endogenous or exogenous contrast agents. Endogenous contrast based techniques include angiographic OCT, OCT elastography and spectroscopic OCT. In recent years, exogenous contrasts agents have been used for OCT imaging applications. These exogenous contrast agents enable enhanced visualization of features such as microvasculature, diseased or abnormal tissue based on selective absorption of the contrast agents by the tissue. Exogenous contrast based OCT include magnetomotive OCT and photothermal OCT.

2.2.1 Structural imaging using OCT

The advantage of optical methods for clinical imaging are high resolution and sensitivity, but biggest limitation for clinical imaging is the relatively small light penetration into a tissue up to a few millimetres. Also, multiple scattering of light within biological tissues reduces the quality of reconstructed images. Therefore, the OCT systems which were developed first targeted weakly scattering biological samples such as eyes and internal organs containing only small amounts of melanin and haemoglobin [2,3]. Presently, OCT has been routinely used in ophthalmology and dermatology for high resolution imaging. Also, OCT has been combined with endoscopic procedures for excisional biopsy and for surgical guidance [7].

SD-OCT is currently the standard for ophthalmic instruments and imaging speeds range from 25,000 to 100,000 A-scans per second [17,18]. Retinal imaging with approximately 5 to 6 μm axial resolution at 1050 nm and 100,000 to 200,000 A-scan per second have been demonstrated. Ophthalmic applications of OCT include anterior segment, crystalline lens and retinal imaging applications [3,17,18]. OCT is routinely used in clinic for monitoring and detecting glaucoma, LASIK surgical procedures, diabetic retinopathy and corneal thickness mapping. It is estimated there are approximately 30 million ophthalmic OCT procedures per year worldwide [17].

Endoscopic OCT tools have been developed to investigate and diagnose clinical issues along the gastrointestinal (GI) tract including the oesophagus, stomach, small intestine, and colon [20,21], intracoronary imaging [3,22] and pulmonary tract imaging [23,24]. Intracoronary OCT imaging aids the detection and formation of coronary atherosclerosis and also helps to monitor the response to intravascular interventions. With the development of Fourier domain OCT technologies, endoscopic OCT imaging has recently been demonstrated with much higher imaging speed and better resolution [25] .

Another field that uses the structural imaging capability of OCT is in developmental biology [26]. The understanding of formation of functional organs requires observation of dynamic changes at the cellular level. OCT provides the ability to image these developmental changes in a living model. Fourier domain OCT systems has enabled the visualisation of developing embryonic heart with high spatial and temporal resolution and also the distribution of individual red blood cells and how it varies over the different developmental stages of an embryo [27].

2.2.2 Functional imaging using OCT

Polarisation-sensitive OCT (PS-OCT), is used as an additional contrast mechanism in OCT image acquisition [28]. PS-OCT generates image contrast based on the polarisation sate of the backscattered light. Birefringent materials are ones in which the velocity of propagating light depends on its polarisation. Such materials have two indices of refraction, in two separate directions. Collagen fibres, or other tissues with highly organised structures, are birefringent [29]. Thus, as light passes through such tissue, its polarisation state will change. PS-OCT can be used to visualise places where such structures may have broken down, due to disease or injury [30]. PS-OCT has been used in detecting atherosclerotic plaques, glaucoma treatment, screening and treatment of keratoconus cornea, imaging macular lesions [31]. PS-

OCT holds strong potential for early detection of plaques and burn depth assessment thus allowing for early intervention and better patient outcome.

Optical coherence elastography (OCE), is another functional extension of OCT which is used to estimate the mechanical properties of tissues. It is well-documented that knowledge of tissue elasticity can aid in the diagnosis of breast cancer, prostate cancer, liver cirrhosis, small tumours and atherosclerosis [32] . Tissue constituent materials and how they are organised are what give rise to the mechanical properties of tissue. The ways in which tissue is structured are essential to their proper functioning. Unhealthy tissue can often be characterised by an increased stiffness. In OCE, the sample of interest is mechanically stimulated and the samples response to stimulus is tracked over time, from which parameters related to stiffness can be estimated [33,34]. The means of inducing sample displacement largely determines what information about the structural and mechanical properties can be obtained. For example, application of compressive loads provides information about sample's elasticity, whereas OCE systems which utilise an impulse or vibration to produce mechanical disturbances aim to monitor the propagation of induced mechanical waves through the sample thereby enabling the measurement of wave velocity, which is another parameter linked to sample mechanical properties.

OCT angiographic techniques are based on the principle that static scatterers within the probed volume of the sample remains stationary whereas moving red blood cells undergo dynamic changes over time which provides the required contrast mechanism in OCT to map the microvasculature [35]. Over the years many different algorithms have been developed for qualitative and quantitative flow imaging. Detailed description of OCT angiographic techniques is given in chapter 3.

Another functional extension of OCT imaging is the use of external contrast agent to aid functional imaging. External contrast agent based OCT detection techniques are of two types: passive techniques and active techniques. Passive detection techniques generate imaging contrast based on the intrinsic optical properties of the contrast agent [36] without any external excitation. An example of passive detection technique is spectroscopic OCT. For example, differences in the absorption of near infrared dyes compared to tissue can be passively detected using spectroscopic OCT. Another example is the use of gold nanoparticles (GNPs) to generate increased image contrast due to their enhanced optical scattering [37]. Active contrast agent detection techniques rely on modulating the property of the external contrast agent to generate imaging contrast. One example of active contrast agent detection is magnetomotive OCT [38,

39]. In this technique, cells that have taken up superparamagnetic iron oxide (SPIO) nanoparticles are exposed to an external magnetic field of 0.06 – 0.5 T that is modulated at 3 – 50 Hz. Modulation of the external magnetic field causes localized motion in regions of the tissue that have taken up the SPIO, and this motion can be detected by fluctuations in the amplitude or phase of the OCT interference signal. Another example of active contrast agent detection technique is photothermal OCT (PT-OCT) [39]. PT-OCT utilises the photothermal efficiency (light to heat conversion) of GNP. Localised heat generation by GNPs leads to thermoelastic expansion of the sample that causes variations in its local refractive index. These variations in the refractive index can be optically imaged with the phase information obtained from the OCT interferogram. Detailed description of PT-OCT is given in chapter 6.

2.3. Conclusions

In this chapter, theoretical framework and working principle of time domain and Fourier domain OCT were introduced. The chapter discussed the advantages of Fourier domain OCT over earlier TD-OCT systems. Also, the chapter described the various OCT system parameters such as axial and lateral resolution, depth of field, signal to noise ratio and sensitivity, mainly focussed on Fourier domain OCT systems. Further, a brief description of various structural and functional imaging applications of OCT was discussed. This chapter provides the theoretical ground work for this thesis.

REFERENCES

1. D. Huang, E. A. Swanson, C. P. Lin, J. S. Schuman, W. G. Stinson, W. Chang, M. R. Hee, T. Flotte, K. Gregory, C. A. Puliafito, and J. G. Fujimoto, "Optical Coherence Tomography," Science **254**, 1178–1181 (1991).
2. J. G. Fujimoto, C. Pitris, S. A. Boppart, and M. E. Brezinski, "Optical Coherence Tomography: An Emerging Technology for Biomedical Imaging and Optical Biopsy," Neoplasia N. Y. N **2**, 9–25 (2000).
3. M. Wojtkowski, "High-speed optical coherence tomography: basics and applications," Appl. Opt. **49**, D30–D61 (2010).
4. J. A. Izatt and M. A. Choma, "Theory of Optical Coherence Tomography," in *Optical Coherence Tomography: Technology and Applications*, W. Drexler and J. G. Fujimoto, eds., Biological and Medical Physics, Biomedical Engineering (Springer Berlin Heidelberg, 2008), pp. 47–72.
5. M. Born and E. Wolf, *Principles of Optics: Electromagnetic Theory of Propagation, Interference and Diffraction of Light* (Elsevier, 2013).
6. R. Leitgeb, C. Hitzenberger, and A. Fercher, "Performance of fourier domain vs. time domain optical coherence tomography," Opt. Express **11**, 889–894 (2003).
7. J. F. de Boer, R. Leitgeb, and M. Wojtkowski, "Twenty-five years of optical coherence tomography: the paradigm shift in sensitivity and speed provided by Fourier domain OCT [Invited]," Biomed. Opt. Express **8**, 3248–3280 (2017).
8. A. F. Fercher, C. K. Hitzenberger, G. Kamp, and S. Y. El-Zaiat, "Measurement of intraocular distances by backscattering spectral interferometry," Opt. Commun. **117**, 43–48 (1995).
9. S. Aumann, S. Donner, J. Fischer, and F. Müller, "Optical Coherence Tomography (OCT): Principle and Technical Realization," in *High Resolution Imaging in Microscopy and Ophthalmology: New Frontiers in Biomedical Optics*, J. F. Bille, ed. (Springer International Publishing, 2019), pp. 59–85.
10. M. A. Choma, K. Hsu, and J. A. Izatt, "Swept source optical coherence tomography using an all-fiber 1300-nm ring laser source," J. Biomed. Opt. **10**, 044009 (2005).
11. B. Potsaid, V. Jayaraman, J. G. Fujimoto, J. Jiang, P. J. S. Heim, and A. E. Cable, "MEMS tunable VCSEL light source for ultrahigh speed 60kHz - 1MHz axial scan rate and long range centimeter class OCT imaging," in *Optical Coherence Tomography and Coherence*

Domain Optical Methods in Biomedicine XVI (International Society for Optics and Photonics, 2012), Vol. 8213, p. 82130M.

12. T. Klein, W. Wieser, L. Reznicek, A. Neubauer, A. Kampik, and R. Huber, "Multi-MHz retinal OCT," Biomed. Opt. Express **4**, 1890–1908 (2013).

13. P. D. Ruiz, J. M. Huntley, and R. D. Wildman, "Depth-resolved whole-field displacement measurement by wavelength-scanning electronic speckle pattern interferometry," Appl. Opt. **44**, 3945–3953 (2005).

14. T. Klein and R. Huber, "High-speed OCT light sources and systems [Invited]," Biomed. Opt. Express **8**, 828–859 (2017).

15. M. Bonesi, M. P. Minneman, J. Ensher, B. Zabihian, H. Sattmann, P. Boschert, E. Hoover, R. A. Leitgeb, M. Crawford, and W. Drexler, "Akinetic all-semiconductor programmable swept-source at 1550 nm and 1310 nm with centimeters coherence length," Opt. Express **22**, 2632–2655 (2014).

16. M. P. Minneman, J. Ensher, M. Crawford, and D. Derickson, "All-Semiconductor High-Speed Akinetic Swept-Source for OCT," in *Optical Sensors and Biophotonics (2011), Paper 831116* (Optical Society of America, 2011), p. 831116.

17. J. Fujimoto and E. Swanson, "The Development, Commercialization, and Impact of Optical Coherence Tomography," Invest. Ophthalmol. Vis. Sci. **57**, OCT1-OCT13 (2016).

18. M. Adhi and J. S. Duker, "Optical coherence tomography – current and future applications," Curr. Opin. Ophthalmol. **24**, 213–221 (2013).

19. T. Mitsui, "Dynamic Range of Optical Reflectometry with Spectral Interferometry," Jpn. J. Appl. Phys. **38**, 6133 (1999)

20. T.-H. Tsai, C. L. Leggett, A. J. Trindade, A. Sethi, A.-F. Swager, V. Joshi, J. J. Bergman, H. Mashimo, N. S. Nishioka, and E. Namati, "Optical coherence tomography in gastroenterology: a review and future outlook," J. Biomed. Opt. **22**, 121716 (2017).

21. T.-H. Tsai, J. G. Fujimoto, and H. Mashimo, "Endoscopic Optical Coherence Tomography for Clinical Gastroenterology," Diagnostics **4**, 57–93 (2014).

22. B. E. Bouma, M. Villiger, K. Otsuka, and W.-Y. Oh, "Intravascular optical coherence tomography [Invited]," Biomed. Opt. Express **8**, 2660–2686 (2017).

23. G. J. Tearney, S. A. Boppart, B. E. Bouma, M. E. Brezinski, N. J. Weissman, J. F. Southern, and J. G. Fujimoto, "Scanning single-mode fiber optic catheter–endoscope for optical coherence tomography," Opt. Lett. **21**, 543–545 (1996).
24. G. J. Tearney, M. E. Brezinski, B. E. Bouma, S. A. Boppart, C. Pitris, J. F. Southern, and J. G. Fujimoto, "In vivo endoscopic optical biopsy with optical coherence tomography," Science **276**, 2037–2039 (1997).
25. F. Prati, M. W. Jenkins, A. Di Giorgio, and A. M. Rollins, "Intracoronary optical coherence tomography, basic theory and image acquisition techniques," Int. J. Cardiovasc. Imaging **27**, 251–258 (2011).
26. A. M. Davis, S. A. Boppart, F. Rothenberg, and J. A. Izatt, "OCT Applications in Developmental Biology," in *Optical Coherence Tomography: Technology and Applications*, W. Drexler and J. G. Fujimoto, eds., Biological and Medical Physics, Biomedical Engineering (Springer Berlin Heidelberg, 2008), pp. 919–959.
27. R. Raghunathan, M. Singh, M. E. Dickinson, and K. V. Larin, "Optical coherence tomography for embryonic imaging: a review," J. Biomed. Opt. **21**, (2016).
28. M. R. Hee, D. Huang, E. A. Swanson, and J. G. Fujimoto, "Polarization-sensitive low-coherence reflectometer for birefringence characterization and ranging," JOSA B **9**, 903–908 (1992).
29. W. Drexler, D. Stamper, C. Jesser, X. Li, C. Pitris, K. Saunders, S. Martin, M. B. Lodge, J. G. Fujimoto, and M. E. Brezinski, "Correlation of collagen organization with polarization sensitive imaging of in vitro cartilage: implications for osteoarthritis," J. Rheumatol. **28**, 1311–1318 (2001).
30. C. E. Saxer, J. F. de Boer, B. H. Park, Y. Zhao, Z. Chen, and J. S. Nelson, "High-speed fiber–based polarization-sensitive optical coherence tomography of in vivo human skin," Opt. Lett. **25**, 1355–1357 (2000).
31. S. D. Giattina, B. K. Courtney, P. R. Herz, M. Harman, S. Shortkroff, D. L. Stamper, B. Liu, J. G. Fujimoto, and M. E. Brezinski, "Assessment of coronary plaque collagen with polarization sensitive optical coherence tomography (PS-OCT)," Int. J. Cardiol. **107**, 400–409 (2006).
32. B. F. Kennedy, X. Liang, S. G. Adie, D. K. Gerstmann, B. C. Quirk, S. A. Boppart, and D. D. Sampson, "In vivo three-dimensional optical coherence elastography," Opt. Express **19**, 6623–6634 (2011).

33. B. F. Kennedy, K. M. Kennedy, and D. D. Sampson, "A Review of Optical Coherence Elastography: Fundamentals, Techniques and Prospects," IEEE J. Sel. Top. Quantum Electron. **20**, 272–288 (2014).
34. K. V. Larin and D. D. Sampson, "Optical coherence elastography – OCT at work in tissue biomechanics [Invited]," Biomed. Opt. Express **8**, 1172–1202 (2017).
35. T. E. de Carlo, A. Romano, N. K. Waheed, and J. S. Duker, "A review of optical coherence tomography angiography (OCTA)," Int. J. Retina Vitr. **1**, 5 (2015).
36. D. C. Adler, S.-W. Huang, R. Huber, and J. G. Fujimoto, "Photothermal detection of gold nanoparticles using phase-sensitive optical coherence tomography," Opt. Express **16**, 4376 (2008).
37. A. Oldenburg, F. Toublan, K. Suslick, A. Wei, and S. Boppart, "Magnetomotive contrast for in vivo optical coherence tomography," Opt. Express **13**, 6597–6614 (2005).
38. J. Kim, J. Oh, H. W. Kang, M. D. Feldman, and T. E. Milner, "Photothermal response of superparamagnetic iron oxide nanoparticles," Lasers Surg. Med. **40**, 415–421 (2008).
39. M. C. Skala, M. J. Crow, A. Wax, and J. A. Izatt, "Photothermal Optical Coherence Tomography of Epidermal Growth Factor Receptor in Live Cells Using Immunotargeted Gold Nanospheres," Nano Lett. **8**, 3461–3467 (2008).

Chapter 3

FEASIBILITY OF cmOCT ANGIOGRAPHY USING 200 kHz SWEPT SOURCE OCT SYSTEM

3.1 Introduction

Microcirculation refers to blood flowing through the circulatory system of an organism comprising a network of vessels (arterioles, capillaries, and venules) that are typically less than 100 μm in diameter. Changes in microcirculation can reflect an underlying change in tissue metabolism or the response of the tissue to a given treatment or an exposure to a stimulant. Over the years, many techniques have been demonstrated for measuring blood flow and related microvascular parameters [2,3]. Among these, light-based techniques have garnered research interest due to their non-invasive and high-resolution imaging capability. Of these, OCT is a promising imaging modality for microcirculation imaging that can reconstruct three-dimensional (3D) images of vascular structures with sufficient axial and lateral resolution to a depth of 3 mm in vivo in the tissue. Imaging the microcirculation helps scientists and clinicians to understand the microvasculature, both structural and functional, whereby early detection in its abnormality can lead to early diagnosis and treatment efficacy. Among the functional variants, angiographic OCT enables visualization of blood vessels from the acquired OCT B-scan images and has been of high research interest in the recent past, with more than 1000 publications per year over the past five years. OCT angiography refers to producing microvasculature maps from the acquired OCT interference spectrum [4]. As OCT detects ballistic photons that are backscattered from the various regions within the tissue, any change in phase or amplitude of the backscattered photons are reflected in the interference spectra. OCT angiographic techniques detect these shifts in phase or amplitude of the backscattered light from the moving red blood cells (RBCs) within the blood vessels over time compared to the static tissue background. Thus, OCT angiography relies on generating vascular maps based on the endogenous contrast mechanism provided by the moving RBC's within the blood vessels.

Based on the detection techniques, OCT angiographic techniques can be divided into phase-based, amplitude-based, and complex angiographic techniques [4]. These include speckle variance (SV) [5], correlation mapping [6], optical microangiography (OMAG) [7], phase variance [8], and Doppler OCT [9,10]. The amplitude-based techniques work on the principle of detecting changes in the OCT intensity images (B scans) over time to generate contrast between the static and dynamic structures within the tissue [11]. Similarly, the phase-based techniques detect the changes in the phase or the extent of decorrelation between the phase of the Fourier transformed spectral data acquired at the same location over time to achieve motion contrast [12]. Phase-based angiographic techniques are further divided into Doppler angiography [9] and phase variance angiography [8]. Complex angiographic techniques use both the amplitude and phase information of the acquired interferometric data to generate microvascular images.

In the following sections, a review of OCT angiographic techniques is described beginning with the earliest Doppler techniques, followed by amplitude and phase based techniques, and finally complex angiographic methods.

3.2 OCT angiographic methods

3.2.1 Doppler OCT

Since the introduction of OCT in the 1990's, attempts were made to extract blood flow information from the OCT signals. These early developments were based on time domain OCT by using the principle of the well-established Doppler Effect. When RBCs undergo movement, there occurs a shift in the frequency of backscattered light compared to the incident light. This induced Doppler shift is proportional to the velocity of blood flow and hence, by extracting the frequency shift of the backscattered light, one could estimate the velocity of blood flow.

In a time domain Doppler OCT system, the frequency shift Δf_D between the backscattered light from the moving RBCs and the translating reference arm mirror of the interferometer can be calculated as given in Eq. (1) to determine the flow velocity [13–15]

$$\Delta f_D = \frac{1}{2\pi}\left(\overrightarrow{k_s} - \overrightarrow{k_i}\right).\vec{v} \tag{3.1}$$

where $k_s \; and \; k_i$ are the wave vectors of incoming and scattered light and v is the velocity vector of the moving scatterers. If the angle between the incident beam and flow direction is θ, the Doppler frequency shift in equation 3.1 can be written as given by equation 3.2 where λ_0 is the mean wavelength of the light source.

$$\Delta f_D = \frac{2\,V cos\theta}{\lambda_0} \tag{3.2}$$

For each pixel of the interference fringe, the localized Doppler velocity v_{ODT} can be calculated as given by equation 3.3 [13,14].

$$v_{ODT} = \frac{\lambda_0\,(\Delta f_D)}{2\pi cos\theta} = \frac{\lambda_0\,(f_c - f_o)}{2\pi cos\theta} \tag{3.3}$$

where f_0 is the centroid of the power spectrum obtained; f_c is the carrier frequency of the reference arm; and θ is the angle between k_i and v. Depending on the flow direction of the scatterers, the Doppler frequency shifts either add or subtract from the carrier frequency f_c of the reference arm. In time-domain OCT, since the interferometric signal is a function of time, the short-time Fourier transform (STFT) was used to obtain the Doppler signals from the acquired interference signals [13–15]. Several studies have demonstrated the applicability of Doppler based time domain OCT angiography. The first studies demonstrating 2D *in vivo* imaging of blood flow was in 1997 on a chick chorioallantoic membrane (CAM) and on rodent skin. Also the same year, bidirectional blood flow mapping was performed showing the presence of artery and vein in the dorsal skin of hamster [15].

After the introduction of Fourier domain OCT systems in early 2000's, Doppler imaging has been performed either by SD-OCT or by swept source based interferometric approach. The first Doppler imaging performed using a SD-OCT was by Leitgeb *et al.* in 2003, on blood flow through glass capillaries [16]. In a SDOCT system, the Doppler shift is obtained by calculating the phase difference ($\Delta\phi$) between adjacent A-lines taken at the same transverse position [16] and the velocity of moving scatterers is given by equation 3.4:

$$v(z) = \Delta\phi(z,\tau)\frac{\lambda}{4\pi\tau cos\theta}, \tag{3.4}$$

where z is the depth; τ is the time between successive A-scans; λ is the source central wavelength and θ the angle between the incident beam and scatterer velocity vector. Eq. 3.4 assumes that the system is highly phase stabilized and any change in phase between successive A-lines at the same transverse location is solely based on movement within the sample. Hence, the minimum detectable velocity is determined by the scan rate of the system and the maximum detectable Doppler frequency is limited by the detection speed of the detector array. For accurate velocity determination, the phase difference $\Delta\phi$ needs to be confined to the interval $[-\pi, \pi]$. Further, to improve the velocity sensitivity in Doppler OCT, which is proportional to the phase noise present in the system, phase averaging has been proposed. In this initial demonstration, real-time imaging of human retinal vasculature at an A-scan rate of 25 kHz with a velocity sensitivity of 200 μm/s was demonstrated [16,17]. Since then, many groups have

shown real-time imaging of blood flow using Doppler SD-OCT [18–21], including Doppler variance imaging using SD-OCT, which provided better mapping of blood vessels [21].

The first Doppler study using SS-OCT was reported by Zhang et al. in 2005 [22]. Doppler shift and flow velocity is calculated as described similar to the spectral domain OCT. Hendargo *et al*. [23] showed that swept source OCT is less subject to fringe washout effects and can image a wide range of flow velocities without signal degradation unlike SD-OCT. Swept source based Doppler OCT angiography is capable of high-speed imaging in the range of hundreds of kHz. However, the output spectrum from the swept source may vary from scan to scan depending on the electrical or mechanical scanning of the laser [24]. This along with timing jitter in swept source OCT's induces a phase error which limits the minimum detectable velocity in swept source OCT's. Though swept sources (MEMS-VCSEL and FDML) are not as phase stable as SD-OCT, faster scan rates enable swept source OCT to be used in clinical angiographic imaging. However, as per equation 3.4, there is a trade-off between scan time and detectable velocity. Increasing the acquisition rate reduces the minimum detectable velocity and decreasing the scan rate limits the maximum detectable velocity. However, swept source based phase angiographic technique require complex post processing techniques for phase stabilization or use a phase stabilised akinetic laser source for imaging [25–28]. Hence, most of the swept source based angiographic techniques have been amplitude based.

3.2.2 Amplitude based techniques

In this section, the theory and applications of amplitude based angiographic techniques mainly speckle variance, correlation mapping OCT and split spectrum amplitude decorrelation angiography are discussed.

3.2.2.1 Speckle variance

The speckle phenomenon was first noticed soon after the experimental demonstration of the laser when it was discovered that optically rough surfaces reflected a distinctive granular pattern under illumination from highly spatially and temporally coherent laser light [29]. Originally, speckle in OCT was viewed largely from the perspective of being detrimental to image quality, since it caused a reduction in contrast and made boundaries less discernible [30]. As a result, reducing the effects of speckle became a focus of research, with techniques such as polarization diversity, signal processing, and speckle temporal averaging [31,32]. In contrast, it was also accepted that speckle was a source of useful

information [32–34]. In 2005, Barton and Stromski were the first to suggest using speckle to extract flow information from OCT, as an alternative to Doppler OCT, due to the limitations of the latter in detecting flow in directions normal to the imaging beam [10]. The use of speckle as a contrast mechanism was adapted to OCT and for the first time, speckle analysis was used to provide a depth-resolved profile using only intensity information [11]. It was shown that the statistics of time-varying speckle could be used to quantitatively measure velocity of flow in a tube phantom and *in vivo* hamster cheek pouch [11].

Mariampillai *et al.* extended speckle variance OCT to the Fourier domain system and visualized the microcirculation of an *in vivo* mouse model using a swept-source laser operating at 36 kHz A- scan rate [4]. The interframe speckle variance was calculated based on repeated OCT intensity scans of the same transverse location over *N* (8) scans given by equation 3.5:

$$SV(x,z) = \frac{1}{N}\sum_{i=1}^{N}(I_i(x,z) - I_{mean})^2 \tag{3.5}$$

where $I_i(x,z)$ is the *i-th* B-scan at lateral and depth indices *x* and *z*. I_{mean} is the mean intensity of a given pixel over a total of *N* scans and is given by equation 3.6:

$$I_{mean} = \frac{1}{N}\sum_{i=1}^{N} I_i(x,z) \tag{3.6}$$

The above equation returns different values for stationary and moving components within a biological tissue due to each component exhibiting different time-dependent scattering properties, which is the mechanism of contrast in speckle variance OCT. Swept source based SV angiography has been used to study microcirculation within the dorsal skin fold [5,35], nail fold [36], functional brain imaging and embryological studies [37,38].

3.2.2.2 Correlation mapping

Correlation mapping (cmOCT) is another amplitude angiographic method that utilizes the time varying properties of speckle patterns to segment moving scatterers from static background. cmOCT was first developed by Jonathan *et al.* and was applied to imaging the *in vivo* mouse brain through a cranial window [6]. Shortly thereafter, Enfield *et al.* applied the technique to *in vivo* human imaging to visualize microcirculation maps on the volar forearm, demonstrating the ability to extract parameters such as capillary density and vessel diameter [39]. Both studies were based on the use of a commercial swept-source OCT system operating at an A-scan rate of 16 kHz (THORLABS OCM1300SS).

The correlation mapping technique is applied to time-separated pairs of intensity-based OCT data, which can either be co-located or separated by a small distance. Generally, this distance must be less than half the optical spot size of the sample beam. The first stage of processing is to find the two-dimensional cross correlation between a window or grid of pixels in one frame (*A*) and the corresponding grid in the subsequent frame (*B*), where the grid has dimensions *M* × *N* pixels. Mathematically, this is described by equation 3.7.

$$cmOCT(x,z) = \frac{\sum_{p=1}^{M}\sum_{q=1}^{N}[I_A(x+p,z+q)-\overline{I_A(x,z)}][I_B(x+p,z+q)-\overline{I_B(x,z)}]}{\sum_{p=1}^{M}\sum_{q=1}^{N}\sqrt{\left(I_A(x+p,z+q)-\overline{I_A(x,z)}\right)^2}\sqrt{\left(I_B(x+p,z+q)-\overline{I_B(x,z)}\right)^2}} \quad (3.7)$$

where $\bar{I}$ is the mean intensity of the OCT intensity signal in the grid. The grid is shifted across the entire *x*-*z* image to give a two-dimensional correlation map containing values in the range of 0 to 1, indicating decorrelated to highly correlated, respectively. For static regions of tissue, a high correlation value (> ~0.6) will be returned whereas for dynamic regions, such as signals from a blood vessel containing flowing blood, a low correlation value will be returned (< ~0). For display purposes, the complement is presented, such that static regions are represented by low values (dark) and regions of flow are represented by high values (bright).

The second stage of processing is to apply a 'structural mask' to suppress the background noise, which for low intensity regions can cause decorrelation, even if the region is static. The mask is generated by blurring the original OCT intensity data by a Gaussian window and then thresholding the resultant image to give a binary mask. The process of thresholding involves setting all intensity values below the threshold value to 0 and above the threshold value to 1. The binary mask is then applied to the correlation mapping image calculated based on equation 3.7. The selection of the threshold value implies a trade-off. If the threshold is too low, noisy, low-intensity values can cause decorrelation and hence produce false flow signals in the final correlation mapping image. If a high threshold value is used, the lower intensity signals are excluded which will reduce the imaging depth of angiographic mapping.

The correlation mapping algorithm is applied to pairs of OCT data frames which means that the scanning protocol can be done in a number of ways. One of them involves applying the correlation mapping technique to adjacent B-scans of a 3D volume, which means that there exists a small separation in space between adjacent frames. In this method, it is important that the step-size between one frame and the next not be too large, else the static regions will be decorrelated producing false angiographic mapping. Ideally, the step size must be less than the resolution in that dimension to ensure a strong correlation between the adjacent static regions.

Typically, a density of 5 – 10 scans per resolution value is used [6,39–44]. Another method to implement cmOCT technique is to scan the same location in time, as a series of BM scans (i.e., acquiring multiple B-scans at the same transverse location). For scanning protocols such as these, it is important that the time separation between consecutive frames not be too small, as this will make it more difficult for the algorithm to detect small flow velocities.

Choosing the size of the window/kernel is an important consideration for cmOCT angiography as this sets the number of data points used to calculate the correlation at any given pixel and there exists a tradeoff between signal-to-noise and transverse resolution. If too large a grid size is used, smaller blood vessels will not be resolved in the correlation map and if too small a size is used, the number of data points used to calculate the correlation will be small and will result in a noisy signal. Typically used values are 5×5 or 7×7.

cmOCT has been used to image microcirculation of the skin [6,39,41], nailfold [43], Xenopus laevis tadpole [40] and to study blood flow dynamics [45].

3.2.2.3 Split spectrum amplitude decorrelation

Split-spectrum amplitude-decorrelation angiography (SSADA) was first developed by Jia *et al.* and this method also extracts flow information from time-varying speckle signals [46]. The basis of SSADA is that for typical swept source OCT systems used in ophthalmology, the resolution cell is anisotropic, i.e., the axial resolution is higher than the transverse resolution, which will result in higher decorrelation sensitivity in the axial direction than in the transverse direction. For retinal imaging applications, retinal and choroidal blood flow is mostly in the direction perpendicular to the sample beam. This means that the flow detection signal-to-noise ratio can be improved by reducing the axial resolution to dampen the axial decorrelation sensitivity and without loss of speckle information.

SSADA requires *N* (8) images to be recorded at the same B-frame location, i.e., BM mode. In general, if the axial resolution is *M* times the transverse resolution, then the spectrum can be separated into *M* bands. The first step in the processing procedure is to reduce the full *k*-space spectrum into the *M* smaller, Gaussian-shaped frequency bands. Conventional Fourier domain OCT algorithms are applied to each of the reduced spectra to give a depth-dependent intensity *I (x,z)*. For each band (i.e., for each *M*), the speckle decorrelation is calculated between pairs of successive B-frames and then averaged via equation 3.8.

$$Flow_{SSADA}(x,z) = 1 - \frac{1}{N-1}\frac{1}{M}\sum_{n=1}^{N-1}\sum_{m=1}^{M}\frac{I_n(x,z)I_{n+1}(x,z)}{\left[\frac{1}{2}I_n(x,z)^2+\frac{1}{2}I_{n+1}(x,z)^2\right]} \quad (M=4, N=8), \qquad (3.8)$$

where N is the number of B-frames acquired at each location; M is the number of bands used; and $I_n(x,z)$ indicates the intensity of the n^{th} frame at lateral position x and at depth z.

It has been demonstrated that the SSADA method improves the signal-to-noise ratio of flow detection [46,47]. Applications for SSADA have been demonstrated across multiple studies including detection of retinal vessels in neovascular age-related macular degeneration (AMD) [47], glaucoma [48], diabetic retinopathy [49] and diabetic macular edema [50].

In the next section, angiographic techniques that use both phase and amplitude of the interference spectra is discussed.

3.2.3 Complex OCT

Complex OCT angiographic techniques use both the amplitude and phase of the interference spectra. Complex OCT angiographic techniques include optical microangiography, imaginary part-based correlation mapping, complex differential variance and eigen decomposition based clutter filtering. The theory of these methods is described in detail in the sections below.

3.2.3.1 Optical microangiography

The first method to use complex information, called optical microangiography (OMAG), was demonstrated by Wang *et al.* in 2007 in a SD-OCT [52], and the method was subsequently refined [7,53]. The rationale for including both phase and amplitude information is explained as follows. Moving red blood cells induce changes in both phase and intensity of the backscattered light. Phase information is strongly dependent on both angle (as explained in Section 3.1) and flow; however, changes in intensity (square of amplitude) are based on decorrelation, which is insensitive to low flow rates. Hence, subtraction of 2 or more complex spectra, will result in improved sensitivity to flow [54]. The OMAG algorithm is given mathematically by Eq. 3.9.

$$I_{OMAG}(x,y,z) = \left[1 - Norm\left(\overline{I(x,y,z)}\right)\right] \frac{1}{N-1} \sum_{i=1}^{N-1} |C_{i+1}(x,y,z) - C_i(x,y,z)| \qquad (3.9)$$

where $C_{i+1}(x,y,z)$ is the complex OCT signal which contains both amplitude and phase information on the *i'th* repeated B scan, $Norm(\overline{I(x,y,z)})$ is the normalized structure signal which scales the image to the range 0 to 1 [55].

Several modifications of the OMAG algorithm has been proposed in the past. In 2014, Choi *et al.* used the correlation mapping procedure to produce a binary mask which was applied to

ultrahigh-sensitive optical microangiography in order to reduce the noise that arises from the static tissue regions [56]. The authors demonstrated that by combining OMAG and correlation mapping, an improved signal-to-noise ratio was achieved in their microcirculation images using SS-OCT. In another study, Huang *et al.* demonstrated retinal angiography using intensity differentiation based OMAG [57]. The performance of OMAG technique has been evaluated for SD-OCT and SS-OCT for retinal angiography and CNV [58,59] and it was found that SS-OCTA imaging was able to detect more vessels than SD-OCTA imaging.

OMAG has been applied to visualization of the vasculature of the mouse brain [7], human microcirculation [55,60] , retinal vasculature [57,61] and disease development [62].

3.2.3.2 Imaginary part-based correlation mapping

In the correlation mapping section (Section 3.2.2.2), it was mentioned that it is possible to increase the signal-to-noise ratio by increasing the window size, but at a cost of reducing the resolution by blurring the information from small blood vessels. In 2015, Chen *et al.* proposed an imaginary part-based version of correlation mapping, which solves this problem, allowing an increase of the SNR without increasing the window grid [63]. Their solution was to use the imaginary component of the depth-resolved complex signal, which is more sensitive to motions than absolute values (i.e., amplitude), to do the correlation calculation. The complex depth-resolved signal is found by taking the Fourier transform of the spectral fringes in the wavenumber domain (i.e., *k*-space). This increase in sensitivity causes greater decorrelation and hence provides a better SNR. The correlation mapping algorithm is described mathematically by equation 3.10.

$$ImcmOCT(x,z) = \frac{\sum_{p=0}^{M}\sum_{q=0}^{N}\left[C_A(x+p,z+q)-\overline{C_A(x,z)}\right]\left[C_B(x+p,z+q)-\overline{C_B(x,z)}\right]}{\sqrt{\sum_{p=0}^{M}\sum_{q=0}^{N}\left[C_A(x+p,z+q)-\overline{C_A(x,z)}\right]^2}\sqrt{\sum_{p=0}^{M}\sum_{q=0}^{N}\left[C_B(x+p,z+q)-\overline{C_B(x,z)}\right]^2}} \quad (3.10)$$

where *C* is the imaginary component of the complex depth-resolved signal; and *A* and *B* represent one frame and the next. Again, the grid is shifted across the entire *x*-*z* image to give a two-dimensional correlation map. In this method, the intensity information is also used (i.e. the square of the absolute value of the complex signal) to calculate the structural OCT image and hence create a binary mask in a similar manner to standard correlation mapping. It has been used to image skin microvasculature using a spectral domain OCT system.

3.2.3.3 Complex differential variance

Complex differential variance (CDV) was introduced by Nam et al. [63] that uses both the amplitude and phase of the co-located OCT A-scans (i.e., A-scan from the same locations) to reconstruct high contrast vascular images. CDV algorithm is given by equation 3.11:

$$f_{CDV} = \sqrt{1 - \frac{\sum_{t=1}^{t=M-1} |\sum_{k=-L}^{k=L} w(k) R(z-k,t) R^*(z-k,t+1)|}{\sum_{t=1}^{t=M-1} \sum_{k=-L}^{k=L} w(k) \frac{1}{2} [|R(z-k,t)|^2 + |R(z-k,t+1)|^2]}} \quad (3.11)$$

where *M* is the number of co-located A-scans at each location; *w(k)* is a window function of length *2L+1* that is used to average across the correlated pixels in depth; $R(z,t)$ represents the A-scan at depth z and time instance t; and $R^*(z,t)$ represents the complex conjugate of $R(z,t)$. The numerator term represents differential phase over time and the denominator accounts for intensity averaging. From the above equation 3.11, it can be seen that CDV is sensitive to change in phase only when the phase changes in depth across the depth window function *w(z)*. Therefore, CDV claims to be immune to small bulk motion artefacts and artefacts arising from lack of synchronization between data acquisition/laser modules. Optimized window size of 24 μm (full width half maximum) in air has been used for the angiographic studies. The authors [64] have shown CDV to be insensitive to bulk motion artefacts by comparing the algorithm performance with Doppler variance imaging of human skin using a 50 kHz swept source OCT system. The technique has been used to image skin microvasculature and dorsal skin fold.

3.2.3.4 Eigen decomposition (ED) based clutter filtering

ED based clutter filtering technique aims to reduce the effect of slowly moving stationary tissues (clutter) within the probed volume while producing vasculature maps [64]. It uses multiple A-scan acquisition protocol. In this technique, A-scans acquired at a particular depth position over time is modelled as a Gaussian process which can be represented as a sum of clutter component (c), an additive noise component (n) and blood components (b).

Suppose, if *X* denotes the ensemble of A-scan signals obtained from a particular depth such that

$X = [x(1), x(2), .. x(N)]^T$, where *N* is the number of A-scans at the same location, then *X* can be written as given by equation 3.12

$$X = c + b + n \quad (3.12)$$

then the correlation matrix R_x is given by equation 3.13,

$$R_x = R_c + R_b + \sigma^2 I \tag{3.13}$$

where R_c is the clutter correlation matrix; R_b is the blood correlation matrix; σ^2 is the variance of the noise; and I is the identity matrix. Based on the assumption that clutter is the dominant signal and is spatially correlated along depth, an estimate of R_c is given by equation 3.14:

$$\hat{R}_c = \frac{1}{M}\sum_{i=1}^{M} X_i X_i^H \tag{3.14}$$

where X_i is the A-scan; i is the depth index; M is the total number of pixels in depth; and H stands for Hermitian. The estimated correlation matrix $\hat{R}_c$ is further decomposed into its corresponding eigenvalues and eigenvectors to which an eigen regression filter is applied to remove the clutter and finally a Doppler center frequency is estimated.

Although the ED-based technique was less sensitive to tissue motion, it was computationally time consuming. Also, when imaging high flows as in the case of arteries, clutter removal failed with ED method. Another challenge was the proper selection of eigen vectors that represents the clutter space.

Yousefi *et al.* [65] has proposed another technique, which was built upon the principle of multiple signal classification similar to the ED based filtering approach. In this technique, the OCT signal from each voxel is treated as the superposition of 3 components (i) signal from the tissue, (ii) hemodynamic component and (iii) noise. One of the major assumptions is that these three signals that make up the OCT voxel are independent and hence can be decomposed into orthogonal basis functions. Also, it assumes that the major contribution of the OCT signal comes from static tissue. By taking the orthogonal basis functions of the OCT signal and calculating its autocorrelation matrix from the eigen vectors, the power spectrum of the hemodynamics may be estimated. Details of the technique can be found in [65]. Though Yousefi *et al.* shows its application to image mouse ear, it does not show much improvement over the ultra-high sensitive OMAG technique. Nevertheless, it was shown to be sensitive to both axial and transverse flow as other complex angiographic techniques. Also other studies have been done based on modified ED based filtering techniques [66,67].

From the above sections based on the literature review, it can be seen that amplitude-based techniques dominate swept source-based OCT angiography. Among the amplitude-based techniques, SSADA was developed for retinal imaging applications to reduce the axial

sensitivity of OCT to the pulsatile flow within the choroid. Hence in this study, we investigate microvascular detection capability of cmOCT and SV techniques using 200 kHz VCSEL based SS-OCT system for *in vivo* imaging applications. To test the performance of cmOCT algorithm, first it is tested on intralipid phantom model to optimize the kernel size for cmOCT mapping and then is extended to nailfold imaging and to preclinical ocular imaging applications.

3.3. EXPERIMENTAL SETUP AND METHODS

3.3.1 High speed SS-OCT system

For conducting the experiments, commercial SS-OCT system from Thorlabs operating at 200 kHz was used. It uses a MEMS vertical-cavity surface-emitting (MEMS-VCSEL) swept laser operating at central wavelength of 1300 nm (spectral bandwidth of 100 nm) and has an imaging depth range of 12 mm. The system uses a 5X objective that provides a lateral resolution of 25 µm and an axial resolution of 11 µm in air. The schematic of the commercial system is shown in figure 3.1. The measured system sensitivity was 100 dB near the zero delay line. The system was capable of imaging using multiple B-scan (BM) protocol, which let the user acquire multiple B-scans at the same lateral position.

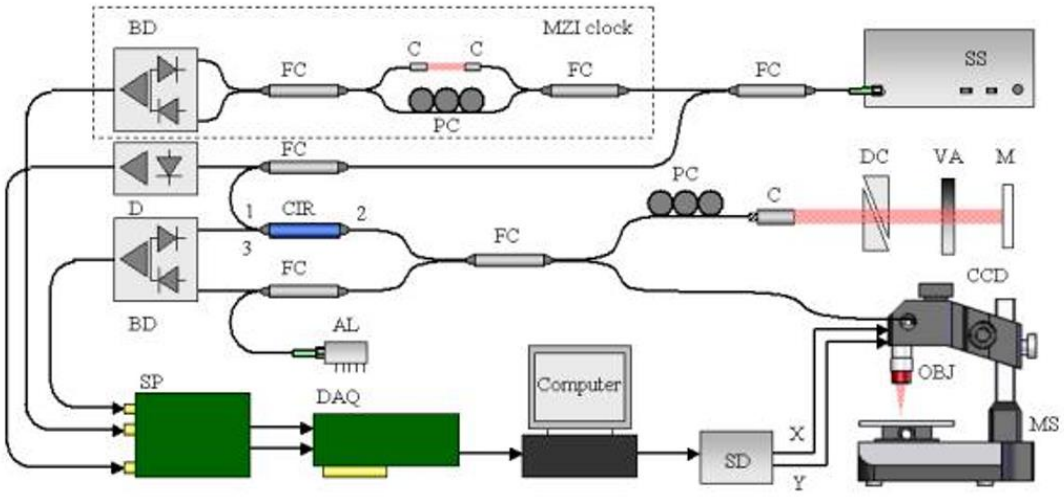

Fig.3.1. Schematic of the VCSEL based 200 kHz swept source OCT (Thorlabs)
(SS - swept laser source, FC- fibre coupler, PC - polarization controller , CIR - circulator, C - collimator, BD – balanced detector, CIR – circulator, DAQ – data acquisition, VA – variable attenuator, D – detector, AP - adjustable pinhole, and M – mirror).

3.3.2 cmOCT processing and data acquisition

The details of cmOCT processing technique are as explained in section 3.2.2.2. In this study, to enhance the regions of flow and suppress the static regions, the resulting cmOCT values obtained from cmOCT processing as given in equation 3.7 are thresholded to the range -0.6 to +0.6 using such that decorrelation values < -0.6 were mapped to the value -0.6 and decorrelation values > 0.6 were thresholded to 0.6.

For this study, 3D volumetric data were acquired with 8 B-scans at each location to generate cmOCT angiographic mapping. The cmOCT algorithm was applied to the successive B- frames (Eq.3.7) within these 8 frames thus resulting in *N*-1, 2 D decorrelation maps (*N*=8 in this case) at a given location. Finally, the correlation maps at each transverse positions are averaged to produce averaged cmOCT maps as given by equation 3.15.

$$Averaged_{cmOCT}(x,y) = \frac{1}{K}\sum_{K=1}^{7} cmOCT\ (x,y) \tag{3.15}$$

The cmOCT map was generated using a custom program written in MATLAB [39]. To compare our proposed cmOCT algorithm with SV angiography, the SV algorithm was implemented in MATLAB. The inter-frame speckle variance (*SV*) based on B-M scan protocol was calculated as given by equations 3.5 and 3.6.

3.3.3 Post processing for motion artefact removal

It is highly desirable to minimize the motion artefact arising from the involuntary sample movement or the inherent rhythmic vibrations within the organism for in vivo imaging of small animal models and clinical applications [19]. These movement artefacts introduce error in the cmOCT maps thereby reducing the image contrast between static and flow regions and thus degrade the signal to noise ratio. Although a 200 kHz axial scanning system was used for data acquisition, bulk motion artefacts tend to occur, and hence axial and lateral motion correction algorithms were used before applying correlation mapping. To compensate the axial motion between the sequential B scans acquired from the same location, we implemented the algorithm described by Makita *et al* [38] which is based on one dimensional cross correlation between the intensity profiles of A-lines within the successive B frames acquired from the same location. After axial motion compensation, the image registration method developed by Thevenaz *et al* [39] was implemented to compensate for the lateral motion occurring between the B-scans,. Finally, after producing cmOCT maps, median filtering of the resulting

correlation maps using a 3x3 kernel was carried out to improve the signal to noise ratio of the resulting images. The same pre-processing steps that were carried out for cmOCT are done for SV angiography. Figure 3.2 shows the processing steps involved for both cmOCT and SV.

Finally, the generated angiographic maps were depth encoded for better visualization of microvasculature. The depth encoded intensity images were generated in Matlab (version 2014). For the depth encoding, each image slice was colour coded using the command 'hsv2rgb' by providing the set hue, saturation and value. For each image in the volume stack, the value of hue was incremented by fixed step size determined by the total number of frames in the volume stack. In this way, mixed colours could be mapped onto the overlapped vessel areas. However, the depth encoding provides only visual information and is not used for comparison between cmOCT and SV techniques.

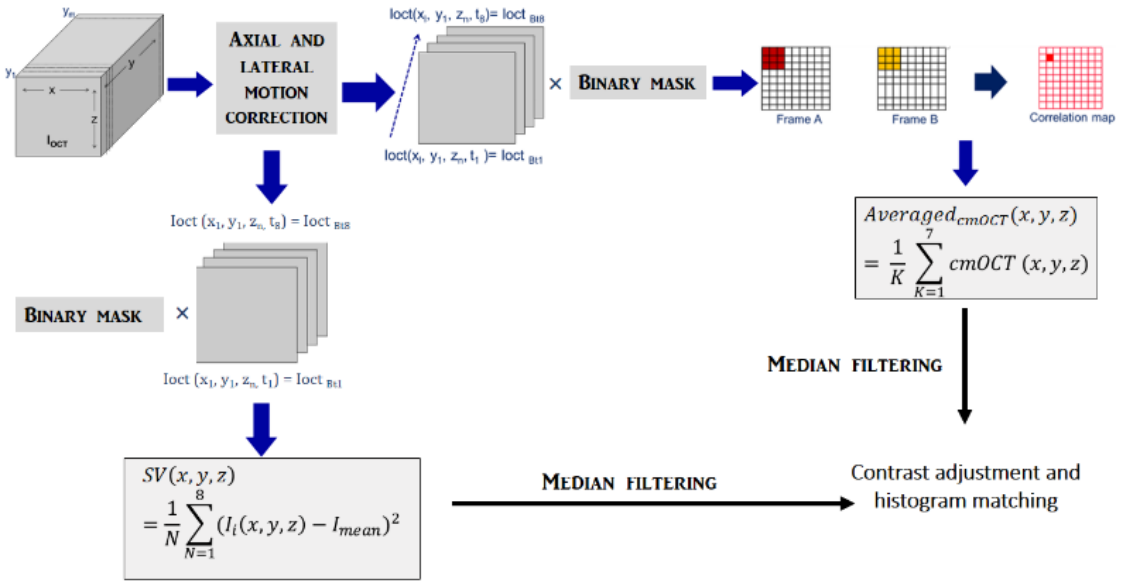

Fig.3.2. The schematic showing cmOCT and SV processing steps.

3.3.4 Measure of contrast

In order to compare cmOCT with SV results based on the obtained angiographic maps, three contrast metrics are used in this study. They are correlation signal to noise ratio (CSNR) [47], signal to noise ratio measurement [46,72] and contrast to noise ratio (CNR) [27].

CSNR of an image is defined as given by equation 3.16 [47]

$$CSNR = \frac{\overline{C_{FLOW}} - \overline{C_{STATIC}}}{\sqrt{\sigma^2_{STATIC}}} \tag{3.16}$$

where $\overline{C_{FLOW}}$ and $\overline{C_{STATIC}}$ are the average correlation values within the flow and static regions of the sample respectively, and $\sigma^2{}_{STATIC}$ is the variance of the correlation within the static region.

To calculate the SNR as given in [46, 72], the standard deviation of signals within the static region (σ) was calculated and this value is used as a threshold for defining the effective detectable flow signals within the flow region of the sample as represented by equation 3.17.

$$SNR = 20 * log \frac{S}{\sigma} \tag{3.17}$$

where S represents the average binary thresholded signal within the flow region.

CNR of an image is calculated by using equation 3.18 [27]

$$CNR = \frac{\overline{C_{FLOW}} - \overline{C_{STATIC}}}{\overline{C_{STATIC}}} \tag{3.18}$$

For effective comparison between cmOCT and SV angiographic techniques using the above described contrast metrics, the cmOCT and SV signals were converted to the same scale range, i.e. all the values were mapped into the interval [0 1] based on the following equation.

If we have numbers *x* in the range *[a, b]* and we want to transform them to numbers *y* in the range *[c, d]*, then

$$y = (x - a)\frac{d-c}{b-a} + c \tag{3.19}$$

3.3.5 Phantom imaging

To demonstrate the feasibility of cmOCT for high speed SS-OCT, experiments were first performed using capillary tubes filled with 2 % of 20 % v/v intralipid solution embedded in synthetic clay to mimic the Brownian motion of dynamic scattering particles. A capillary tube with an inner diameter of ~300 μm was embedded in Blu-Tack to simulate the static background tissue optical heterogeneity. 3 D volume data covering an area of 3 x 5 x 5 mm^3 with 8 B-scans at each location was acquired. In the Y scan direction, 200 scan locations covering 5 mm were acquired with 1000 A -lines in each B-scan, thus generating a total volume of 1600 images using the B-M scan protocol. The total time for 3 D volume acquisition was 27 seconds. The spectral interferograms were processed to produce intensity B-scan images following conventional Fourier domain processing. The processed intensity images were

subjected to axial and lateral motion compensation as discussed in section 3.3.3 and finally processed using averaged cmOCT angiographic technique.

To optimize the kernel size for cmOCT processing using the present SS-OCT system, cmOCT mapping with different kernel sizes ranging from 3x3 to 7x7 were carried out and the results obtained are shown in table 3.1. Based on the obtained contrast measurement parameters as indicated in table 3.1, a kernel size of 5×5 was chosen for the cmOCT processing for *in vivo* imaging applications.

Comparison Metric	Kernel size (3 ×3)	Kernel size (5 ×5)	Kernel size (7X7)
CSNR	**5.1**	**11.1**	**12.5**
SNR	**77.1 dB**	**91.8 dB**	**87.8 dB**
CNR	**394.4**	**3.1055×10^3**	**1.470×10^3**

Table 3.1 Comparison metric for motion contrast for phantom experiment for different kernel sizes

Figure 3.3 shows the result of modified scanning protocol based cmOCT algorithm on the capillary phantom model using a kernel size of 5×5. Figure 3.3 (a) shows the representative B-scan image of the intralipid filled capillary tube embedded in Blu Tack and figure 3.3(b) and 3.3(c) shows MIP of enface images obtained using cmOCT and SV technique respectively. Figure 3.4(a) and 3.4(b) shows the cmOCT and SV maps obtained from the B scan image shown in figure 3.3(a). From figure 3.4(a), it can be observed that cmOCT effectively supresses the background noise from static regions and produce bright pixel values in regions where dynamic scattering over time occurs. Figures 3.4(c) and 3.4(d) shows the flow profiles extracted from the regions marked (white line) in 3.4(a) and 3.4(b) respectively, with SV and cmOCT values mapped onto the same scale range (0 to 1) for comparison. The results obtained from the motion contrast analysis is shown in table 3.2. From table 3.2, we can observe that there is an improvement of approximately two-fold in CSNR and 20 dB in SNR calculation for cmOCT compared to SV technique with the current scanning protocol.

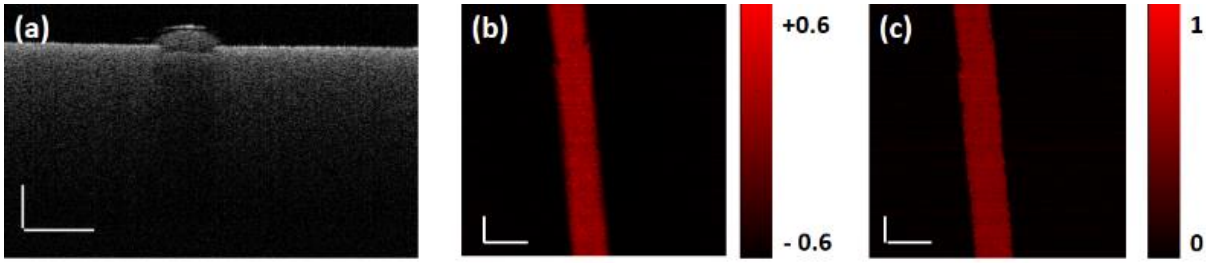

Fig. 3.3. (a) B scan image of intralipid filled capillary tube embedded in synthetic clay, (b) MIP of enface cmOCT images (c) MIP of enface SV images (Scalebars in x and y direction is 500 µm).

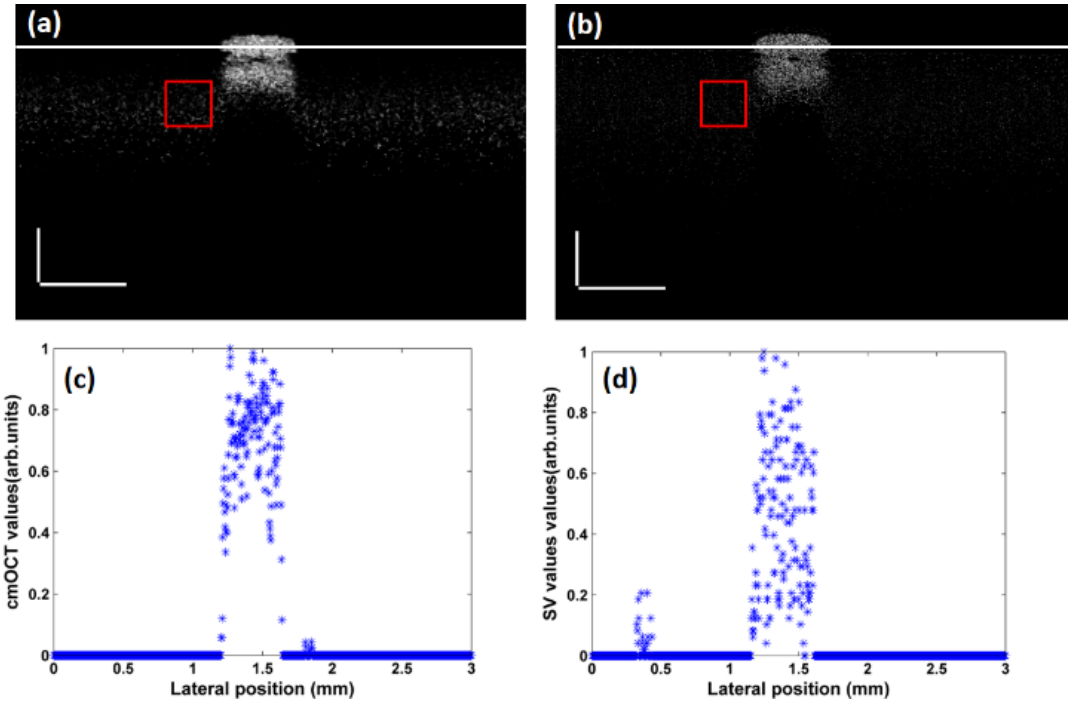

Fig. 3.4. (a) cmOCT image obtained from the transverse scan shown in Fig. 2(a) with static region of interest marked in red, (b) corresponding SV image with static region of interest marked in red (c) Profile plot obtained over the marked line in (a), (d) Profile plot obtained over the marked line in (b) (scale bar is 500 µm).

Comparison Metric	cmOCT	SV
CSNR	11.1	4.7
SNR	91.8 dB	73.2 dB
CNR	3.1055×10^3	232.3

Table3.2. Comparison metric for motion contrast for phantom experiment

From table 3.2, it can be inferred that cmOCT has better motion contrast compared to SV in flow phantom experiments.

3.4. Results and discussion – *in vivo* imaging

To test the performance of cmOCT for high speed angiographic imaging in high motion *in vivo* scenario, nailfold vasculature of a healthy human volunteer was imaged. For these experiments, informed consent was obtained from the participants. For the study, the little finger of the volunteer was fixed on a custom built imaging mount so that the dorsal skin surface faced the OCT probe beam. Imaging was performed using the B-M scan protocol over an area of 5 mm × 3 mm. The scanning protocol was set to capture 1000 A-scans per B-scan over a scan distance of 5 mm. For 3D volumetric imaging, 300 B-scan sampling positions were set to cover a scan range of 3 mm and 8 repeated B-scans were captured at every C-scan position thus generating 2400 B scans per volume. Figures 3.5 (a)-(e) show the results obtained from the nailfold imaging studies. Figure 3.5(b) shows the resulting cmOCT map of the structural image in figure 3.5(a) and figure 3.5(c) shows the corresponding SV image. Figures 3.5(d) and 3.5(e) show the depth encoded intensity projection image obtained from enface cmOCT and SV images respectively. From figure 3.5(d), it can be observed that the cm-OCT technique clearly maps the hair pin shaped capillary loops within the nail-fold using the present high-speed system. However, the lateral resolution of the system limits the resolvability of individual capillary loops.

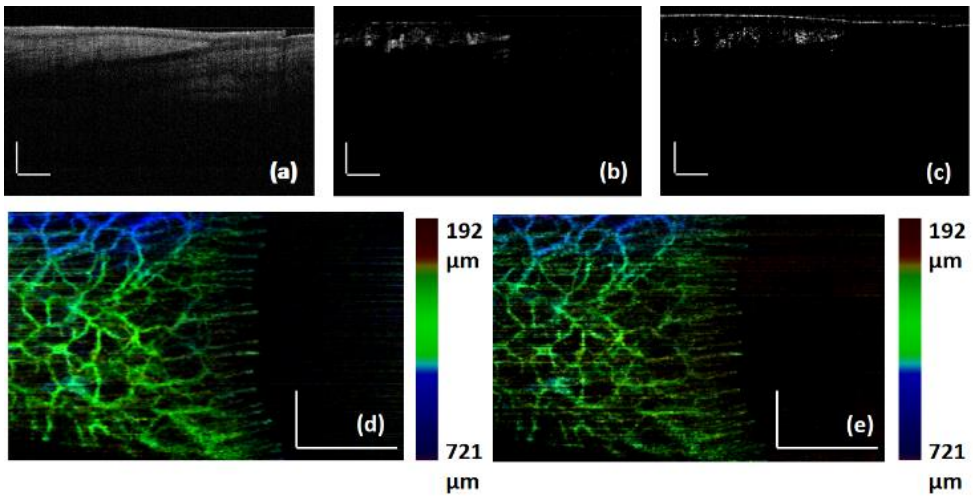

Fig. 3.5. (a) Representative B-scan image of the little finger of adult volunteer, (b) corresponding cmOCT image, (c) corresponding cmOCT image (d) depth encoded intensity projection image of enface cmOCT images, (e) depth encoded intensity projection image of enface SV images (scale bars in x and y directions are 500 µm).

Comparing the MIP's of cmOCT and SV maps shown in figures 3.6(a) and (b), we can observe that cmOCT provides better signal to noise ratio than SV technique using the same B-M scan protocol. Table 3.3 provides the CSNR, SNR and CNR measurements for SV and cmOCT techniques. For calculation of CSNR, SNR and CNR, flow region signals were obtained from

the profile plot marked by yellow colour passing through the hair pin loops and noise region signals were obtained from the profile plot marked in white as shown in figure 3.6(a) and 3.6(b). For comparison between both techniques, the profile plots were mapped to the range 0-1. From the profile plots shown in figure 3.5(c), it can be observed that noise is reduced in cmOCT mapping method compared to SV technique. From table 3.3, it can be inferred that there is an improvement of four- fold in CSNR calculation and an improvement of 10 dB in SNR calculation for cmOCT technique compared to the SV technique.

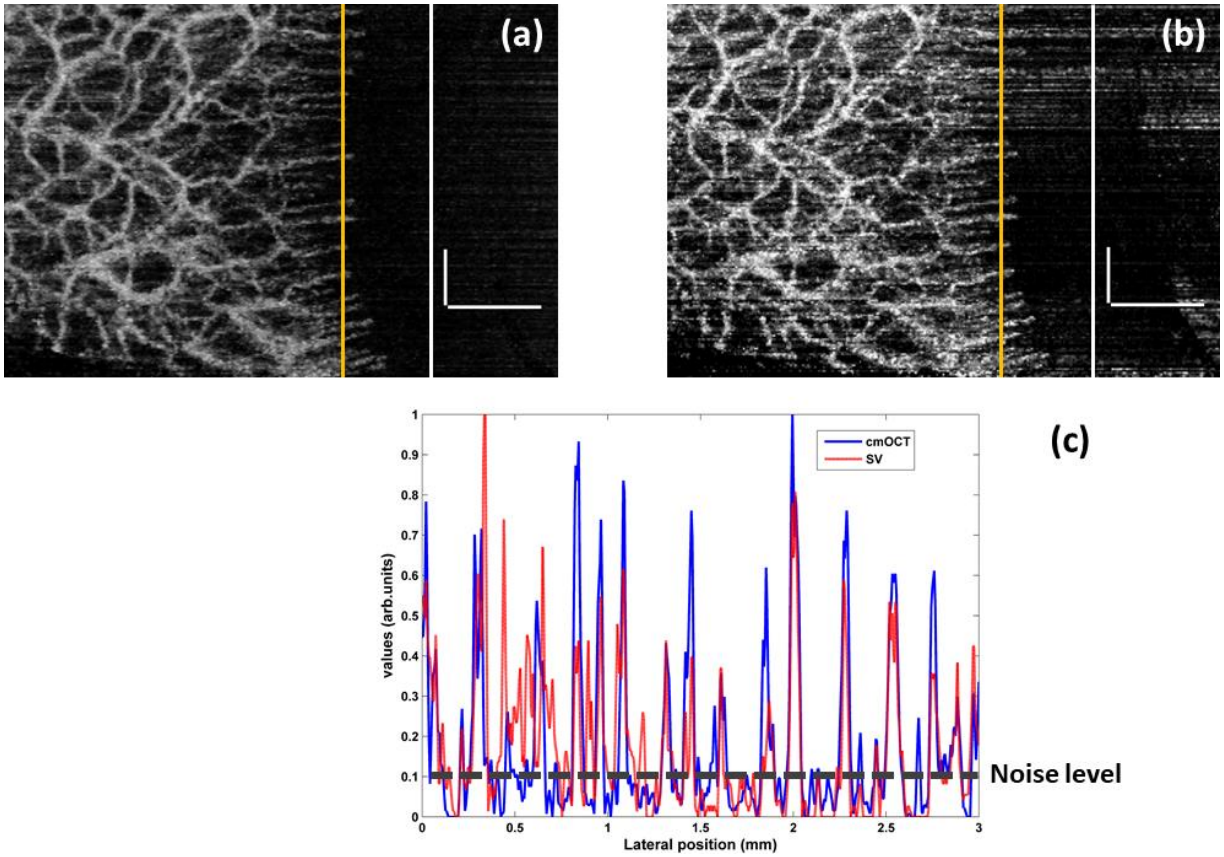

Fig. 3.6. (a) MIP of enface cmOCT images from nailfold (b) MIP of SV enface images (c) signal profile extracted from the position marked in yellow vertical line in (a); (d) signal profile extracted from the position marked in yellow vertical line in (b), Scalebars are 500 µm.

Comparison Metric	cmOCT	SV
CSNR	2.8	0.61
SNR	67.1 dB	55.8 dB
CNR	2.33	0.91

Table 3.3. Comparison metric for motion contrast obtained from nailfold

Also, to evaluate the proposed method for ocular studies, angiographic studies on a rodent model were carried out. This is the first study that has tested the suitability of cmOCT technique to ocular studies. Monitoring ocular circulation is vital as many of the vision related issues begin with changes in the microcirculatory flow or the vascular pattern. Since the introduction of OCT, it has found tremendous applications in ophthalmology and has led to commercialization of the technology with FDA approved clinical ophthalmic OCT systems widely in use both in research and in clinics. However, it is to be noted that very few studies have been carried out to investigate the blood perfusion and vasculature of iris tissue beds compared to retinal angiography. Few studies have been conducted that evaluated the suitability of commercial ophthalmic spectral domain OCT systems during disease conditions such as iris micro-hemangiomatosis, iris nevus, iris hemangioma [44]–[46], normal iris vasculature [47], in staging neovascularization [48] and in iris tumours [49]. Most of these studies are based on spectral domain systems operating at 70 kHz A-scan rate with an inbuilt SSADA technique. Iris vasculature studies have been performed using the OMAG based technique on rodent models using spectral domain OCT system [50]. Similar studies on rodent models have been carried out using photoacoustic microscopic imaging [51], [52].

The current gold standard for ocular angiography is fluorescence angiography. One of the drawbacks of fluorescence angiography is that the imaging requires injection of contrast agents, fluorescein. This causes pain, discomfort and in some cases allergic reactions due to the injected dye. As angiographic OCT provides label free endogenous contrast mechanism from the moving RBC's, it has the potential in replacing fluorescence angiography. Based on these observations, cmOCT angiography was performed on a preclinical rat model. For the experiments, the rat was mounted on an in-house built imaging platform that minimized the head movement and the blinking of the eye. The preclinical rat model was anaesthetized during the entire imaging session using a mixture of 1.5% isoflurane, 80 % air, and 20 % oxygen inhaled through the attached breathing mask. The body temperature of the animal was maintained constant at 37 °C using a temperature-controlled heating pad. For the data acquisition, B-M mode scanning protocol with 8 scans at each location, with 200 transverse scans covering 5 mm x 5 mm was performed. Throughout the experiment, the focal plane of imaging was fixed midway between the iris. The 3D volume data was acquired in 27 s. Figure 3.7 shows the results of the experiment. Figure 3.7(a) shows a representative OCT B-scan image formed by averaging the repeated B-scan images at a given position and figure 3.7(b) shows the corresponding averaged 2-D correlation map as calculated from section 2.2. Figures

3.7(d) and 3.7(f) shows the depth encoded intensity projection image and MIP of enface images of the vasculature over the entire scanned area using cmOCT technique. From the B-scan image in figure 3.7(a), one can see the structures within the anterior segment of the eye namely the avascular cornea and highly vascularized iris. Since the focal plane was fixed midway of the iris, we can observe the mirror artefact that occurs in FD-OCT systems. Figures 3.7(c) and (e) and (g), show the corresponding SV images of the B-scan, the depth encoded intensity projection image and MIP of enface images obtained by SV technique respectively.

It can be seen that the cmOCT is capable of being applied to high speed OCT systems with wide field of view imaging applications comparable to OMAG based angiography reported by Choi *et al* [79] for a smaller field of view. The dense small capillaries of the iris which are typically less than 10 µm could not be well resolved by our low NA objective lens. However, the general microvasculature of the rat iris consisting of radial branches of vessels and dense capillary network surrounding the pupil is clearly visible in figure 3.7(d). Also, we can see the major iris circle (MIC), which bifurcates into multiple radial iris arteries (RIA) which then feed into the lesser iris circles (LIC) around the pupillary margin. It is to be noted that some of the RIA and the LIC appear to be slightly blurred. This could be due to the combined effect of low objective NA and degradation of signal quality of the structures out of the focal plane.

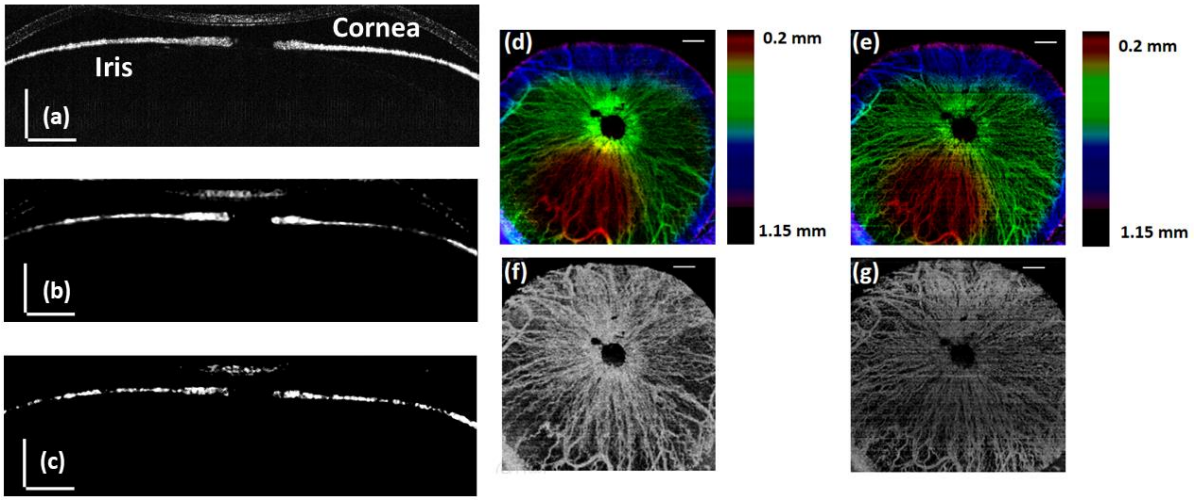

Fig. 3.7 (a) Representative B scan image of anterior chamber of rat, (b) corresponding cmOCT image, (c) corresponding SV image (d) depth encoded intensity projection image of enface cmOCT maps, (e) depth encoded intensity projection image of enface cmOCT maps, (f) – (g) MIP of enface images of cmOCT and SV (scale bars is 500 µm).

Figures 3.7 (f) and (g) indicates reduced signal to noise ratio of SV images compared to cmOCT images. However, the structures within the vasculature namely MIC, RIA and LIC are visible with reduced contrast.

Next, imaging of a rodent eye that had undergone a failed corneal grafting procedure was carried out. The cornea is the transparent, smooth avascular region within the anterior segment of the eye and plays an important role in focussing light onto the retina. The corneal layer can be damaged or scarred by factors such as chemical injury, infections or genetic dystrophy. Corneal grafting or penetrating keratoplasty is one of the treatment approaches undertaken when the corneas have become opaque. However, it has been reported that, in 35% of cases undergoing the procedure, there is a possibility of graft rejection [53], [54]. Major clinical symptoms of graft rejection include corneal oedema, stromal infiltration, and corneal vascularization. OCT offers great potential in the treatment monitoring of such grafted corneas over time. Introducing corneal vascularization can be used as a tool to study the neovascularization process in general and in particular within the eye for clinical researchers. High resolution, high speed OCT's have the potential to be used as a non-invasive imaging tool to study the functional processes over time that lead to neovascularization as well as the structural changes that occur. In view of this, a rat eye with a failed corneal graft was imaged using OCT. cmOCT was able to capture the newly formed vessels within the cornea. Figure 3.8(a) shows a representative B scan image obtained from the failed transplant model and figure 3.8(b) shows the corresponding cmOCT map. Corneal inflammation and penetration of the iris into the cornea along with loss of corneal transparency can be observed from figure 3.8(a). From the corresponding cmOCT image shown in figure 3.8(b), one can see the capillary vessels within the cornea that lead to corneal vascularization. Finally, figure 3.8(d) shows the depth encoded intensity projection images obtained from the cmOCT *enface* images. The projection map enables the visualization of the vasculature within the cornea that may be of interest to clinicians and researchers studying vascularization/neovascularization of the cornea following corneal injury or treatment models and also in studying the vascular development during ocular tumour or any other cancerous tissue. Figures 3.8(f) and (g) shows the MIP of enface images from cmOCT and SV techniques respectively. Fig. 3.9 shows the profile plots obtained from the region marked in yellow horizontal line in Fig. 3.8(b) and 3.8(c) showing detected capillaries by cmOCT and SV angiography techniques.

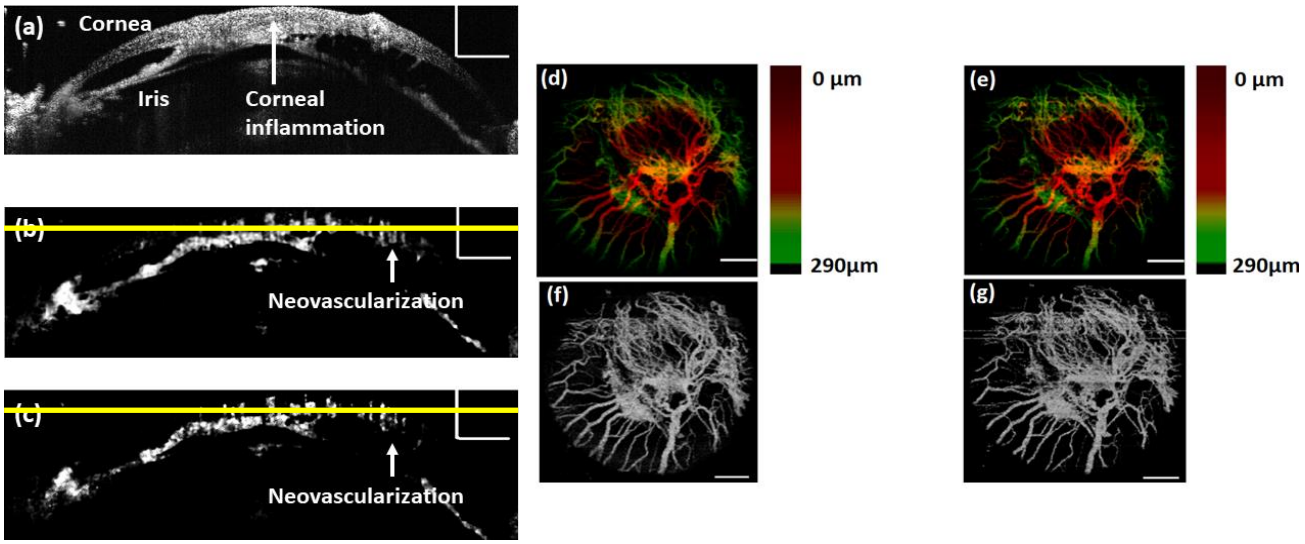

Fig. 3.8 (a) Representative B scan image of the anterior chamber with a failed corneal graft, (b) corresponding cmOCT image (c) corresponding SV image (d)-(e) depth encoded intensity projection image of enface cmOCT and SV maps (f) –(g) MIP of enface images of cmOCT and SV (scale bars is 500 µm).

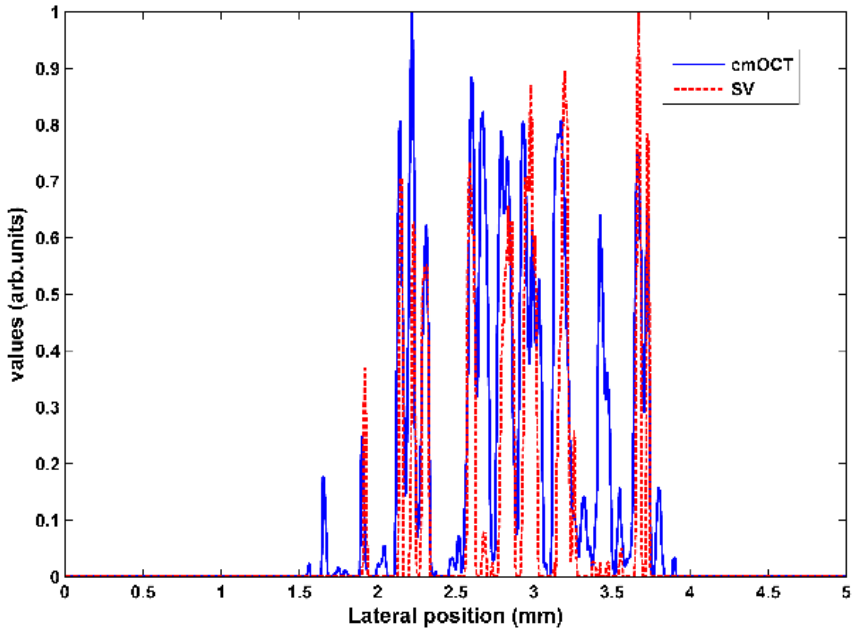

Fig. 3.9 Signal profile extracted from the position marked in yellow horizontal line in fig. 3.8(b) and (c).

From the profile plots, we can observe that, cmOCT detects more capillaries (peak signals) compared to SV imaging.

Theoretically, the resolution in the B-scan plane used for cmOCT kernelling is worse by a factor of five in each dimension for a 5x5 kernel. The resolution in the other dimension (y) is unaffected. We also notice that vessels significantly smaller than the theoretical resolution are

easily visible. From the above experiments and results, the suitability of cmOCT angiography for 200 kHz SS-OCT system is demonstrated.

3.5. Conclusions

In this chapter, the applicability of the cmOCT angiography incorporating a modified scanning protocol using high-speed SS-OCT is demonstrated. Also, the suitability of the cmOCT technique for *in vivo* ocular imaging in a rodent model is presented for the first time. The modified scanning protocol based on acquiring 8 scans at each location is shown to produce angiographic maps with better SNR compared to speckle variance algorithm that used the same number of multiple B-scans for the calculation of variance. However, unlike SV, cmOCT can be operated on just two B-scans, especially if SNR is good, where faster scanning and processing is desired. Further studies have to be carried out to optimize cmOCT technique for high speed SS-OCT by optimizing the B-M scan protocol. The technique presented using 200 kHz SS-OCT system operating at 1300 nm offers great potential in clinical imaging as it can be used to rapidly acquire 3D-OCT volumes over a wide field of view and larger penetration depths without compromising structural- angiographical details.

REFERENCES

1. S. M. Daly and M. J. Leahy, "“Go with the flow”: A review of methods and advancements in blood flow imaging," J. Biophotonics **6**, 217–255 (2013).
2. J. Allen and K. Howell, "Microvascular imaging: techniques and opportunities for clinical physiological measurements," Physiol. Meas. **35**, R91–R141 (2014).
3. C.-L. Chen and R. K. Wang, "Optical coherence tomography based angiography [Invited]," Biomed. Opt. Express **8**, 1056–1082 (2017).
4. A. Mariampillai, B. A. Standish, E. H. Moriyama, M. Khurana, N. R. Munce, M. K. K. Leung, J. Jiang, A. Cable, B. C. Wilson, I. A. Vitkin, and V. X. D. Yang, "Speckle variance detection of microvasculature using swept-source optical coherence tomography," Opt. Lett. **33**, 1530–1532 (2008).
5. E. Jonathan, J. Enfield, and M. J. Leahy, "Correlation mapping method for generating microcirculation morphology from optical coherence tomography (OCT) intensity images," J. Biophotonics **4**, 583–587 (2011).
6. R. K. Wang, "Optical Microangiography: A Label-Free 3-D Imaging Technology to Visualize and Quantify Blood Circulations Within Tissue Beds In Vivo," IEEE J. Sel. Top. Quantum Electron. **16**, 545–554 (2010).
7. D. M. Schwartz, J. Fingler, D. Y. Kim, R. J. Zawadzki, L. S. Morse, S. S. Park, S. E. Fraser, and J. S. Werner, "Phase-Variance Optical Coherence Tomography," Ophthalmology **121**, 180–187 (2014).
8. Z. Chen, Y. Zhao, S. M. Srinivas, J. S. Nelson, N. Prakash, and R. D. Frostig, "Optical Doppler tomography," IEEE J. Sel. Top. Quantum Electron. **5**, 1134–1142 (1999).
9. R. A. Leitgeb, R. M. Werkmeister, C. Blatter, and L. Schmetterer, "Doppler Optical Coherence Tomography," Prog. Retin. Eye Res. **41**, 26–43 (2014).
10. J. K. Barton and S. Stromski, "Flow measurement without phase information in optical coherence tomography images," Opt. Express **13**, 5234–5239 (2005).
11. M. S. Mahmud, D. W. Cadotte, B. Vuong, C. Sun, T. W. H. Luk, A. Mariampillai, and V. X. D. Yang, "Review of speckle and phase variance optical coherence tomography to visualize microvascular networks," J. Biomed. Opt. **18**, 050901 (2013).
12. Z. Chen, T. E. Milner, S. Srinivas, X. Wang, A. Malekafzali, M. J. C. van Gemert, and J. S. Nelson, "Noninvasive imaging of in vivo blood flow velocity using optical Doppler tomography," Opt. Lett. **22**, 1119–1121 (1997).

13. Z. Chen, T. E. Milner, D. Dave, and J. S. Nelson, "Optical Doppler tomographic imaging of fluid flow velocity in highly scattering media," Opt. Lett. **22**, 64–66 (1997).
14. J. A. Izatt, M. D. Kulkarni, S. Yazdanfar, J. K. Barton, and A. J. Welch, "In vivo bidirectional color Doppler flow imaging of picoliter blood volumes using optical coherence tomography," Opt. Lett. **22**, 1439–1441 (1997).
15. R. A. Leitgeb, L. Schmetterer, W. Drexler, A. F. Fercher, R. J. Zawadzki, and T. Bajraszewski, "Real-time assessment of retinal blood flow with ultrafast acquisition by color Doppler Fourier domain optical coherence tomography," Opt. Express **11**, 3116–3121 (2003).
16. R. A. Leitgeb, L. Schmetterer, C. K. Hitzenberger, A. F. Fercher, F. Berisha, M. Wojtkowski, and T. Bajraszewski, "Real-time measurement of in vitro flow by Fourier-domain color Doppler optical coherence tomography," Opt. Lett. **29**, 171–173 (2004).
17. B. H. Park, M. C. Pierce, B. Cense, S.-H. Yun, M. Mujat, G. J. Tearney, B. E. Bouma, and J. F. de Boer, "Real-time fiber-based multi-functional spectral-domain optical coherence tomography at 1.3 μm," Opt. Express **13**, 3931–3944 (2005).
18. B. R. White, M. C. Pierce, N. Nassif, B. Cense, B. H. Park, G. J. Tearney, B. E. Bouma, T. C. Chen, and J. F. de Boer, "In vivo dynamic human retinal blood flow imaging using ultra-high-speed spectral domain optical Doppler tomography," Opt. Express **11**, 3490–3497 (2003).
19. B. Cense, N. A. Nassif, T. C. Chen, M. C. Pierce, S.-H. Yun, B. H. Park, B. E. Bouma, G. J. Tearney, and J. F. de Boer, "Ultrahigh-resolution high-speed retinal imaging using spectral-domain optical coherence tomography," Opt. Express **12**, 2435–2447 (2004).
20. H. Ren, T. Sun, D. J. MacDonald, M. J. Cobb, and X. Li, "Real-time in vivo blood-flow imaging by moving-scatterer-sensitive spectral-domain optical Doppler tomography," Opt. Lett. **31**, 927–929 (2006).
21. L. Wang, Y. Wang, S. Guo, J. Zhang, M. Bachman, G. P. Li, and Z. Chen, "Frequency domain phase-resolved optical Doppler and Doppler variance tomography," Opt. Commun. **242**, 345–350 (2004).
22. J. Zhang and Z. Chen, "In vivo blood flow imaging by a swept laser source based Fourier domain optical Doppler tomography," Opt. Express **13**, 7449–7457 (2005).
23. H. C. Hendargo, R. P. McNabb, A.-H. Dhalla, N. Shepherd, and J. A. Izatt, "Doppler velocity detection limitations in spectrometer-based versus swept-source optical coherence tomography," Biomed. Opt. Express **2**, 2175–2188 (2011).

24. Y. Ling, Y. Gan, X. Yao, and C. P. Hendon, "Phase-noise analysis of swept-source optical coherence tomography systems," Opt. Lett. **42**, 1333–1336 (2017).
25. Z. Chen, M. Liu, M. Minneman, L. Ginner, E. Hoover, H. Sattmann, M. Bonesi, W. Drexler, and R. A. Leitgeb, "Phase-stable swept source OCT angiography in human skin using an akinetic source," Biomed. Opt. Express **7**, 3032–3048 (2016).
26. S. Song, J. Xu, S. Men, T. T. Shen, and R. K. Wang, "Robust numerical phase stabilization for long-range swept-source optical coherence tomography," J. Biophotonics **10**, 1398–1410 (2017).
27. G. Liu, Y. Jia, A. D. Pechauer, R. Chandwani, and D. Huang, "Split-spectrum phase-gradient optical coherence tomography angiography," Biomed. Opt. Express **7**, 2943–2954 (2016).
28. Y. Ling, X. Yao, and C. P. Hendon, "Highly phase-stable 200 kHz swept-source optical coherence tomography based on KTN electro-optic deflector," Biomed. Opt. Express **8**, 3687–3699 (2017).
29. J. D. Rigden and E. I. Gordon, "Granularity of scattered optical maser light," Proc IRE **50**, 6564–6574 (1962).
30. J. M. Schmitt, S. H. Xiang, and K. M. Yung, "Speckle in optical coherence tomography," J. Biomed. Opt. **4**, 95–106 (1999).
31. M. Bashkansky and J. Reintjes, "Statistics and reduction of speckle in optical coherence tomography," Opt. Lett. **25**, 545–547 (2000).
32. T. R. Hillman, S. G. Adie, V. Seemann, J. J. Armstrong, S. L. Jacques, and D. D. Sampson, "Correlation of static speckle with sample properties in optical coherence tomography," Opt. Lett. **31**, 190–192 (2006).
33. A. Curatolo, B. F. Kennedy, D. D. Sampson, and T. R. Hillman, "Speckle in optical coherence tomography," in *Advanced Biophotonics: Tissue Optical Sectioning*, R. K. Wang and V. V. Tuchin, eds. (Taylor & Francis Group, 2014), pp. 211–277.
34. A. Mariampillai, M. K. K. Leung, M. Jarvi, B. A. Standish, K. Lee, B. C. Wilson, A. Vitkin, and V. X. D. Yang, "Optimized speckle variance OCT imaging of microvasculature," Opt. Lett. **35**, 1257–1259 (2010).
35. N. De Carvalho, S. Ciardo, A. Cesinaro, G. Jemec, M. Ulrich, J. Welzel, J. Holmes, and G. Pellacani, "In vivo micro-angiography by means of speckle-variance optical coherence tomography (SV-OCT) is able to detect microscopic vascular changes in naevus to melanoma transition," J. Eur. Acad. Dermatol. Venereol. **30**, e67–e68 (2016).

36. S. Caujolle, R. Cernat, G. Silvestri, M. J. Marques, A. Bradu, T. Feuchter, G. Robinson, D. K. Griffin, and A. Podoleanu, "Speckle variance OCT for depth resolved assessment of the viability of bovine embryos," Biomed. Opt. Express **8**, 5139–5150 (2017).
37. O. A. Grishina, S. Wang, and I. V. Larina, "Speckle variance optical coherence tomography of blood flow in the beating mouse embryonic heart," J. Biophotonics **10**, 735–743 (2017).
38. J. Enfield, E. Jonathan, and M. Leahy, "In vivo imaging of the microcirculation of the volar forearm using correlation mapping optical coherence tomography (cmOCT)," Biomed. Opt. Express **2**, 1184–1193 (2011).
39. P. M. McNamara, H. M. Subhash, and M. J. Leahy, "*In vivo* full-field *en face* correlation mapping optical coherence tomography," J. Biomed. Opt. **18**, 126008 (2013).
40. A. Zam, R. Dsouza, H. M. Subhash, M.-L. O'Connell, J. Enfield, K. Larin, and M. J. Leahy, "Feasibility of correlation mapping optical coherence tomography (cmOCT) for anti-spoof sub-surface fingerprinting," J. Biophotonics **6**, 663–667 (2013).
41. P. Gong, R. A. McLaughlin, Y. M. Liew, P. R. T. Munro, F. M. Wood, and D. D. Sampson, "Assessment of human burn scars with optical coherence tomography by imaging the attenuation coefficient of tissue after vascular masking," J. Biomed. Opt. **19**, 021111 (2013).
42. H. M. Subhash and M. J. Leahy, "Microcirculation imaging based on full-range high-speed spectral domain correlation mapping optical coherence tomography," J. Biomed. Opt. **19**, 021103 (2013).
43. Y. M. Liew, R. A. McLaughlin, P. Gong, F. M. Wood, and D. D. Sampson, "*In vivo* assessment of human burn scars through automated quantification of vascularity using optical coherence tomography," J. Biomed. Opt. **18**, 061213 (2013).
44. S. Smirni, M. P. MacDonald, C. P. Robertson, P. M. McNamara, S. O'Gorman, M. J. Leahy, and F. Khan, "Application of cmOCT and continuous wavelet transform analysis to the assessment of skin microcirculation dynamics," J. Biomed. Opt. **23**, 076006 (2018).
45. Y. Jia, O. Tan, J. Tokayer, B. Potsaid, Y. Wang, J. J. Liu, M. F. Kraus, H. Subhash, J. G. Fujimoto, J. Hornegger, and D. Huang, "Split-spectrum amplitude-decorrelation angiography with optical coherence tomography," Opt. Express **20**, 4710–4725 (2012).
46. S. S. Gao, G. Liu, D. Huang, and Y. Jia, "Optimization of the split-spectrum amplitude-decorrelation angiography algorithm on a spectral optical coherence tomography system," Opt. Lett. **40**, 2305–2308 (2015).

47. Y. Jia, S. T. Bailey, D. J. Wilson, O. Tan, M. L. Klein, C. J. Flaxel, B. Potsaid, J. J. Liu, C. D. Lu, M. F. Kraus, J. G. Fujimoto, and D. Huang, "Quantitative Optical Coherence Tomography Angiography of Choroidal Neovascularization in Age-Related Macular Degeneration," Ophthalmology **121**, 1435–1444 (2014).

48. Y. Jia, E. Wei, X. Wang, X. Zhang, J. C. Morrison, M. Parikh, L. H. Lombardi, D. M. Gattey, R. L. Armour, B. Edmunds, M. F. Kraus, J. G. Fujimoto, and D. Huang, "Optical Coherence Tomography Angiography of Optic Disc Perfusion in Glaucoma," Ophthalmology **121**, 1322–1332 (2014).

49. R. F. Spaide, "Volume-Rendered Optical Coherence Tomography of Diabetic Retinopathy Pilot Study," Am. J. Ophthalmol. **160**, 1200–1210 (2015).

50. L. Mao, S. Weng, Y. Gong, and S. Yu, "Optical coherence tomography angiography of macular telangiectasia type 1: Comparison with mild diabetic macular edema," Lasers Surg. Med. **49**, 225–232 (2017).

51. R. K. Wang, S. L. Jacques, Z. Ma, S. Hurst, S. R. Hanson, and A. Gruber, "Three dimensional optical angiography," Opt. Express **15**, 4083–4097 (2007).

52. R. K. Wang, L. An, S. Saunders, and D. J. Wilson, "Optical microangiography provides depth-resolved images of directional ocular blood perfusion in posterior eye segment," J. Biomed. Opt. **15**, 020502 (2010).

53. A. Zhang, Q. Zhang, C.-L. Chen, and R. K. Wang, "Methods and algorithms for optical coherence tomography-based angiography: a review and comparison," J. Biomed. Opt. **20**, 100901 (2015).

54. J. Xu, S. Song, W. Wei, and R. K. Wang, "Wide field and highly sensitive angiography based on optical coherence tomography with akinetic swept source," Biomed. Opt. Express **8**, 420–435 (2017).

55. W. J. Choi, R. Reif, S. Yousefi, and R. K. Wang, "Improved microcirculation imaging of human skin *in vivo* using optical microangiography with a correlation mapping mask," J. Biomed. Opt. **19**, 036010 (2014).

56. Y. Huang, Q. Zhang, M. R. Thorell, L. An, M. K. Durbin, M. Laron, U. Sharma, G. Gregori, P. J. Rosenfeld, and R. K. Wang, "Swept-source OCT angiography of the retinal vasculature using intensity differentiation-based optical microangiography algorithms," Ophthalmic Surg. Lasers Imaging Retina **45**, 382–389 (2014).

57. Q. Zhang, C. S. Lee, J. Chao, C.-L. Chen, T. Zhang, U. Sharma, A. Zhang, J. Liu, K. Rezaei, K. L. Pepple, R. Munsen, J. Kinyoun, M. Johnstone, R. N. Van Gelder, and R. K.

Wang, "Wide-field optical coherence tomography based microangiography for retinal imaging," Sci. Rep. **6**, 22017 (2016).

58. A. R. Miller, L. Roisman, Q. Zhang, F. Zheng, J. Rafael de Oliveira Dias, Z. Yehoshua, K. B. Schaal, W. Feuer, G. Gregori, Z. Chu, C.-L. Chen, S. Kubach, L. An, P. F. Stetson, M. K. Durbin, R. K. Wang, and P. J. Rosenfeld, "Comparison Between Spectral-Domain and Swept-Source Optical Coherence Tomography Angiographic Imaging of Choroidal Neovascularization," Invest. Ophthalmol. Vis. Sci. **58**, 1499–1505 (2017).
59. L. An, J. Qin, and R. K. Wang, "Ultrahigh sensitive optical microangiography for in vivo imaging of microcirculations within human skin tissue beds," Opt. Express **18**, 8220–8228 (2010).
60. L. An, T. T. Shen, and R. K. Wang, "Using ultrahigh sensitive optical microangiography to achieve comprehensive depth resolved microvasculature mapping for human retina," J. Biomed. Opt. **16**, 106013–106013 (2011).
61. R. K. Wang, A. Zhang, W. J. Choi, Q. Zhang, C. Chen, A. Miller, G. Gregori, and P. J. Rosenfeld, "Wide-field optical coherence tomography angiography enabled by two repeated measurements of B-scans," Opt. Lett. **41**, 2330–2333 (2016).
62. C. Chen, W. Shi, and W. Gao, "Imaginary part-based correlation mapping optical coherence tomography for imaging of blood vessels in vivo," J. Biomed. Opt. **20**, 116009–116009 (2015).
63. A. S. Nam, I. Chico-Calero, and B. J. Vakoc, "Complex differential variance algorithm for optical coherence tomography angiography," Biomed. Opt. Express **5**, 3822–3832 (2014).
64. S. Yousefi, Z. Zhi, and R. K. Wang, "Eigendecomposition-Based Clutter Filtering Technique for Optical Micro-Angiography," IEEE Trans. Biomed. Eng. **58**, (2011).
65. S. Yousefi, J. Qin, and R. K. Wang, "Super-resolution spectral estimation of optical micro-angiography for quantifying blood flow within microcirculatory tissue beds in vivo," Biomed. Opt. Express **4**, 1214–1228 (2013).
66. Q. Zhang, J. Wang, and R. K. Wang, "Highly efficient eigen decomposition based statistical optical microangiography," Quant. Imaging Med. Surg. **6**, 557–563 (2016).
67. A. Zhang and R. K. Wang, "Feature space optical coherence tomography based micro-angiography," Biomed. Opt. Express **6**, 1919–1928 (2015).
68. R. F. Spaide, J. G. Fujimoto, and N. K. Waheed, "IMAGE ARTIFACTS IN OPTICAL COHERENCE TOMOGRAPHY ANGIOGRAPHY," Retina Phila. Pa **35**, 2163–2180 (2015).

69. S. Makita, Y. Hong, M. Yamanari, T. Yatagai, and Y. Yasuno, "Optical coherence angiography," Opt. Express **14**, 7821–7840 (2006).
70. P. Thévenaz, U. E. Ruttimann, and M. Unser, "A pyramid approach to subpixel registration based on intensity," IEEE Trans. Image Process. Publ. IEEE Signal Process. Soc. **7**, 27–41 (1998).
71. R. K. Wang and L. An, "Doppler optical micro-angiography for volumetric imaging of vascular perfusion in vivo," Opt. Express **17**, 8926–8940 (2009).
72. A. S. Kang, R. J. Welch, K. Sioufi, E. A. T. Say, J. A. Shields, and C. L. Shields, "Optical coherence tomography angiography of iris microhemangiomatosis," Am. J. Ophthalmol. Case Rep. **6**, 24–26 (2017).
73. D. Allegrini, G. Montesano, and A. Pece, "Optical Coherence Tomography Angiography of Iris Nevus: A Case Report," Case Rep. Ophthalmol. **7**, 450–456 (2016).
74. J. L. Chien, K. Sioufi, S. Ferenczy, E. A. T. Say, and C. L. Shields, "Optical Coherence Tomography Angiography Features of Iris Racemose Hemangioma in 4 Cases," JAMA Ophthalmol. **135**, 1106–1110 (2017).
75. D. Allegrini, G. Montesano, and A. Pece, "Optical Coherence Tomography Angiography in a Normal Iris," Ophthalmic Surg. Lasers Imaging Retina **47**, 1138–1139 (2016).
76. P. K. Roberts, D. A. Goldstein, and A. A. Fawzi, "Anterior Segment Optical Coherence Tomography Angiography for Identification of Iris Vasculature and Staging of Iris Neovascularization: A Pilot Study," Curr. Eye Res. **42**, 1136–1142 (2017).
77. A. H. Skalet, Y. Li, C. D. Lu, Y. Jia, B. Lee, L. Husvogt, A. Maier, J. G. Fujimoto, C. R. Thomas, and D. Huang, "Optical Coherence Tomography Angiography Characteristics of Iris Melanocytic Tumors," Ophthalmology **124**, 197–204 (2017).
78. W. J. Choi, Z. Zhi, and R. K. Wang, "In vivo OCT microangiography of rodent iris," Opt. Lett. **39**, 2455–2458 (2014).
79. S. Hu, B. Rao, K. Maslov, and L. V. Wang, "Label-free Photoacoustic Ophthalmic Angiography," Opt. Lett. **35**, 1–3 (2010).
80. B. Rao, L. Li, K. Maslov, and L. Wang, "Hybrid-scanning optical-resolution photoacoustic microscopy for in vivo vasculature imaging," Opt. Lett. **35**, 1521–1523 (2010).
81. D. J. Coster, "Mechanisms of corneal graft failure : The erosion of corneal privilege," Eye **3**, 251–262 (1989).
82. M. O. Price, R. W. Thompson, and F. W. Price, "Risk Factors for Various Causes of Failure in Initial Corneal Grafts," Arch. Ophthalmol. **121**, 1087–1092 (2003).

Chapter 4

STRUCTURAL IMAGING OF RAT CORNEA USING 200 kHz SWEPT SOURCE OCT

4.1 Introduction

Since its introduction, OCT has transformed the clinical practice of ophthalmology. The first commercial OCT used in ophthalmology was based on time domain detection principles such as used by the Stratus OCT (Carl Zeiss Meditec, Inc, Dublin, CA) introduced in 1996 [1]. These TD-OCT systems performed A-scan rates of 400 A-scans per second with an axial resolution of 8–10 μm in tissue. Later, in 2006, the first commercial Fourier domain OCT (Optovue) based on spectral detection approach was introduced. SD-OCT systems were able to achieve scan rates of 20000–52000 A-scans per second and a resolution of 5–7 μm in tissue [1]. SD-OCT is currently the standard for ophthalmic instruments and imaging speeds range from 25,000 to 80,000 A-scans per second [1]. In 2008, the first SS-OCT was introduced in the market (Casia, Tomey, Japan). The Casia SS-OCT uses a 1310 nm swept-source laser and was specifically designed to scan the anterior segment with 30,000 A scans per second and an imaging depth of 6 mm. Currently, commercial SS-OCT devices available in the market operate at 100 kHz A scan rate (Triton, Topcon, Tokyo, Japan and Thorlabs, USA). Figure 4.1 indicates the major OCT developmental milestones in the field of ophthalmology [1].

Clinical ophthalmic OCT systems have been used to monitor posterior and anterior segment pathologies. Some of the applications of anterior segment OCT include evaluation of pterygium [2], ocular surface neoplasia [3,4], measuring central corneal thickness [5–8], monitoring keratoconus progression [9,10], and for pre-operative, intra-operative and post-operative assessment of patients requiring corneal surgeries [11,12], to study intra ocular pressure [13,14], and also for imaging anterior chamber for the diagnosis, management and follow-up of angle closure diseases [7,15,16]. Posterior ophthalmic OCT has been clinically used for *in vivo* imaging of the retina, optic nerve head, and retinal nerve fibre layer to evaluate progression of glaucoma, macular oedema and age related macular degeneration [17,18].

1970	Photographing light in flight and "seeing inside" tissue
1987	Demonstration of femtosecond optical ranging (A-scans)
1991	Demonstration of OCT in vitro
1992	First OCT startup company
1993	First in vivo images of the retina
1994	Humphrey Instruments (Zeiss) acquires startup
1995	Clinical studies (glaucoma, AMD, diabetic retinopathy)
1996	First commercial ophthalmic OCT device (Zeiss)
1999	Approximately 180 units sold
2000	Second generation ophthalmic OCT instrument
2001	Approximately 400 units sold
2002	Third generation Stratus OCT
2003	Demonstration of FD OCT sensitivity advantage
2004	~10 million OCT procedures world wide
2005	OCT becoming a standard of care
2006	Approximately 6000 Stratus OCT systems sold
2006	Lucentis FDA approved for exudative AMD
2006	Spectral-domain OCT enters the ophthalmic market
2010	Cumulative procedures pass ~100 million world wide
2014	Commercial OCTA introduced

Fig.4.1 Major OCT developmental milestones in ophthalmology [1]

The cornea is the outermost layer of the eye that acts as a filter and structural barrier protecting the lens and the retina from the damaging ultraviolet rays, germs, dust and other harmful substances. It is a transparent avascular tissue and acts like a window by controlling the entry of light into the eye and also helps the light to focus onto the retina. Corneal transparency, curvature and structure are determined by the intrinsic biochemical structure and extrinsic environment. Any change in corneal structure or transparency affects the visual quality. Chemical burns are among the most common eye injuries. Corneal injuries arising from chemical burns account for 5 – 22% of eye injuries [19,20]. Chemical and thermal eye burns pose a significant risk of blindness and require immediate and intensive care. The severity of chemical injury depends on the type, volume and pH of the injurious substance and on the duration of exposure. Alkali exposure is the most common cause of severe corneal burn, as alkaline substances being lipophilic penetrate more deeply than acids. Alkali first damages the epithelium, and then penetrates rapidly through the corneal stroma into the anterior chamber causing widespread inflammation of iris, lens, and ciliary body [19,20].

Recent advances in wound healing therapy have highlighted the potential efficacy of mesenchymal stem cells (MSCs) and pluripotent stem cells [21–23]. It has been demonstrated that the beneficial effects of MSCs operate – at least in part – by the mediation of extracellular

vesicles (EV). EV's are nano-sized (30 – 100nm) vesicles of endosomal origin secreted by most cells and tissues. EV's contain miRNA, mRNA and proteins that mediate physiological intercellular crosstalk. MSC-derived extracellular vesicles (MSC-EVs) have been shown to have high potential as a novel cell-free therapy in regenerative medicine. As such, they have garnered interest from the ophthalmic community to evaluate the MSC-EV based regenerative therapy in cases of acute ocular surface injury over the widely used corticosteroid treatments to suppress the inflammation and promote wound healing [24].

In the present study, in collaboration with Prof. Thomas Ritter, REMEDI, NUI Galway, the therapeutic effect of topically applied EVs derived from human mesenchymal stem cells (hMSC) on corneal wound healing is investigated using a commercial OCT operating at 200 kHz A-scan rate. The chapter presents graph based segmentation technique to measure the central corneal thickness (CCT) to monitor the corneal wound healing process. The measured CCT is used as a parameter for evaluating the efficacy of hMSC – EV treatment. Further, distance regularized level set based segmentation approach is used to generate corneal pachymetry maps from the 3D volumetric data acquired using the raster scanning protocol.

4.2 Imaging system and scanning protocol

The study used Thorlabs – 200 kHz VCSEL based SS-OCT system as depicted in figure 3.1 in chapter 3. The swept laser source has a central wavelength of 1310 nm and an axial resolution and lateral resolution of 11 µm and 25 µm in air respectively. For all the experiments, BM mode scanning protocol was utilized acquiring 8 scans at each location. The 3 D volume acquisition covered a field of view 5 x 5 x 5.6 mm^3. A total of 200 positions were covered in the Y – scan direction thus generating 1600 B frames using the B-M scan protocol.

All procedures performed were conducted in a fully accredited animal housing facility, under approval by the Animals Care Research Ethics Committee of the National University of Ireland, Galway and authorization from the Health Products Regulatory Authority of Ireland. Male Lewis rats aged 8-14 weeks were obtained from Harlan Laboratories UK and were housed with food and water.

Application of alkali to one cornea was performed under anaesthesia with isoflurane followed by topical tetracaine. Animals were divided into two groups namely the control group and the treated group. To induce the injury, a piece of Whatman filter paper (3mm diameter) was soaked in NaOH (4µl of a 1M solution) and applied to the centre of the cornea of right eye for

60 seconds. The eye was rinsed with 10ml of saline for 15 min following which hMSC-EV (30mg in 50ml of sterile PBS) was applied topically for treated group or an equivalent volume of sterile PBS was applied for the control group.

OCT imaging was performed on the animals on day 1 and day 7 following the alkali injury. For both the control and treated groups, OCT imaging was carried out before, after the alkali injury and after the treatment application.

4.3 Corneal segmentation

Image segmentation is the process of portioning an image into multiple regions of homogenous areas. Though significant progress has been made in the field of image segmentation, poor image contrast and noise pose challenges for medical image segmentation. Image segmentation algorithms can be classified into three categories namely pixel-based, edge-based and region-based methods. Pixel-based methods are based solely on the grey level values of the pixels within an image. Edge-based methods operate by detecting the edges (pixel intensity gradients) within an image and then use that information to separate the image into regions. Region-based segmentation considers grey-level values from neighbouring pixels starting with a seed pixel (or group of pixels) and then by growing or splitting the seed, homogeneous regions are grouped together.

4.3.1 Graph based image segmentation

In recent years, among the many approaches to image segmentation, graph based methods have become a major trend. In OCT imaging, graph based segmentation techniques have been used to segment retinal layers, corneal boundaries and lumen from intravascular images [25–30].

In graph based approach, image to be segmented is modelled as a graph and further divided into many subgraphs such that each of them represents a meaningful object of interest. The first step is mapping the image elements onto a graph made of many nodes or vertices. These nodes may be pixels or regions within an image and each of these nodes are connected to other nodes on the graph by a set of edges. I.e. an image may be represented in terms of a graph, $G = (V, E)$ where each node $v_i \in V$ corresponds to a pixel in the image, and the edges in E connect certain pairs of neighbouring pixels. A weight is associated with each edge based on some property of the pixels that it connects, such as their pixel intensities. In one of the many graph based segmentation approaches, called the shortest path methods, the object boundary is defined as a set of shortest paths connecting the pairs of nodes in a graph. Hence, in shortest

path graph based segmentation technique, the shortest path connecting two nodes with the minimized sum of edge weights is computed with Dijkstra's algorithm [31].

The processing steps of graph based corneal segmentation are given in figure 4.2. The details of the processing technique are explained in the sub sections given below.

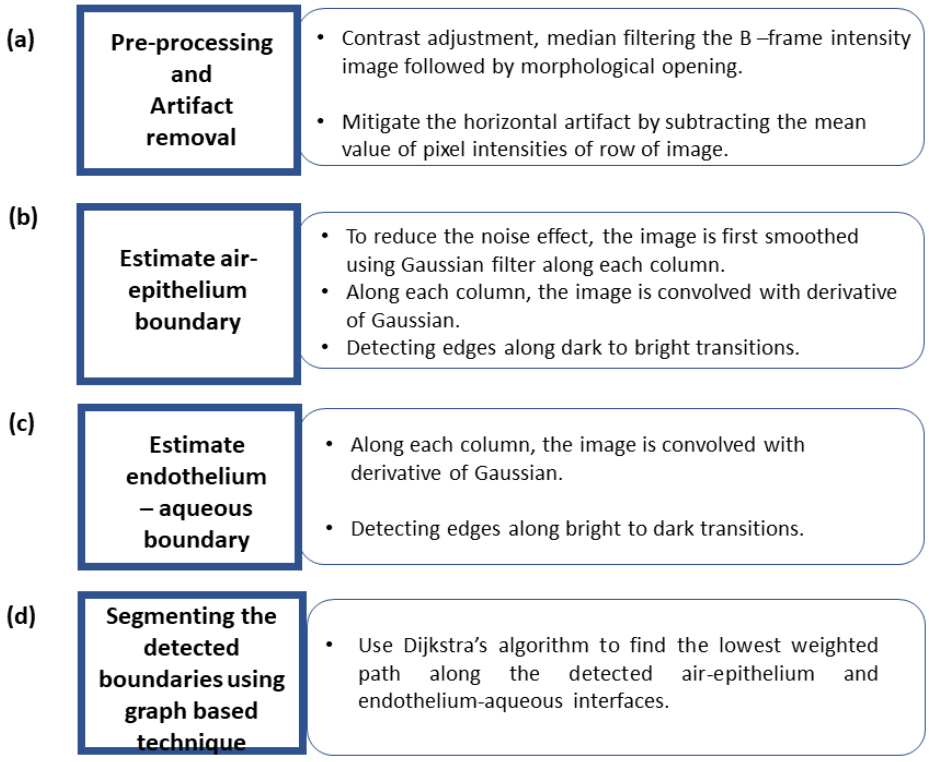

Fig.4.2. Flowchart showing the processing steps of graph based corneal segmentation

4.3.1.1 Pre-processing and artefact removal

To increase the signal to noise ratio of the B – frame images acquired using the 200 kHz system, at each transverse position, the acquired 8 frames were averaged together. The averaged image was then subjected to contrast enhancement by mapping the normalised pixel intensities between 0 and 0.7 of the original image to normalised intensity values between 0.7 and 1 in the contrast enhanced image.

In corneal OCT images, there are two main types of artefacts that often interfere with accurate automatic segmentation, namely the central artefact and the horizontal artefacts [32]. While imaging the rat cornea using the Thorlabs swept source system, effects due to central artefacts were minimal, however horizontal artefacts were present. Rows that are corrupted by the horizontal artefact have higher mean intensities than other rows. To mitigate the horizontal artefacts within corneal images, the mean pixel intensity across each row of the image was

calculated and consequently subtracted from each pixel within that row (*x* direction). This simple subtraction was sufficient to minimize the effects of horizontal artefacts interfering with the edge detection.

4.3.1.2 Estimating air- epithelial boundary

To estimate the air epithelial boundary, edge detection technique was applied along each column of the image. Prior to detecting the edges, the images were blurred using a normalised zero mean, unit variance one dimensional Gaussian window given by Eq.4. 1 along each of the columns to prevent false edge detection.

$$G = e^{\frac{-x^2}{2\sigma^2}} \tag{4.1}$$

where σ and x are the standard deviation and width of the Gaussian kernel respectively. For the Gaussian kernel, a width of 6σ was chosen for present computations. Next, the derivative of the Gaussian given in Eq. (4.1) is computed and convolved with the image to detect the edges. Further to suppress all the gradient values except the local maxima corresponding to the air-epithelial boundary, edge thinning is applied. To enable edge thinning, the edge strength of the current pixel is compared with the edge strength of the pixel in the positive and negative gradient directions. If the edge strength of the current pixel is greater than the edge strength of the pixels in the positive and negative directions, the edge detected is considered to belong to 'dark to bright transition' indicating the air - epithelial boundary.

4.3.1.3 Estimating endothelial - aqueous boundary

To estimate the endothelium – aqueous boundary, edge detection using derivative of Gaussian as described in section 4.3.1.2 was applied along each column of the image. However, in this case, the edge strength of the current pixel is compared with the edge strength of the pixels in the positive and negative directions and the edge belonging to 'bright to dark transition' is selected as the endothelium – aqueous boundary.

4.3.1.4 Segmenting the detected boundaries using Dijkstra's graph based segmentation

To segment the detected edges from the previous steps, an undirected weighted graph was created using adjacency matrix as described in [32,33]. The general idea behind the technique is to assign low weights to the borders or edges within an image, and then using computationally efficient techniques such as Dijkstra's algorithm to determine the lowest weighted path of a graph between arbitrary endpoints. For finding the minimum weighted path

using Dijkstra's algorithm, the weight values assigned must be positive and range from 0 to 1. Such a table of graph weights is defined as the adjacency matrix of a graph, where one axis represents the start node and the other axis indicates the end node [32, 33]. Figure 4.3 shows example weights for three connected nodes. This example illustrates node 1's preference for node 3 due to its lower weight value compared to node 2.

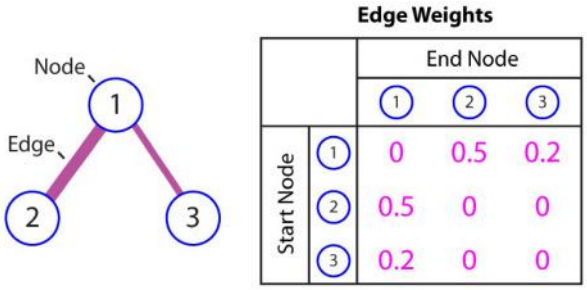

Fig. 4.3 Example graph weights (adjacency matrix) for three connected nodes [33].

To enable automatic initialization of segmentation by weighted graph based technique, two columns with an edge weight of 1×10^{-5} are added at both ends of the B-scan image. Furthermore, the start and end points are initialized to the top left and bottom right corners. Edges are assigned weights as a function of pixel intensity, where darker pixels are assigned lower weights. To generate the weighted graph, each pixel in the edge image is assigned a weight as per equation (4.2) [33].

$$w_{ab} = 2 - (g_a + g_b) + w_{min} \tag{4.2}$$

where w_{ab} is the weight assigned to the pixel connecting nodes *a* and *b* and g_a and g_b are the vertical gradient at nodes *a* and *b* respectively. Next, Dijkstra's algorithm is used to determine the least cost path from the weighted graph between the assigned end points of the image matrix. The above steps are repeated for each 'dark to bright' and 'bright to dark intensity' transitions so as to detect air - epithelium boundary and endothelium - aqueous boundary layers respectively.

Finally, to extend the segmented endothelial - aqueous boundary to the low noise regions and to regions where the estimated boundaries are inaccurate, fourth order polynomial fit was made to the detected endothelial - aqueous boundary following Dijkstra's shortest path algorithm. Fourth order polynomial fit was also made to the air – epithelial boundary detected by Dijkstra's shortest path algorithm to smooth the traced boundary.

Figure 4.4 shows the output images produced at each of the processing steps described in the flowchart given in figure 4.2.

Figures 4.5 shows the representative segmented corneal images of a healthy cornea and injured cornea on day 1 following the above described segmentation approach. Figures 4.6 shows the representative segmented corneal images of the injured rats belonging to control and treated group on day 7 post injury.

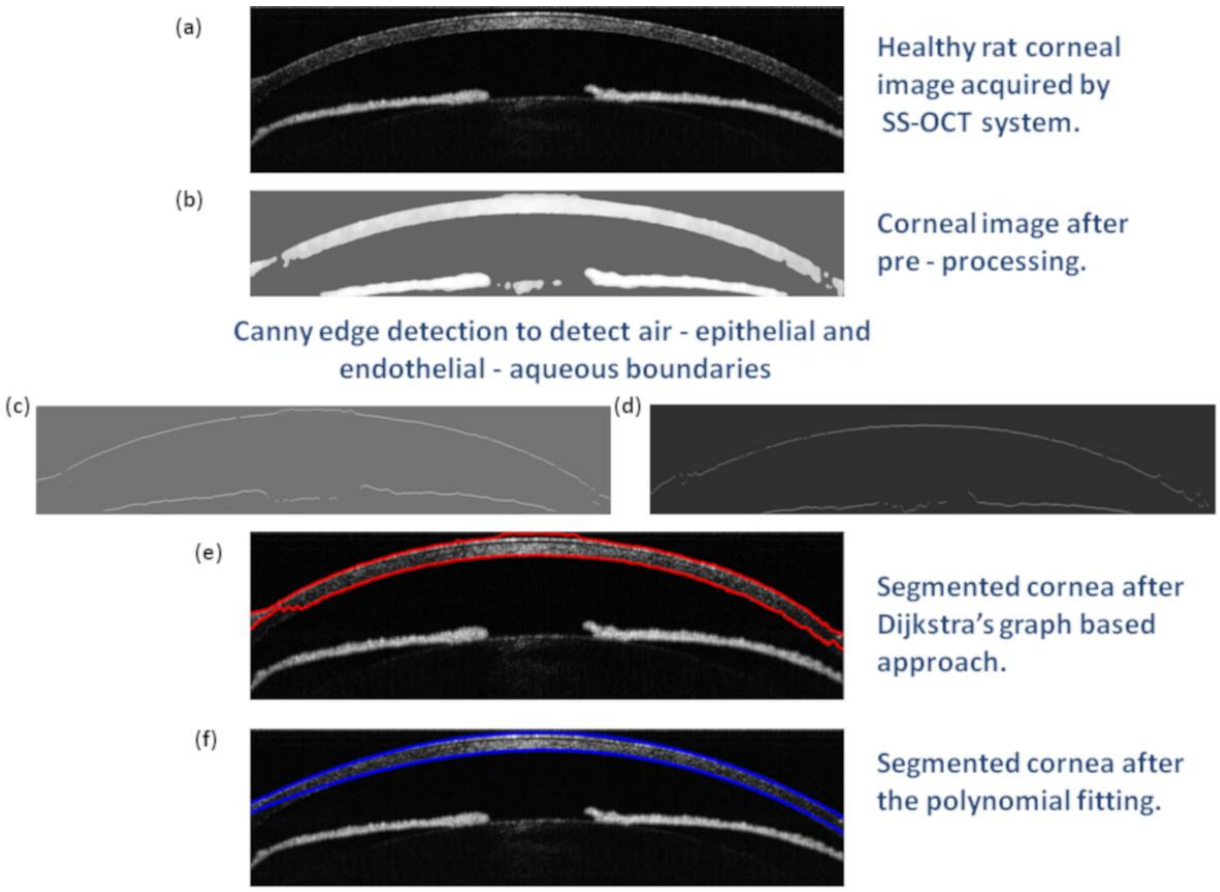

Fig. 4.4 Image processing steps of graph based corneal segmentation

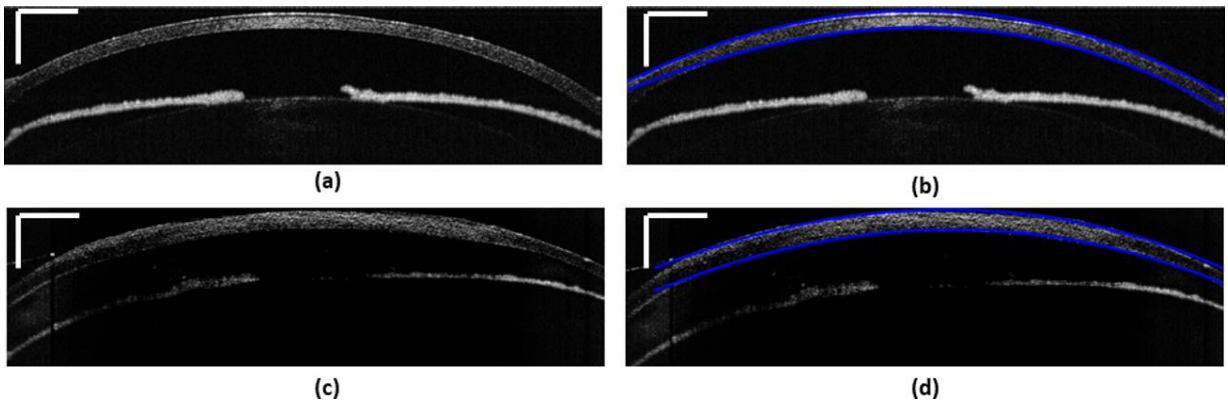

Fig. 4.5 Representative images of the segmented cornea on day 1 (a) OCT-B frame of a healthy cornea (b) OCT-B frame with the segmented cornea (c) OCT-B frame of an injured cornea (d) OCT-B frame showing the segmented cornea after the injury; Scale bars – 500 µm.

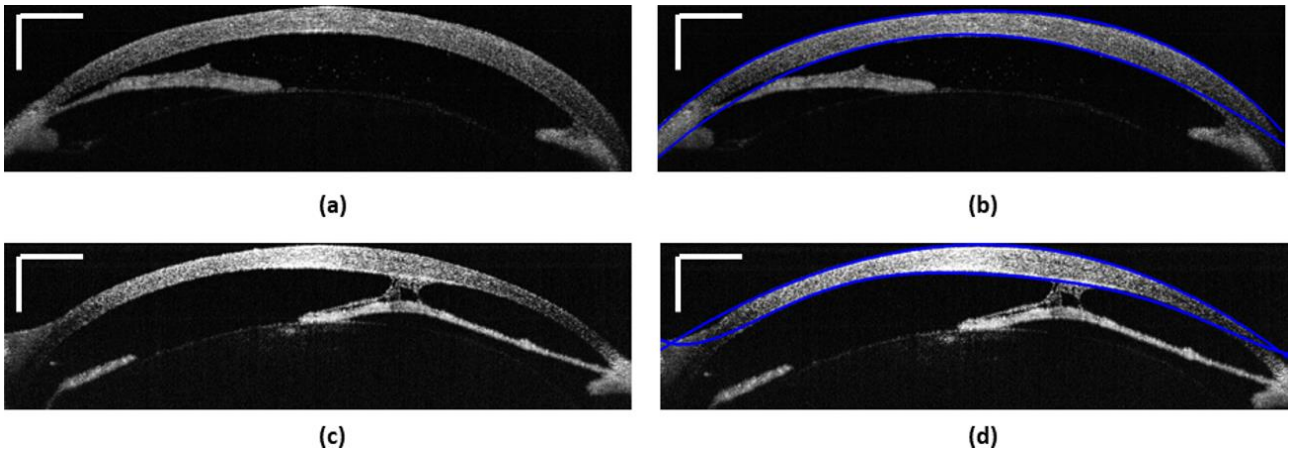

Fig.4.6 Representative images of the segmented cornea on day 7 (a) OCT-B frame of injured cornea from the control group, (b) segmented corneal boundaries overlaid on (a), (c) OCT-B frame of the injured cornea from the treated group (d) segmented corneal boundaries overlaid on (c); Scale bars – 500 µm.

From figures 4.5 and 4.6, it can be observed that even after the polynomial fitting to the segmented corneal boundaries, segmentation was not accurate towards the ends of the cornea where the OCT – B frame has low signal to noise ratio. Hence for evaluating the treatment efficacy of stem cell derived EV's in reducing the corneal inflammation and promoting epithelial cell growth, the detected corneal boundaries at both ends of the cornea were not considered for the calculation of CCT. For calculating the corneal thickness from the segmented cornea, the detected boundary layers spanning 100 pixels from both ends were neglected.

Further to calculate the corneal thickness from the segmented boundaries of anterior and posterior cornea, the detected boundaries obtained after polynomial fitting was straightened. The detected corneal boundaries were straightened by shifting each point within the polynomial fit with respect to the central vertical coordinate. Next, the difference in pixel locations along each column between the straightened anterior and posterior corneal boundaries were used to calculate the corneal thickness. The axial scan depth was set to 5.6 mm in air. Each axial scan was sampled digitally at 624 points, giving an axial pixel size of 8.9 µm in air (6.5 µm in the cornea).

The mean corneal thickness of healthy cornea of male Lewis rats calculated as per the segmentation approach was 150 ± 3.6 µm (mean ± standard error). After introducing the alkali injury, the calculated corneal thickness was 270 ± 10 µm ($p < 0.001$). Figure 4.7 shows the bar

graphs depicting the corneal thickness of healthy and injured cornea. As expected, alkali injury damages the epithelium, penetrates the stroma and results in corneal inflammation. The cornea was still inflamed on day 7 after the alkali injury, however we found that the corneal thickness was reduced by 25 µm in the MSC EV treated group compared to the control group. The CCT thickness in the MSC EV treated group was 294.5 ± 22 µm compared to 315 ± 39 µm of the control group ($p = 0.6$). Figure 4.8 shows the bar graphs depicting corneal thickness between control and treated group on day 7 post injury.

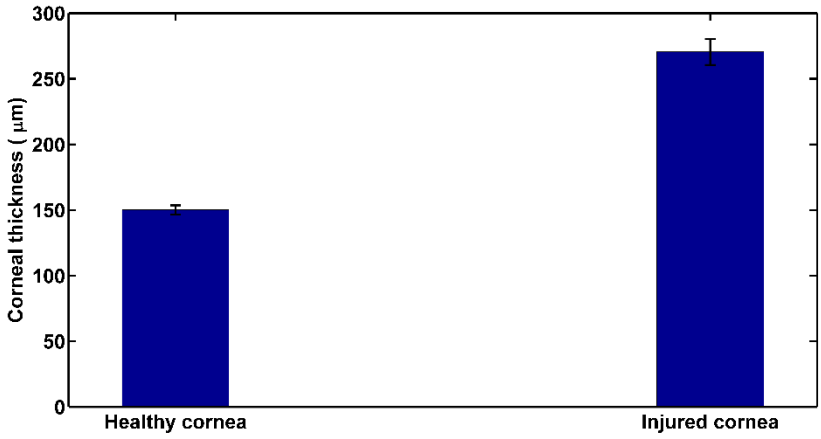

Fig.4.7 Bar graph showing the CCT measurements (mean ± standard error).

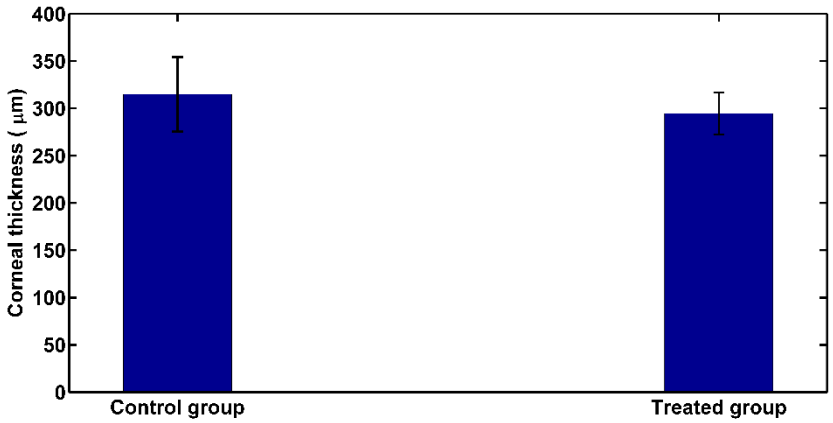

Fig.4.8 Bar graph showing the CCT measurements between the control group and treated group on day 7 (mean ± standard error).

The results obtained demonstrate that topical, single-treatment administration of EV isolated from human MSC-conditioned medium promotes the healing of the ocular surface by reducing inflammation and enhancing re-epithelisation in a rat alkali burn model compared to PBS – control group.

In this section, graph based segmentation technique was developed that was able to detect the corneal boundaries in low noise OCT images. The developed technique was then used to measure the wound healing efficiency of hMSC – EV treatment applied for alkali induced corneal injury model by measuring the central corneal thickness between the PBS – control and treated groups.

4.4 Pachymetry mapping

Corneal pachymetry is the process of measuring the thickness of the cornea. Level set method is a type of active contour based segmentation approach used for numerical analysis of the motion of an interface. The level set method was first presented by Osher and Fedkiv [34] for front propagation, to model ocean waves and burning flames. The method has been adopted within the field of machine vision for segmentation problems, especially for 3D segmentation. Level set based methods have found to be a flexible tool in shape modelling and image segmentation. The idea behind the level set method is to imbed a curve within a surface, defined as the zero level set of a level set function. The zero level set is evolved over time along the surface such that the final level set encloses the region or object of interest. Advantages of level set approach includes the ability to handle complex geometry and topological changes with numerical stability and complete automation of the segmentation procedure.

In the earliest level set formulations, the level set function developed irregularities during its evolution, which caused numerical errors and eventually destroyed the level set function in many image segmentation applications. Over the years, different groups have come up with different mathematical methods to improve the numerical stability of the level set evolution such as partial differential equation level set formulation (PDE), fuzzy based level set and distance regularized level set approach (DRL) [34–37]. It is shown that DRL approach is simpler and efficient compared to other level set formulations. Since the introduction of level sets, it has been adapted to medical image segmentation problems and is routinely used to segment tumour regions in MRI scans, hippocampus from MRI data sets [38,39], liver, kidney and lungs from CT [40–42] scans and breast and bone cartilages from ultrasound images [43,44]. Recently, level set based segmentation has been applied to OCT images as well. In OCT, level set based segmentation has been used to segment retinal layers, segment retinal fluid and also to segment lumen area from intravascular OCT images [45,46].

Corneal Pachymetry is essential prior to a refractive surgery procedure for ensuring sufficient corneal thickness to prevent abnormal bulging of the cornea and to monitor the corneal injury healing process. Generally, pachymetry mapping is carried out using ultrasound methods and more recently optical methods such as confocal microscopy and OCT [1,47–49]. Most of the commercial OCT based pachymetry are based on SD-OCT systems that uses radial scanning protocol across 8 equally spaced meridians centred at corneal apex. High speed SS-OCT devices are predicted to become the future of OCT technology, and hence in this study we present the feasibility of pachymetry mapping using a 200 kHz SS-OCT system. In this study, DRL based level set approach is adopted to segment cornea from the acquired 3D volumetric data using raster scanning to generate corneal pachymetry maps to monitor the burn injury and treatment progress.

Li et al. [37] introduced the level set method of distance regularized level set (DRLS) model. The DRLS method utilizes an edge-based active contour approach to direct the defined level set function (LSF) to the desired object boundary. In two dimensions, the level set method evolves a closed contour by manipulating the defined level set function. I.e., in two dimensions, the level-set method amounts to representing a closed curve C (desired boundary to be segmented) using an auxiliary function ϕ, called the level-set function. C is then represented as the zero-level set of ϕ, defined as

$$C = \{(x, y) | \phi(x, y) = 0\} \tag{4.3}$$

The DRLS method manipulates C implicitly, through the function ϕ such that, the function ϕ is assumed to take negative values inside the region delimited by the curve C and positive values outside the region. Further, to enable the evolution of ϕ, so that the zero level set of ϕ (C) captures the desired image boundary, an additional term is introduced called the energy function $\varepsilon(\phi)$.

Mathematically, the evolution of the level set function can be described by the following equations [37].

Let $\phi : \Omega \rightarrow \Re$ be a level set function defined over the domain Ω, then the energy function $\varepsilon(\phi)$ can be expressed as:

$$\varepsilon(\phi) = \beta R_p(\phi) + \epsilon_{ext}(\phi) \tag{4.4}$$

where $\beta > 0$ is a constant and $R_p(\phi)$ denotes the level set regularization term, given by:

$$R_p(\phi) = \int_\Omega p(|\nabla \phi|) dx \tag{4.5}$$

where *p* stands for an energy density function (double well potential function) $p:[0,\infty) \rightarrow \Re$ defined as

$$p(s) = \begin{cases} \frac{1}{2}(s-1)^2, & if\ s > 1 \\ \frac{1}{(2\pi)^2}(1-\cos(2\pi s)), & otherwise \end{cases} \quad (4.6)$$

and *s* is a spatial parameter in [0,1]. This potential function has two minimum points at *s* = 0 and *s* = 1.

Minimization of the energy $\varepsilon(\phi)$ can be attained by solving a level set evolution equation. For LSF, an external energy function can be formulated as:

$$\epsilon_{ext}(\phi) = \lambda L_g(\phi) + \alpha A_g(\phi) \quad (4.7)$$

where λ and α are the coefficient of the length term $L_g(\phi)$ and area term $A_g(\phi)$, which is given by

$$L_g(\phi) = \int g\delta_\epsilon(\phi)|\nabla \phi|dx \quad (4.8)$$

$$A_g(\phi) = \int g\, H_\epsilon(-\phi)\, dx \quad (4.9)$$

where $g \in [0,1)$ is an edge indicator function given by

$$g = \frac{1}{1+|\nabla G_\sigma * I|^2} \quad (4.10)$$

And δ_x and H_x are the Dirac delta function and Heaviside function respectively.

In equation 4.10, G_σ is a Gaussian kernel with a standard deviation σ, and *I* is the input image.

$L_g(\phi)$ estimates the line integral of the function g along the zero level contour of ϕ. $L_g(\phi)$ maintains the curve smooth during the evolution of the level set ϕ at the object boundaries. The area term $A_g(\phi)$ computes the weighted area enclosed by the evolving contour and is used to control the speed of the evolving contour depending on its proximity to the desired object boundary. Usually the Dirac delta function δ and the Heaviside function *H* are approximated by the following smooth function.

$$\delta_\epsilon(s) = \begin{cases} \frac{1}{2\epsilon}\left[(1+\cos\frac{\pi t}{\epsilon}\right] & if\ |t| < \epsilon \\ 0 & otherwise \end{cases} \quad (4.11)$$

$$H_\epsilon(s) = \begin{cases} \frac{1}{2}\left[(1 + \frac{t}{\epsilon} + \frac{1}{\pi}\sin(\frac{\pi t}{\epsilon}))\right] & if\ |t| < \epsilon \\ 0 & if\ t < -\epsilon \\ 1 & if\ t > \epsilon \end{cases} \qquad (4.12)$$

In the above equations, ϵ is a constant, set to 1.5.

Substituting the smooth functions for the Dirac delta function and the Heaviside function into equations 4.4) and 4.7, the energy function can be expressed by

$$\varepsilon(\phi) = \beta \int_\Omega p(|\nabla \phi|)dx + \lambda \int g\delta_\epsilon(\phi)|\nabla \phi|dx + \alpha \int g\, H_\epsilon(-\phi)\, dx \qquad (4.13)$$

This energy function is minimized to get the optimal result. The solution is obtained by solving the gradient flow given below.

$$\frac{\partial \phi}{\partial t} = \beta.div(d_p(|\nabla\phi|)\nabla\phi) + \delta_\epsilon(\phi).\lambda.div\left(g\frac{\nabla\phi}{|\phi|}\right) + \delta_\epsilon(\phi).\alpha.g \qquad (4.14)$$

where *div*(.) is the divergence operator and d_p is a function given by

$$d_p(s) = \frac{p_s'}{s} \qquad (4.15)$$

By iteratively updating the level set equation given in 4.14 at each time interval, the solution to the partial differential equation can be obtained.

The initial contour is user defined as a rectangular surface and placed outside the cornea. The initial level set ϕ_0 is defined as given by the equation

$$\phi_0(x) = \begin{cases} -K & for\ x \in Z \\ K & otherwise \end{cases} \qquad (4.16)$$

where *K* is a constant greater than zero and *Z* is a region in the domain Ω. For the present study, empirically the values of β, λ, and α were set to 0.04, 5 and 1.5 respectively based on factors such as speed and stability of the level set contour for optimal corneal segmentation. Figure 4.9 describes the processing steps involved in the generation of pachymetry maps using DRLS based segmentation approach.

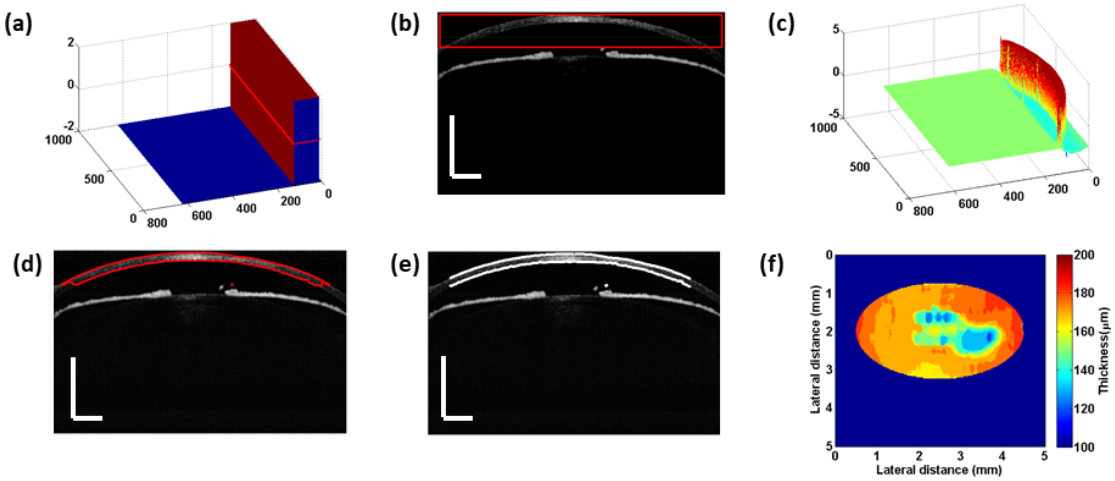

Fig. 4.9 Image processing steps for the generation of pachymetry maps using DRLS based segmentation approach (a) Initial level set (shown upside down for easy visualization) in space, (b) initial level set contour overlaid on a representative corneal image, (c) Final zero level set contour (shown upside down for easy visualization) in space, (d) Final zero level set contour overlaid on the representative corneal image, (e) Final zero level set contour after removing 100 pixels from the ends overlaid on the representative corneal image (f) Extraction of corneal boundaries from (d), Representative pachymetry map generated from the 3 D volumetric data; Scale bars : 500 μm.

As mentioned in section 4.3, since the signal to noise ratio was low towards the ends of the cornea within the acquired OCT – B frames, the detected corneal boundaries spanning 100 pixels from both the ends were not considered for generating pachymetry maps. Pachymetry maps were generated from a set of 100 B – frames spanning an area of 5 mm by 2 mm in x and y directions respectively. From figure 4.9 (f), one can observe that the thinnest area of the cornea is located at the vertex and inferotemporal to the vertex with the thickness gradually increasing towards the periphery of the cornea.

4.5 Results of pachymetry mapping

Following the methodology described in section 4.4, the pachymetry mapping was carried out on the 3 D volumetric data sets acquired (described in section 4.2). For the pachymetry mapping, corneal thickness was calculated by subtracting the anterior and posterior surfaces of the cornea. Figure 4.10 shows representative corneal pachymetry images of healthy rat cornea and an injured cornea just after inducing the alkali burn respectively. As expected, the corneal inflammation following alkali injury is clearly visible from figure 4.9 (b). Comparing figures 4.10 (a) and 4.10 (b) we can observe that the generated pachymetry maps are able to reveal abnormal corneal thickness patterns following the inflammation.

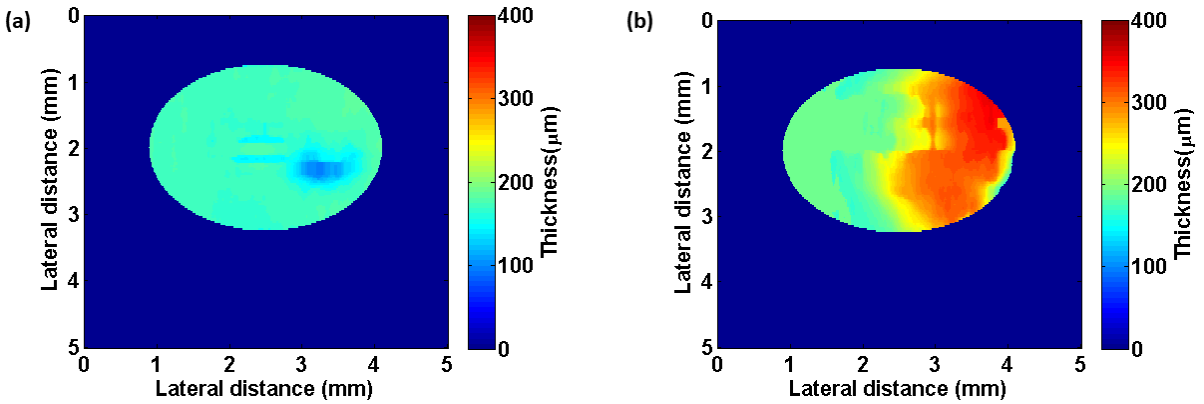

Fig. 4.10 Representative pachymetry maps (a) Healthy rat cornea (b) Injured cornea on day 0

To assess the impact of the alkali burn and the efficacy of MSC-EV treatment at areas other than just the centre of the cornea, pachymetry mapping was performed on the control group and treated group on day 7 following the injury. Figure 4.11 shows representative pachymetry maps of control and treated group.

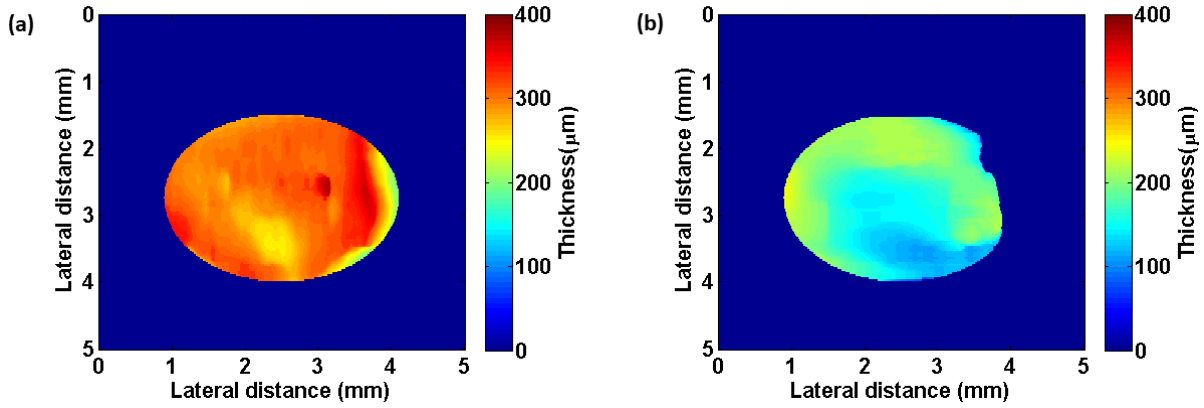

Fig. 4.11 Representative pachymetry maps (a) Control cornea on day 7 (b) Treated cornea on day 7

Figure 4.11 indicates that the developed DRLS based pachymetry mapping can be used as a clinical and research tool to assess corneal oedema following corneal injury and treatment.

However, for accurate pachymetry mapping, it is essential that the apex of the cornea is well centred. Also, difficulties in aligning the fixation axis of the eye along the optic axis of the instrument in anesthetized rats determine potential sources of error that limit the generation of uniform pachymetry maps across the samples within the same group. Misalignments between the fixation axis of the eye and the optic axis of the instrument can result in elevated readings of corneal thickness.

4.6 Conclusions

This chapter investigated the therapeutic effect of topically applied EVs derived from hMSC on corneal wound healing using a commercial OCT operating at 200 kHz A-scan rate. The chapter also introduced the scanning protocol for 3 D volume acquisition and details of alkali induced burn model which is used for further analysis in the next chapter. To measure the CCT for evaluation of corneal inflammation and wound healing process following the superficial alkali burn, a segmentation approach based on Dijkstra's graph based segmentation technique was developed to detect the corneal boundaries in low noise OCT images. The results obtained from the CCT measurements indicate that post injury, the mean corneal thickness of male Lewis rats increased to 270 ± 10 µm from the baseline measurement of 150 ± 3.6 µm ($p < 0.001$). On day 7, during the acute reparative phase of the injury, the measured CCT thickness in the hMSC - EV treated group was 294.5 ± 22 µm compared to 315± 39 µm of the control group ($p = 0.6$). These results indicated the potential therapeutic capability of the hMSC – EV treatment.

Further, to evaluate the corneal thickness at areas other than the central cornea, DRLS based segmentation approach was used to generate corneal pachymetry maps from the acquired 3D volumetric data following the raster scanning protocol. The generated pachymetry maps revealed varying thickness along the scanned volume.

REFERENCES

1. J. Fujimoto and E. Swanson, "The Development, Commercialization, and Impact of Optical Coherence Tomography," Invest. Ophthalmol. Vis. Sci. **57**, OCT1-OCT13 (2016).
2. W. Soliman and T. A. Mohamed, "Spectral domain anterior segment optical coherence tomography assessment of pterygium and pinguecula," Acta Ophthalmol. (Copenh.) **90**, 461–465 (2012).
3. S. Singh, R. Mittal, A. Ghosh, D. Tripathy, and S. Rath, "High-Resolution Anterior Segment Optical Coherence Tomography in Intraepithelial Versus Invasive Ocular Surface Squamous Neoplasia," Cornea **37**, 1292–1298 (2018).
4. I. O. Sayed-Ahmed, S. Palioura, A. Galor, and C. L. Karp, "Diagnosis and Medical Management of Ocular Surface Squamous Neoplasia," Expert Rev. Ophthalmol. **12**, 11–19 (2017).
5. M. K. Jahromi, R. Kafieh, H. Rabbani, A. M. Dehnavi, A. Peyman, F. Hajizadeh, and M. Ommani, "An automatic algorithm for segmentation of the boundaries of corneal layers in optical coherence tomography images using gaussian mixture model," J. Med. Signals Sens. **4**, 171 (2014).
6. H. Rabbani, R. Kafieh, M. Kazemian Jahromi, S. Jorjandi, A. Mehri Dehnavi, F. Hajizadeh, and A. Peyman, "Obtaining Thickness Maps of Corneal Layers Using the Optimal Algorithm for Intracorneal Layer Segmentation," https://www.hindawi.com/journals/ijbi/2016/1420230/.
7. M. Ang, M. Baskaran, R. M. Werkmeister, J. Chua, D. Schmidl, V. Aranha dos Santos, G. Garhöfer, J. S. Mehta, and L. Schmetterer, "Anterior segment optical coherence tomography," Prog. Retin. Eye Res. **66**, 132–156 (2018).
8. M. V. Sarunic, S. Asrani, and J. A. Izatt, "Imaging the Ocular Anterior Segment With Real-Time, Full-Range Fourier-Domain Optical Coherence Tomography," Arch. Ophthalmol. **126**, 537 (2008).
9. V. A. dos Santos, L. Schmetterer, H. Stegmann, M. Pfister, A. Messner, G. Schmidinger, G. Garhofer, and R. M. Werkmeister, "CorneaNet: fast segmentation of cornea OCT scans of healthy and keratoconic eyes using deep learning," Biomed. Opt. Express **10**, 622–641 (2019).
10. A. Gokul, H. R. Vellara, and D. V. Patel, "Advanced anterior segment imaging in keratoconus: a review," Clin. Experiment. Ophthalmol. **46**, 122–132 (2018).

11. VorosImi, "Evaluation of corneal changes in chemical burns with anterior segment optical coherence tomography," http://www.seeos.eu/index.php/2015/12/15/evaluation-of-corneal-changes-in-chemical-burns-with-anterior-segment-optical-coherence-tomography/.
12. "Evaluation of a Micro-Optical Coherence Tomography for the Corneal Endothelium in an Animal Model | Scientific Reports," https://www.nature.com/articles/srep29769.
13. R. S. Chong, L. M. Sakata, A. K. Narayanaswamy, S.-W. Ho, M. He, M. Baskaran, T. Y. Wong, S. A. Perera, and T. Aung, "Relationship between Intraocular Pressure and Angle Configuration: An Anterior Segment OCT Study," Invest. Ophthalmol. Vis. Sci. **54**, 1650–1655 (2013).
14. S. Salim, "The Role of Anterior Segment Optical Coherence Tomography in Glaucoma," https://www.hindawi.com/journals/joph/2012/476801/.
15. E. Wylegala, D. Dobrowolski, A. Nowińska, and D. Tarnawska, "Anterior segment optical coherence tomography in eye injuries," Graefes Arch. Clin. Exp. Ophthalmol. **247**, 451–455 (2009).
16. N. Venkateswaran, A. Galor, J. Wang, and C. L. Karp, "Optical coherence tomography for ocular surface and corneal diseases: a review," Eye Vis. **5**, 13 (2018).
17. G. J. Jaffe and J. Caprioli, "Optical coherence tomography to detect and manage retinal disease and glaucoma," Am. J. Ophthalmol. **137**, 156–169 (2004).
18. A. H. Kashani, C.-L. Chen, J. K. Gahm, F. Zheng, G. M. Richter, P. J. Rosenfeld, Y. Shi, and R. K. Wang, "Optical coherence tomography angiography: A comprehensive review of current methods and clinical applications," Prog. Retin. Eye Res. (2017).
19. M. Eslani, A. Baradaran-Rafii, A. Movahedan, and A. R. Djalilian, "The Ocular Surface Chemical Burns," J. Ophthalmol. **2014**, (2014).
20. J.-J. Gicquel, "Management of ocular surface chemical burns," Br. J. Ophthalmol. **95**, 159–161 (2011).
21. G. T. S. Kirby, S. J. Mills, A. J. Cowin, and L. E. Smith, "Stem Cells for Cutaneous Wound Healing," BioMed Res. Int. **2015**, 285869 (2015).
22. L. Rodriguez-Menocal, S. Shareef, M. Salgado, A. Shabbir, and E. Van Badiavas, "Role of whole bone marrow, whole bone marrow cultured cells, and mesenchymal stem cells in chronic wound healing," Stem Cell Res. Ther. **6**, 24 (2015).
23. S. Rani and T. Ritter, "The Exosome - A Naturally Secreted Nanoparticle and its Application to Wound Healing," Adv. Mater. Deerfield Beach Fla **28**, 5542–5552 (2016).

24. J. Y. Oh, M. K. Kim, M. S. Shin, H. J. Lee, J. H. Ko, W. R. Wee, and J. H. Lee, "The anti-inflammatory and anti-angiogenic role of mesenchymal stem cells in corneal wound healing following chemical injury," Stem Cells Dayt. Ohio **26**, 1047–1055 (2008).
25. Z. Gao, W. Bu, Y. Zheng, and X. Wu, "Automated layer segmentation of macular OCT images via graph-based SLIC superpixels and manifold ranking approach," Comput. Med. Imaging Graph. **55**, 42–53 (2017).
26. A. González, M. G. Penedo, S. G. Vázquez, J. Novo, and P. Charlón, "Cost Function Selection for a Graph-Based Segmentation in OCT Retinal Images," in *Computer Aided Systems Theory - EUROCAST 2013*, R. Moreno-Díaz, F. Pichler, and A. Quesada-Arencibia, eds., Lecture Notes in Computer Science (Springer Berlin Heidelberg, 2013), pp. 125–132.
27. A. Lang, A. Carass, O. Al-Louzi, P. Bhargava, H. S. Ying, P. A. Calabresi, and J. L. Prince, "Longitudinal graph-based segmentation of macular OCT using fundus alignment," Proc. SPIE-- Int. Soc. Opt. Eng. **9413**, (2015).
28. V. A. Robles, B. J. Antony, D. R. Koehn, M. G. Anderson, and M. K. Garvin, "3D graph-based automated segmentation of corneal layers in anterior-segment optical coherence tomography images of mice," in *Medical Imaging 2014: Biomedical Applications in Molecular, Structural, and Functional Imaging* (International Society for Optics and Photonics, 2014), Vol. 9038, p. 90380F.
29. R. Srivastava, A. P. Yow, J. Cheng, D. W. K. Wong, and H. L. Tey, "Three-dimensional graph-based skin layer segmentation in optical coherence tomography images for roughness estimation," Biomed. Opt. Express **9**, 3590–3606 (2018).
30. A. Stankiewicz, T. Marciniak, A. Dąbrowski, M. Stopa, P. Rakowicz, and E. Marciniak, "Improving Segmentation of 3D Retina Layers Based on Graph Theory Approach for Low Quality OCT Images," Metrol. Meas. Syst. **23**, 269–280 (2016).
31. E. W. Dijkstra, "A note on two problems in connexion with graphs," Numer. Math. **1**, 269–271 (1959).
32. F. LaRocca, S. J. Chiu, R. P. McNabb, A. N. Kuo, J. A. Izatt, and S. Farsiu, "Robust automatic segmentation of corneal layer boundaries in SDOCT images using graph theory and dynamic programming," Biomed. Opt. Express **2**, 1524–1538 (2011).
33. S. J. Chiu, X. T. Li, P. Nicholas, C. A. Toth, J. A. Izatt, and S. Farsiu, "Automatic segmentation of seven retinal layers in SDOCT images congruent with expert manual segmentation," Opt Express **18**, 19413–19428 (2010).

34. S. Osher and R. P. Fedkiw, "Level Set Methods: An Overview and Some Recent Results," J. Comput. Phys. **169**, 463–502 (2001).
35. F. Gibou, R. Fedkiw, and S. Osher, "A review of level-set methods and some recent applications," J. Comput. Phys. **353**, 82–109 (2018).
36. R. Tsai and S. Osher, "REVIEW ARTICLE: Level Set Methods and Their Applications in Image Science," Commun. Math. Sci. **1**, 1–20 (2003).
37. C. Li, C. Xu, C. Gui, and M. D. Fox, "Distance Regularized Level Set Evolution and Its Application to Image Segmentation," IEEE Trans. Image Process. **19**, 3243–3254 (2010).
38. I. Despotović, B. Goossens, and W. Philips, "MRI Segmentation of the Human Brain: Challenges, Methods, and Applications," Comput. Math. Methods Med. **2015**, (2015).
39. Y. Chen, J. Zhang, and J. Macione, "An improved level set method for brain MR images segmentation and bias correction," Comput. Med. Imaging Graph. Off. J. Comput. Med. Imaging Soc. **33**, 510–519 (2009).
40. L. Fernandez-de-Manuel, J. L. Rubio, M. J. Ledesma-Carbayo, J. Pascau, J. M. Tellado, E. Ramon, M. Desco, and A. Santos, "3D liver segmentation in preoperative CT images using a level-sets active surface method," Conf. Proc. Annu. Int. Conf. IEEE Eng. Med. Biol. Soc. IEEE Eng. Med. Biol. Soc. Annu. Conf. **2009**, 3625–3628 (2009).
41. F. Khalifa, A. Elnakib, G. M. Beache, G. Gimel'farb, M. A. El-Ghar, R. Ouseph, G. Sokhadze, S. Manning, P. McClure, and A. El-Baz, "3D Kidney Segmentation from CT Images Using a Level Set Approach Guided by a Novel Stochastic Speed Function," in *Medical Image Computing and Computer-Assisted Intervention – MICCAI 2011*, G. Fichtinger, A. Martel, and T. Peters, eds., Lecture Notes in Computer Science (Springer Berlin Heidelberg, 2011), pp. 587–594.
42. P. Swierczynski, B. W. Papież, J. A. Schnabel, and C. Macdonald, "A level-set approach to joint image segmentation and registration with application to CT lung imaging," Comput. Med. Imaging Graph. **65**, 58–68 (2018).
43. L. Liu, K. Li, W. Qin, T. Wen, L. Li, J. Wu, and J. Gu, "Automated breast tumor detection and segmentation with a novel computational framework of whole ultrasound images," Med. Biol. Eng. Comput. **56**, 183–199 (2018).
44. Y. Guo, A. Şengür, and J.-W. Tian, "A novel breast ultrasound image segmentation algorithm based on neutrosophic similarity score and level set," Comput. Methods Programs Biomed. **123**, 43–53 (2016).

45. F. Mohammad, R. Ansari, J. Wanek, A. Francis, and M. Shahidi, "Feasibility of level-set analysis of enface OCT retinal images in diabetic retinopathy," Biomed. Opt. Express **6**, 1904–1918 (2015).

46. Y. Cao, K. Cheng, X. Qin, Q. Yin, J. Li, R. Zhu, and W. Zhao, "Automatic Lumen Segmentation in Intravascular Optical Coherence Tomography Images Using Level Set," Comput. Math. Methods Med. **2017**, 1–11 (2017).

47. Y. Li, R. Shekhar, and D. Huang, "Corneal Pachymetry Mapping with High-speed Optical Coherence Tomography," Ophthalmology **113**, 792–799.e2 (2006).

48. M. Ayala and R. Strandås, "Accuracy of optical coherence tomography (OCT) in pachymetry for glaucoma patients," BMC Ophthalmol. **15**, 124 (2015).

49. C. Wirbelauer, C. Scholz, H. Hoerauf, D. T. Pham, H. Laqua, and R. Birngruber, "Noncontact corneal pachymetry with slit lamp-adapted optical coherence tomography," Am. J. Ophthalmol. **133**, 444–450 (2002).

Chapter 5

NANOSENSITIVE OPTICAL COHERENCE TOMOGRAPHY TO PROBE STATIC (IN SPACE) AND DYNAMIC (IN TIME) STRUCTURAL CHANGES WITHIN THE CORNEA

5.1 Introduction

As stated in the introductory chapter, since its introduction in early 1990's, OCT has been clinically demonstrated in a diverse set of medical and surgical applications, including ophthalmology, gastroenterology, dermatology, cardiology, and oncology, among others. Although OCT offers axial resolution of 6–15 μm in air and penetration depth of 2–3 mm in biological tissues, there has been several attempts to improve the axial resolution of OCT systems. Over the years, numerous techniques have been proposed and implemented to improve the axial resolution of conventional OCT systems [1]. Most of these techniques used Ti - sapphire lasers or light sources based on super continuum generation from photonic crystal fibres for imaging [2–4]. However, the best ultra-high resolution OCT systems are limited to detecting structural changes with a sensitivity of 1 micron *on a single frame* within very limited depth [3]. Currently, there exist a trade-off between the axial resolution of an optical imaging system and its penetration depth ($penetration\ depth/axial\ resolution \sim 200$) [5].

As described in chapter 2, OCT can be used for both structural and functional imaging. However, most of these functional imaging techniques are unable to determine sub-micron changes within the tissue and are capable of only determining the structural changes within the optical resolution of the OCT system. In recent past, several methods have been proposed in combination with OCT to detect nanoscale structural changes. One of them is based on phase sensitive OCT which uses the Fourier analysis of phase differences of acquired interference spectra (A- scans) at particular depth positions [6]. Nano scale detection with phase sensitive

technique was used to determine the sub-micron movement of basilar membrane within the organ of Corti and neural action potential in a squid [7,8]. Another technique called inverse spectroscopic OCT (ISOCT) was developed wherein wavelength dependent backscattering coefficient and scattering coefficient is determined by fitting an autocorrelation function to the detected A-scan signal of the OCT and from the fit model, the mass density distribution in a biological sample is quantified [9]. The mass density distribution obtained using ISOCT was used to study extra cellular matrix remodelling in *in vitro* cancer models [10] and to study field carcinogenesis [11]. Recently, nano-sensitive OCT has been developed by Alexandrov *et al*. [12,17]. This is based on spectral encoding of spatial frequencies [13-16], that demonstrated nano-scale sensitivity to structural changes and super-resolution imaging. In contrast to phase sensitive OCT techniques the nsOCT permits detection and visualization of some nanoscale structural changes using just single frame. The nsOCT has been used to detect both structural and dynamic changes in *ex vivo* and *in vivo* biological tissues [12,17,18]. Studying nanoscale structural and dynamic changes *in vivo* is fundamental to understanding changes occurring at cellular level before the changes manifest at the tissue level. Detecting these sub-micron structural changes can help scientists and clinicians to diagnose the onset of a disease, its progression and in determining treatment effectiveness of drugs. Herein, OCT offers great potential whereby combining nano-detection techniques together with real time, wide field OCT structural imaging capability, can provide sub voxel resolution by mapping nanoscale structural changes without the need to improve the actual optical resolution. Such an imaging technology can overcome partially the scale range issue in optical imaging modalities, without the need to use expensive high resolution imaging optics.

5.2 Nanosensitive OCT -Theory

Nano-sensitive OCT, (nsOCT), is a novel, label-free imaging technique which has been shown to provide axial structural information with nanoscale sensitivity. nsOCT is based on encoding each spatial frequency component of an object with a corresponding wavelength [14,19]. It has been known that the Fourier spectrum of spatial frequencies is informative and sensitive to structural changes at nanoscale and can provide information regarding the spatial frequency of the object probed [20]. The nsOCT has been invented to keep information about small, sub-micron structure and pass it to image domain. In nsOCT, the high frequency information is retained by encoding each axial spatial frequency with one unique wavelength. Wavelength is unchanged by the Fourier transform from wavenumber domain to image domain, so the encoded spatial frequency information is not lost when it is transmitted from object space to

image space. Hence, nsOCT approach is able to map the spatial frequency content obtained from the Fourier spectra within the volume of the sample probed.

In OCT, the sample signal is made up of backscattered light, originating from a depth interval in the sample, set by the coherence gate of the system. Thus, the backscattered signal from the sample can be analysed using scattering theory. Consider a monochromatic electric field with time dependence e^{iwt} incident on an isotropic, non magnetic medium of finite volume *V* as shown in figure 5.1.

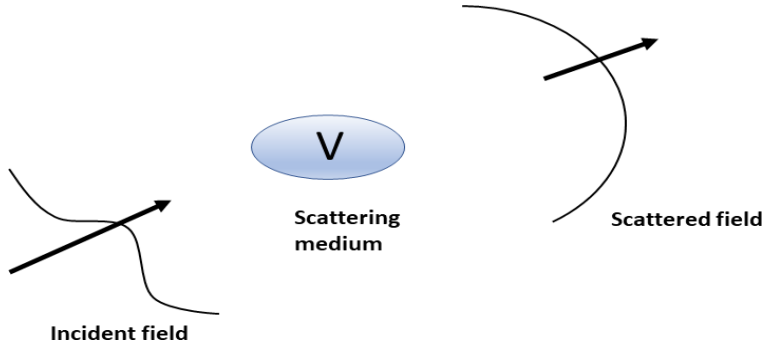

Fig.5.1 Schematic showing scattering by an incident plane wave

Then assuming that there are no sources within *V*, the space dependent part of complex electric field will satisfy the following equation 5.1 [20]

$$\nabla^2 E(r,w) + k^2 \varepsilon(r,w) E(r,w) + grad[E(r,w).grad \ln \varepsilon(r,w)] = 0 \qquad (5.1)$$

If we consider the dielectric medium $\varepsilon(r)$ to vary slowly over the volume, i.e. we can approximate it as constant over distances comparable to λ, then equation 5.1 can be rewritten to obtain equation 5.2, where *n* is the refractive index of the medium.

$$\nabla^2 E(r,w) + k^2 n^2(r,w) E(r,w) = 0 \qquad (5.2)$$

For a single cartesian component *U(r,w)* of *E(r,w)*, the scattered field equation may be rewritten as given by Eq. 5.3

$$\nabla^2 U(r,w) + k^2 n^2(r,w) U(r,w) = 0 \qquad (5.3)$$

The terms in Eq.(5.3) may be rearranged and written in the form as given by Eq.(5.4)

$$\nabla^2 U(r,w) + k^2 U(r,w) = -4\pi F(r,w) U(r,w) \qquad (5.4)$$

where *F(r,w)* is called the scattering potential of the medium and is given by Eq.(5.5)

$$F(r,w) = \frac{1}{4\pi} k^2 (n^2(r,w) - 1) \qquad (5.5)$$

Further, the total field *U(r,w)* can be expressed as a sum of incident field $U_i(r,w)$ and scattered field $U_s(r,w)$.

$$U(r,\omega) = U_i(r,\omega) + U_s(r,\omega) \tag{5.6}$$

Since the incident plane wave $U_i(r,\omega)$ satisfies Helhmoltz equation, $\nabla^2 U_i(r,\omega) + k_0^2 U_i(r,\omega) = 0$ throughout the space, equation 5.4 can be written as given below

$$\nabla^2 U_s(r,w) + k^2 U_s(r,w) = -4\pi F(r,w)U(r,w) \tag{5.7}$$

The above differential equation converted into an integral equation by replacing the Helmholtz operator with a symmetric Green's function and solving for the scattered field in the far field. In this way, we obtain equation 5.8 [20] where r^1 is the spatial location of the scatterer (position vector) within the volume V and *r* is the spatial location in the far field.

$$U_s(r,w) = \int_V F(r^1,w)U(r^1,w)\frac{e^{ik|r-r^1|}}{|r-r^1|}d^3r^1 \tag{5.8}$$

Now suppose the incident field is propagating in the direction specified by a real unit vector s_o, with unit amplitude and frequency ω, from equation 5.6 and Eq. 5.8, it follows that,

$$U(r,\omega) = e^{ik s_o r} + \int_V F(r^1,w)U(r^1,w)\frac{e^{ik|r-r^1|}}{|r-r^1|}d^3r^1 \tag{5.9}$$

In any real imaging system, the sample signal is measured at a very large distance with respect to the distance between scatterers, i.e. r >> r^1 as shown in figure 5.2,

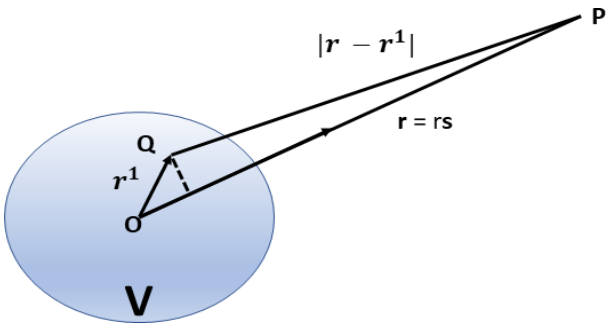

Fig.5.2 Schematic describing the scattering in the far field

Q is a point within the scattering volume *V*, and P a point in the far field, then |r-r^1| can be approximated as |r-r^1| ~ r - **s**r^1 and $\frac{e^{ik|r-r^1|}}{|r-r^1|} \sim \frac{e^{ikr}}{r} e^{-iks.r^1}$, where ***s*** is the unit vector. Substituting this approximation into Eq. (5.9), gives us

$$U(r,\omega) = \mathrm{e}^{\mathrm{ik}s_o\mathrm{r}} + \int_V F(r^1,w)U(r^1,w)\frac{e^{ikr}}{r}e^{-iks.r^1}d^3r^1 \quad (5.10)$$

where $\int_V 4\pi F(r^1,w)U(r^1,w)e^{-iks.r^1}d^3r^1$ is the scattering amplitude.

By considering the medium to be weakly scattering, the term $U(r^1,w)$ in equation 5.10 may be replaced by the incident field $\mathrm{e}^{\mathrm{ik}\boldsymbol{s_o}\mathrm{r}}$. Hence by first order Born approximation in the far field, equation 5.10 may be written as given below :

$$U(r,\omega) = \mathrm{e}^{\mathrm{ik}\boldsymbol{s_o}\mathrm{r}} + \int_V F(r^1,w)e^{ik\boldsymbol{s_o}r^1}\frac{e^{ikr}}{r}e^{-iks.r^1}d^3r^1 \quad (5.11)$$

The term $\int F(r^1,w)e^{-ik(\boldsymbol{s}-\boldsymbol{s_o})r^1}d^3r^1$ is the scattering amplitude in the far field obtained by first order Born approximation denoted by $f(s,s_0;w)$. ie.

$$f(s,s_0;w) = \int_V F(r^1,w)e^{-ik(\boldsymbol{s}-\boldsymbol{s_o})r^1}d^3r^1 \quad (5.12)$$

Now, if we consider taking a Fourier transform of the scattering potential,

$$F(\boldsymbol{K}) = \int_V F(r^1,w)e^{-iKr^1}d^3r^1 \quad (5.13)$$

where *K* is the spatial frequency vector, $\boldsymbol{K} = k(\boldsymbol{s}-\boldsymbol{s_0})]$

By comparing equation 5.12 and 5.13,

$$f(s,s_0;w) = F[k(\boldsymbol{s}-\boldsymbol{s_0})] \quad (5.14)$$

From equation 5.14, it can be seen that the amplitude of the scattered field at a particular location in the far field is equal to the Fourier transform of the scattering potential at that same location. Therefore, using equation 5.14, for an incident wave travelling in direction s_0 , by measuring the scattered field in direction s, one unique Fourier component of the scattering potential can be accessed - the spatial frequency vector, K. Keeping the direction of the incident wave constant (fixed illumination angle), and measuring the scattered field in all possible directions then gives access to a set of spatial frequency vectors. This set of K -vectors will form an Ewald sphere of reflection via their end-points, as shown in figure 5.3. The radius of the sphere is given by $\frac{2\pi}{\lambda}$.

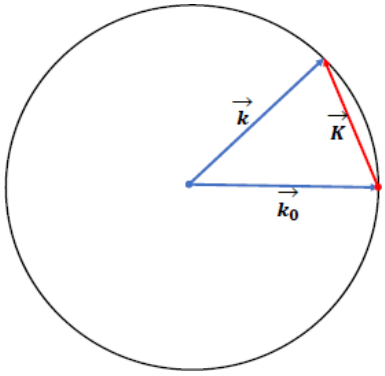

Fig.5.3 Formation of an Ewald sphere of reflection

If this analysis is extended to measure the Fourier components of the scattering potential for all directions of illumination and scattering, the sample's scattering potential can be reconstructed through an inverse Fourier transform as given by equation 5.15.

$$F(r) = \frac{1}{2\pi^3} \int F(\boldsymbol{K}) e^{i\boldsymbol{K}r} d^3K \qquad (5.15)$$

However, there is a limit on the range of spatial frequencies that can be measured in such a way. The reconstructed scattering potential here is actually a low-pass filtered approximation of the true scattering potential, limiting the structural information available about the sample to the scale of about half a wavelength.

OCT is a one-dimensional solution to the inverse scattering problem. In OCT, the directions of illumination and measurement of backscattering are the same. Under these conditions, the only Fourier components of the scattering potential measured, are the ones which are labelled by a K-vector whose endpoints fall on the corresponding points on the Ewald sphere of reflection associated with that particular direction of incidence. However, in OCT a broadband source is used, so for that one direction of illumination and backscattering, multiple Ewald's spheres are obtained - one for each wavelength within the light source used, as illustrated in figure 5.4. The Ewald's spheres, as shown in figure 5.4, are directly related to the spatial frequency vectors of the sample scattering potential. Thus, in OCT each wavelength is encoded with a single axial spatial frequency component. This enables high spatial frequency information to be passed from object space to image space and mapped for each image point. In this way, three-dimensional structural information can be visualised at each pixel within a two-dimensional image.

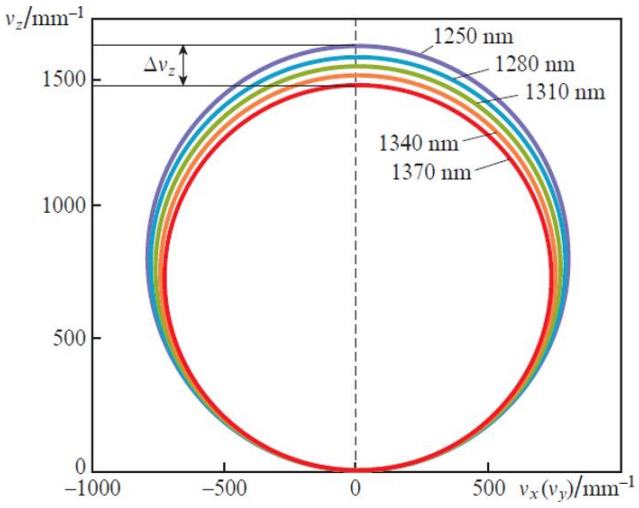

Fig.5.4 Ewald spheres at various wavelength

5.3 nsOCT image formation

Nano-sensitive OCT accesses the three-dimensional spatial frequency components of a sample, as a two-dimensional spatial frequency distribution in the Fourier plane. It accomplishes this by spectrally encoding the axial spatial frequency vectors, and in a spectral domain configuration, measuring the wavelength distribution for each pixel [12]. Considering a single OCT A-line, the Fourier components of the scattering potential are collected along one dimension only. This results in an incident wave vector, $\overrightarrow{ks_0} = -kcos\theta$ and a scattered wave vector $\vec{ks} = kcos\alpha$ where θ and α are the illumination and scattering angles respectively. The measured components of the scattering potential, k_z, are given by $\vec{k}(\vec{s} - \overrightarrow{s_0})$.

$$k_z = kcos\alpha - (-kcos\theta) \tag{5.16}$$

Since in one-dimensional OCT, the illumination light and the backscattered light travel the same path, which coincides with the optical axis, i.e. the z-axis, $\theta = \alpha = 0$.

Hence, equation 5.16 becomes

$$k_z = 2k \tag{5.17}$$

Substituting, $k = 2\pi v$, where v is the spatial frequency and including the refractive index of the sample (n) in equation 5.17, we obtain,

$$2\pi\gamma_z = \frac{4\pi n}{\lambda} \tag{5.18}$$

$$\gamma_z = \frac{2n}{\lambda} \tag{5.19}$$

From equation 5.19, the spatial frequency period H_z may be defined as

$$H_z = \frac{1}{\gamma_z} \tag{5.20}$$

Equations 5.19 and 5.20 indicates that by scaling each of the spatial frequencies, or spatial frequency periods, to the corresponding wavelength, the information about sub-micron structural changes is preserved when transforming from K-space to image space. In conventional OCT, however, while taking the inverse Fourier transform of the interference signal to reconstruct the OCT structural image, the spatial frequency information which corresponds to small, submicron structure, is lost. This reduces the sensitivity of conventional OCT signal processing to detect sub-micron changes in the scattering structures. In nsOCT, by scaling each of the spatial frequencies, or spatial frequency periods, to the corresponding wavelength, spatial frequency of the scattering structures is preserved when transforming from K - space to the image space.

Depending on the source bandwidth, there exist a range of spatial frequencies that can be captured on a spectrometer, as given by equation 5.21, where λ_2 and λ_1 are the longest and shortest wavelengths of the source and $\Delta\lambda = \lambda_2 - \lambda_1$ (bandwidth of the source).

$$\Delta\nu = \frac{2\,\Delta\lambda}{\lambda_1\lambda_2} \tag{5.21}$$

Hence the spectral resolution of OCT technique in terms of axial spatial frequency is given by equation 5.22

$$\delta\nu = \frac{\Delta\nu}{No.pixels\ on\ the\ spectrometer} \tag{5.22}$$

In order to realise nsOCT, first the *k* space linearized spectral interferogram $I(\lambda)$ is converted to corresponding axial spatial frequency $I\ (\nu_z)$ using equation 5.19. The spectrum of axial spatial frequency is then divided into N zones. For each of the N zones, the axial spatial frequency profile is inverse Fourier transformed to reconstruct the OCT image for each particular spatial frequency. From the reconstructed OCT images of *N* zones, the dominant spatial frequency/period that contributes the most at each point is determined by finding the maximum intensity values at each point across the *N* zones and assigning that zone's central value to the pixel in question, the maximum spatial frequency contribution. The schematic describing the nsOCT processing is shown in figure 5.5.

Since maximum spatial period contribution can be known for each pixel in a 2D image by the nsOCT approach, sub-micron structural information about the sample's 3D structure can be visualised at each pixel through a single OCT scan. By considering the spatial frequency zone corresponding to the maximum intensity and assigning that zone's central value to the pixel in question, the maximum spatial frequency contribution can be found. If this is then evaluated at each pixel, and colour-coded, a nsOCT image displaying the spatial frequency periods at maximum signal is formed. This method is highly sensitive and characterises the dominant structure size within the image, with lower spatial frequency periods corresponding to a smaller dominant structure size.

Similarly, nsOCT image can be plotted as a median spatial frequency/period (*msf*) distribution by evaluating the spatial period/frequency distribution as given by equation 5.23.

$$msf = \frac{\sum_{n=1}^{N} f(n)x(n)}{\sum_{n=1}^{N} x(n)} \tag{5.23}$$

where *x(n)* represents the intensity of the spatial frequency/period profile at the frequency/period *f(n)*. This method characterises the median local structure size within the sample.

An important consideration to be made in nsOCT image reconstruction is the number of zones chosen. Obviously, as the number of zones increases, the spectrum must be divided into narrower and narrower bands. The width of each of these zones, or bands, pertains to a range of spatial frequencies. As a result, the axial size of each volume of interest is determined by the width of the spatial frequency zones. However, the number of zones is equivalent to the number of spatial frequency values that can be assigned to the pixels when reconstructing the axial spatial period profiles. For example, using 12 zones of spatial frequency means that each pixel is assigned one of the 12 values corresponding to the centre of each zone. i.e., there is an inherent trade-off which must be optimised, depending on the application.

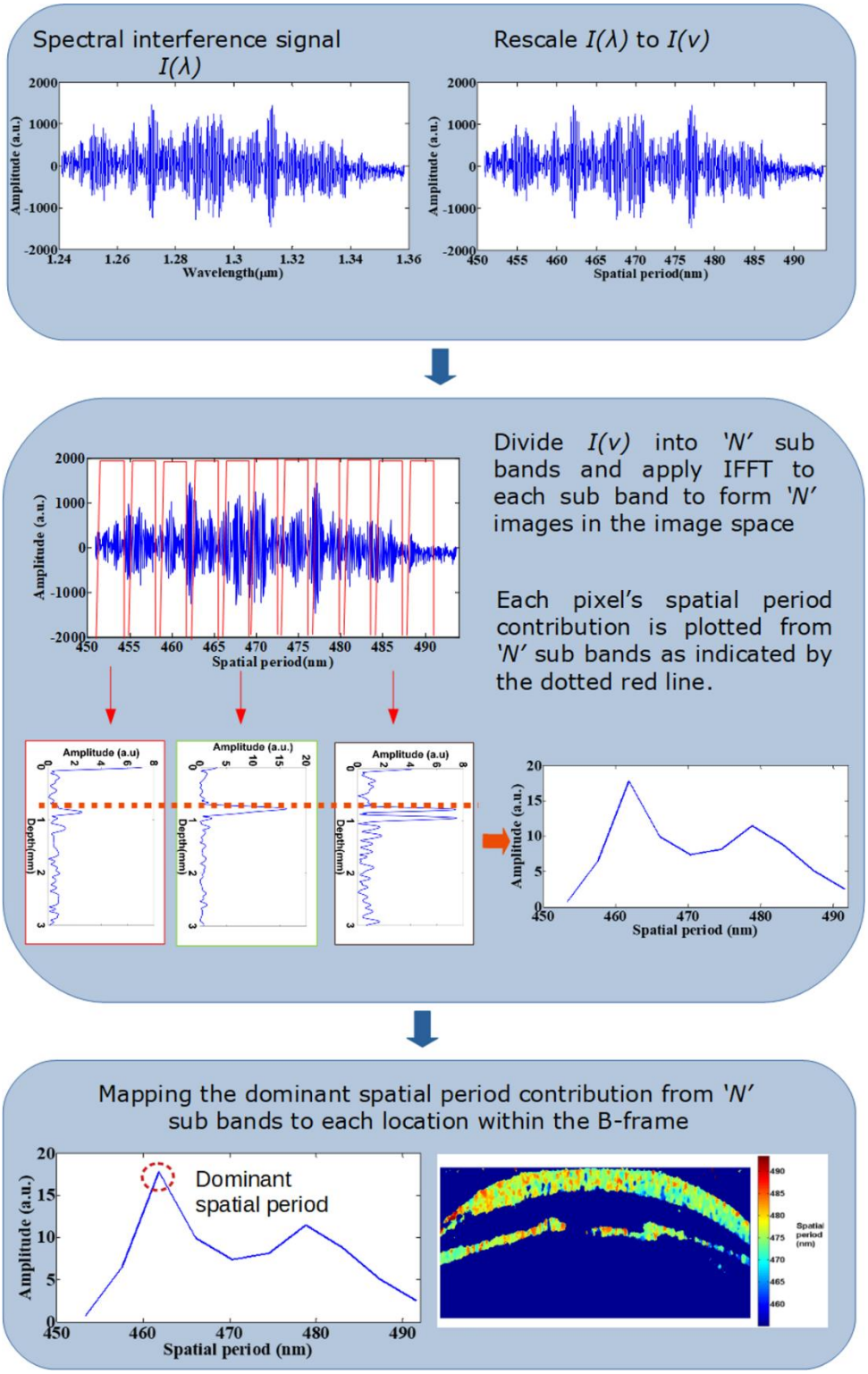

Fig. 5.5 Schematic of nsOCT processing.

5.4 nsOCT approach to probe structural changes within cornea

The cornea is a transparent, avascular layer of the eye that controls the entry of light into the eye and also helps to refract the light onto the retina. Corneal transparency is vital to preserve

its structure and function. Corneal injuries generally arise from thermal and chemical burns [21,22]. Of these, 11.5 – 22% of all ocular injuries occur from chemical burns, from both acids and alkali [23]. Over the years, OCT has been routinely used in ophthalmic applications and some recent studies have reported its use in evaluating the chemical ocular burns and its healing process [24–27]. All of these studies were based on the analysis of the structure of the anterior segment of the injured eye from the OCT B frames.

Among chemical induced corneal burns, alkali burn causes more damage to the corneal stroma and anterior chamber compared to acid injury. Alkali ions being lipophilic, penetrate into the corneal stroma disrupting the cells and denaturing the collagen matrix, which promotes further penetration into the anterior chamber [28,29]. The corneal stroma plays a vital role in maintaining corneal transparency and acts as load bearing agents by protecting the ocular tissues from changes in intra ocular pressure. Any change within the micro structures of the cornea results in loss of transparency and increases the light scattering [30]. The corneal stroma is made up of collagens, proteoglycans, glycoproteins and keratocytes and it has been shown that, it is the nanoscale arrangement of collagen fibrils that ensures corneal transparency [30]. It has been reported that any change in the diameter of the collagen fibrils or creation of voids between the fibrils causes increased light scattering within the cornea and leads to corneal opacity [30]. Another factor that increases light scattering within the cornea is the activation of keratocytes within the stroma in response to corneal wound healing process. Based on these studies, it is imperative to understand the nano scale structural changes occurring during ocular injury and subsequent wound healing process *in vivo* for assessment of wound repair and monitor treatment efficacy.

As these chemical agents alter the structural integrity of the cornea upon contact, nsOCT provides the possibility to detect and visualize the sub-micron structure just from one frame and the submicron changes using two frames which otherwise cannot be obtained from conventional OCT and other images. The results obtained by nsOCT is validated with results from corneal histology sections.

5.4.1 Materials and methods

5.4.1.1 Experimental set up:

In the present study, a commercial OCT system operating at 200 kHz (Thorlabs) was used. The system was based on MEMS-VCSEL swept laser technology operating at central wavelength of 1300 nm (source bandwidth of 117.2 nm) and an imaging range of 12 mm in depth. The longest and shortest wavelength of the source is 1358.2 nm and 1241 nm respectively. For the study, we used 5X objective that provided a lateral resolution of 25µm.

5.4.1.2 Rat corneal alkali burn model:

Application of alkali to one cornea of the rat was performed under anaesthesia with isoflurane followed by topical tetracaine. To induce alkaline injury, a piece of Whatman filter paper (3mm diameter) was soaked in NaOH (4µl of a 1M solution) and applied to the centre of the cornea of the right eye for 60 seconds followed by rinsing with 10 ml of saline for fifteen minutes. All procedures performed were conducted in a fully accredited animal housing facility, under approval by the Animals Care Research Ethics Committee of the National University of Ireland, Galway and authorization from the Health Products Regulatory Authority of Ireland. Male Lewis rats aged 8-14 weeks were obtained from Harlan Laboratories UK and were housed with food and water for the study. For the OCT imaging, the rats were mounted on an inhouse developed mounting system such that the eyes were stabilized and caused minimal movement artefact. OCT interferograms were acquired prior to alkali injury and after the injury (time, t =0) of the study (immediate phase). To assess the wound healing process, subsequent imaging was performed on day 7 following the alkali injury (acute reparative phase). For all the imaging, 3 D volume data were acquired over a field of view of 5x5 x5 mm^3, with 200 B - frames covering the entire scan range.

5.4.2 nsOCT processing

Following the nsOCT approach as described in section 5.5, the spectral interference signal was divided into 10 zones with each zone having spatial frequency bandwidth ($\delta\nu_n$) of $\frac{\Delta\nu}{10}$ where $\Delta\nu$ is the spectral bandwidth of the source. Since the longest and shortest wavelength of the source is 1358 nm and 1241 nm respectively, we had a spectral bandwidth of 117 nm. The corresponding spatial periods ranged from 620nm to 675 nm (using equations 5.19 and 5.20).

5.4.3 Results and Discussion

For the present study, twelve rats were included in the immediate phase group and raw OCT spectral interference signals were recorded before and after inducing the alkali injury. To analyse the structural changes occurring within the cornea during the acute phase of the injury, five rats from the immediate phase group were imaged on the 7th day following the injury.

In this study, along with conventional Fourier domain processing of OCT spectral interferograms, nsOCT algorithm was implemented so as to determine nano scale structural changes occurring within the cornea over time which cannot be assessed from conventional OCT intensity images.

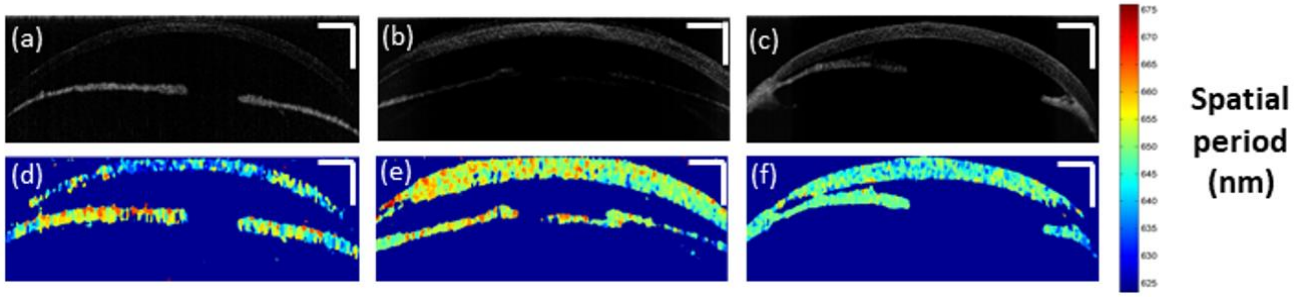

Fig. 5.6. Conventional OCT B- frames (a) uninjured cornea (b) after alkali induced corneal burn (c) injured cornea on 7th day (d) nsOCT B – frame of corresponding uninjured cornea (e) nsOCT B frame following alkali induced corneal burn (f) nsOCT B frame on 7th day following the injury. Scale bars – 500 µm.

Figure 5.6 shows the representative OCT B - frames of a healthy cornea, injured cornea and cornea on day 7 post injury. Alkali burn results in corneal oedema and increased light scattering within the cornea as can be observed from OCT intensity B – frame images in figure 5.6(b) and 5.6(c), but there is no information about structural changes within the cornea. While reconstructing OCT intensity B – frames following conventional approach, we lose the sensitivity of OCT to sub-micron spatial period information. From figures 5.6(d) – (e) we can observe that nsOCT processed B - fames differ significantly in the spatial period of the structures within the cornea between a healthy cornea, at the onset of alkali injury and during the acute phase of the injured cornea. The corneal inflammation and denaturization of the collagen matrix in response to alkali injury results in an increase in spatial period of the structures within the cornea as observed in nsOCT images in figure 5.6(e) and 5.6(f) compared to figure 5.6(d). As stated before, alkali injury penetrates the corneal stroma and leads to the damage of anterior chamber. Hence, for better visualization of the nano scale structural changes within the cornea at each depth, *enface* images were reconstructed from the processed nsOCT and conventional B frames. Figure 5.7 and 5.8 shows representative *enface* OCT images at a

depth of 60 µm and 120 µm respectively of the rat burn model before and after the injury. From the figures 5.7 and 5.8, it can be observed that conventional OCT *enface* intensity images fails to distinguish between healthy cornea and injured cornea. However, nsOCT processed *enface* images clearly indicates changes in spatial period within the cornea and helps to distinguish between healthy and injured cornea as shown in figure 5.7(d) and 5.7(e). Also, nsOCT processing is able to track structural changes happening within the cornea at the onset of an injury and also in assessing the healing process based on the changes in the spatial period as can be observed in figures 5.7(e) and 5.7(f).

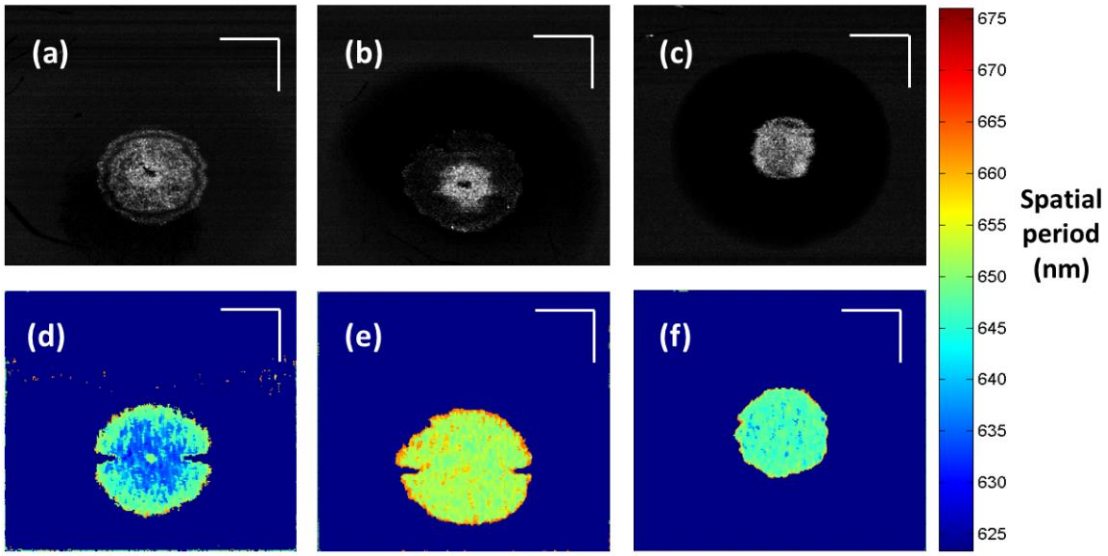

Fig. 5.7 *Enface* intensity and nsOCT images at a depth of 60 µm (a), (d) healthy cornea (b), (e) after alkali induced burn (c), (f) injured cornea on 7th day. Scale bars – 500 µm.

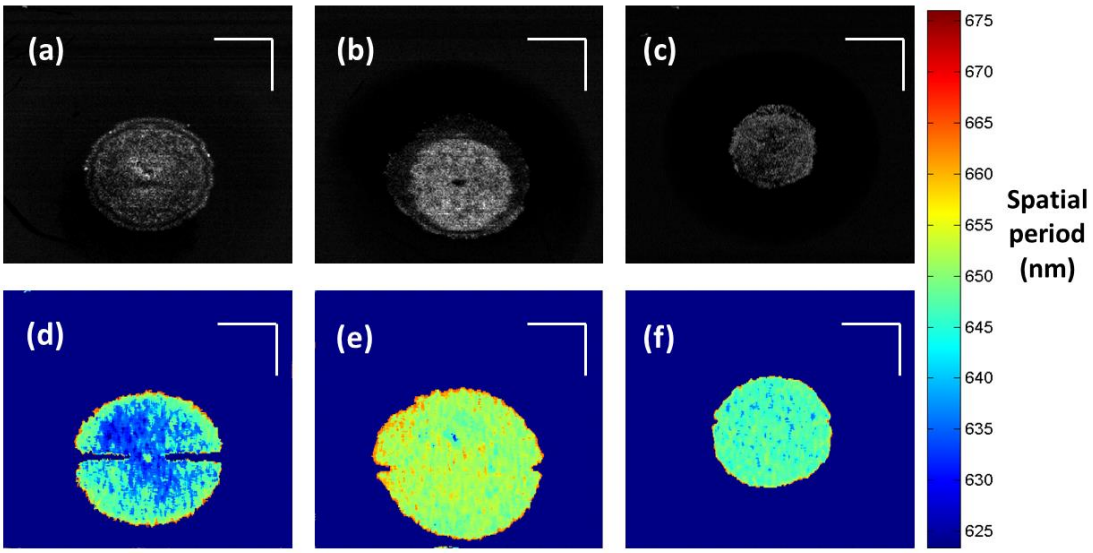

Fig. 5.8 Enface intensity and nsOCT images at a depth of 120 µm (a), (d) healthy cornea (b), (e) after alkali induced burn (c), (f) injured cornea on 7th day. Scale bars - 500 µm.

Figure 5.9 shows the comparison of spatial period changes across the corneal depth for the healthy group and the immediate phase group. Statistical analysis using paired t test (samples -12 per group) shows significant difference ($p < 10^{-7}$) in spatial period changes over the corneal depth between the healthy uninjured cornea and the immediate phase group.

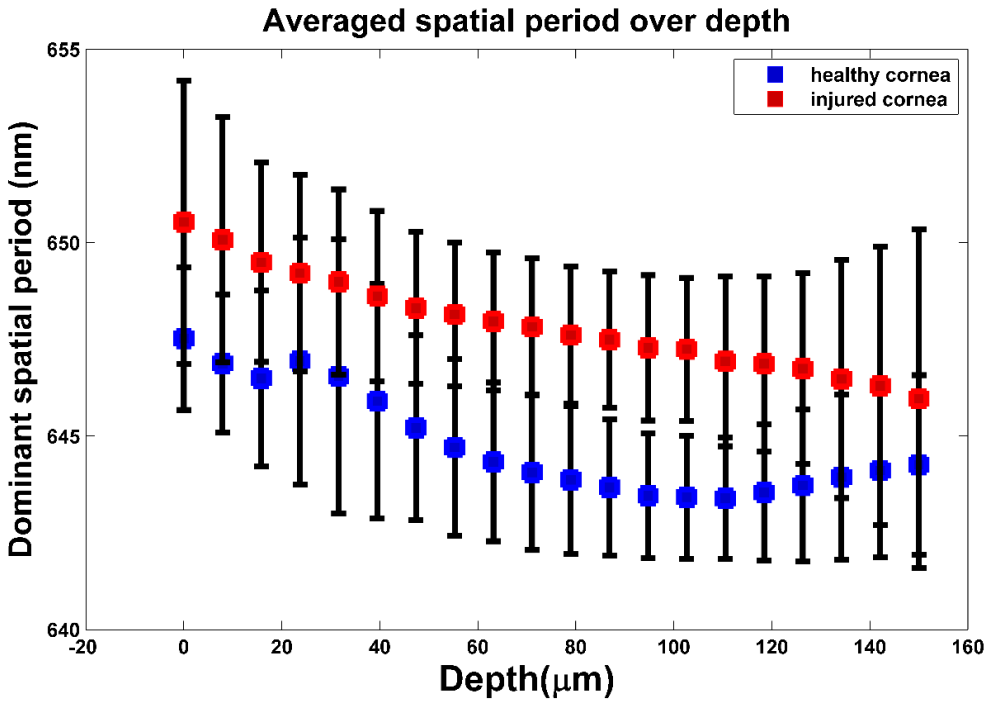

Fig. 5.9 Spatial period changes across the corneal depth for the healthy group and the immediate phase group

Figure 5.9 indicates that at the onset of an alkali injury, the spatial period of the structures within the cornea increases at all depths. This is in accordance with the fact that alkali injury penetrates deep into the cornea. The exact reason for this increase in spatial period is not known, however it must be linked to the changes occurring within the collagen matrix of the stroma and due to swelling within the cornea upon the activation of keratocytes within the stroma.

Figure 5.10 shows the comparison of spatial period changes across the corneal depth between the immediate phase group and acute phase group. Statistical analysis using paired t test (samples - 5 per group) shows significant difference ($p < 10^{-10}$) in spatial period changes over the corneal depth between two groups.

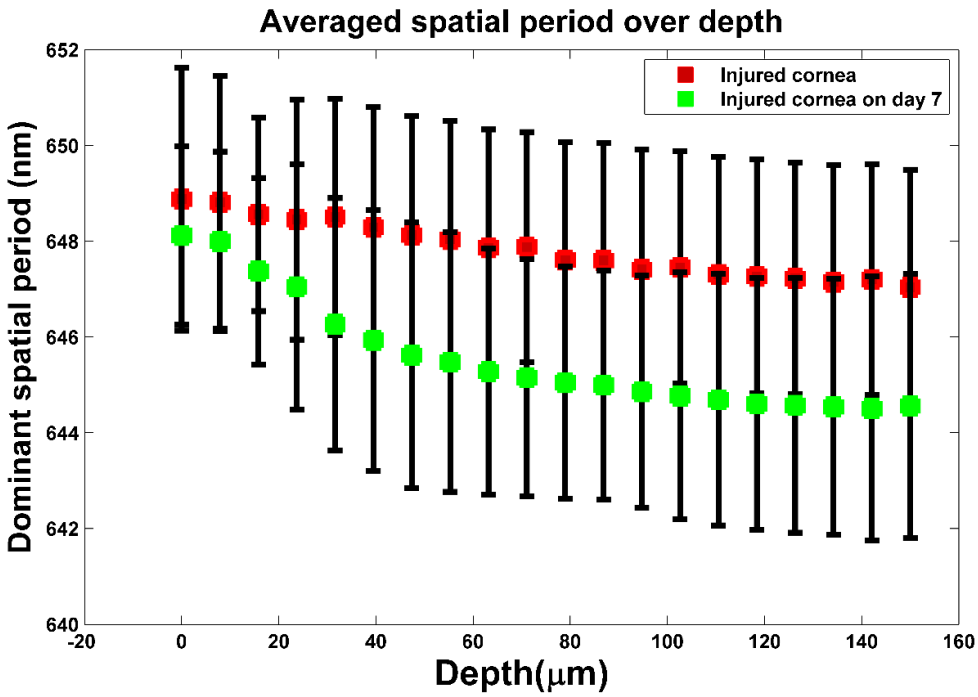

Fig. 5.10 Plot showing spatial period changes across the corneal depth between the immediate phase group and acute phase group

From figure 5.10, it can be observed that during the acute phase of alkali induced corneal injury, the spatial period of the structures at all depths within the cornea tends to reduce compared to the cornea in the immediate phase group. This result indicate that during the acute phase, corneal recovery is taking place by clearing the contaminants within the tissue and by the reestablishment of corneal epithelium [29]. Also, it is to be noticed that, most prominent reduction in spatial period occurs within the corneal stroma at depths 50 – 150 μm. These results also indicate that there are significant changes happening within the collagen matrix of the stroma during the acute reparative phase.

To compare the structural integrity of the cornea after the acute reparative phase of the injury with that of the healthy group, statistical significance test (samples – 5 per group) was performed ($p < 10^{-10}$) between the two groups, and shown in figure 5.11.

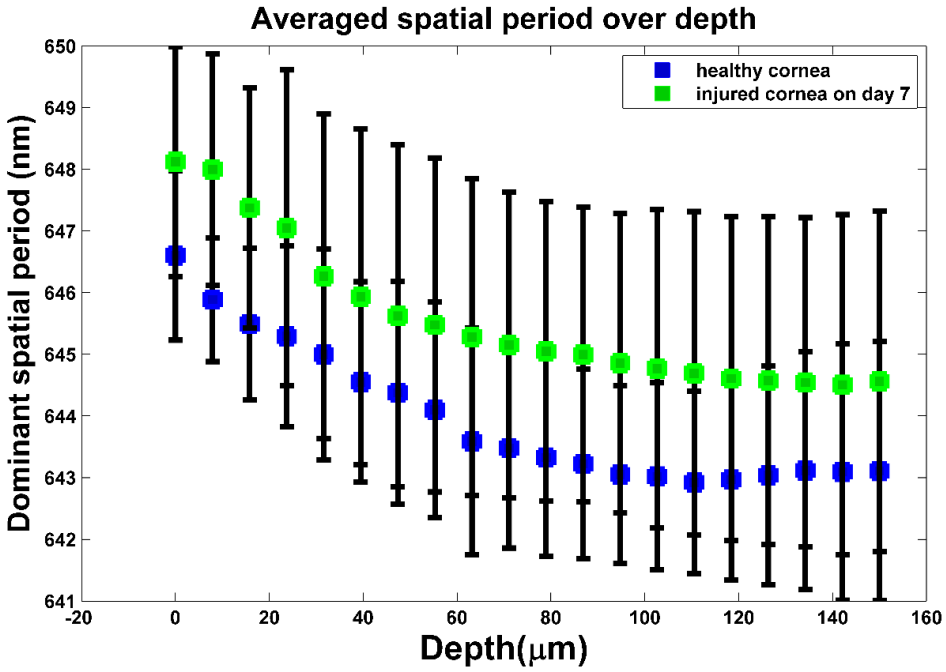

Fig. 5.11 Plot showing spatial period changes across the corneal depth between the healthy group and acute reparative phase group

From figure 5.11, it can be observed that during the acute reparative phase of the injury, the structural spatial period of the injured cornea across all depths is higher than that of healthy group, however follows a consistent pattern similar to that of the healthy group. This indicates that the cornea is self - healing post the acute reparative phase [31] . From figures 5.9,5.10 and 5.11, it is evident that nsOCT is able to capture the nano scale structural changes within the cornea during the wound healing process *in vivo* thus enabling nsOCT to be a powerful processing method sensitive to nano scale structural changes within the sample of interest.

Currently, stained histology imaging is the gold standard to assess mciro/nano scale structural changes within a biological tissue. To validate the results obtained using nsOCT processing of spectral interferograms, corneal histology sections of the cornea before and after the injury were analysed. For histology analysis, animals were euthanized on the 7th day and the intact enucleated eyes were fixed in 10% neutral buffered formalin and paraffin embedded using Leica ASP300 tissue processor. Paraffin-embedded eyes were then sectioned (5μm; Leica Microtome) and deparaffinised by sequential washing with xylene followed by washing in a descending series of ethanol and stained using hematoxylin and eosin (Sigma-Aldrich). The stained sections were examined by Olympus light microscopy (20x magnification).

Figure 5.12 (a) and (b) shows the representative histology sections of a healthy cornea and an injured cornea on day 7 post injury respectively. As seen from figure 5.12 (a), the healthy cornea is characterized by intact epithelium, and well-arranged collagen fibres within the

stroma. However, histological examination of the cornea on day 7 post injury reveals vacuolization of the surface layer of the epithelium along with degenerative changes in the stroma.

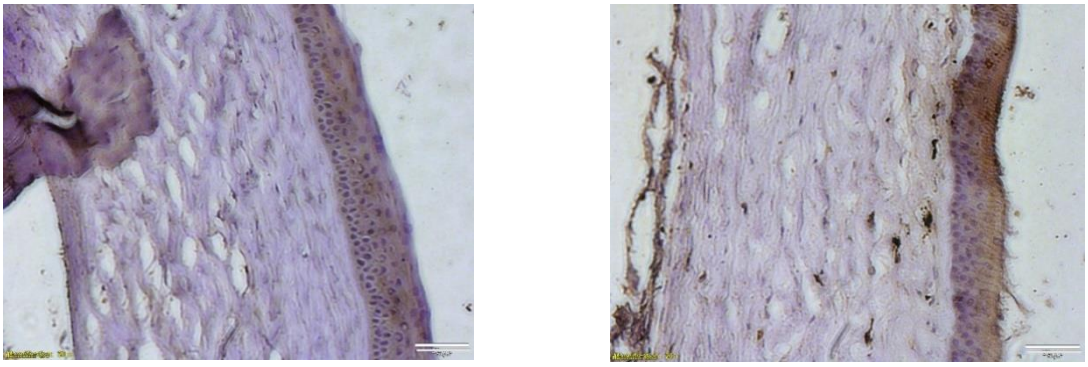

(a) (b)

Fig. 5.12 Corneal histological sectioning (a) healthy cornea (b) injured cornea on day 7; Scale bars – 50 µm.

Furthermore, we hypothesize that to validate nsOCT results with the histological sectioning, spatial frequency changes of the structures within the corneal histology images can be analysed. In order to analyse the spatial frequency profiles from the histology images, we analysed thirty profile lines across the histology cross section (from the epithelium to the stroma) in a given region and Fourier transform of these profiles were calculated to obtain the spectrum of spatial period distribution of the structures. From the Fourier spectrum of the profiles, median spatial frequencies/periods (*msf*) of the spectrum was calculated according to Eq. 5.23. The calculated values were then averaged across the thirty profiles to indicate changes within the periodicity of the structures within the cornea pre and post corneal injury. The flow chart showing the processing steps is given in figure 5.13.

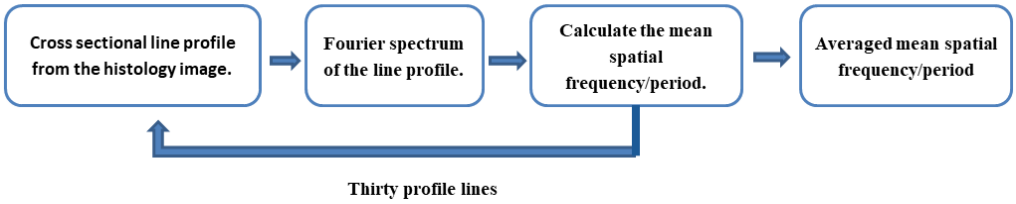

Fig. 5.13 Flow chart showing *msf* calculation of the line profiles from the histological images.

Figures 5.14 (a) and (b) shows representative spectrum of the line profiles along with the median spatial period values for healthy cornea and injured cornea respectively. From figure 5.14 (a) and 5.14 (b), it can be observed that the median spatial period tends to move towards the right end of the spectrum for the injured cornea indicating an increase in the spatial period

of the structures within cornea post injury. This observation validates our results obtained using nsOCT technique. For statistical comparison between the median spatial period values of the pre and post injury corneal histology sections, ten sections from each group were analysed. Unpaired t test results (sample – 10 per group) show statistical significance between the two groups with $p < 0.05$. Box plot showing the distribution of mean spatial periods of healthy cornea and cornea on day 7 post injury calculated from the histology line profile is shown in figure 5.14 (c).

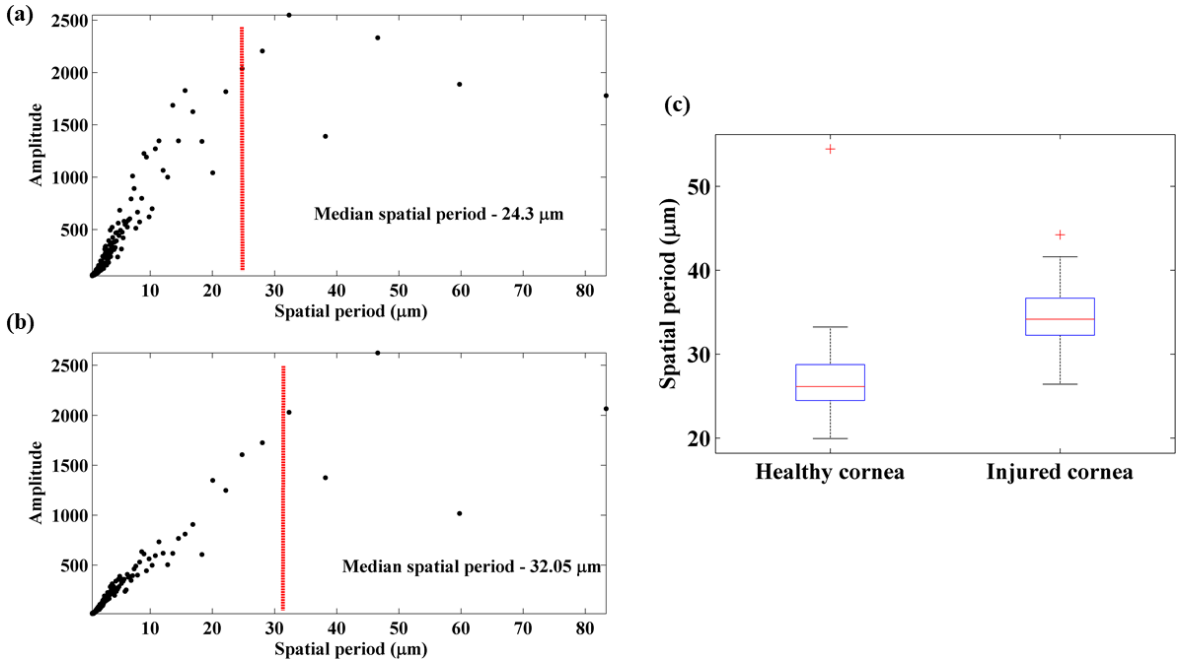

Fig. 5.14 Spatial period profiles obtained by Fourier transform of histology line profiles (a) healthy cornea (b) injured cornea (c) Box plot showing the spatial period distribution of healthy and injured cornea.

From figure 5.14 (c), it can be observed that post injury, the spatial period of the sub-micron structures within the cornea has increased compared to that of a healthy cornea. For the healthy cornea, the mean spatial period distribution is 29.3 ± 6.8 µm and for the injured cornea on day 7, it is 34.6 ± 5 µm. So, the results of the Fourier analysis of the histology images confirmed results obtained using nsOCT approach.

5.4.4 Summary

In this section, we have elucidated the capability of nsOCT technique to detect structural changes within the cornea to assess the impact of alkali injury and also to study the wound healing process. nsOCT offers much higher sensitivity to structural changes within the cornea compared to conventional OCT processing. The study reveals that nsOCT is able to detect

structural changes with nano scale sensitivity between healthy cornea, injured cornea and also during the reparative phase of the injury at all depths within the cornea with high statistical significance ($p < 10^{-7}$). Further studies are required to assess the suitability of the method described to measure the corneal transparency based on the sensitivity of nsOCT to the structural integrity of collagen network within the stroma.

5.5 nsOCT to probe dynamic changes within cornea

In this section, nsOCT approach to detect the dynamic changes within the cornea is described. In mammals, various physiological processes, such as energy metabolisms, cardiovascular functions and circadian rhythms exhibit fluctuations in response to change in the local and external environment. These rhythmic oscillations within the body have been observed within the neurons [32,33], microvasculature [34–36], muscles [37], heart [38,39] and within the medulla part of the kidney [40] and play a vital role in modulating the biological processes and associated response by an organism. One of the two commonly researched sites for rhythmic oscillations include the brain and the skin. LDF studies have shown that the skin microcirculatory changes are controlled by a combination of complex central and local mechanisms and are regulated by low frequency oscillations ranging from 0 to 5 Hz in mammals [41–43].

Since 1990's, wavelet analysis has been used extensively in biomedical signal processing. Unlike the Fourier transform which transforms the time series into the frequency domain without retaining time information, the Short-time Fourier transform (STFT) and Wavelet transform (WT) simultaneously retain time and frequency information [44]. STFT analysis can provide the time-frequency content within a signal, but with a constant frequency and time resolution due to the fixed window length used for the analysis, whereas continuous wavelet transform (CWT) retrieves the time-frequency content information within the signal with an improved resolution due to the multiresolution property of the wavelets [45,46] . CWT is a scale-independent method and has been used to analyse the time–frequency characteristics of wide band, non -stationary signals. CWT has been used to analyse the scale-dependent structure of a signal as it varies in time [47]. The CWT uses a mother wavelet and by scaling and translating the mother wavelet along the length of the signal, the wavelet transform performs the time scale decomposition, thus providing time localisation and multiresolution capability. The CWT of a signal *f (t)* is defined as

$$F(\tau, s) = \frac{1}{\sqrt{|s|}} \int_{-\infty}^{\infty} f(t)\ \ \phi^* \left(\frac{t-\tau}{s}\right)\ dt \tag{5.24}$$

where s is the scaling and τ is the translational parameter of the mother wavelet φ [48]. Numerous studies have used CWT analysis to study the frequency oscillations within biological signals obtained from EEG, EMG, ECG and LDF. Most of these studies have used complex Morlet wavelet as the mother wavelet for CWT. Complex Morlet wavelet is a wavelet composed of a Gaussian exponential (cosine wave) multiplied by a Gaussian window which was introduce by Jean Morlet that provides best trade-off between time and spatial frequency resolution. The Gaussian function guarantees a minimum time-bandwidth product and has been used as a mother wavelet for signals that require high-frequency resolution at low frequencies such as EEG, EMG, ECG and blood flow oscillations. Complex Morlet in time domain is defined as

$$\phi(t) = \frac{1}{\sqrt{\pi f_b}} e^{i2\pi f_c t} e^{\frac{-t^2}{f_b}} \tag{5.25}$$

where f_b is the bandwidth parameter, f_c is the wavelet centre frequency and *φ(t)* represents the wavelet coefficients at time *t*.

Hence, based on the literature review, nsOCT processed corneal spatial period profiles were analysed in time using complex Morlet wavelet to explore the corneal dynamics before and after superficial corneal injury. In the next sections, the signal acquisition and processing steps carried out for the study are described in detail.

5.5.1 Materials and methods

The experimental procedures are as described in section 5.4. Multiple B-frames (MB mode) were acquired over time at a single y-scan location before and after introducing the alkali injury. In total, 1000 B frames were acquired from a single transverse position covering a distance of 5 mm in the lateral direction. The total scan time for the image acquisition was 17 s, thus the sampling frequency was set at 58.5 Hz.

For the acquired M-B frames, the raw interferograms were processed using nsOCT approach as described in section 5.3. To construct the nsOCT B frame, the raw spectral interferograms were divided into 10 windows, and the median spatial period of the spatial period profile were mapped using equation 5.23. Thus, 1000 nsOCT B frames were generated covering a time span of 17 s. From the processed nsOCT B frames, a region of 10 x 10 pixels is chosen close to the apex of the cornea as indicated in figure 5.15, and the mean spatial period

within the 10 by 10 kernel is calculated. Thus, we obtain 1000 points (from 1000 frames) corresponding to the average median spatial period of the chosen region.

Figures 5.15 (a) and (b) shows representative images of processed nsOCT B frame before and after the injury and figures (c) and (d) shows the corresponding averaged median spatial period over time. From figures 5.15(c) and (d), one can readily observe the presence of a rhythmic oscillatory pattern embedded within the time varying median spatial period plot. Fourier analysis of the time varying spatial period reveals the presence of low frequency signals as can be seen in figure 5.16. For the present study, control data sets were acquired from 4 healthy rats and injured data sets were acquired from 5 injured rats.

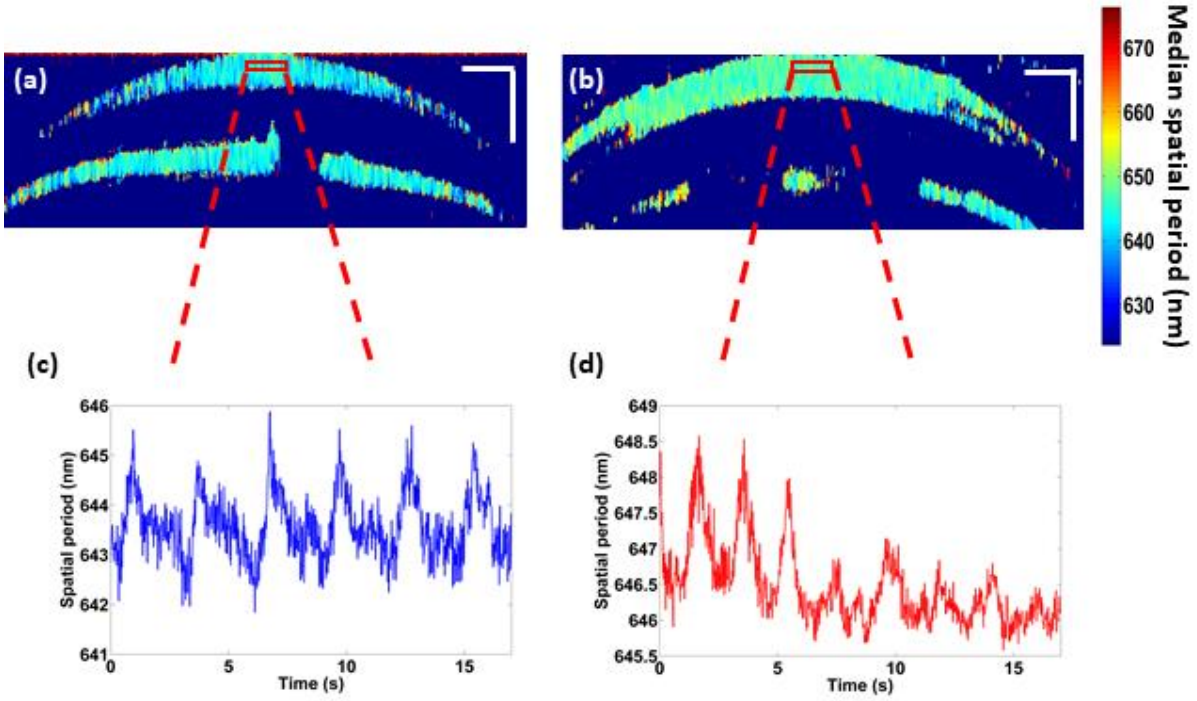

Fig. 5.15 Median spatial period profiles (a) healthy cornea (b) injured cornea (c) time varying spatial period plot of healthy cornea (d) time varying spatial period plot of injured cornea; Scale bars -500 µm.

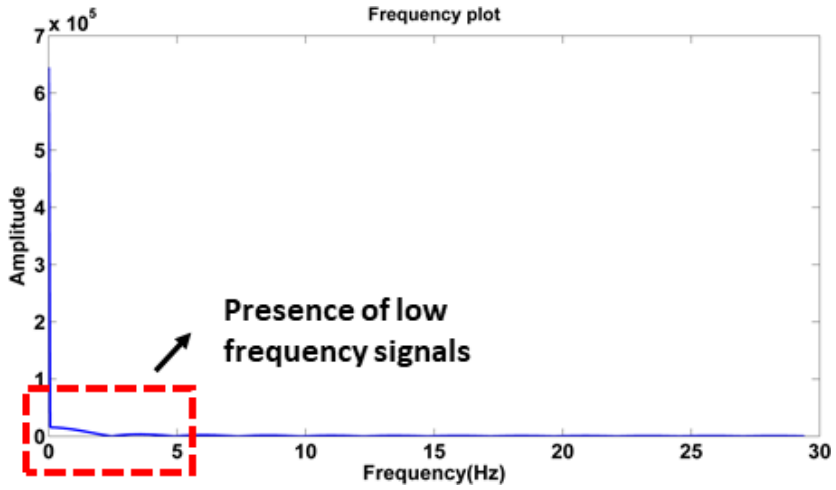

Fig. 5.16. Frequency spectrum of the time varying median spatial signal shown in figure 5.15 (c).

As discussed in section 5.10, since wavelet analysis provide better frequency resolution compared to Fourier transform, the time varying averaged median spatial period signals were processed using CWT approach.

5.5.2 Signal processing

Prior to the CWT analysis, the averaged median spatial period profiles were mean subtracted. For a signal sampled with sampling period Δ, the scale *s* of the Morlet wavelet is related to the frequency *f (Hz)* as given in Eq. 5.26

$$f = \frac{f_c}{\Delta s} \tag{5.26}$$

In this study, complex Morlet with centre frequency (f_c) of 1 Hz and bandwidth (f_b) of 2 was used. In order to analyse the time varying spatial period signals sampled at 58.5 Hz and for a frequency range of 0.02 Hz to 10 Hz using Morlet wavelet with f_c 1 Hz, scale *s* was varied from 6 to 61920 as per Eq. 5.26. All the signal processing was carried out using MATLAB Signal Processing Toolbox.

From the obtained wavelet scalograms, average energy density in each frequency band was analysed. Average energy density in each band $(\varepsilon(f_1,f_2))$ is given by Eq.5.27.

$$\left(\varepsilon(f_1,f_2)\right) = \frac{1}{t}\int_0^t \int_{s_1}^{s_2} \frac{1}{s^2}|g(s,t)|^2 dsdt \tag{5.27}$$

where f_1, f_2 are the lower and upper limit of the frequency band of interest, s_1, s_2 are the scales corresponding to $f_1 \& f_2$ and $g(s,t)$ is the continuous wavelet transform of the analysed signal at scale *s* and time *t*.

Also, to reduce the inter individual variability among the samples, the relative energy contribution of each band was calculated as given by Eq.5.28 and was used to evaluate the functional response of the cornea to the alkali stimuli.

$$e(f_1, f_2) = \frac{\varepsilon_i(f_i, f_2)}{\varepsilon_i(\text{Total})} \quad (5.28)$$

5.5.3 Results and discussion

The wavelet analysis of time varying averaged median spatial period profiles revealed five characteristic frequency bands within the frequency range 0 to 5 Hz. These 5 frequency bands are:

(1) Endothelial band (0.02 - 0.085 Hz)
(2) Neurogenic band (0.085 - 0.25 Hz)
(3) Myogenic band (0.25 – 0.6 Hz)
(4) Respiratory band (0.6 – 1.5 Hz)
(5) Cardiac band (1.5 -5 Hz)

In a rodent model, these oscillations within the LDF signal reflect the cardiogenic activity (1.5-5Hz) representing the heart beat dynamics; respiratory (0.6-1.5 Hz) the rhythmicity of breath; myogenic activity (0.25-0.6 Hz) the rhythmic activity of vessels; neurogenic activity (0.085-0.25 Hz) and endothelial activity (0.02-0.085 Hz) corresponding to the metabolic activity [42,43,49,50] that regulate the vasomotion within the capillaries.
Representative plots showing the 5 characteristic frequency bands of a healthy cornea and the injured cornea obtained from the same sample is shown in figure 5.17(a) and (b) respectively. Comparing figures 5.17(a) and (b), we can clearly observe an increase in amplitude of the signal within the endothelial (0.02-0.085 Hz) and neurogenic (0.085 – 0.25 Hz) frequency bands following the alkali injury.

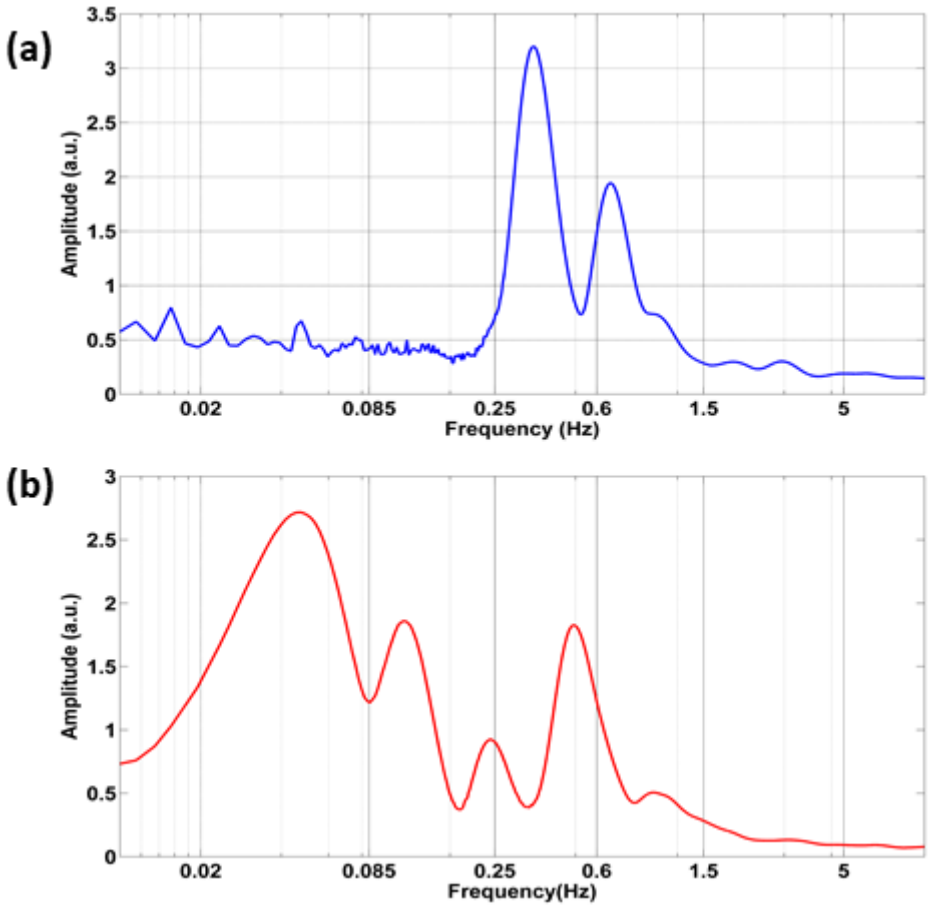

Fig. 5.17 Plots showing time averaged wavelet transform (a) healthy cornea (b) Injured cornea.

Given below in Table 5.1, is the normalised relative power in various frequency bands of the healthy and injured corneal models tabulated using Eq. 5.28. As can be seen in Table 5.1, the changes occurring in the endothelial band and neurogenic band may provide insights into the underlying physiological processes occurring within the cornea at the onset of an alkali burn. It is found that the normalised power in the endothelial and neurogenic is increased in an injured cornea compared to healthy cornea. However, a decrease in the relative energy within the respiratory band was observed in the injured rat cornea compared to the healthy cornea. Figure 5.18 shows the relative energy distribution within each of the five bands for healthy cornea and injured cornea.

Frequency band	*Healthy cornea*	*Injured cornea*
Metabolic	0.044 ± .01	0.16 ± .01
Neurogenic	0.04 ± .01	0.11 ± .03
Myogenic	0.34 ± .1	0.34 ± .02
Respiratory	0.38 ± .08	0.20 ± .02
Cardiac	0.19 ± .03	0.19 ± .04

Table 5.1. The average relative energy in different frequency bands for healthy and injured cornea (mean ± standard error)

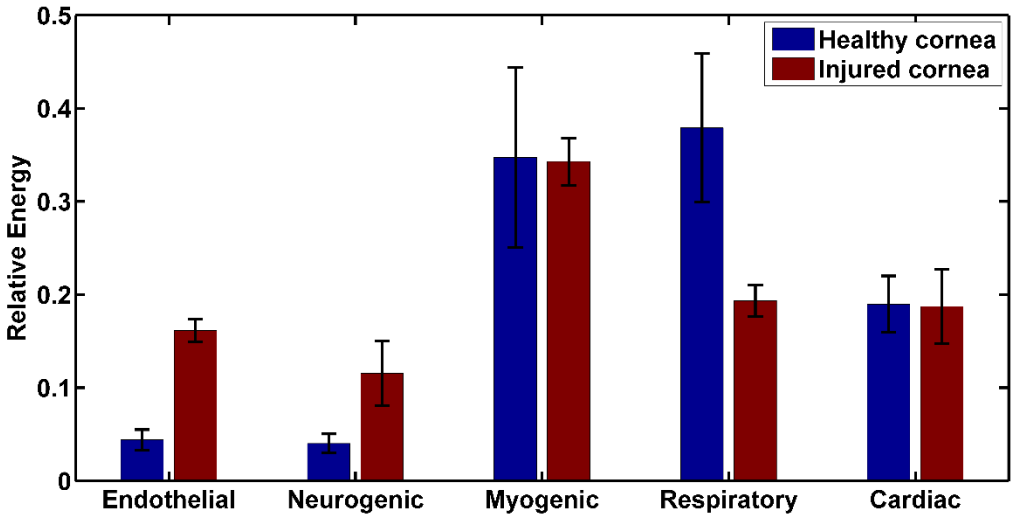

Fig.5.18 Bar graph showing relative energy distribution in various bands in for healthy and injured cornea (mean ± standard error)

Unpaired t test revealed significant differences within the endothelial band between the healthy group and the injured group ($p < 10^{-3}$). However, statistically significant differences were not observed within the neurogenic, myogenic, respiratory and cardiac bands between the two groups.

The increase in relative energy contribution within the endothelial band after alkali burn might be due the presence of endothelial pump within the cornea [51]. Apart from providing the transport of nutrients from the aqueous to the corneal epithelium, corneal endothelium also helps in maintaining the hydration within the stroma through active transport mechanisms. It

is well known that there exist a “Pump-Leak” mechanism within the corneal endothelium that is responsible for the maintenance of corneal hydration and transparency [51]. As described in sections 5.6, the maintenance of corneal transparency is vital for optimum vision, and this is ensured by the avascular cornea, evenly spaced collagen fibrils of uniform diameter within the stroma, and also the level of hydration within the stromal layer. It has been shown that, when the hydration of the stroma is ~3.5 mg H_2O/mg dry tissue or less, the stroma is relatively transparent [51,52]. Past research has shown that, bare stroma is susceptible to swelling due to the presence of negatively charged stromal glycosaminoglycan (GAG) and the stromal pressure increases to 60 mmHg [51]. In order to overcome this increase in stromal pressure, the endothelial pump rate must be equal to the GAG driven leak. Hence, this inherent endothelial pump is so vital that, any change in the endothelial ion transport mechanisms can lead to non-uniform spacing between the collagen fibres, corneal oedema, increased light scattering further leading to loss of corneal transparency. When a superficial alkali burn is induced by applying NaOH solution, the electrochemical ionic balance is disrupted, leading to enhanced active ion transport by the endothelial pump mechanisms, which may have led to the observed increase in relative energy contribution within the endothelial band following alkali injury. From figure 5.17 (a) and (b), it can be observed that the signal amplitude within the endothelial band is increased after the alkali stimulus compared to the healthy cornea. This suggests the presence of active ion transport mechanisms that have characteristic oscillations within the frequency band 0.02 to 0.085 Hz. Recently, a pulsatile fluid transport model has been proposed for fluid transport across corneal endothelium [52] which further establishes the possibility of rhythmic oscillations that responds to an osmotic challenge and regulate the fluid volume across the anterior segment of the eye. The endothelial frequency band observed within the cornea is found to have similarities to that observed from the LDF perfusion studies. In LDF studies, this characteristic frequency band is regulated by the vascular endothelial smooth muscle cells that line the inner capillary walls and is responsible for ensuring tissue perfusion. Endothelial cells that line the inner surface of the blood vessels regulate the vasomotor tone by production of vasoactive substances that either constricts or dilates the vessels based on a combination of complex central and local mechanisms. Hence, the signals detected within the frequency band 0.02-0.085 Hz using the nsOCT approach may correspond to changes in the endothelial cell activity within cornea following alkali injury.

Also, from figures 5.17 and 5.18, one can observe that, there is an increase in relative energy content within the neurogenic band following alkali induced injury, although not

statistically significant ($p = 0.14$). Cornea is the most richly innervated organ within the body. It is estimated that the cornea contains 300–600 times more sensory endings than the skin and 20–40 times more than the tooth pulp [53]. This abundance in nociceptive terminals, together with the absence of blood vessels and the structural simplicity of the supporting tissues, has made the cornea a good model for analysing the morphological and functional properties of peripheral nociceptors. Studies based on LDF technique have shown that the frequency band between 0.085 – 0.25 Hz is related to neurogenic activity [42,50] that regulates vasomotion. Recent studies based on heart rate variability signals have related this frequency band to nociception in humans [54,55]. Time-frequency decomposition of EEG signals in neonates have revealed nociception frequency to be within the frequency band 2 - 4 Hz [56]. Though there are differences within the exact frequencies corresponding to nociception, past research studies indicate nociceptive frequencies to be within 0-5 Hz. Mechanical stimulus such as alkali injury can innervate the nociceptors, and the increased energy content observed within the neurogenic band following the injury may be due to nociceptor activation. Due to the small sample population used in this study, statistically significant conclusions could not be obtained. However, this study opens up further research avenues pertaining to the assessment of corneal nociception using OCT which has not been attempted before. Such studies present great potential in pain management / drug research that can elucidate the associated neurochemical mechanisms of action

Further studies are required to explore whether time frequency decomposition of nsOCT signals can provide insights into nociception frequencies.

5.6 Conclusions

In this chapter, nsOCT approach for OCT was described and nsOCT technique was used to probe the structural and dynamic changes within cornea during alkali induced injury which otherwise cannot be obtained from conventional OCT processing. The technique described bridges the gap between high resolution imaging and increased depth of imaging in OCT by enhancing the sensitivity of OCT to nano scale structural changes within the sample. The chapter described the capability of nsOCT to detect structural changes with nano scale sensitivity between healthy cornea, injured cornea and also during the reparative phase of the injury at all depths within the cornea with high statistical significance ($p < 10^{-7}$). The technique presented can be used to study the effects of pharmaceutical drugs on diseased tissues, or to study the morphological changes in biomedical samples, for example, to image

progression of cancerous cells and tumours as they are known to undergo nano scale structural changes within its vicinity long before the manifestation of the disease.

The chapter also reported the description of corneal dynamics from the processed nsOCT images. Analysis of time varying spatial period signals within the cornea has revealed five frequency bands corresponding to endothelial (0.-2 – 0.085 Hz), neurogenic (0.085 – 0.25 Hz), myogenic (0.25 -0.5 Hz), respiratory (0.5 – 1.5 Hz) and cardiac band (1.5 -5 Hz). Further, changes in energy content within the endothelial and neurogenic bands were observed between the healthy cornea and injured cornea that suggest the potential of the described technique for functional assessment. Analysis of these dynamic changes within the cornea can be used as a tool to study the effects of noxious stimuli on the corneal surface and its effects on the physiological signalling within the organism.

The methods presented in this chapter offer great potential for *in vivo* imaging applications especially in clinical imaging where sensitivity to changes in structure is of significance either to detect the onset of a disease or to evaluate the efficacy of treatment and for functional assessment which cannot be obtained from conventional OCT images.

REFERENCES

1. J. F. de Boer, R. Leitgeb, and M. Wojtkowski, "Twenty-five years of optical coherence tomography: the paradigm shift in sensitivity and speed provided by Fourier domain OCT [Invited]," Biomed. Opt. Express **8**, 3248–3280 (2017).
2. W. Drexler, U. Morgner, R. K. Ghanta, F. X. Kärtner, J. S. Schuman, and J. G. Fujimoto, "Ultrahigh-resolution ophthalmic optical coherence tomography," Nat. Med. **7**, 502–507 (2001).
3. R. M. Werkmeister, S. Sapeta, D. Schmidl, G. Garhöfer, G. Schmidinger, V. A. dos Santos, G. C. Aschinger, I. Baumgartner, N. Pircher, F. Schwarzhans, A. Pantalon, H. Dua, and L. Schmetterer, "Ultrahigh-resolution OCT imaging of the human cornea," Biomed. Opt. Express **8**, 1221–1239 (2017).
4. A. D. Aguirre, N. Nishizawa, J. G. Fujimoto, W. Seitz, M. Lederer, and D. Kopf, "Continuum generation in a novel photonic crystal fiber for ultrahigh resolution optical coherence tomography at 800 nm and 1300 nm," Opt. Express **14**, 1145–1160 (2006).
5. C. Lal and M. J. Leahy, "An Updated Review of Methods and Advancements in Microvascular Blood Flow Imaging," Microcirculation **23**, 345–363 (2016).
6. R. K. Wang and A. L. Nuttall, "Phase-sensitive optical coherence tomography imaging of the tissue motion within the organ of Corti at a subnanometer scale: a preliminary study," J. Biomed. Opt. **15**, (2010).
7. T. Akkin, D. Landowne, and A. Sivaprakasam, "Detection of Neural Action Potentials Using Optical Coherence Tomography: Intensity and Phase Measurements with and without Dyes," Front. Neuroenergetics **2**, (2010).
8. Y.-J. Yeh, A. J. Black, D. Landowne, and T. Akkin, "Optical coherence tomography for cross-sectional imaging of neural activity," Neurophotonics **2**, (2015).
9. J. Yi, A. J. Radosevich, J. D. Rogers, S. C. P. Norris, İ. R. Çapoğlu, A. Taflove, and V. Backman, "Can OCT be sensitive to nanoscale structural alterations in biological tissue?," Opt. Express **21**, 9043–9059 (2013).
10. G. L. C. Spicer, S. M. Azarin, J. Yi, S. T. Young, R. Ellis, G. M. Bauer, L. D. Shea, and V. Backman, "Detection of Extracellular Matrix Modification in Cancer Models with Inverse Spectroscopic Optical Coherence Tomography," Phys. Med. Biol. **61**, 6892–6904 (2016).
11. J. Yi, A. J. Radosevich, Y. Stypula-Cyrus, N. N. Mutyal, S. M. Azarin, E. Horcher, M. J. Goldberg, L. K. Bianchi, S. Bajaj, H. K. Roy, and V. Backman, "Spatially resolved

optical and ultrastructural properties of colorectal and pancreatic field carcinogenesis observed by inverse spectroscopic optical coherence tomography," J. Biomed. Opt. **19**, 36013 (2014).

12. S. A. Alexandrov, H. M. Subhash, A. Zam, and M. Leahy, "Nano-sensitive optical coherence tomography," Nanoscale **6**, 3545–3549 (2014).
13. "Novel approach for label free super-resolution imaging in far field | Scientific Reports," https://www.nature.com/articles/srep13274.
14. S. Uttam, S. A. Alexandrov, R. K. Bista, and Y. Liu, "Tomographic imaging via spectral encoding of spatial frequency," Opt. Express **21**, 7488–7504 (2013).
15. S. Alexandrov, J. McGrath, C. J. R. Sheppard, F. Boccafoschi, C. Giannini, T. Sibillano, H. Subhash, J. Hogan, and M. Leahy, "Label-free ultra-sensitive visualization of structure below the diffraction resolution limit," J. Biophotonics **11**, e201700385 (2018).
16. "Spectral encoding of spatial frequency approach for characterization of nanoscale structures: Applied Physics Letters: Vol 101, No 3," https://aip.scitation.org/doi/10.1063/1.4737209.
17. S. Alexandrov, H. Subhash, and M. Leahy, "Nanosensitive optical coherence tomography for the study of changes in static and dynamic structures," Quantum Electron. **44**, 657 (2014).
18. R. Dsouza, J. Won, G. L. Monroy, M. C. Hill, R. G. Porter, M. A. Novak, and S. A. Boppart, "In vivo detection of nanometer-scale structural changes of the human tympanic membrane in otitis media," Sci. Rep. **8**, (2018).
19. S. A. Alexandrov, S. Uttam, R. K. Bista, K. Staton, and Y. Liu, "Spectral encoding of spatial frequency approach for characterization of nanoscale structures," Appl. Phys. Lett. **101**, 033702 (2012).
20. M. Born and E. Wolf, *Principles of Optics: Electromagnetic Theory of Propagation, Interference and Diffraction of Light* (Elsevier, 2013).
21. "A new classification of ocular surface burns | British Journal of Ophthalmology," https://bjo.bmj.com/content/85/11/1379.
22. "Management of ocular surface chemical burns | British Journal of Ophthalmology," https://bjo.bmj.com/content/95/2/159.
23. "Chemical (Alkali and Acid) Injury of the Conjunctiva and Cornea - EyeWiki," http://eyewiki.aao.org/Chemical_(Alkali_and_Acid)_Injury_of_the_Conjunctiva_and_Cornea.

24. "Confocal Microscopy and Anterior Segment Optical Coherence Tomography Findings After Chemical Alkali Corneal Burn. - PubMed - NCBI," https://www.ncbi.nlm.nih.gov/pubmed/27467040.
25. "SEEOS - Evaluation of corneal changes in chemical burns with anterior segment optical coherence tomography," http://www.seeos.eu/index.php/2015/12/15/evaluation-of-corneal-changes-in-chemical-burns-with-anterior-segment-optical-coherence-tomography/.
26. "Dynamic analysis of chemical eye burns using high-resolution optical coherence tomography. - PubMed - NCBI," https://www.ncbi.nlm.nih.gov/pubmed/17867792.
27. "Anterior segment optical coherence tomography in eye injuries. - PubMed - NCBI," https://www.ncbi.nlm.nih.gov/pubmed/18766361.
28. "Treating Acute Chemical Injuries of the Cornea," https://www.aao.org/eyenet/article/treating-acute-chemical-injuries-of-cornea.
29. M. Eslani, A. Baradaran-Rafii, A. Movahedan, and A. R. Djalilian, "The Ocular Surface Chemical Burns," J. Ophthalmol. **2014**, (2014).
30. K. M. Meek and C. Knupp, "Corneal structure and transparency," Prog. Retin. Eye Res. **49**, 1–16 (2015).
31. A. V. Ljubimov and M. Saghizadeh, "Progress in corneal wound healing," Prog. Retin. Eye Res. **49**, 17–45 (2015).
32. G. Buzsáki and B. O. Watson, "Brain rhythms and neural syntax: implications for efficient coding of cognitive content and neuropsychiatric disease.," Dialogues Clin. Neurosci. **14**, 345–367 (2012).
33. C. E. Schroeder and P. Lakatos, "Low-frequency neuronal oscillations as instruments of sensory selection," Trends Neurosci. **32**, (2009).
34. A. Stefanovska, M. Bracic, and H. D. Kvernmo, "Wavelet analysis of oscillations in the peripheral blood circulation measured by laser Doppler technique," IEEE Trans. Biomed. Eng. **46**, 1230–1239 (1999).
35. P. Kvandal, S. A. Landsverk, A. Bernjak, A. Stefanovska, H. D. Kvernmo, and K. A. Kirkebøen, "Low-frequency oscillations of the laser Doppler perfusion signal in human skin," Microvasc. Res. **72**, 120–127 (2006).
36. J. L. Cracowski, C. T. Minson, M. Salvat-Melis, and J. R. Halliwill, "Methodological issues in the assessment of skin microvascular endothelial function in humans," Trends Pharmacol. Sci. **27**, 503–508 (2006).

37. M. B. I. Raez, M. S. Hussain, and F. Mohd-Yasin, "Techniques of EMG signal analysis: detection, processing, classification and applications," Biol. Proced. Online **8**, 11–35 (2006).
38. B. Ergen, Y. Tatar, and H. O. Gulcur, "Time-frequency analysis of phonocardiogram signals using wavelet transform: a comparative study," Comput. Methods Biomech. Biomed. Engin. **15**, 371–381 (2012).
39. T. Tsutsumi, Y. Okamoto, N. Kubota-Takano, D. Wakatsuki, H. Suzuki, K. Sezaki, K. Iwasawa, and T. Nakajima, "Time–frequency analysis of the QRS complex in patients with ischemic cardiomyopathy and myocardial infarction," IJC Heart Vessels **4**, 177–187 (2014).
40. M. Hara, Y. Minami, M. Ohashi, Y. Tsuchiya, T. Kusaba, K. Tamagaki, N. Koike, Y. Umemura, H. Inokawa, and K. Yagita, "Robust circadian clock oscillation and osmotic rhythms in inner medulla reflecting cortico-medullary osmotic gradient rhythm in rodent kidney," Sci. Rep. **7**, 7306 (2017).
41. D. G. Buerk and C. E. Riva, "Vasomotion and Spontaneous Low-Frequency Oscillations in Blood Flow and Nitric Oxide in Cat Optic Nerve Head," Microvasc. Res. **55**, 103–112 (1998).
42. A. Humeau, A. Koïtka, P. Abraham, J.-L. Saumet, and J.-P. L\textquotesingleHuillier, "Time–frequency analysis of laser Doppler flowmetry signals recorded in response to a progressive pressure applied locally on anaesthetized healthy rats," Phys. Med. Biol. **49**, 843–857 (2004).
43. R. Zegarra-Parodi, E. J. Snider, P. Y. S. Park, and B. F. Degenhardt, "Laser Doppler Flowmetry in Manual Medicine Research," J. Am. Osteopath. Assoc. **114**, 908–909 (2014).
44. A. W. Galli, G. T. Heydt, and P. F. Ribeiro, "Exploring the power of wavelet analysis," IEEE Comput. Appl. Power **9**, 37–41 (1996).
45. L. A. Barford, R. S. Fazzio, and D. R. Smith, *An Introduction to Wavelets* (Citeseer, 1992).
46. C. Liner, "An overview of wavelet transform concepts and applications," Univ. Houst. 1–17 (2010).
47. O. Rioul and M. Vetterli, "Wavelets and signal processing," IEEE Signal Process. Mag. **8**, 14–38 (1991).
48. I. De Moortel, S. A. Munday, and A. W. Hood, "Wavelet Analysis: the effect of varying basic wavelet parameters," Sol. Phys. **222**, 203–228 (2004).

49. F. Bajrovic, M. Čenčur, M. Hožič, S. Ribarič, and A. Stefanovska, "The contribution of lumbar sympathetic neurones activity to rat's skin blood flow oscillations," Pflüg. Arch. - Eur. J. Physiol. **439**, R158–R160 (2000).
50. Z. Li, E. W. C. Tam, M. P. C. Kwan, A. F. T. Mak, S. C. L. Lo, and M. C. P. Leung, "Effects of prolonged surface pressure on the skin blood flowmotions in anaesthetized rats--an assessment by spectral analysis of laser Doppler flowmetry signals," Phys. Med. Biol. **51**, 2681–2694 (2006).
51. J. A. Bonanno, ""Molecular Mechanisms Underlying the Corneal Endothelial Pump,"" Exp. Eye Res. **95**, 2–7 (2012).
52. J. Fischbarg, "Mechanism of fluid transport across corneal endothelium and other epithelial layers: a possible explanation based on cyclic cell volume regulatory changes," Br. J. Ophthalmol. **81**, 85–89 (1997).
53. B. Carlos and G. Juana, *Corneal Nociceptors* (Oxford University Press, 1996).
54. F. Weber, N. J. E. Geerts, H. G. Roeleveld, A. T. Warmenhoven, and C. A. Liebrand, "The predictive value of the heart rate variability-derived Analgesia Nociception Index in children anaesthetized with sevoflurane: An observational pilot study," Eur. J. Pain **22**, 1597–1605 (2018).
55. "Analgesia nociception index: evaluation as a new parameter for acute postoperative pain - British Journal of Anaesthesia," https://bjanaesthesia.org/article/S0007-0912(17)32357-7/fulltext.
56. L. Fabrizi, M. Verriotis, G. Williams, A. Lee, J. Meek, S. Olhede, and M. Fitzgerald, "Encoding of mechanical nociception differs in the adult and infant brain," Sci. Rep. **6**, 28642 (2016).

Chapter 6

PLASMONIC GOLD NANOSTARS AS A CONTRAST AGENT FOR NIR PHOTOTHERMAL OCT

6.1 Introduction

As described in the previous chapters, OCT can be used for tissue imaging up to a depth of 2-3 mm, intense optical scattering from biological tissues have limited its penetration depth to 1-1.5 mm within biological tissue. To better visualize the internal biological structures, exogenous contrasts agents have been used for OCT imaging applications in the recent past. These exogenous contrast agents enable enhanced visualization of features such as microvasculature, diseased or abnormal tissue based on selective absorption of an external contrast agent by the tissue. The use of exogenous contrast agents would also allow targeted imaging of specific cells and receptors that also enables OCT for targeted molecular imaging applications. In the recent past, OCT contrast enhancement has been demonstrated using scattering microspheres, iron oxide micro particles, and nanoparticles [1–4]. In the past, GNP's have been widely used for OCT imaging primarily due to its customizable absorption and scattering properties, biocompatibility, and ease of bioconjugation. These characteristics make gold nanoparticles as ideal exogenous contrast agents for OCT imaging acting as targeting probes, image contrast enhancers, and therapeutic agents. Different varieties of GNP's such as nanorods, nanocages, nano shells and nanorose have been used as contrast enhancers in conjunction with OCT [2,5–13].

PT-OCT is an active contrast based detection technique that utilises the photothermal efficiency (light to heat conversion) of GNP. Localised heat generation by GNPs leads to thermoelastic expansion of the sample which causes variations in the local refractive index within the sample. These shifts in refractive index can be optically imaged with the phase information obtained from the OCT interferogram [1,2,14]. PT-OCT provides high specificity

and sensitivity in identifying photon absorbing targets from the scattering background based on the photothermal heating phenomenon. Also, within the NIR optical window, where tissue scattering and absorption is low, PT-OCT can detect signals at greater depth.

In this chapter, we describe the development of a PT-OCT system to image gold nanostars (GNS) having an absorption peak at 1064 nm. The near infrared absorption peak of GNS makes it an ideal external contrast agent for deep tissue imaging. We report an imaging depth of 2.25 mm using the novel GNS in agar phantom models. Also, we report that Si- coating of GNS enhances the photothermal signal for PT-OCT imaging applications. We show that silica coated nanostars are more photothermally stable and efficient in conducting heat compared to uncoated nanostars.

6.2 PT-OCT theory and related literature

As described in the introduction, PT-OCT is a functional extension of OCT based on an exogenous contrast agent. The ability of plasmonic gold nanostructures to act as contrast agents for PT-OCT is based on the non-radiative relaxation of the plasmons, which results in light to heat conversion thereby causing the photothermal response. PT-OCT is based on the photothermal heating phenomenon, wherein absorption of photon by a nanoparticle leads to increase in temperature surrounding the absorber. These local temperature changes cause thermoelastic expansion within the sample which further leads to changes in the local index of refraction [1]. These photothermal-induced shifts in the local index of refraction alter the local optical path length (OPL), and by detecting these induced OPL changes, nanoparticles can be imaged.

To induce these localised temperature gradients within the sample containing GNP's, an excitation laser operating at the absorption wavelength of the GNP is used [1-3]. To increase the sensitivity of OCT to absorbing targets within the sample, the excitation laser beam is modulated at any particular stimulating frequency. By modulating the laser at a known frequency and by mapping the changes in OPL occurring only at that particular frequency, the nanoparticles can be detected. In PT-OCT imaging, a single transverse location is temporally scanned (M mode imaging) hundreds of times and photothermal signals are identified at each depth from the phase of acquired OCT interferogram using a post-acquisition frequency analysis. To perform a B mode imaging, the galvo is scanned in the lateral direction over the sample and M mode signals are acquired at each lateral position. For each M mode scan of an

A-line, the adjacent phase difference between the M-scans are calculated according to Eq. (6.1) [2]

$$\Delta\phi\,(z,t) = \arctan(Im[\,I(z,t_j)I^*\,(z,t_{j-1})]/Re[I(z,t_j)I^*\,(z,t_{j-1})]\,) \qquad (6.1)$$

where $I(z, t_j)$ is the signal at depth z and time t of an M-scan. Fourier transform (FT) of these phase differences along the time axis for each depth pixel gives the frequency components present within the data. The magnitude of the FT data within ± 20 Hz of the laser excitation frequency is used to calculate the photothermal signal. The magnitude of the FT at the photothermal excitation frequency is converted to corresponding optical path length (OPL) changes given by Eq. (6.2) [2]:

$$OPL\,(z) = (|FT\,(\Delta\phi(z,t)|_{f_0}\,\lambda)\,/\,(4pi^2\,f_0\,\Delta t) \qquad (6.2)$$

where f_0 is the laser stimulation frequency, λ is the laser excitation wavelength and Δt is the sampling period between the consecutive A -scans. The schematic of the working principle of PT- OCT is shown in figure 6.1.

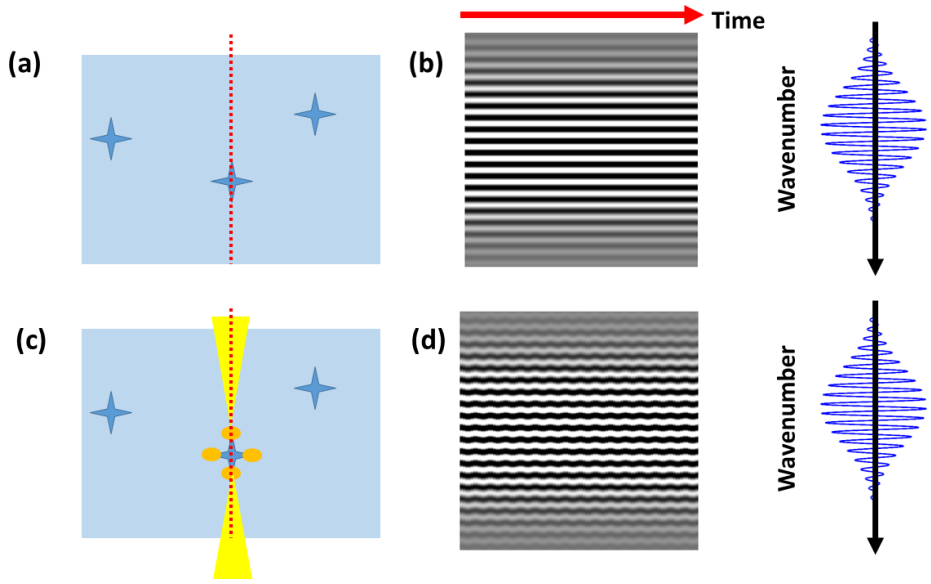

Fig.6.1 Schematic showing the working principle of PT-OCT (a) In conventional OCT, the presence of a contrast agent (stars) within a sample, with a refractive index unequal to the sample will result in (b) a time invariant interference spectra (c) If the contrast agent undergoes temporally modulated photon absorption and thus photothermal heating, (d) the modulations in OPL will cause phase oscillations in the interference pattern.

PT-OCT has been studied in recent years for imaging tissue phantoms and ex- vivo samples. Adler et al. [1] described photothermal detection of gold nanoparticles using phase-sensitive OCT. They reported photothermal detection of gold nano shells in deionised water at a laser excitation wavelength of 808 nm and detection using Fourier domain mode locked swept

source OCT based phase microscope. The paper also evaluated the effect of different pump beam modulation frequencies on the detected signal to noise ratio (SNR) of the photo-thermal signal. They found that increasing the laser modulation frequency increased SNR by shifting the detected peak to a region where *1/f* noise is reduced. However, increasing the modulation frequency reduced the signal peak as the sample volume had less time to heat and cool, resulting in a smaller optical path modulation and lower FT peak amplitude. They concluded that the optimal modulation frequency depends on the optical properties of the sample, nano shell concentration, and the laser power level. In another study by the same group, feasibility of PT-OCT in ex vivo imaging of human breast tissue was demonstrated [15]. In this study, 50 μl of 5×109 ml^{-1} bare gold nano shell (having an absorption peak at 780 nm) solution was injected into a freshly excised human breast tissue sample and photothermal signals were detected 300 – 600 μm deep within the tissue using laser power of 22 mW at 830 nm excitation wavelength. These studies demonstrated the feasibility of PT-OCT imaging in scattering tissues. Gold nanospheres having absorption at 532 nm have also been utilized for PT-OCT imaging in cells [3] and also in 3D tissue constructs [14,16,17]. Kim *et al.* [18] developed a time-domain PT-OCT system for detection of superparamagnetic iron oxide nanoparticles (SPION) in a tissue phantom.

Further, Tucker *et al.* demonstrated gold nanorods (GNR's) as contrast agents for PT-OCT [2]. They demonstrated for the first time *in vivo* imaging of contrast agents with PT-OCT using GNR as contrast agents in the near infrared wavelength region (725 nm –laser, 860 nm imaging beam, with a modulation frequency of 200 Hz) in a rabbit ear. By using GNR as the contrast agent at 725 nm peak absorption wavelength, photothermal signals were obtained from an imaging depth of 1 mm from both, *in vivo* studies in rabbit ear and experiments performed using GNR embedded agar phantom. Recently, full range PT-OCT has also been demonstrated using GNR contrasts embedded in an agarose phantom model [19]. Full range imaging allows for increased imaging depth as well as increased signal to noise ratio of PT-OCT signal by avoiding signal falloff with depth. The group has also demonstrated the use of single-walled carbon nanotubes (CNTs) as multimodal imaging contrasts for use with PT-OCT [20]. In another study, Tucker *et al.* has demonstrated the application of PT-OCT for in vivo 3D imaging of nanoparticle delivery to tumours [21]. In this study, GNRs were used as contrast agents having a plasmon resonance at 740 nm. The laser excitation was modulated at 500 Hz modulation and at an average power of 25 mW on the sample over one modulation period. The study probed into the heterogeneities in nanoparticle uptake by the tumour tissues and also the

assessment of microvascular function to optimize nanoparticle delivery into cancerous cells. PT-OCT has also been demonstrated using nano rose as contrast agent for detection of macrophages in ex- vivo sample [8]. Indocyanine green (ICG) has also been used as a contrast agent for PT-OCT in the excitation wavelength of 808 nm [3].

In a recent study, Kuranov *et al.* [22] introduced a dual-wavelength PT- OCT (DWP-OCT) that uses both the excitation and probe light in the NIR spectral region for depth-resolved blood oxygenation (SaO2) monitoring in tissue phantoms. In this study, two different excitation laser wavelengths (800 nm or 765 nm) are used to induce optical pathlength changes in the sample. Differences in the absorption spectra between oxy and deoxy haemoglobin in two spectral regions is utilized by DWP-OCT to determine SaO2. In another work, they reported proof-of-concept study of *in vivo* depth-resolved measurement of SaO2 levels in selected 30 μm diameter arterioles in the murine brain using DWP-OCT with 800 nm and 770 nm photothermal excitation wavelengths [23,24]. By using two different excitation laser modulation frequencies (770 nm at f_1 = 400 Hz and 800 nm at f_2 = 380 Hz), they were able to separate OPL changes introduced by each of the wavelengths. DWP-OCT has also been used to detect multiple nanoparticle species within the same sample with two excitation wavelengths matched to their distinct absorption peaks [25]. In this work, lasers with excitation wavelengths of 532 nm and 405 nm (excitation power 22 mW and 17 mW respectively) were used to detect nanosphere solution containing gold and silver nanospheres trapped between two coverslips.

Though PT-OCT has tremendous potential in biological imaging, there are certain limitations associated with it. One of the major drawback of PT-OCT imaging in living tissue is optical scattering induced phase noise. Another source of phase noise is from interference speckle. However, as the influence from these sources is mainly at low frequency, by modulating the excitation laser to higher frequencies, these phase noise have been shown to be reduced [1]. However, there is a trade - off between photothermal signal SNR and calculated OPL changes, as at increased modulation frequencies, the response of nanoparticles to heating may be reduced [15]. Another potential limitation of nanoparticle based PT-OCT in tissue, is the bulk heating within the sample. During photothermal excitation, the imaged tissue sample is exposed to bulk heating that raises the temperature of the sample [25]. To minimize the bulk heating of the sample, the authors [25] proposed single pulse excitation technique utilizing a 400 μs pulse. Another factor that limits the imaging speed of PT-OCT system is the requirement of M mode acquisition needed to extract the photothermal signal. In a recent paper, to overcome the bulk data acquisition and post processing time, optical lock in detection technique, has been

applied to PT-OCT imaging of i*n vivo* tissues [26]. Though they were able to achieve ten - fold increase in imaging speed compared to traditional PT-OCT scanning methodology, it also required higher irradiance power.

In conclusion, many studies have reported the use of gold nanorods, nano shells, nanospheres, nanorose and single walled CNT as contrast agents for PT-OCT imaging. However, these studies used laser excitation wavelengths of 800 nm or below [1–3]. Gold nanoparticles that have a localised surface plasmon resonance (LSPR) in the NIR region of the electromagnetic spectrum where both the absorption and scattering would be at their minimum can facilitate deeper imaging and provide better scattering contrast for biological tissue imaging.

6.3 Gold nanoparticle as contrast agent

Nanoparticles are particles with sizes ranging from 0 – 100 nm [27]. Among the different varieties of nanoparticles, a special category of nanoparticles called 'plasmonics' exhibits surface plasmonic effect in response to optical excitation [28]. The term 'plasmonics' refers to the oscillations of conduction electrons within metallic nanostructures when irradiated with light. These oscillations of electrons on the surface of the metallic nanoparticles, produce intense electromagnetic (EM) fields, leading to enormous increase in Raman scattering by 6-8 orders of magnitude. This plasmonic effect of metallic nanoparticles has enabled them to be used as a sensor for the optical detection of molecular and vibrational spectral information in applications ranging from detection of chemical explosives to sensing cancerous biomarkers. In the past decade, gold nanoparticles have gained great research interest owing to their plasmonic properties, versatile surface functionalisation, efficiency in penetrating cells and biocompatibility and have been researched in applications ranging from drug and gene delivery to cancer imaging and photodynamic therapy [27]. It has been shown that variation in shape of the gold nanoparticle leads to modification of the optoelectronic properties of the nanomaterial, making them tuneable across the visible to NIR region of the spectrum. In recent years, various gold nanostructures have been produced, including triangles, stars, cubes, octahedrons, plates, spheres, rods and prisms [28].

6.3.1 Uncoated gold nanostars

Gold nanostars are a type of nanoparticle that consists of a spherical core and multiple branches surrounding it, resembling a 'star' [29]. Compared to other nanoparticles, GNS are able to localize the electron density at the sharp tips of their branches, thus increasing

the effective cross sectional area for photon interaction. Also, multiple branches along with highly curved corners in GNS's increases the electron density within them, creating 'lightening rod' effects that increase the local EM field by many fold compared to that of a symmetrically shaped gold nanospheres or nanorods [30]. This EM field enhancement induces strong light absorption by GNS, leading to localised heating effects. The localized heating produced by GNS has been utilized in heating up of tumour cells in nanoparticle-mediated photothermal therapy studies [31].

In this study, in house developed GNS's were used for PT-OCT imaging. The synthesis protocol used for GNS, preparation is as described in [32]. GNS's were chemically synthesized by reducing gold precursor using ascorbic acid and silver ions as shape directing agent. Briefly, 400 μL of 10 mM of hydrogen tetra-chloroaurate (HAuCl4) and 40 μL of 10 mM silver nitrate (AgNO3) were mixed thoroughly in 20 mL deionised water. Further, 80 μL of 100 mM reducing agent, ascorbic acid, was added to the reaction mixture to produce multibranched GNS. The TEM images and the absorption spectra of synthesized GNS are as shown in figure 6.2.

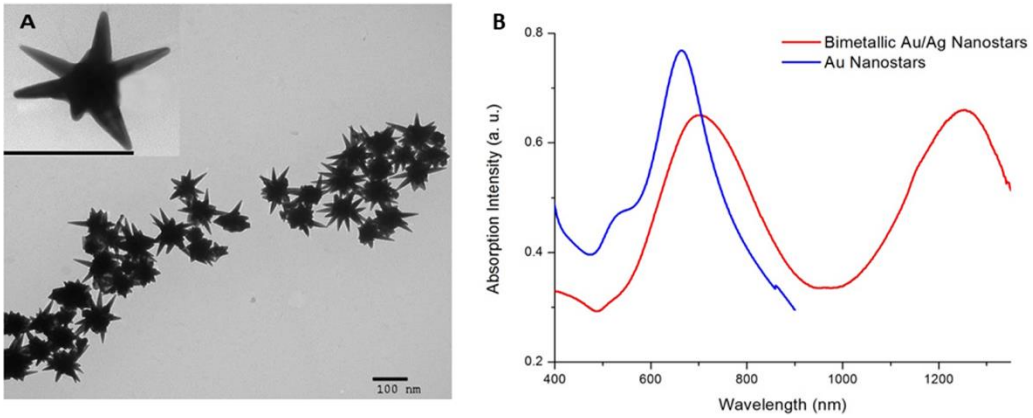

Fig. 6.2 (A) TEM image of NIR GNS and inset showing high magnification image of single nanostar (scale bar – 100 nm); (B) Absorption spectra of NIR GNS

6.3.2 Si- coated gold nanostars

Bare GNP's are susceptible to aggregation in solution and can melt and change their shape under high powers or prolonged laser irradiation, that leads to a change in their optical properties [33,34]. It has been shown that silica coating of gold nanoparticles greatly enhances their thermodynamic stability, by resisting aggregation and shape change, thus preserving their optical properties [5,33].

Radloff *et al.* [35] reported that coating nano shells with silica layer provides enhanced thermal stability to the nanoparticle, thereby raising its melting temperature by 300° relative to uncoated nanoshells. Also, Hu et al., demonstrated that silica coating of gold nanoshells enhances the heat transfer rate in water compared to bare gold nanoshells [36]. In photoacoustic imaging studies, Chen et al. have demonstrated that silica coated gold nanorods of the same optical density can produce about 3-fold higher photoacoustic signals than nanorods without silica coating [33]. Their results suggest that, silica coating causes a reduction of gold interfacial thermal resistance with the solvent which enhances the heat transfer efficiency.

It is shown that, silica shell thickness of up to 20 nm on GNR amplified the photoacoustic signal response without significantly modifying the optical properties of GNR [33]. However, no such studies have been carried out for PT-OCT imaging.

The in house developed PEGylated GNS were coated with silica using a modified Stober method [32,33]. Silica coating of the GNS was achieved by incubating GNS with tetraethyl orthosilicate in isopropanol solution. Figure 6.3 shows TEM images of bare GNS and silica coated GNS indicating a silica shell thickness of 10 nm.

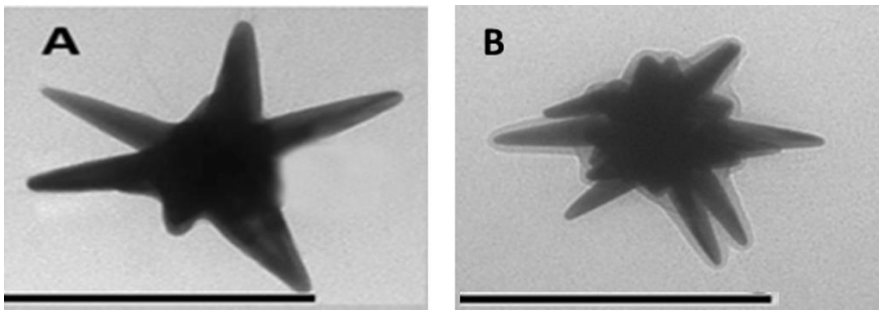

Fig.6.3 (A) Uncoated GNS (B) Silica coated GNS displaying 10 nm; Scalebars - 100 nm.

The resonance of this plasmonic GNS lies in the range of 1050 - 1100 nm, which is within the second NIR window (1000 – 1350 nm) where both the absorption and scattering would be at their minimum [37] thus facilitating deeper imaging of tissues.

6.4 PT-OCT system development and characterization

A spectral domain OCT (SD-OCT) was built for the photothermal experiments and is shown in Figure 6.4. The SD-OCT system consists of a super luminescent diode (SLD) operating at 1310 nm centre wavelength and FWHM of 130 nm. The light from the SLD is fibre coupled and split between the reference arm and sample arm by a 90/10 fibre coupler (FC). The sample beam was steered by a pair of galvanometer mirrors (GVS-001, Thorlabs, USA) controlled via LabVIEW through a connector block (SCC-68 and PCI-6731, National Instruments). Light

from the sample and reference arm was passed through a spectrograph (Bayspec, USA) centered at 1310 nm, with a spectral resolution of 0.12 nm. The spectrally separated light was detected by a 14-bit 1024 pixel InGaAs digital line scan camera (SU1024LDH, Goodrich Ltd, USA). The camera signal was transferred to a PC via a high-speed frame grabber (PCIe-1427, National Instruments) and images were acquired using LabVIEW. A real-time signal integration (RTSI) cable enabled synchronised scanning and data acquisition. For the photothermal excitation, a pumped diode laser (MIL-III-1064 DPSS, CNI, China) having an excitation wavelength of 1064 nm (around the absorption peak of GNS) was used. Light from the diode laser was collimated via a collimator (Thorlabs,USA) and directed to a tilt mirror aligned 45° to the vertical axis. Laser beam reflected from the tilt mirror is made to pass through a dichroic mirror (Thorlabs,USA) along with the SLD beam and directed to the X-Y galvanometer scanners for the lateral scanning.

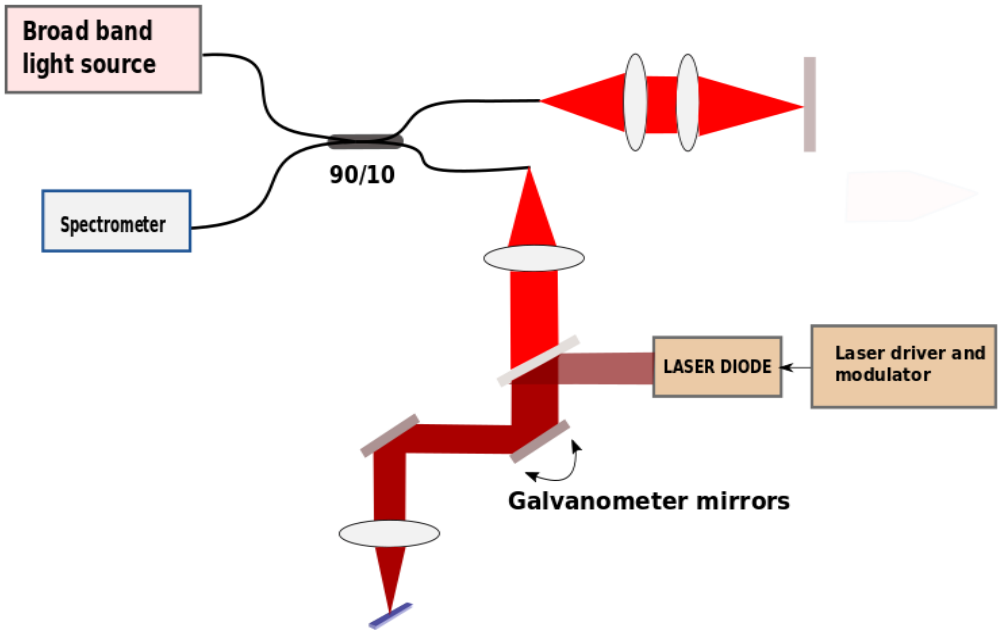

Fig 6.4. Schematic of the PT-OCT system

The axial resolution of an OCT system is governed by the coherence length of the light source used, which can be calculated by equation 2.5. In this work, the SLD used (Denselight, DL-BX9-CS3159A) was centred at 1310 nm. The spectral bandwidth of the light source was measured as the FWHM of the source spectrum and was found to be 74 nm. The theoretical value of axial resolution calculated according to Eq.2.5 is 6 µm. In order to experimentally determine the axial resolution, the axial PSF was measured. This was done by placing a mirror in the sample arm of the interferometer. The axial PSF broadens as the distance between the mirror and the zero optical path difference increases. The mirror was positioned such that the

optical path difference was 65 µm. The envelope of the detected interferogram represents the axial PSF and the axial resolution is determined by its FWHM. As seen in figure 6.5, the measured axial resolution is 10 µm which corresponds well to the calculated theoretical value.

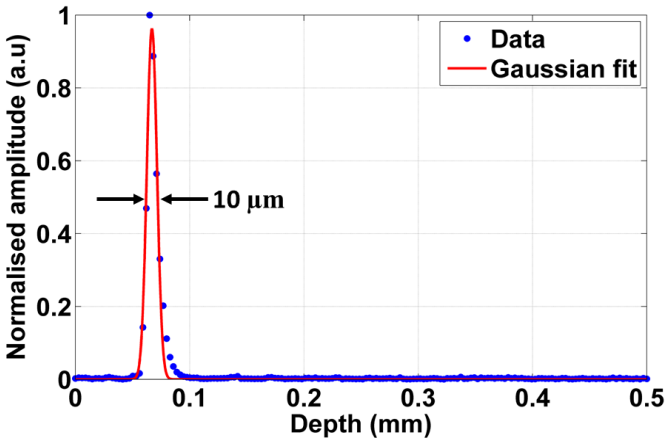

Fig. 6.5 Axial point spread function measured from a mirror at an optical path length difference of 75 µm

The lateral resolution of an OCT system, as per equation 2.6, is determined by the numerical aperture of the focusing lens in the sample arm. For the objective lens used in this work (Thorlabs LSM03), the theoretical lateral resolution was calculated as 17.6 µm by using values d = 3.4 mm, f = 36 mm and λ_0 = 1310 nm. The beam diameter at the objective lens, d, was estimated by the theoretical output beam diameter from the collimator (Thorlabs F280- APC-C). The theoretical depth of focus achievable was also calculated, using equation 2.8, which yielded a value of 0.49 mm. The lateral resolution can also be approximated by the beam spot size, (lateral PSF), at the focus position of the sample arm objective lens. A slit scanning beam profiler (Thorlabs, BP109-IR) was placed in the sample arm in order to measure this experimentally.

The lateral PSF was recorded starting at 4.75 mm above the focus and ending 4.75 mm below the focus with a step size of 250 µm. Figure 6.6 shows the beam waist about the focus. The zero position indicates the position of the focus of the objective lens, with all distances measured relative to this location. Using this method, the lateral resolution was measured to be about 11.6 µm, giving a corresponding depth of focus of 161 µm (using equation 2.8).

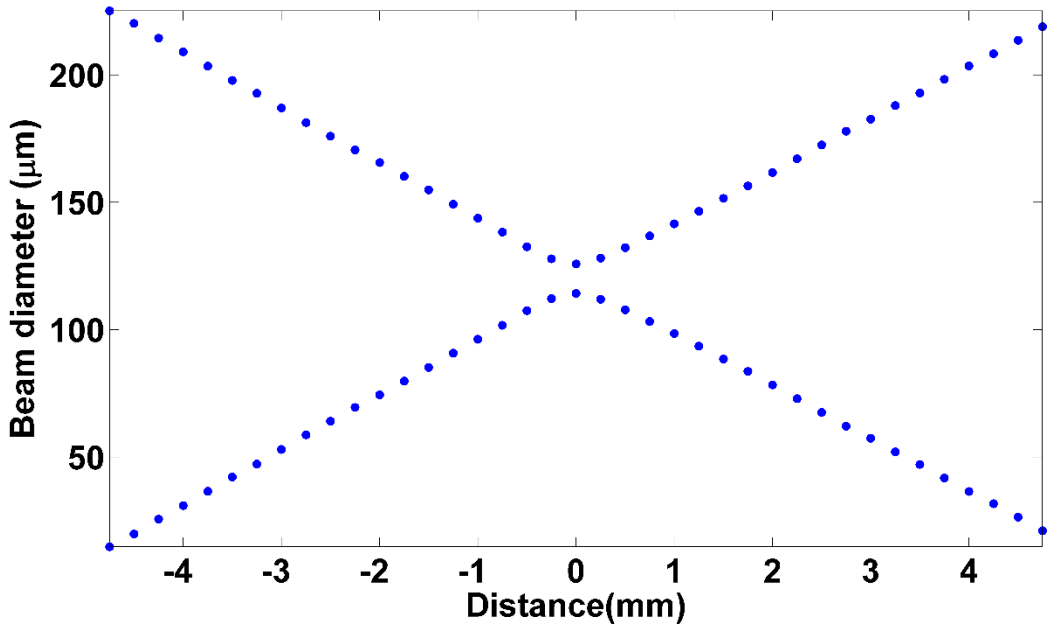

Fig.6.6 Beam waist about the sample arm focal point.

To measure the transverse resolution experimentally, a resolution target (1951 USAF) was imaged using LSM03 objective lens and is shown in figure 6.7(a). The smallest line on the group 5 target has a width of 8.7 μm which the LSM03 was able to resolve. Also, the intensity profile (complement of original image) of group 5 (taken at the position of the yellow lines) of the target is shown in figure 6.7(b).

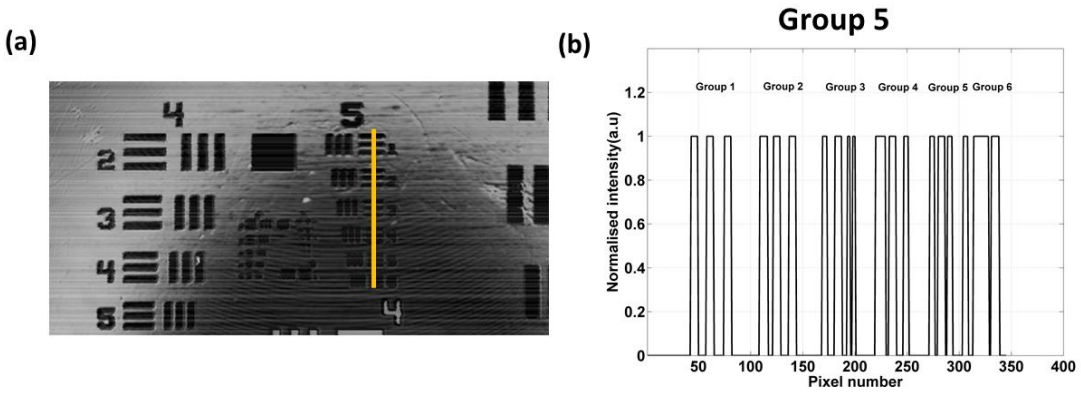

Fig. 6.7 (a) Image of group 5 of a USAF target taken with LSM03 objective. The thickness of a single line of the smallest element resolved is 8.7 μm. (b) vertical intensity profile of Group 5 taken at the yellow line shown in (a).

Another important consideration to be made in SD-OCT is the requirement to resample or recalibrate the detected OCT interference-fringe signals prior to Fast Fourier transformation (FFT), in order to provide data evenly sampled in optical frequency. Also, factors such as dispersion effects and misalignments of the system optics can further worsen the non-uniform distribution of spectral width across each pixel [38]. Such non-linearities lead to the signal peak

becoming broader at longer optical path lengths, resulting in a loss in the image quality achievable at greater imaging depths [39]. Hence, it is essential to remap SD-OCT signal from the wavelength domain to the wavenumber domain. Many methods have been proposed for mapping the correct wavelength to the pixels of the charge coupled device camera [38,40]. Most of these techniques required the use of additional equipment for the calibration process. Another method has been proposed by Wang et al. [41] that is based on phase linearization approach. This technique tries to eliminate the dispersion mismatch between the reference and sample arm of the SD-OCT system by measuring interference spectra with different optical path delays using a single reflective surface. Since the technique uses no additional instruments, any slight adjustments needed due to unwanted thermal or mechanical drifts in the spectrometer could be accounted for. The broadening of axial point spread function before and after the calibration is shown in figure 6.8.

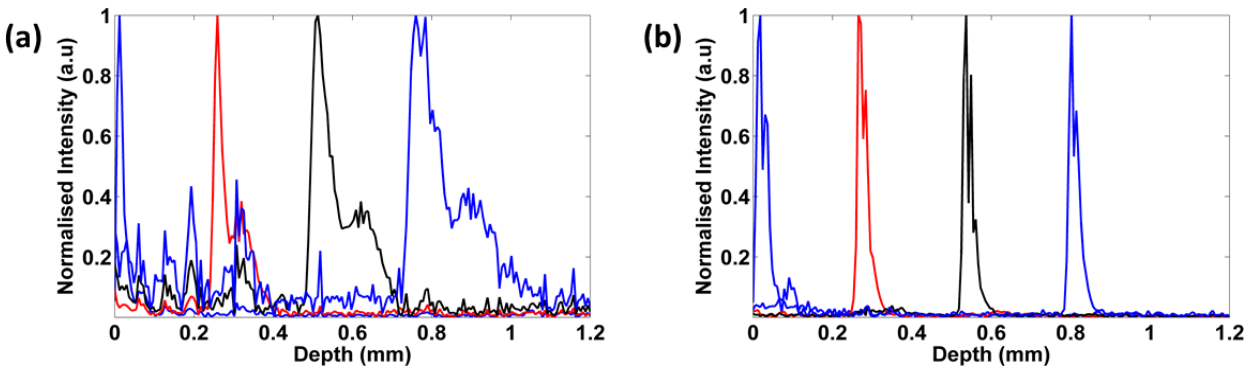

Fig. 6.8 Axial point spread functions for a mirror at different depths (a) before calibration (b) after calibration.

The SNR is defined as the ratio of the signal amplitude at a certain point in the image to the noise floor. It is therefore, a property of the image. The sensitivity, on the other hand, is the maximum measurable signal attenuation that can be distinguished from the noise floor, therefore it is a property of the imaging system. The sensitivity is an extremely important parameter of any imaging system, as it gives the best possible SNR that can be achieved. The SNR determines the image contrast while sensitivity determines the maximum useful imaging depth of a system.

The sensitivity of the system used in this work was measured experimentally using a mirror in the sample arm as the sample. In order to avoid detector saturation, a variable optical density (OD) filter was placed in the sample arm. This was adjusted until the amplitude of the interference signal lay just below the detector saturation limit. The round-trip attenuation

resulting from the OD filter in this experiment was found to be approximately 40 dB. The mirror was mounted to a translation stage and moved away from the zero optical path length difference position over a depth range from 20 µm to 3 mm, in steps of 0.25 mm. An interferogram was recorded at each location of the mirror. At each position the SNR was calculated as given by equation (6.3):

$$SNR = 20\ log_{10}\left(\frac{Signal}{standard\ deviation\ of\ noise\ floor}\right) \tag{6.3}$$

Here, signal refers to the maximum amplitude of the Fourier transformed interference signal associated with the mirror.

The sensitivity of the system was then calculated at each mirror position using equation (6.4) given by

$$Sensitivity = SNR + 2.OD \tag{6.4}$$

where OD refers to the optical density value in decibels. Figure 6.9 shows the measured signal intensity roll off over depth for the SD-OCT system. Figure 6.10 shows the sensitivity roll of the SD-OCT system with depth.

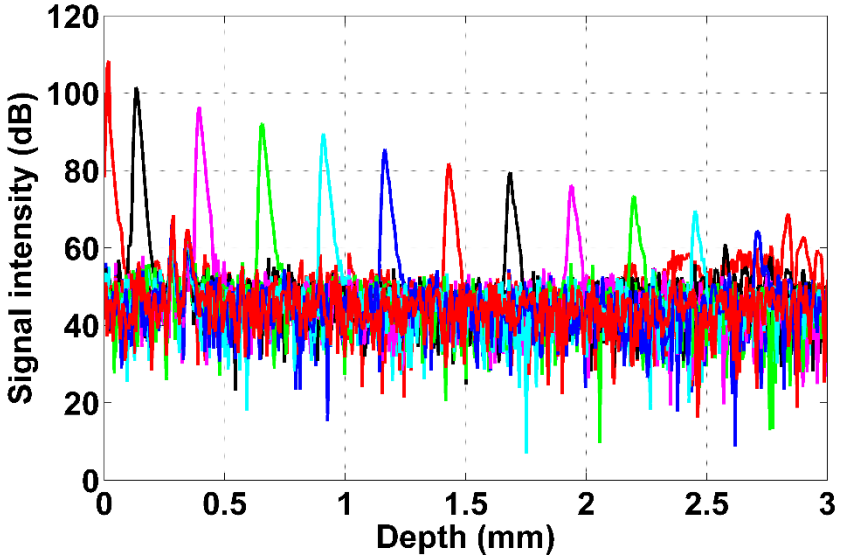

Fig. 6.9 Signal intensity roll-off of the SD-OCT system used in this work. Each peak pertains to a reflection from the static mirror as it is translated in 0.25 mm steps through a distance of 3 mm.

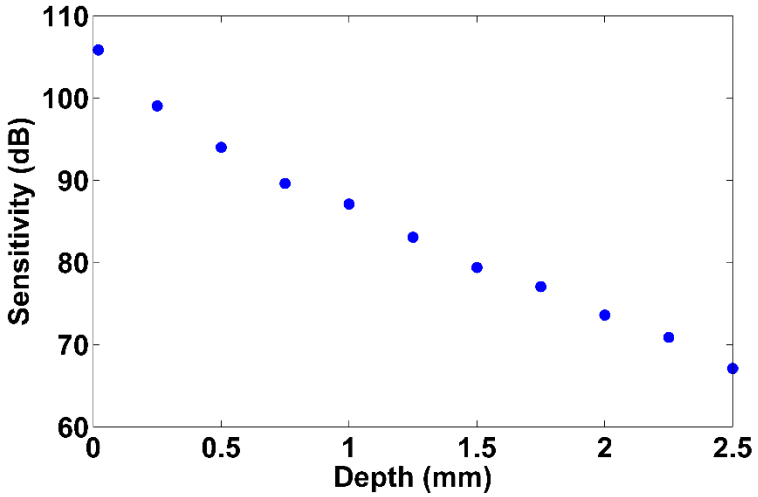

Fig.6.10 Sensitivity roll-off of the SD-OCT system.

As seen in figures 6.9 and 6.10, the sensitivity decreases with increasing depth. This signal roll-off is characteristic of SD-OCT. However, as evidenced by the figures, the sensitivity of the system is still over 60 dB at a depth of 2.5 mm, which makes the developed system suitable for photothermal imaging studies at deeper depths within a scattering medium.

6.4.1 Phase stability

The phase stability is an important system parameter, which describes the sensitivity of an OCT system to phase measurements. Since OCT is an interferometric technique, it is capable of detecting changes in optical path length equal to half the wavelength of the light source used. Changes within the phase of an OCT signal are related to the changes in optical path lengths and can be utilised to resolve sub-wavelength movements of a sample. In theory the phase of a single stationary scatterer should remain constant. However, in practice, there is always noise present in the phase of a signal. Phase noise limits the minimum phase shift that can be detected by an OCT system. Thermal drift, external environmental vibrations, mechanical instabilities in the system and galvanometer positioning inaccuracies (galvanometer jitter) are all typical sources of noise which affect the phase of an OCT system [42]. The phase stability quantifies these variations, giving a measure of the minimum phase difference that can be reliably attributed to anything other than noise.

To determine the phase stability of the SD-OCT system used in this work, a stationary mirror was placed in the sample arm, and multiple A-lines were recorded at a single location. In total 512 A-lines were acquired, at a rate of a 10.8 kHz. The phase differences between each of the adjacent A-lines were then calculated and analysed, as shown in figure 6.11 (a). The

phase stability is quantified by the standard deviation of the phase difference distribution [43]. The measured system phase stability was 26 mrad. Any noise present in the phase of the signal was assumed to originate at random. For this reason, the phase differences were expected to follow a Gaussian distribution and figure 6.11 (b) shows the Gaussian-shaped profile fit to the histogram of phase differences between adjacent A-lines.

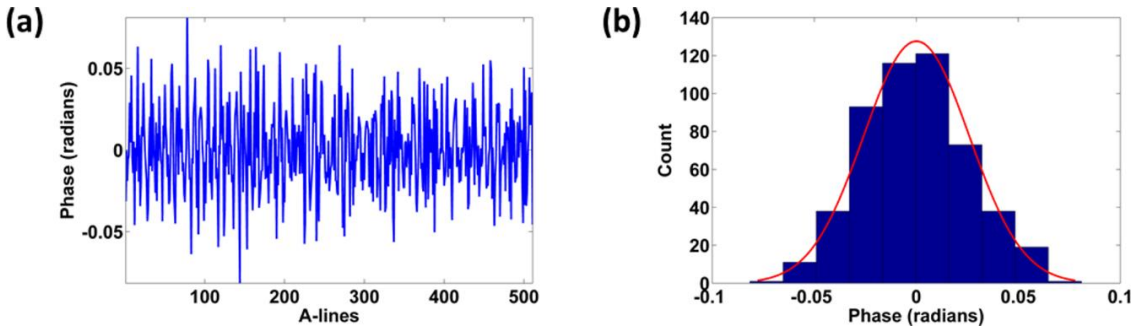

Fig. 6.11 (a) Phase differences between adjacent A-lines for a fixed mirror as sample. (b) Distribution of the measured phase differences. The solid red line represents a Gaussian fit for the distribution.

The phase sensitivity is a theoretical quantity which represents the smallest resolvable phase difference that can be quantified based on the stability of an ideal imaging system. For an OCT system operating within the shot-noise limit, theoretically the phase sensitivity ($s_{\Delta\phi}$) is related to the SNR as given by equation (6.5) [44,45].

$$s_{\Delta\phi} \approx \frac{1}{\sqrt{SNR}} \tag{6.5}$$

The theoretical best value for phase sensitivity calculated for a SNR of 64 dB was approximately 0.63 mrad. However, the phase sensitivity derived from the SNR may not be achievable in a real system. In practice, an SD-OCT system may not be shot noise limited and also may be influenced by mechanical noise arising from galvanometer jitter. Hence, phase stability was measured with the galvanometer switched off. With galvanometer switched off, a phase stability value of 6.8 mrad is obtained. Figure 6.12 indicates the result obtained.

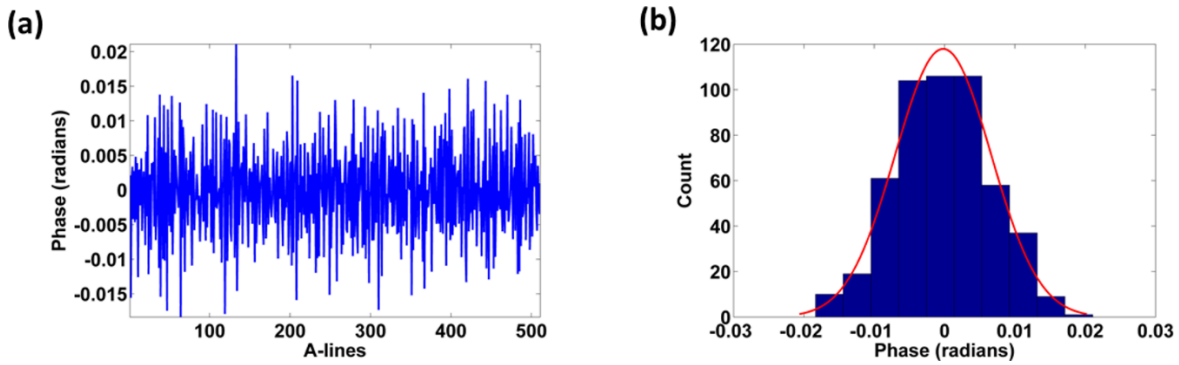

Fig. 6.12 (a) Phase differences between adjacent A-lines for a fixed mirror as sample with galvo switched off. (b) Distribution of the measured phase differences. The solid red line represents a Gaussian fit for the distribution.

The displacement sensitivity of an OCT system refers to the minimum displacement that it is capable of measuring. The displacement sensitivity can be quantified from the phase stability [46] through the following relation given by equation (6.6)

$$s_d = \frac{s_{\Delta\phi}\lambda_0}{4\pi n} \tag{6.6}$$

where s_d is the displacement sensitivity, $s_{\Delta\phi}$ is the measured phase stability, λ_0 is the central wavelength of the source and n is the refractive index of the sample. The phase stability measured for the system described corresponds to a displacement sensitivity of about 2.7 nm in air, or 2 nm in biological tissue.

For photothermal experiments using GNS, it is essential that both the OCT imaging beam and the excitation laser beam overlaps for the entire imaging depth. Hence, the laser output was collinearly coupled to the imaging beam (1310 nm) using a dichroic mirror (DCM) as shown in Fig. 6.4. The collinearity of the 1310 nm SLD beam with the 1064 nm laser beam was analysed for 4.75 mm above and below the focus of SLD beam and is shown in figure 6.13.

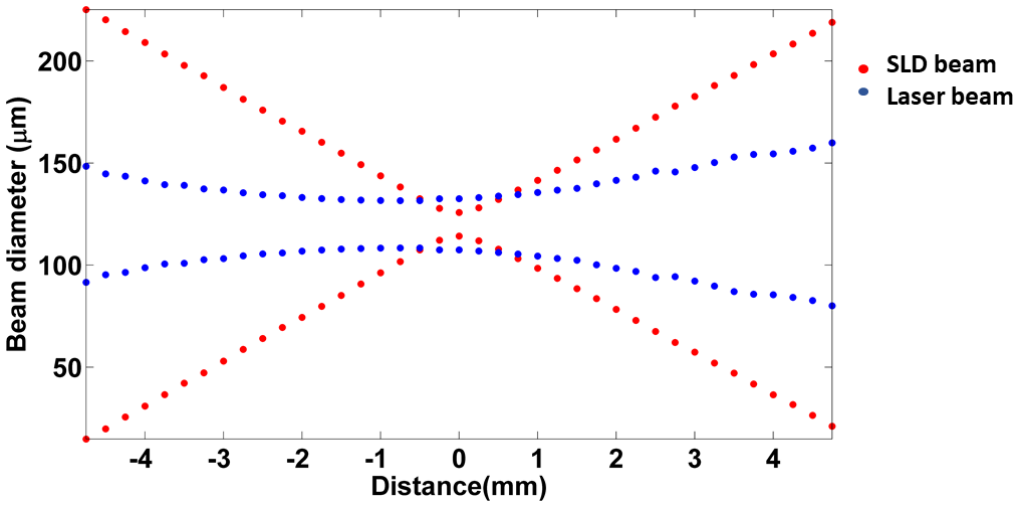

Fig.6.13 Plot showing SLD and laser beam alignment

6.5 Phantom imaging: materials and methods

To demonstrate the photothermal detection of GNS with PT-OCT, GNS embedded agarose phantoms were used. Equal volumes of 4% agarose solution (99.99%, Sigma Aldrich) were mixed with 25 nM and 50 nM of GNS and left to set at room temperature after loading into the capillary tubes of 2 mm diameter. As a control sample, phantom with 2% agarose solution was also prepared in a capillary tube of 2 mm diameter.

Further, to demonstrate the enhancement of photothermal signals by Si-coating, Si-coated GNS phantoms were prepared as described in section 6.2. Equal volumes of Si-coated GNS (2% v/v) were prepared and loaded into capillary tubes of 2 mm diameter and 4 mm diameter.

6.5.1 Signal processing

For the photothermal imaging, the SD-OCT system was operated in the M-B scan mode. For each location, 512 A-lines were recorded at an A-scan rate of 10.8 kHz using the custom developed LabVIEW acquisition protocol. For the present study, the 1064 nm DPSS laser was used for photothermal excitation and was modulated at a frequency of 300 Hz (duty cycle of 50%) using a signal generator. Prior to photothermal signal extraction, the raw interference spectrum (A-scan) was k-space linearized and DC reference spectrum subtracted. Photothermal signals were extracted from the acquired M mode A-scans by using Eq. (6.1). Fourier transform (FT) of these phase differences along the time axis gives the frequency at which the laser beam is modulated. From the Fourier spectrum, the magnitude of the FT data within ± 20 Hz of the laser excitation frequency is used to calculate the photothermal signal. To effectively detect the photothermal signal from the background noise, a Butterworth bandpass filter having a

bandpass frequency of 400 Hz was applied to the phase difference signal. The magnitude of the FT at the photothermal excitation frequency is then converted to corresponding optical path length (OPL) changes using Eq. (6.2). To improve the signal to noise ratio of the detected photothermal signal, photothermal noise, defined as the mean magnitude of nearby frequencies (330-400 Hz) in the FT of the phase signal was subtracted at each depth location [17]. This process is repeated for all the M scans and finally a B frame is reconstructed that maps the depth wise distribution of photothermal signal within the sample. The final PT-OCT B frame image was median filtered with a 4x4 kernel to reduce noise. All the PT-OCT processing was carried out offline after image acquisition using a custom Matlab script. The flowchart describing the processing steps is shown in figure 6.14. A representative plot showing detected photothermal signal from the GNS sample within the capillary tube is shown in figure 6.15.

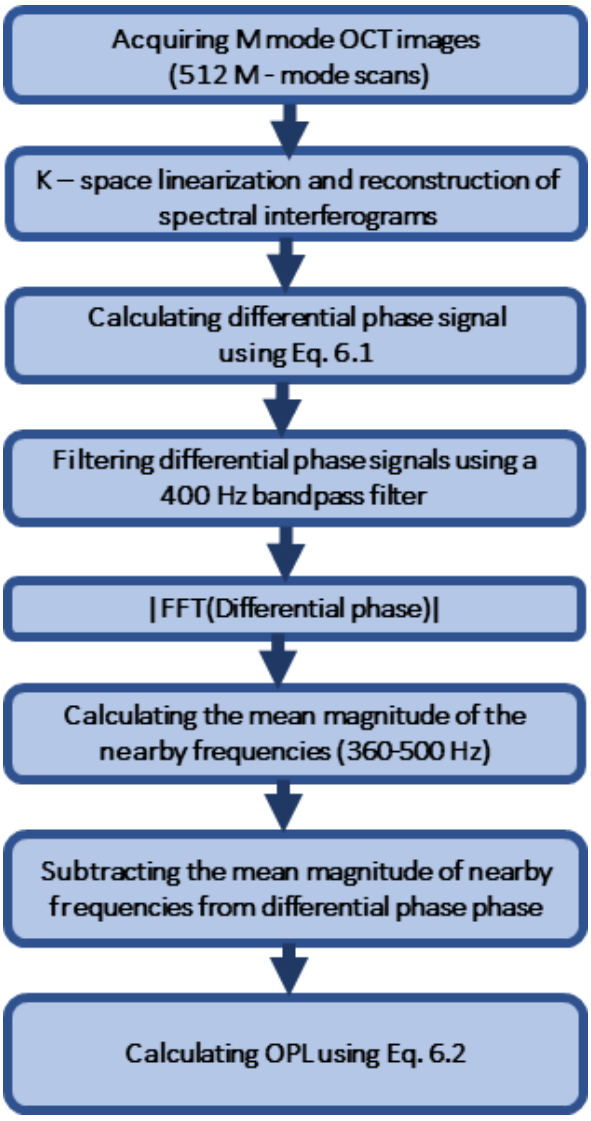

Fig. 6.14 Flowchart describing the extraction of photothermal signal

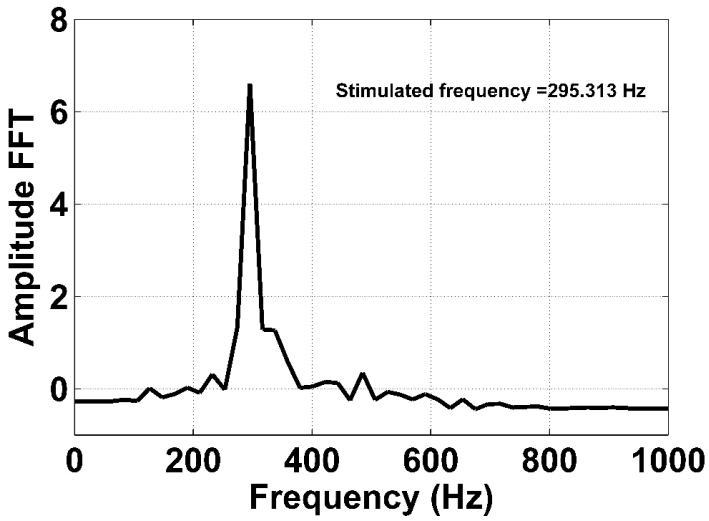

Fig. 6.15 Representative plot showing detected photothermal signal at 295 Hz

6.6 Results

To demonstrate the PT-OCT imaging of GNS using the developed system, control phantom made of only 2% agarose was imaged with laser turned on at 40 mW power and with laser turned off. The results are shown in figure 6.16. A total of 512 M-scans were acquired at each location in the lateral direction at an A-scan rate of 10.8 kHz. A total of 200 A-scans were acquired covering a distance of 3 mm in the transverse direction using the M-B-mode imaging protocol. Figure 6.16 indicates that, laser excitation of the control phantom (agar only) did not produce any photothermal signal.

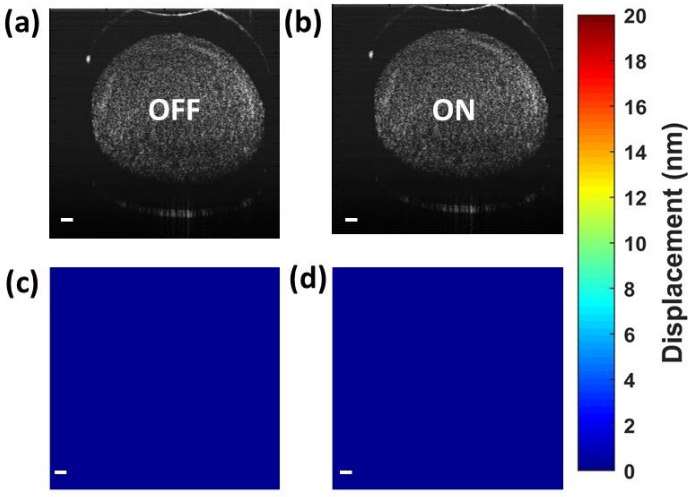

Fig. 6.16 PTOCT images of capillary tube control phantoms (a) magnitude image with laser off, (b) magnitude image with laser on at 40 mW, (c) PT-OCT image with laser off, (d) PT-OCT image with laser on.

To demonstrate photothermal imaging of GNS, GNS embedded agarose phantoms were imaged. For the initial experiments, two different concentrations of GNS were prepared. To prepare the phantom models, equal volumes of 4% agarose solution (99.99%, Sigma Aldrich) were mixed with 5 nM,10 nM, 25 nM and 50 nM GNS and loaded into capillary tubes of 2 mm inner diameter and were left to set at room temperature. Laser power was varied from 5 to 40 mW for these experiments. As the excitation laser was modulated at 50% duty cycle, the effective power on the sample is one half of the excitation laser power over one complete cycle.

The photothermal signals were detectable only for GNS concentration of 25 nM and 50 nM and is shown in figures 6.17 and 6.18 respectively. From figure 6.17 and 6.18, it can be observed that, with increasing laser power, the detected OPL changes also increased. This increase in PT-OCT signal, with increasing pump beam power, has been previously demonstrated by theoretical modelling and experimental data with other gold nanoparticles [2].

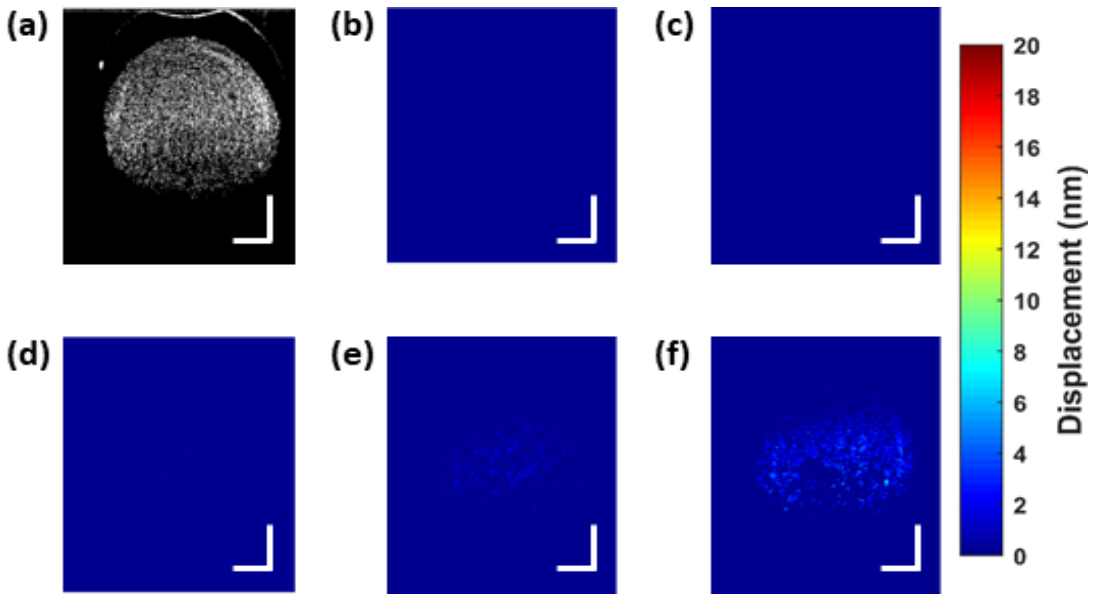

Fig. 6.17 PTOCT images of 25 nM GNS loaded capillary tube phantoms (a) Conventional OCT structural image (b) PT-OCT image at 5 mW (c) 10 mW (d) 20 mW (e) 30mW (f) 40 mW; Scalebars – 500 µm.

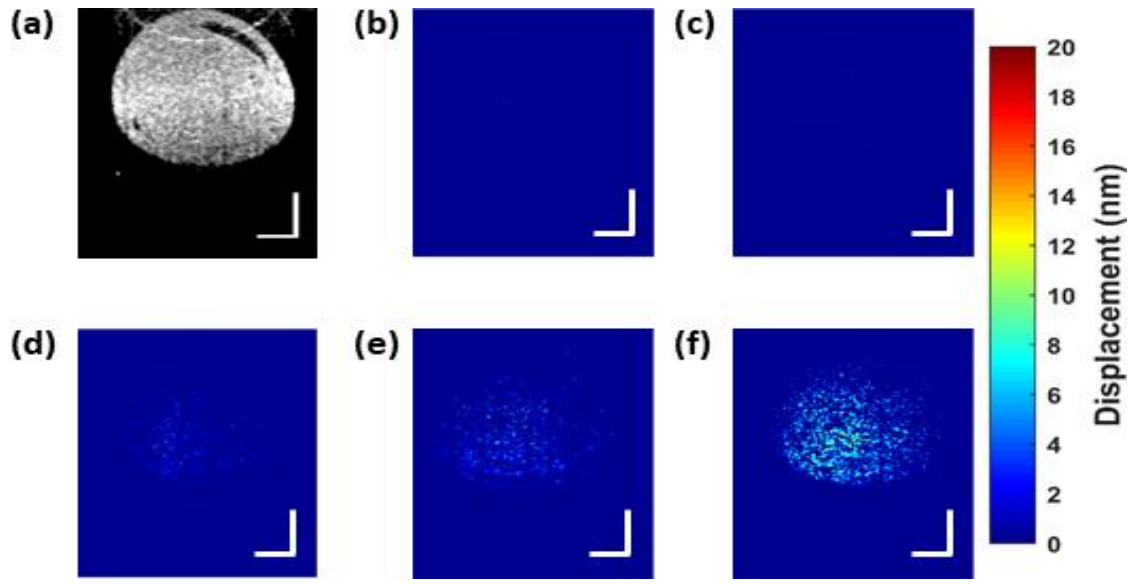

Fig. 6.18 PTOCT images of 50 nM GNS loaded capillary tube phantoms (a) Conventional OCT structural image (b) PT-OCT image at 5 mW (c) 10 mW (d) 20 mW (e) 30mW (f) 40 mW; Scalebars – 500 µm.

Next, to investigate the enhancement in photothermal image contrast by silica coating of gold nanoparticles, silica coated GNS were prepared as mentioned in section 6.2 and PT-OCT imaging was performed. The photothermal imaging maps for silica coated GNS for 25 nM and 50 nM concentrations are shown in figures 6.19 and 6.20 respectively.

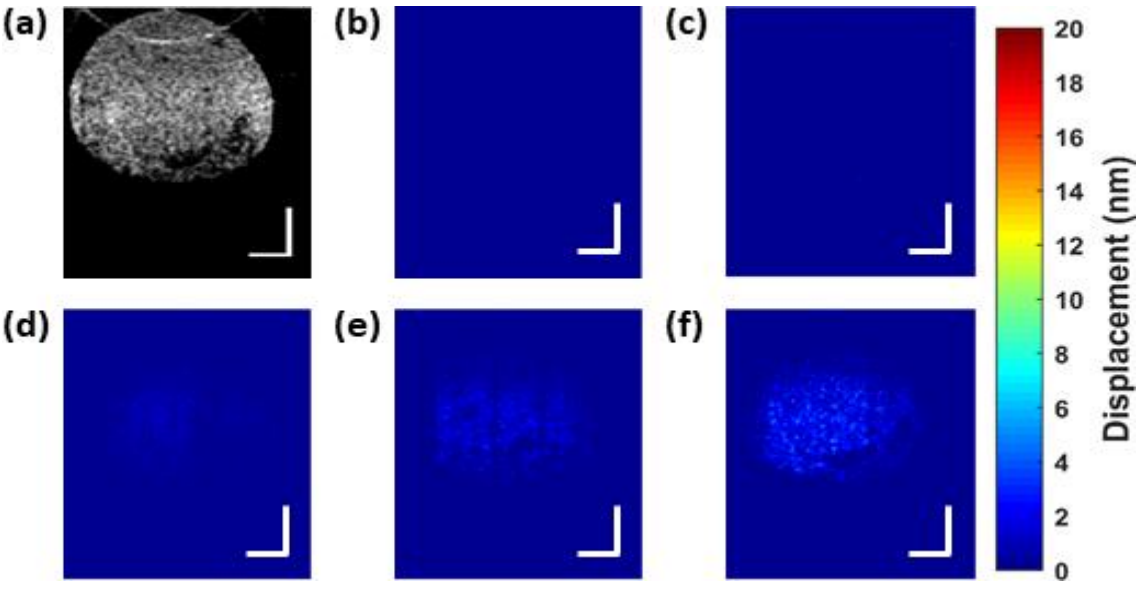

Fig. 6.19 PTOCT images of 25 nM Si-GNS loaded capillary tube phantoms (a) Conventional OCT structural image (b) PT-OCT image at 5 mW (c) 10 mW (d) 20 mW (e) 30mW (f) 40 mW; Scalebars – 500 µm.

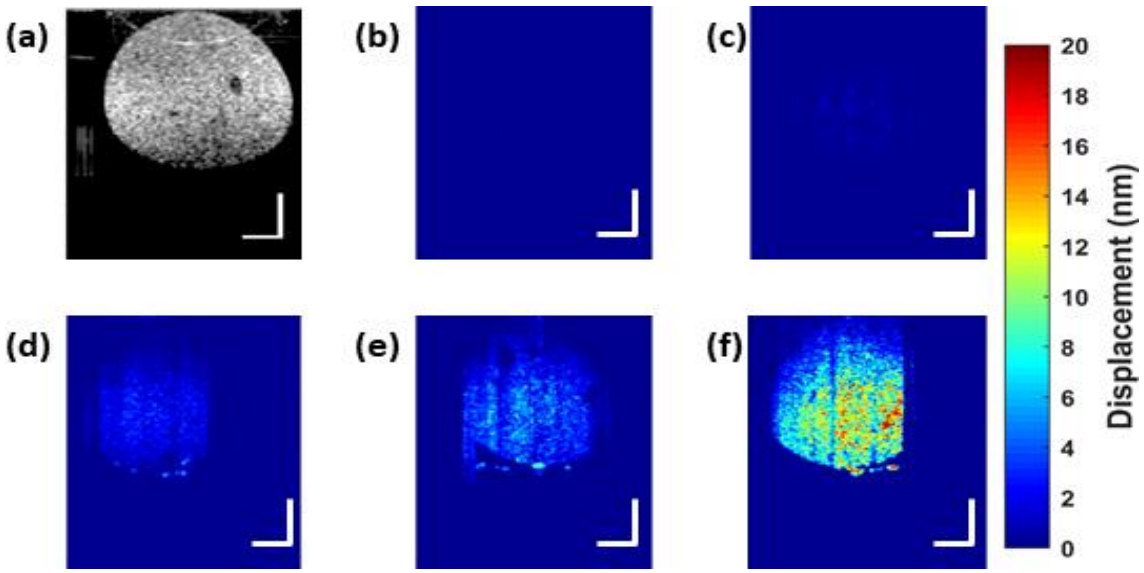

Fig. 6.20 PTOCT images of 50 nM Si-GNS loaded capillary tube phantoms (a) Conventional OCT structural image (b) PT-OCT image at 5 mW (c) 10 mW (d) 20 mW (e) 30mW (f) 40 mW; Scalebars – 500 µm.

Comparing figures 6.17 and 6.19, and figures 6.18 and 6.20, it can be observed that photothermal induced OPL changes increased with silica coating of GNS samples. Also, the silica coating of GNS facilitated the heat conduction within the agar medium as indicated by the enhancement in image contrast of photothermal maps compared to photothermal maps of uncoated GNS samples. These results are in accordance with that obtained by Chen *et al.* for photoacoustic imaging using silica coated GNR samples [33]. They demonstrated that this enhancement in the photoacoustic signal of silica coated nanorods arose due to faster heat transfer into the medium enabled by the silica coating rather than changes in the absorption coefficient of the GNR.

Figure 6.21 shows the mean OPD changes for silica coated and uncoated agar phantoms of different concentrations (25 nM and 50 nM) with increasing laser power. The mean OPD in each case was taken to be the average value of non-zero path length changes within the capillary tube over the entire imaged area of the tube. Silica coating enhanced the photothermal OCT signals at least by one fold at all powers and by two fold at higher powers compared to uncoated GNS.

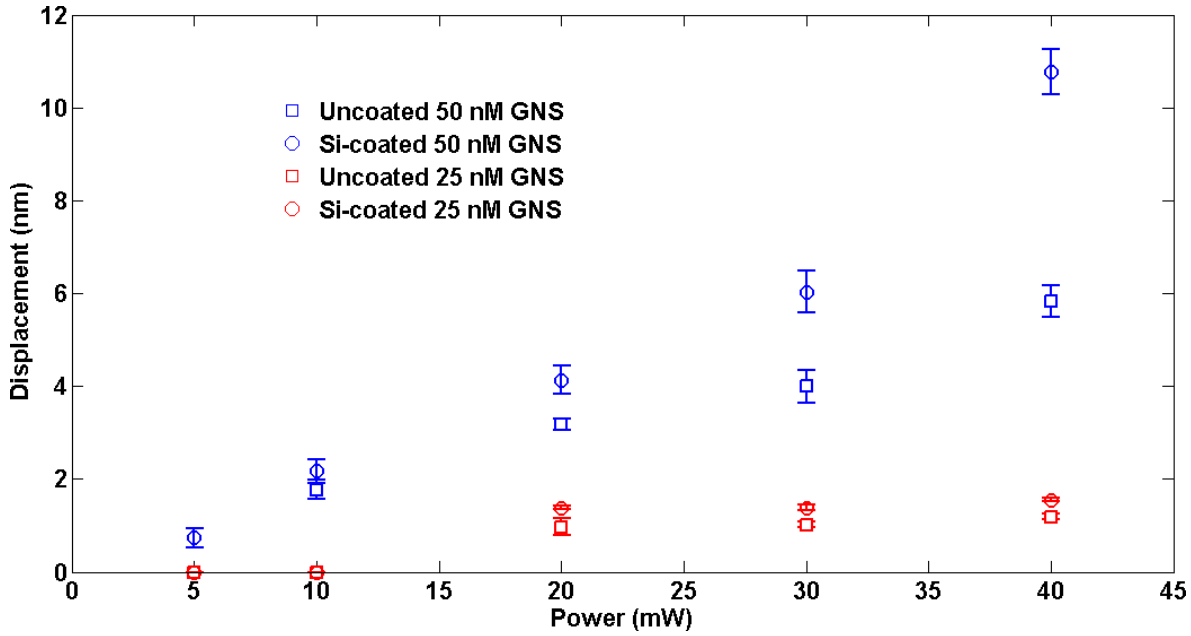

Fig. 6.21 Plot showing increase in OPL with increasing laser power for silica coated and uncoated GNS-agar phantoms.

Further, to investigate the deeper imaging capability of silica coated GNS's within a scattering medium, photothermal studies were carried out on capillary phantoms having an inner diameter of 4 mm. Figures 6.22 (a) and (b) show the structural image and a PT-OCT map of GNS's embedded agar phantom excited at 40 mW (20 mW average power on the sample), with the photothermal signal clearly visible at depths beyond 2 mm within the phantom. As can be seen from figure. 6.22 (b), photothermal signals were detectable up to a depth of 2.25 mm, thus providing the proof of concept for the enhanced imaging depth capability at depths greater than 2 mm using silica coated GNS's.

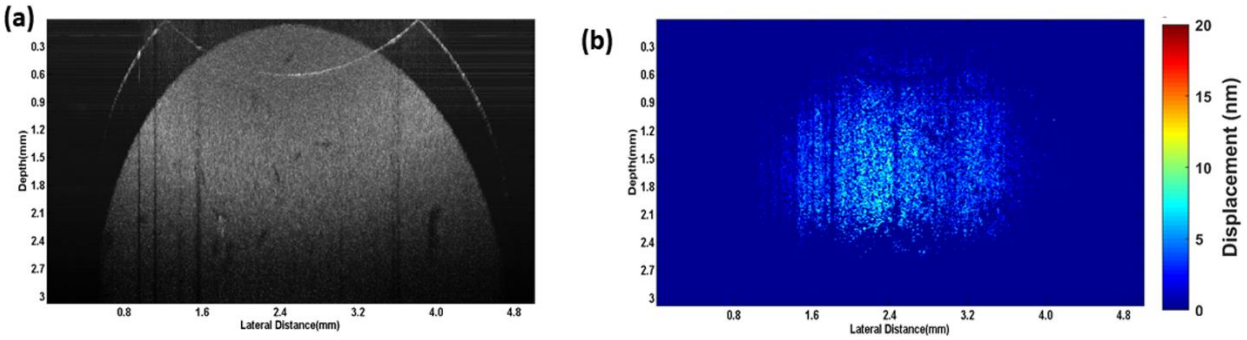

Fig. 6.22 Enhanced imaging depth capability of Si coated GNS embedded agar phantom in a 4 mm capillary tube. (a) conventional B frame (b) PT-OCT image showing photothermal signals from a depth of 2.25 mm.

6.7 Conclusions

In conclusion, we have demonstrated the capability of GNS as contrast agent for PT-OCT imaging at NIR photothermal excitation. To mimic tissue scattering, GNS were embedded in agar phantom models for the photothermal imaging. As stated in the literature, increase in laser excitation power caused an increase in photothermal induced OPL changes within the phantom model. Also, silica coated GNS embedded phantoms were imaged to investigate the enhancement in PT-OCT image contrast. It is observed that silica coating enhances the photothermal signals by over 50% compared to uncoated GNS in PT-OCT imaging. The results indicate that, silica coating of GNS enables faster and less resistance for heat conduction across the medium as observed from the enhancement in image contrast. Further, depth resolved functional imaging has been demonstrated beyond 2 mm using GNS embedded phantoms. The discussed technique offers a promising tool for molecular imaging at increased penetration depths within biological tissue.

REFERENCES

1. D. C. Adler, S.-W. Huang, R. Huber, and J. G. Fujimoto, "Photothermal detection of gold nanoparticles using phase-sensitive optical coherence tomography," Opt. Express **16**, 4376–4393 (2008).
2. J. Tucker-Schwartz, T. Meyer, C. Patil, C. Duvall, and M. Skala, "In vivo photothermal optical coherence tomography of gold nanorod contrast agents," Biomed. Opt. Express **3**, 2881–2895 (2012).
3. H. M. Subhash, E. Connolly, M. Murphy, V. Barron, and M. Leahy, "Photothermal optical coherence tomography for depth-resolved imaging of mesenchymal stem cells via single wall carbon nanotubes," in (International Society for Optics and Photonics, 2014), p. 89540C–89540C–6.
4. T.-T. Chi, Y.-C. Tu, M.-J. Li, C.-K. Chu, Y.-W. Chang, C.-K. Yu, Y.-W. Kiang, and C. C. Yang, "Photothermal optical coherence tomography based on the localized surface plasmon resonance of Au nanoring," Opt. Express **22**, 11754 (2014).
5. Y.-S. Chen, W. Frey, S. Kim, K. Homan, P. Kruizinga, K. Sokolov, and S. Emelianov, "Enhanced thermal stability of silica-coated gold nanorods for photoacoustic imaging and image-guided therapy," Opt. Express **18**, 8867–8878 (2010).
6. A. L. Oldenburg, M. N. Hansen, T. S. Ralston, A. Wei, and S. A. Boppart, "Imaging gold nanorods in excised human breast carcinoma by spectroscopic optical coherence tomography," J. Mater. Chem. **19**, 6407–6411 (2009).
7. A. M. Gobin, M. H. Lee, N. J. Halas, W. D. James, R. A. Drezek, and J. L. West, "Near-Infrared Resonant Nanoshells for Combined Optical Imaging and Photothermal Cancer Therapy," Nano Lett. **7**, 1929–1934 (2007).
8. A. S. Paranjape, R. Kuranov, S. Baranov, L. L. Ma, J. W. Villard, T. Wang, K. V. Sokolov, M. D. Feldman, K. P. Johnston, and T. E. Milner, "Depth resolved photothermal OCT detection of macrophages in tissue using nanorose," Biomed. Opt. Express **1**, 2–16 (2010).
9. M. C. G. Aalders, M. Triesscheijn, M. Ruevekamp, M. de Bruin, P. Baas, D. J. Faber, and F. A. Stewart, "Doppler optical coherence tomography to monitor the effect of photodynamic therapy on tissue morphology and perfusion," J. Biomed. Opt. **11**, (2006).
10. A. L. Oldenburg, R. L. Blackmon, and J. M. Sierchio, "Magnetic and Plasmonic Contrast Agents in Optical Coherence Tomography," IEEE J. Sel. Top. Quantum Electron. Publ. IEEE Lasers Electro-Opt. Soc. **22**, (2016).

11. P. Si, E. Yuan, O. Liba, Y. Winetraub, S. Yousefi, E. D. SoRelle, D. W. Yecies, R. Dutta, and A. de la Zerda, "Gold Nanoprisms as Optical Coherence Tomography Contrast Agents in the Second Near-Infrared Window for Enhanced Angiography in Live Animals," ACS Nano **12**, 11986–11994 (2018).
12. A. Oldenburg, F. Toublan, K. Suslick, A. Wei, and S. Boppart, "Magnetomotive contrast for in vivo optical coherence tomography," Opt. Express **13**, 6597–6614 (2005).
13. A. L. Oldenburg, V. Crecea, S. A. Rinne, and S. A. Boppart, "Phase-resolved magnetomotive OCT for imaging nanomolar concentrations of magnetic nanoparticles in tissues," Opt. Express **16**, 11525–11539 (2008).
14. M. Skala, M. Crow, A. Wax, and J. Izatt, "Photothermal Optical Coherence Tomography for Molecular Imaging," in (OSA, 2011), p. OTuA3.
15. C. Zhou, T.-H. Tsai, D. C. Adler, H.-C. Lee, D. W. Cohen, A. Mondelblatt, Y. Wang, J. L. Connolly, and J. G. Fujimoto, "Photothermal optical coherence tomography in ex vivo human breast tissues using gold nanoshells," Opt. Lett. **35**, 700–702 (2010).
16. M. C. Skala, M. J. Crow, A. Wax, and J. A. Izatt, "Photothermal Optical Coherence Tomography of Epidermal Growth Factor Receptor in Live Cells Using Immunotargeted Gold Nanospheres," Nano Lett. **8**, 3461–3467 (2008).
17. M. Skala, M. Crow, A. Wax, and J. Izatt, "Three-Dimensional Molecular Imaging with Photothermal Optical Coherence Tomography," in *NanoBiotechnology Protocols*, S. J. Rosenthal and D. W. Wright, eds., Methods in Molecular Biology No. 1026 (Humana Press, 2013), pp. 85–92.
18. J. Kim, J. Oh, H. W. Kang, M. D. Feldman, and T. E. Milner, "Photothermal response of superparamagnetic iron oxide nanoparticles," Lasers Surg. Med. **40**, 415–421 (2008).
19. J. M. Tucker - Schwartz, M. J. Schultis, K. Beavers, C. Duvall, and M. C. Skala, "Full Range Photothermal Optical Coherence Tomography of Gold Nanoparticles," in (OSA, 2013), p. MTh2C.4.
20. J. M. Tucker-Schwartz, T. Hong, D. C. Colvin, Y. Xu, and M. C. Skala, "Dual-modality photothermal optical coherence tomography and magnetic-resonance imaging of carbon nanotubes," Opt. Lett. **37**, 872 (2012).
21. J. M. Tucker-Schwartz, K. R. Beavers, W. W. Sit, A. T. Shah, C. L. Duvall, and M. C. Skala, "In vivo imaging of nanoparticle delivery and tumor microvasculature with multimodal optical coherence tomography," Biomed. Opt. Express **5**, 1731 (2014).
22. R. V. Kuranov, J. Qiu, A. B. McElroy, A. Estrada, A. Salvaggio, J. Kiel, A. K. Dunn, T. Q. Duong, and T. E. Milner, "Depth-resolved blood oxygen saturation measurement by

dual-wavelength photothermal (DWP) optical coherence tomography," Biomed. Opt. Express **2**, 491 (2011).

23. T. Wang, J. Jacob Mancuso, V. Sapozhnikova, J. Dwelle, L. L. Ma, B. Willsey, S. M. Shams Kazmi, J. Qiu, X. Li, R. Asmis, K. P. Johnston, M. D. Feldman, and T. E. Milner, "Dual-wavelength multifrequency photothermal wave imaging combined with optical coherence tomography for macrophage and lipid detection in atherosclerotic plaques using gold nanoparticles," J. Biomed. Opt. **17**, 036009 (2012).
24. R. V. Kuranov, S. Kazmi, A. B. McElroy, J. W. Kiel, A. K. Dunn, T. E. Milner, and T. Q. Duong, "In vivo depth-resolved oxygen saturation by dual-wavelength photothermal (DWP) OCT," Opt. Express **19**, 23831 (2011).
25. S. Kim, M. T. Rinehart, H. Park, Y. Zhu, and A. Wax, "Phase-sensitive OCT imaging of multiple nanoparticle species using spectrally multiplexed single pulse photothermal excitation," Biomed. Opt. Express **3**, 2579 (2012).
26. J. M. Tucker-Schwartz, M. Lapierre-Landry, C. A. Patil, and M. C. Skala, "Photothermal optical lock-in optical coherence tomography for in vivo imaging," Biomed. Opt. Express **6**, 2268 (2015).
27. L. A. Dykman and N. G. Khlebtsov, "Gold Nanoparticles in Biology and Medicine: Recent Advances and Prospects," Acta Naturae **3**, 34–55 (2011).
28. P. K. Jain, X. Huang, I. H. El-Sayed, and M. A. El-Sayed, "Noble Metals on the Nanoscale: Optical and Photothermal Properties and Some Applications in Imaging, Sensing, Biology, and Medicine," Acc. Chem. Res. **41**, 1578–1586 (2008).
29. C. G. Khoury and T. Vo-Dinh, "Gold Nanostars For Surface-Enhanced Raman Scattering: Synthesis, Characterization and Optimization," J. Phys. Chem. C Nanomater. Interfaces **2008**, 18849–18859 (2008).
30. T. Vo-Dinh*1, Y. Liu1, B. M. Crawford1, H.-N. Wang1, H. Yuan1, J. K. Register1, C. G. K. 1Fitzpatrick I. for Photonics, D. of B. Engineering, D. of Chemistry, D. University, Durham, NC 27708-0281, and USA, "Shining Gold Nanostars: From Cancer Diagnostics to Photothermal Treatment and Immunotherapy," **2**, 1–8 (2018).
31. S. Liang, C. Li, C. Zhang, Y. Chen, L. Xu, C. Bao, and X. Wang, "CD44v6 Monoclonal Antibody-Conjugated Gold Nanostars for Targeted Photoacoustic Imaging and Plasmonic Photothermal Therapy of Gastric Cancer Stem-like Cells," Theranostics **5**, 970 (2015).
32. V. Raghavan, C. O'Flatharta, R. Dwyer, A. Breathnach, H. Zafar, P. Dockery, A. Wheatley, I. Keogh, M. Leahy, and M. Olivo, "Dual plasmonic gold nanostars for photoacoustic imaging and photothermal therapy," Nanomed. **12**, 457–471 (2017).

33. Y.-S. Chen, W. Frey, S. Kim, P. Kruizinga, K. Homan, and S. Emelianov, "Silica-coated Gold Nanorods as Photoacoustic Signal Nano-amplifiers," Nano Lett. **11**, 348–354 (2011).
34. L. Guerrini, R. A. Alvarez-Puebla, and N. Pazos-Perez, "Surface Modifications of Nanoparticles for Stability in Biological Fluids," Materials **11**, 1154 (2018).
35. C. Radloff and N. J. Halas, "Enhanced thermal stability of silica-encapsulated metal nanoshells," Appl. Phys. Lett. **79**, 674–676 (2001).
36. M. Hu, X. Wang, G. V. Hartland, V. Salgueiriño-Maceira, and L. M. Liz-Marzán, "Heat dissipation in gold–silica core-shell nanoparticles," Chem. Phys. Lett. **372**, 767–772 (2003).
37. A. M. Smith, M. C. Mancini, and S. Nie, "Bioimaging: second window for in vivo imaging," Nat. Nanotechnol. **4**, 710–711 (2009).
38. A. Payne and A. G. Podoleanu, "Direct electronic linearization for camera based spectral domain optical coherence tomography," in *Optical Coherence Tomography and Coherence Domain Optical Methods in Biomedicine XVII* (International Society for Optics and Photonics, 2013), Vol. 8571, p. 85712D.
39. R. A. Leitgeb, W. Drexler, A. Unterhuber, B. Hermann, T. Bajraszewski, T. Le, A. Stingl, and A. F. Fercher, "Ultrahigh resolution Fourier domain optical coherence tomography," Opt. Express **12**, 2156–2165 (2004).
40. C. Ding, P. Bu, X. Wang, and O. Sasaki, "A new spectral calibration method for Fourier domain optical coherence tomography," Optik **121**, 965–970 (2010).
41. K. Wang and Z. Ding, "Spectral calibration in spectral domain optical coherence tomography," Chin. Opt. Lett. **6**, 902–904 (2008).
42. G. Liu, Z. Zhou, and P. Li, "Phase registration based on matching of phase distribution characteristics and its application in FDOCT," Opt. Express **21**, 13241–13255 (2013).
43. G. Liu and Z. Chen, "Phase-Resolved Doppler Optical Coherence Tomography," Sel. Top. Opt. Coherence Tomogr. (2012).
44. B. H. Park, M. C. Pierce, B. Cense, S.-H. Yun, M. Mujat, G. J. Tearney, B. E. Bouma, and J. F. de Boer, "Real-time fiber-based multi-functional spectral-domain optical coherence tomography at 1.3 μm," Opt. Express **13**, 3931–3944 (2005).
45. S. Yazdanfar, C. Yang, M. V. Sarunic, and J. A. Izatt, "Frequency estimation precision in Doppler optical coherence tomography using the Cramer-Rao lower bound," Opt. Express **13**, 410–416 (2005).

46. L. Chin, A. Curatolo, B. F. Kennedy, B. J. Doyle, P. R. T. Munro, R. A. McLaughlin, and D. D. Sampson, "Analysis of image formation in optical coherence elastography using a multiphysics approach," Biomed. Opt. Express **5**, 2913–2930 (2014).

Chapter 7

CONCLUSIONS AND FUTURE WORK

In this thesis entitled "Advancements in structural and functional imaging using Fourier domain optical coherence tomography", we have explored the enhancement of structural and functional imaging capability of OCT based on endogenous and exogenous contrast mechanisms. The work described in the previous chapters detailed the development of techniques and methodologies to monitor the structural and functional changes based on contrast mechanisms derived from OCT signal. The work presented in this thesis falls into two categories namely technical developments and pre-clinical imaging applications using OCT.

Although OCT has established itself as a clinical imaging modality in ophthalmology and intravascular imaging, the present commercial clinical OCT systems operate at less than 200 kHz A- scan rate. In the first part of this thesis, we have explored the biological imaging applications of a 200 kHz SS-OCT for pre-clinical imaging. As a proof of concept, the techniques developed in the thesis were applied to monitor the wound healing process of a rat alkali burn model. The second part of the thesis discussed the application of a novel gold nanostar having plasmon resonance at 1064 nm for increased depth of imaging for photothermal OCT.

Chapters 3-5 discussed methodologies and advanced signal and image processing techniques that can be applied to OCT data to monitor the structural and functional integrity of cornea and iris.

Chapter 3 presented the feasibility study of correlation mapping based OCT angiographic imaging using a 200 kHz swept source system for *in vivo* imaging applications. At first, the correlation mapping technique was optimized for the 200 kHz swept source OCT system based on capillary phantom experiments. Quantitative analysis using three image quality parameters namely correlation signal to noise ratio, contrast to noise ratio and signal to noise ratio demonstrated that use of 5x5 kernel was optimum for the present OCT system. Further, the performance of correlation mapping angiography (cmOCT) was compared with the widely used speckle variance technique. Based on the image quality parameters discussed above, it

was found that cmOCT was better than speckle variance angiography technique. Although in the present study, 8 B-frames were used to obtain the measure of decorrelation at each transverse location for both techniques, unlike speckle variance, correlation mapping can be applied to just 2 B -frames if the SNR is good, where faster scanning and processing is desired. In the future, further studies will be carried out to optimize cmOCT technique for high speed SS-OCT by optimizing the B-M scan protocol and by increasing the SNR by signal processing techniques.

Chapter 4 investigated the therapeutic effect of topically applied exosome vesicles derived from human mesenchymal stem cells (hMSC) on alkali induced corneal wound healing process using the high speed swept source OCT. To automate the diagnosis process based on corneal wound healing and reduction of corneal inflammation, a graph based segmentation technique was adapted to measure the central corneal thickness from the acquired B-frames. The developed segmentation technique was then used to compare the central corneal thickness of untreated and hMSC treated rats. Although not statistically significant, it was found that the hMSC treated corneal wound healed faster than the untreated cornea based on the derived central corneal thickness values. Further, to generate corneal elevation maps from the acquired 3-D volumetric OCT data, a distance regularized level set based segmentation technique was applied. The pachymetry map thus generated can be used to monitor the burn injury and treatment progress. The techniques and methods described in this chapter can be applied to corneal segmentation problems in low SNR OCT scans. At present, the pachymetry mapping takes 150 minutes to segment corneal boundary from 120 B-fames based on the level set based approach. Further studies must be carried out to reduce the computation time in segmenting the cornea using level set based approach.

In chapter 5, nsOCT approach for OCT was described and nsOCT technique was used to probe the structural and dynamic changes within cornea during alkali induced injury which otherwise cannot be obtained from conventional OCT processing. The technique described bridges the gap between high resolution imaging and increased depth imaging in OCT by enhancing the sensitivity of OCT to nano scale structural changes within the sample. The chapter described the capability of nsOCT to detect structural changes with nano scale sensitivity between healthy cornea, injured cornea and also during the reparative phase of the injury at all depths within the cornea with high statistical significance ($p < 10^{-7}$). The chapter also reported the first description of corneal dynamics from the processed nsOCT images which otherwise have not been observed by conventional OCT processing techniques. Analysis of time varying spatial

period signals within the cornea revealed five frequency bands corresponding to endothelial (0.-2 – 0.085 Hz), neurogenic (0.085 – 0.25 Hz), myogenic (0.25 -0.5 Hz), respiratory (0.5 – 1.5 Hz) and cardiac band (1.5 -5 Hz). Further, changes in energy content within the endothelial and neurogenic bands were observed between the healthy cornea and injured cornea that suggested the potential of the described technique for functional assessment. Analysis of these dynamic changes within the cornea can be used as a tool to study the effects of noxious stimuli on the corneal surface and its effects on the physiological signalling within the organism. However, further studies are required to validate the hypothesis obtained from this study for the assessment of nociceptor activation and endothelial pumping mechanisms. The techniques presented in this chapter can be used for other ophthalmic applications such as for detecting the structural and functional changes occurring during corneal crosslinking and to detect and monitor the treatment progress on retinal pathologies such as macular degeneration and diabetic retinopathy.

In chapter 6, OCT system development for detecting exogenous contrast agent is described. The developed photothermal OCT system is used to image gold nanostars having an absorption peak at 1064 nm. The near infrared absorption peak of GNS makes it an ideal external contrast agent for deep tissue imaging. As a proof of concept study, preliminary experiments were carried out on gold nanostar embedded agar phantoms. As stated in the literature, an increase in photothermal induced OPD changes were observed with increase in laser power within the phantom model. Also, silica coated GNS's were imaged to investigate the enhancement in PT-OCT image contrast compared to uncoated GNS's. It was observed that silica coating enhanced the photothermal signals by over 50% compared to uncoated GNS's in PT-OCT imaging. This enhancement in image contrast and increased OPD changes indicate that, silica coating of GNS's enables faster and less resistance for heat conduction across the medium. Further, we report an imaging depth of 2.25 mm using the novel silica coated GNS's in an agar phantom model. The discussed technique offers a promising tool for molecular imaging at increased penetration depths within biological tissue. Future works in this area could target molecular imaging of cancerous cells *in vivo* that has taken up the novel GNS using PT-OCT imaging at depths greater than microscopy (>1 mm) and at higher resolution than photoacoustic tomography. Also, another research area that can be explored is optimization of nanoparticle tagged drug delivery, for e.g. in stem cell treatments, where, by imaging and tracking the accumulation and distribution of tagged GNS's, the drug distribution and its effects can be

tracked. Also, in such applications, PT-OCT can be used to optimize the shape and size of tagged nanoparticles for optimum drug uptake and tracking.

In conclusion, this dissertation represents advancements in structural and functional imaging using high speed Fourier domain OCT. The techniques presented in this thesis namely cmOCT angiography, nano-sensitive OCT and PT - OCT are able to detect the microstructural changes and morphological changes within the tissue as a function of space and time, all of which are critical features in medical imaging especially, to detect the onset of a disease, its pathogenesis and in monitoring treatment efficacy. The techniques developed in this thesis can be integrated together thereby providing information on morphological transitions, vascular remodelling, increased sensitivity to microstructural changes in space and time, and targeted molecular imaging, from the same OCT data set useful for clinical and preclinical applications.